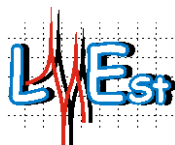# DYNAMICS OF MECHANICAL SYSTEMS:
A PERSPECTIVE FROM THE LMEST-UFU

Marcelo Samora Sousa Jr.
Izabela Batista da Silva
Jefferson Silva Barbosa
Aldemir Ap. Cavalini Jr.
Valder Steffen Jr.
Organizadores

UFU

LMEst

NAVEGANDO

DYNAMICS OF MECHANICAL SYSTEMS: A PERSPECTIVE FROM THE LMEST-UFU

1ª Edição Eletrônica

Marcelo Samora Sousa Jr
Izabela Batista da Silva
Jefferson Silva Barbosa
Aldemir Ap Cavalini Jr
Valder Steffen Jr
(Orgs.)

DYNAMICS OF MECHANICAL SYSTEMS: A PERSPECTIVE FROM THE LMEST-UFU

1ª Edição Eletrônica

NAVEGANDO

Navegando Publicações

NAVEGANDO

Índice para catálogo sistemático

Engenharia   620

Editores

Carlos Lucena – UFU, Brasil
José Claudinei Lombardi – Unicamp, Brasil
José Carlos de Souza Araújo – Uniube/UFU, Brasil

Conselho Editorial Multidisciplinar

Summary

PREFACE[*]

Dynamics of Mechanical Systems is an important subject in Engineering Sciences. It encompasses a number of classical topics such as vibration and acoustics; modal analysis, identification and control; mathematical modeling; experimental techniques and signal analysis. More recently, various new topics have been incorporated, such as smart structures; optimization and inverse problems; uncertainty analysis; and robust design and machine learning. Some of these new topics are mathematical tools that are used to improve engineering system characteristics and fulfill specific design requirements. Applications are found in a number of engineering areas, including aerospace, mechanical and mechatronics, naval, and civil, to mention only the most significant ones. This means that university laboratories dedicated to dynamics of mechanical systems would hardly touch all these challenging topics and application areas. For this reason, this book gives a modest overview of the dynamics of mechanical systems from the perspective of the Laboratory of Mechanical Structures (LMEst) "José Eduardo Tannus Reis", School of Mechanical Engineering (FEMEC), Federal University of Uberlândia (UFU) in Brazil.

In this context, the present book is intended to give a general picture of the research work that is currently developed at the Laboratory of Structural Mechanics, LMEst-UFU. All graduate students have been invited to submit a chapter regarding the work performed for their MSc theses and PhD dissertations. In this sense, some of the chapters contain substantial scientific material (since the students involved had already been working for two or three years on their subject) and others are devoted to general aspects of the topics studied (since the students have been recently enrolled in the laboratory). However, all the chapters considers important aspects of the dynamics of mechanical systems and points out relevant research efforts on subjects that encompass structural health monitoring, smart materials, acoustic levitation, viscoelastic

---

[*] doi - 10.29388/978-85-53111-97-8-0-f.1-2

materials, hydrodynamic and magnetic bearings, and smart rotating machines.

<div align="right">Professor Valder Steffen Jr
July 2019</div>

ACKNOWLEDGMENTS

Damage Detection Integrating ISHM and LWSHM Techniques[*]

Lucas Altamirando de Andrade da Rocha
lucasaarocha@ufu.br

Advisors: Valder Steffen Jr and Roberto Mendes Finzi Neto

Abstract: Currently, structural health monitoring (SHM) represents one of the main areas of interest in engineering, being applied both for maintenance cost reduction and operational safety. In this contribution, a hybrid SHM system is proposed as a complementary methodology for the damage diagnosis of a typical aeronautical material panel (aeronautical aluminum plate 2024-T3), through the integration of two SHM techniques, namely the electromechanical impedance technique and the Lamb waves. For the diagnosis, a damage metric extracted from the impedance signatures of the structure was used in conjunction with an algorithm for localization of the damage by considering Lamb waves. In addition, temperature compensation techniques were systematically employed to avoid false diagnoses and a statistical model was developed to establish threshold indices according to a predefined confidence level. Thus, this work presents an evaluation of the sensitivity of the proposed techniques. Finally, the results show the great potential for the integration of the two techniques together with statistical approach.

Keywords: Structural Integrity Monitoring, Electromechanical Impedance, Lamb Waves, Temperature Compensation, Fault Diagnosis

INTRODUCTION

Two examples of active local sensing for damage detection using PZT sensors are the Lamb Wave-based SHM (LWSHM) (Su et al. 2004) and the impedance-based SHM (ISHM) (Annamdas *et al.* 2014). Advantageous features of these transducers include low cost, they generally require low power consumption and operate at higher frequency ranges (typically above 30 kHz) providing high sensitivity for

---

the sensors. However, high-frequency signals also reduce the sensitivity area of the sensors (Ramadas et al. 2011). The LWSHM method monitors the properties of elastic mechanical waves that travel in the structure carrying information for damage along their path. On the other hand, the ISHM method monitors variations in the electromechanical impedance of a piezoelectric sensor bonded to (or embedded into) the monitored structure. The ISHM method generally uses the real part of the impedance since the imaginary part, which corresponds to the capacitive part of the response, is more sensitive to temperature variation.

A major drawback for active SHM systems that use piezoelectric transducers is the influence of temperature. Small temperature variation can lead the SHM system to give false positive diagnostics where no mechanical damage exists in the monitored structure (Palomino et al. 2014). Therefore, temperature compensation is imperative to obtain a reliable diagnostic of the structural integrity (Cavalini et al. 2015, Baptista et al. 2014).

For the ISHM technique, the effective frequency shift (EFS) through correlation analysis is the most commonly used temperature compensation method. Sun (1995). The frequency shift for temperature compensation through this technique is usually chosen from the result of a simple optimization problem aiming to maximize the correlation coefficient. Consequently, the damage metric (DM) is always minimized even when damage is found in the impedance signature. As the impedance signatures are well correlated, this characteristic can mitigate the low sensitivity of the technique since the DM is always minimized in the temperature compensation procedure, as shown by Rabelo (2015). In the present work, the authors propose the use of a pre-recorded set of measurements corresponding to the pristine condition encompassing several temperatures to apply only a frequency shift that corresponds to the temperature gradient of each measurement. As a result, the horizontal frequency shift due to temperature change will be compensated according to the optimization result.

In the LWSHM technique, a review of the different methods is presented in the literature (Rocha et al. 2014). The technique of temperature compensation selected for the Lamb Wave method is the reconstruction of the baseline signal to the analysis temperature,

presented by Liu (2016). The method was developed to compensate the baseline signal for the current signal temperature. The Hilbert transform is used to compensate for the phase of the baseline signal. Orthogonal Match Search (OMP) is used to compensate for the amplitude of the baseline signal. Temperature compensation methods based on numerical modeling have been studied by many researchers. Marzani and Salamone (2012) propose a comprehensive Lamb wave propagation model to predict the full pitch-catch signals under varying temperature. Numerical versus experimental studies demonstrate that the high accuracy of temperature compensation of Lamb waves signals can be obtained on metallic structures. However, regarding applications on composite structures, an accurate physical model is difficult to be derived.

The statistical analysis in the decision-making process is one of the main tools of a SHM system. Previous research works on LWSHM, such as the ones by (Ramadas et al. 2011, Sorohan et al. 2011) and others on ISHM (Annamds et al. 2014, Palomino et al. 2014) have been typically used to identify structural damage in different contexts.

This work investigates the use of the interaction between two SHM techniques, namely the electromechanical impedance technique and the Lamb waves, since such interaction has not yet been explored enough. The interaction is based on the actuator efficiency (Liang et al. 1994) so it is possible to select an optimal frequency from the impedance curve of the structure, reducing the error in the location of the damage. A limiting factor is that there is no commercial equipment that allows this interaction, therefore, this work used a hardware capable of using both cited techniques simultaneously (developed for this application), in addition, the present paper took into account the condition of variable temperature to improve system performance when diagnosing structure damage. Next, a statistical model was developed to determine the damage threshold indices according to a predefined confidence level. In addition, this work seeks to bring to light the importance of the interaction of the two techniques, especially in cases where there is variation of temperature during the monitoring.

LAMBWAVE-BASED STRUCTURAL HEALTH MONITORINNG (LWSHM)

In this section, the principles on which the technique of Lamb waves are based on are discussed in conjunction with the methodology through which structural damage is detected. Problems related to temperature variation are also presented.

Physical principles of the Lamb Wave (LW) technique

Basically, Lamb waves are elastic waves that propagate through solid media and thus are subject to reflections and attenuations imposed by this propagation medium. When considering the monitored structure as the propagation medium, structural damage also changes this medium. This technique has proven to be a reliable method to detect the presence of damage in structures, including its location, severity, and the type of damage (Raghavan and Cesnik 2005).

Raghavan and Cesnik (2005) define two usual methods of diagnosis associated with the LW technique, namely, the pulse-echo and the pitch-catch methods. Both LW approaches make use of digital signal processing algorithms in order to extract features related to the propagation medium of the acquired signal.

Temperature compensation

The temperature effects on the time variant signal can be observed as a change in signal amplitude and phase (Roy et al. 2014). Based on these effects, it can be assumed that a temperature effect on a LW signal can be approximated by a time-stretch signal and amplitude.

It was used temperature compensation method based on the baseline signal reconstruction for monitoring the temperature of the damage detection signal based on Lamb wave (Liu et al. 2016). So, Liu used the Hilbert transform to compensate for the signal phase of the baseline. Orthogonal matching pursuit (OMP) is used to counterbalance signal amplitude. In Figure 1 is the flowchart proposed by Liu for the reconstruction of the baseline to the desired temperature.
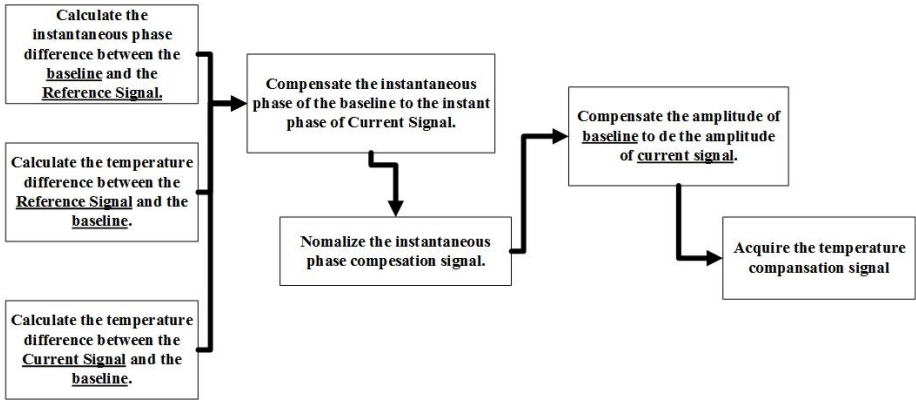
Figure 1: The flowchart of the proposed temperature compensation method (Adapted from Liu (2016))

One can find more details on Liu's (2016) approach.

In the present study, the temperature dependence is highlighted showing that a temperature variation can influence on decision-making, leading to a false interpretation of the current structural health state.

IMPEDANCE-BASED STRUCTURAL HEALTH MONITORING

In this section, the basics of the Impedance-based SHM technique is briefly described in conjunction with the methodology used to detect structural damage. Problems related to temperature variation are also discussed.

Physical principle of ISHM technique

The ISHM technique uses the piezoelectric properties of the PZT patch that is installed in the structure being monitored. The PZT patch is bonded to a structure and a low electric voltage is applied (Raju 1997), generating a strain in the PZT patch. Then, the response of the mechanical vibration is transmitted to the sensor in the form of an electrical response. If a structural modification occurs, such as damage,

the electric response of the PZT patch will change accordingly. The well-known mechatronic model that describes the measurement process is shown in Fig. 2 for a single-degree-of-freedom (DOF) system:
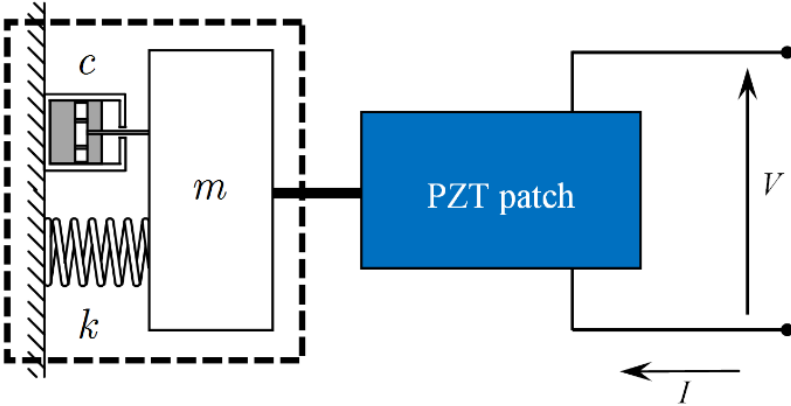
Figure 2: Single DOF model illustrating the ISHM method.

For this system, Liang (1994) demonstrated that the PZT's admittance, $Y(\omega)$, which is the inverse of the impedance, can be written as a function of the combined PZT actuator and structure mechanical impedance, as given by Eq. (1):

$$Y\left(w\right) = jwa\left[\bar{e}_{33}^{T}\left(1 - j\delta\right) - \frac{Z_{s}\left(w\right)}{Z_{s}\left(w\right) + Z_{a}\left(w\right)}d_{3x}^{2}\hat{Y}_{xx}^{E}\right] \tag{1}$$

Where $Z_a(\omega)$ and $Z_S(\omega)$ are the actuator's and structure's mechanical impedances, respectively. $\hat{Y}_{xx}^{E}$ is the complex Young's modulus of the PZT with zero electric field, d_{3x}^{2} is the piezoelectric coupling constant in the arbitrary x direction, $\bar{\varepsilon}_{33}^{T}$ is the dielectric constant at zero stress, δ is the dielectric loss tangent of the PZT, ω is the excitation frequency, a is a geometric constant of the PZT and j is the imaginary unit. Assuming that the mechanical properties of the PZT patch do not vary during the measurement procedure, Eq. (1) shows that the electrical impedance of the PZT patch is directly related to the structure's impedance.

Damage Index

The curve that represents the impedance response provides a qualitative assessment of the damage. For a quantitative assessment of the failure, a previously defined Damage Metric (DM) is used (Palomino et al. 2014). In the present contribution, the damage metric used is the Correlation Coefficient Deviation (CCD). This DM uses two signals, where the first corresponds to the baseline and the second corresponds to the test measurement. The CCD is given by Eq. (2):

$$CCD = 1 - \frac{1}{n}\sum_{i=1}^{n}\left\{\frac{\left[\mathrm{Re}\left(Z_{1,i}\right) - \mathrm{Re}\left(\bar{Z}_1\right)\right]\left[\mathrm{Re}\left(Z_{2,i}\right) - \mathrm{Re}\left(\bar{Z}_2\right)\right]}{S_{Z_1}S_{Z_2}}\right\} \qquad (2)$$

where $\mathrm{Re}(Z_{1,j})$ and $\mathrm{Re}(Z_{2,j})$ are the real parts of the impedance from the baseline and test measurement at frequency i, respectively; n is the number of frequency points, $\mathrm{Re}(\bar{Z}_1)$ and $\mathrm{Re}(\bar{Z}_2)$ are the average of the baseline and test measurements, respectively; S_{Z_1} and S_{Z_2} are the standard deviations of the baseline and test measurements, respectively.

Temperature compensation: Effective Frequency Shift (EFS)

Temperature variation effects are known to cause horizontal (frequency) and vertical (amplitude) shifts on impedance signatures. Figure 3 shows a flowchart to illustrate a temperature rate approach developed by (Rabelo et al. 2015). The method starts by obtaining the impedance signatures of the healthy system evaluated. The impedance signatures of the system for an unknown condition are also required, so that the optimizer is responsible for shifting both the frequency and amplitude values. The Impunknown signatures are compared with the Impbaseline ones by means of a given objective function, i.e., a damage metric, as presented by Eq. (1) and Eq. (2).
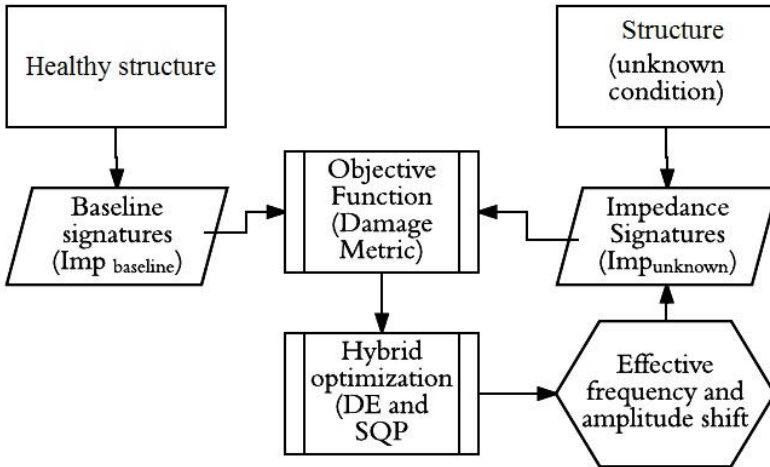
Figure 3: Proposed temperature compensation flowchart.

In Fig. 3, if the procedure converges to a minimum value of the objective function, the effects of temperature variation are compensated through frequency shifts and vertical shifts of the design variables. If this is not the case, the optimization procedure continues the search for new frequency and amplitude shifts. The optimization process proceeds iteratively until convergence is achieved, which can lead either to temperature compensation (if the objective function is close to zero) or, otherwise, represents a damage indication associated with temperature compensation.

DETERMINATION OF THRESHOLD

In SHM, it is highly desirable that a reliable threshold level is established based on the information acquired for the pristine condition of the structure. After the data is acquired and processed, next step is the preparation of the raw data for analysis. The first data operation is data editing. This refers to the pre-analysis operations that are designed to detect and eliminate spurious or degraded data signals that might have resulted from acquisitions and recording processes such as excessive noise, signal dropouts, or even from an external cause such as a power supply failure (Bendat and Piersol 2000).

Threshold Determination with Statistical Process Control and Confidence Intervals

A concept from Statistical Process Control (SPC) was used to determine the Upper Control Limit (UCL) and the Lower Control Limit (LCL) of the damage indexes, since the SPC technique assumes successive deviations from a normally distributed function. Since this is not always the case and we are interested on the upper limit value for the threshold, this work proposes a methodology for the determination of the threshold by using the concept of confidence interval.

Therefore, after obtaining these intervals the threshold was determined according to Eq. 12:

$$DI_{threshold} = m_{x_{max}} + 3S_{x_{max}} \tag{3}$$

where $\mu_{x_{max}}$ $\mu_{x_{max}}$ is the upper limit of the population mean and $\sigma_{x_{max}}$ the upper limit of the population standard deviation, both obtained choosing a significance level $\alpha = 1\%$. It should be noted that the choice of the decision threshold influences both the detectable size and the probability of a false positive.

EXPERIMENTAL DESIGN AND SETUP

For testing the methodology presented in this contribution, a 2024-T3 aeronautical aluminum plate, with dimensions 500x500x1,6mm and mass of 1,120 kg was selected. This panel was instrumented with eight PZT patches (diameter 10 mm x 0.5 mm thickness, of type 5H). The actuator sensors were bonded using an epoxy-based adhesive (Hysol EA9320NA). The test specimen was prepared as shown in Fig. 4 a).

The arrangement of the PZT patches was chosen so that the damage localization procedure is facilitated, thus covering a large area of the structure. The idea is not to interfere with the functionality of the structure (the sensors are grouped in the center of the plate). In addition, the position of the inserts was inspired by the *CLoVER* sensor architecture developed by Salas and Cesnik (2008). In Fig. 4 b) we can observe the architecture of the instrumentation used on the panel.
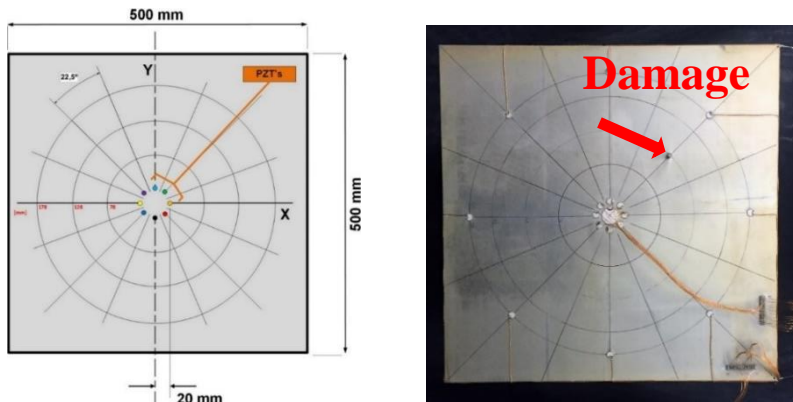
Figure 4: a) Positions of the sensor network, b) Structure of instrumented aeronautical material.

To simulate the damage in the structure, a structural modification was made by adding a small mass to the plate. To this end, a pair of NdFeB, Grade N52 (B444-N52) magnets of dimensions 6.35x6.35x6.35mm and 1.92g weight were used. For signal generation, a National Instruments function generator (PXI-5412) was used. Digitizer (PXI-5105) was used to acquire the signal.

For temperature control a climate chamber EPL-4H series Platinous was used, which employs a system BTHC (Balanced Temperature and Humidity Control) for controlling temperature and humidity. Thus, EPL-4H chamber operates at temperatures ranging from -40°C to 180°C with a resolution of ±0.5°C.

All tests were performed in free-free situation, to minimize interference from other sources of noise during the experiment (for example, any vibration of the climatic chamber, among others). The cable stiffness that connects the structure to the data acquisition equipment is another important factor when considering the repeatability of the experiment, especially when the impedance analysis is made. Thus, an intermediate connector with low rigidity is used.

The time to stabilize the temperature inside the environmental chamber was set to 45 minutes (Incropera 2006). Thus, with the stable temperature, the baselines of the healthy structure were acquired at the target temperatures. The impedance frequency range was selected according to the highest peak density to have the best sensitivity to damage (Moura 2006).

Table 1: The settings required for the collection of database signals.

Impedance	Lamb Waves:
Frequency range: 80000 Hz to 90000 Hz;	Sampling rate 6ms / s to 3000 samples
500 points per frequency;	Amplitude of actuation of $20V_{pk-pk}$;
100 samples per average frequency point;	Hann modulation of 3.5 (SOHN, 2005);
30 signatures for temperature readings.	Readings interval of 100 ms;
	Number of readings equal to 100 per PZT.

The proposed SHM system uses multiplexers similar to the topology proposed by Finzi Neto (2010). In addition, hardware has been implemented in a second network enabling multiplexers to operate simultaneously with the two SHM techniques considered here (LWSHM and ISHM).

Hybrid SHM System

The focus of this work is to incorporate the interaction of two techniques (ISHM and LWSHM) in the task of diagnosing damage in the analyzed structure (Fig. 5), thereby reducing the false negative responses.

For this task, it is acquired the impedance curves of each of the 8 PZT's; from these curves, it is possible to identify the presence of damage to the structure but does not locate. With the impedance curves are selected the best frequency for each sensor to implement the analysis with Lamb waves. Accordingly, the frequency is selected where the impedance curve has the smallest value within the frequency range selected, in other words, where the elastic Lamb wave will have greater amplitude, facilitating damage locating algorithm (where the actuator efficiency is maximum - according to Liang (1994)). This step has the function of estimating and locating the damage by the triangulation method from the TOF of the wave (note also that the effect of temperature is considered in this step and compensated). With identified and localized damage begins the statistical analysis that will finally lead to the diagnosis of the state of the structure.
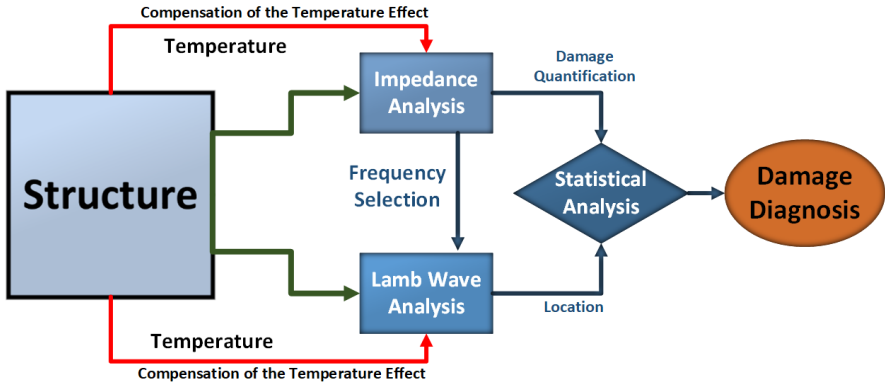
Figure 5: Functional diagram of the proposed SHM system.

RESULTS

With the available database, it is possible to analyze the structure to any temperature within the range studied. To test the system, a temperature of 25°C and a random damage in the structure at the position given by 73×64mm was selected, as shown in Fig. 4 b).

Then the impedance signatures of all PZT pellets were collected. In Figure 6 are present in the average (30 signatures) signatures of eight PZT wafers already offset the effect of temperature. Also note that the trend curves of signatures have already been subtracted to demonstrate the selection of frequencies for the evaluation through the Lamb waves.

In Figure 6 it can be noted that the CCD damage index structure with a random damage point to the existence of damage. Also in Fig. 6, "ND" represents the structure without giving and "D" the damage condition, since the threshold value is calculated independently for each actuator. In Table 1show the frequencies selected.

For the analysis with the Lamb waves it is necessary to select the best frequency within the selected range (80 kHz to 90 kHz). Table 1 shows the frequencies selected by the impedance signature curves of the 8 PZT's.

With the selected frequencies, 100 readings were performed for each PZT sensor, in addition to the readings of four PZT sensors neighboring the PZT actuator. To exemplify the procedure, consider PZT#2 as the actuator. PZT#2 is then responsible for the excitation and the signal is collected by PZT#n-2, that is, by PZT # 8. After completing the 100

readings, the same process is repeated, but now using PZT#1 (PZT#n-1) as the sensor, until you reach PZT#4 (PZT#n+2).
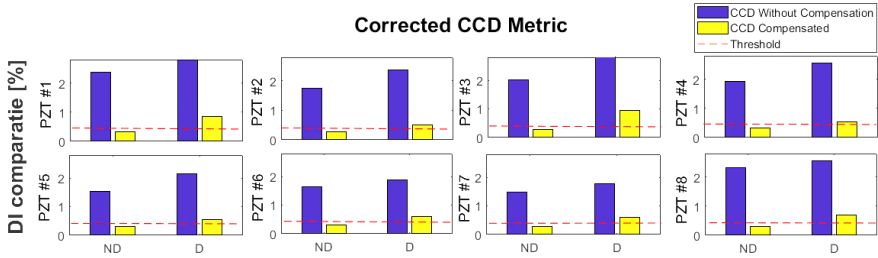
Figure 6: CCD values in the complete analysis for the conditions with and without temperature compensation, for the condition with random damage.

As in impedance, the effect of temperature in this case is also an error factor to be considered, especially when determining the TOF of each signal. Considering the temperature compensation algorithm for Lamb waves, based on the reconstruction of the baseline signal for the temperature of the monitoring signal, all the baselines are compensated for the temperature of 25ºC. The signals then pass through a high-pass FIR filter with a cutoff frequency of 1 kHz to minimize the effects of the thermal chamber vibration.

Figure 7 a) shows a collection of the possible locations (black point) of the damage and their average position (red point).
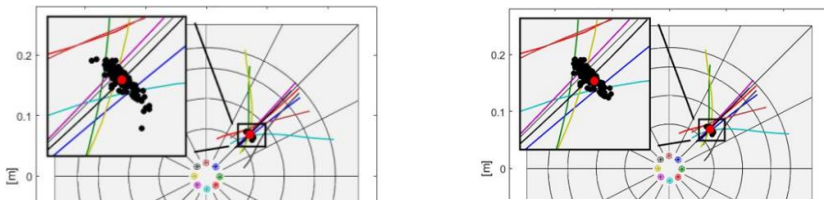
Figure 7: a) possible locations for the damage, b) damage location results after statistical processing.

At this point of processing, the error value can still be reduced by applying the Chauvenet criterion and excluding outliers. In addition, it is necessary that the sample has a normal distribution and, for that, the JB test was applied. Table 2 shows the result of the normality test.

In Table 2, the skewness and kurtosis are the statistical moments of the sample analyzed. A simple normality test was performed to verify

the asymmetry (skewness) of the sample (this should be close to zero), characterizing the PDF symmetry (Gauss probability density). It is also seen that the value of kurtosis is of the order of 3.0, indicating the peak shape similar to a classical bell-shape of a Gaussian distribution-corresponds to the null hypothesis, i.e., the sample follows a normal distribution (the result being 0 means that the null hypothesis should not be rejected). The p-value indicates the result for the hypothesis test. If the value of p is less than the level of significance, (in this case,) it indicates that the null hypothesis should not be rejected.

Table 2: Results of the Normality Test for the Lamb Waves Technique.

Skewness	Kurtosis	H_0	p-value [%]	Lim. Val.	Crit. Val.
0,0278	2,9831	0	0,5000	0,4032	5,8581

The last two columns correspond to the limit values and the critical values of the normality tests. To accept the null hypothesis, the critical value must be greater than the limit value. Therefore, it can be concluded that the sample originates from a Gaussian distribution with 99% confidence.

Figure 7 b) shows the possible Cartesian location of the damage after the statistical treatment, being estimated in 72.3mm in the X axis and 66.4mm in the Y axis, which corresponds to a relative error percentage of 1,14%.

Considering Figures 6 and 7 b) it is possible to make a fault diagnosis of the structure, where the damage was detected by the impedance signatures and quantified by the CCD metric. Since the location can be estimated from Lamb waves with error less than 2%.

CONCLUSIONS

Considering that the integration of the two SHM techniques is considered somewhat new, this paper presents a combination between the technique known as electromechanical impedance and Lamb waves, with the purpose of obtaining better diagnostics of damaged structures (aeronautical structure, in the present case). One of the main limitations of studies and applications in this area is the requirement of specific instrumentation that meet the needs of the techniques involved.

Statistical methods were proposed in order to verify the success rate of damage detection considering the barely-visible impact damage introduced under the influence of varying temperature. Temperature compensation procedures were applied to reduce undesired effects in the signal analysis as due to temperature change.

The detection system successfully detected the damage introduced with an error of less than 2%.

The experiment conducted through this study used a temperature compensation method for both SHM techniques. These procedures showed good results in the considered temperature (25°C). Statistical analysis included normality tests to ensure that the samples followed a Gaussian distribution for all sensors.

The proposed hybrid monitoring system was able to identify and locate the damage with a 1.14% error. The temperature chosen for the experiments was 25ºC with the aid of the climatic chamber EPL-4H. Clearly, the choice of this temperature range does not correspond to the full temperature range of an aircraft wing surface (-55°C to +60°C). However, the intention was to provide an illustration of the proposed method.

Finally, the combination of the two SHM techniques considered not only detect damage in the aeronautical structure, but also locate the damage. The present contribution demonstrated that both techniques (LW and ISHM) present interesting characteristics when working together to achieve successful SHM.

REFERENCES

Annamdas, V. G. M.; Ian, L. S.; Pang, H. L. J.; Soh, C. K., 2014 "Monitoring of Fatigue in Welded Beams Using Piezoelectric Wafer Based Impedance Technique". J. Nondestruct. Eval., 33(1): 124-140.

Baptista, F. G.; Budoya, D. E.; Almeida, V. A. D.; Ulson, J. A. C. An Experimental Study on the Effect of Temperature on Piezoelectric Sensors for Impedance-Based Structural Health Monitoring. Sensors v. 14, p. 1208-1227, 2014.

Bendat, J. S.; Piersol, A. G., 2000 "Random Data" – Analysis and Measurement Procedures. 4th edition. ISBN: 978-0470248775. John Wiley, New York, NY, USA.

Cavalini Jr., A. A.; Oliveira, D. D.; Rabelo, D. S.; Finzi Neto, R. M.; Steffen Jr., V., 2015 "Fault detection in a rotating shaft by using the electromechanical impedance method and a temperature compensation approach". In: Proc. CILAMCE 2015, Rio de Janeiro, Brazil, November.

Finzi Neto, R. M., 2010 "A Low-cost electromechanical impedance-based SHM architecture for multiplexed piezoceramic actuators". Journal of Structural Health Monitoring.

Incropera, F. P.; Dewitt, D. P.; Bergamn, T. L., 2006 "Fundamentals of Heat and Mass Transfer". Wiley edition 6, p. 272-275.

Liang, C.; Sun, F. P.; Rogers, C. A., 1994 "Coupled electromechanical analysis of adaptive material system – determination of actuator power consumption and system energy transfer". Journal of Intelligent Material Systems and Structures, p. 21-20.

Liu G, Xiao Y, Zhang H, Ren G 2016 "Baseline signal reconstruction for temperature compensation in Lamb wave based, damage detection". Sensors 16(8): 1273.

Marzani, A.; Salamone, S., 2012 "Numerical Prediction and Experimental Verification of Temperature Effect on Plate Waves" Generated and Received by Piezoceramic Sensors. Mechanical Systems and Signal Processing, 30:204–217.

Moura Jr., J.R.V., Steffen Jr., V. 2006 "Impedance-Based Health Monitoring for Aeronautic Structures using Statistical Meta-modeling". J. Intell. Mater. Syst. Struct. 17(11): 1023-1036.

Palomino, L.V.; Steffen Jr., V.; Finzi Neto, R. M., 2014 "Probabilistic Neural Network and Fuzzy Cluster Analysis Methods Applied to Impedance-Based SHM for Damage Classification. Shock and Vibration", vol. Article ID 401942.

Rabelo, D. S.; Guimarães, C. G.; Cavalini Jr.; A. A.; Steffen Jr., V., 2015 "A comparative study of temperature compensation techniques for impedance-based structural health monitoring systems" In: Proc. of the 1st Workshop in Industrial Mathematics, Modelling and Optimization. Catalão, GO, Brazil.

Raghavan, A., Cesnik, C. E. S., 2005 "Lamb-Wave Based Structural Health Monitoring. Damage Prognosis for Aerospace, Civil and Mechanical System", Wiley, Cap.11, pp. 235-274.

Ramadas, C.; Balasubramaniam, K.; Joshi, M.; Krishnamurthy, C. V., 2011 "Interaction of Lamb mode (A0) with Structural Discontinuity and Generation of Turning modes" in a T-joint, Elsevier.

Rocha, L. A. A.; Rabelo, D. S.; Steffen Jr., V., 2014 "Identification of Damage in Structures with Rivets using Impedance techniques and controls of Lamb Waves", CONEM 2014 no. 0503.

Roy, S.; Lonkar, K.; Janapati, V.; Chang, F. K., 2014 "A Novel Physics-Based Temperature Compensation Model for Structural Health Monitoring Using Ultrasonic Guided Waves". Structural Health Monitoring: DOI: 10.1177/1475921714522846.

Salas, K. I.; Cesnik, C. E. S., 2008 "Design and Characterization of the CLoVER transducer for structural health monitoring". Proceedings of the 15th SPIE Symposium on Smart Structures and Materials & Nondestructive Testing and Health Monitoring, March 2008, Paper #6935-11.

Sorohan, S.; Constantin, N.; Gavan, M., Anghel, V., 2011 "Extraction of Dispersion Curves for Waves Propagating in Free Complex Waveguides by Standard Finite Element Codes", Ultrasonics 51.

Su, Z.; Ye, L., 2004 "Lamb Wave-based Quantitative Identification of Delamination in CF/EP Composite Structures Using Artificial Neural Algorithm", Composite Structures 66.

Sun, F. P.; Chaudhry, Z.; Liang, C.; Rogers, C. A., 1995 "Truss structure integrity identification using PZT sensor–actuator". J. Intelligent Material Systems and Structures, vol. 6, 134–139.

Comparison of Mathematical Models of Magnetorheological Actuators[*]

Philippe César Fernandes Teixeira
phil@ufu.br

Advisors: Valder Steffen Jr and Aldemir Ap. Cavalini Jr

Abstract: Semi-active actuators have been gaining more attention in systems engeneering design. An interesting alternative is the magnetorheological damper that is applied, for instance, in the support of vehicle seats and smart suspensions of bridges and buildings. Parametric and non-parametric approaches can be used to model magnetorheological actuators, in which the former presents well-established models in the literature and has, as an advantage, fast convergence. In this context, the present work aims at comparing the Bingham, modified Bouc-Wen, and Hysteretic models dedicated to magnetorheological actuators. Typical inverse problems were solved to minimize the difference between the studied models with experimental data. The obtained results demonstrated that the Hysteretic model is better adapted to represent the experimental data, presenting lower computational cost and easy implementation.

Keywords: MR actuator, Mathematical Model, Fuzzy Logic, Differential Evolution, Smart Materials.

INTRODUCTION

The area of mechanical vibration has been increasingly investigated over the years. Lately, issues related to vibration control, mathematical modeling of systems, and identification of sensitive parameters have been a cause for concern and investment as a way to better understand how mechanical systems work. This becomes more complicated when nonlinear behavior appears, making their modeling and dynamic behavior prediction more difficult.

---

[*] doi - 10.29388/978-85-53111-97-8-0-f.23-38

Regarding energy absorbing systems, Bai, Wereley, and Cho (2016) affirm that passive energy absorbers can only be adapted to a specific level or type of excitation and payload weight. The authors mentioned that magnetorheological (MR) actuators are appropriate to improve performance and attenuate the vibration of dynamic systems, being possible to adapt the actuation force to different excitation and useful weight configurations.

According to Zhang et al. (2016), MR fluids behave as a Newtonian fluid without applying the magnetic field. Thus, concerning vibration control applications, MR actuators operate as a passive device in the absence of magnetic field. However, Cavalini Jr et al. (2015) affirm that when the magnetic field is applied, the rheological properties are modified considerably, becoming a semi-solid, with viscoplastic characteristics, and explain that the equivalent damping and stiffness properties of the MR damper are modified when the fluid is subjected to a magnetic field.

MR actuators are commonly applied to different engineering systems for vibration control purposes, such as semi-active suspension of vehicles. According to Crosby and Karnopp (1973), when this concept emerged in the early 1970s, researchers saw in this new suspension an opportunity for various engineering applications. Klinger et al. (1976) used the concept of semi-active MR dampers in trains. Margolis and Hrovat (1976) applied a similar system in tractors and off-road vehicles. Miller and Nobles (1988) used this technology in military tanks.

Zhang et al. (2016) studied the effect of the ferromagnetic particles size embedded in the MR fluid. For this, they performed three different experiments with particles of different sizes. The results showed that MR fluids with particles between 1.5 μm and 2.8 μm mean diameter are better for engineering applications. Barber (2013) mentioned that the MR fluid and the devices using it were successfully marketed for the first time in 1998 by LORD Corporation. They marketed a product called Motion Master, which was a suspension system for vehicle seats.

The motivation for using actuators with MR fluid is associated with the low energy requirement for its operation. In addition, they have the advantage of changing the magnetization state of the embedded particles instantaneously; they are controllable and completely reversible. These characteristics are important from the vibration control point of view

(Cavalini Jr et al., 2015). It is noticed that MR actuators are non-expensive devices that contribute, for example, to the comfort and safety of passengers in vehicles, buildings, and bridges.

In this context, the present work is devoted to the comparison of existing mathematical models of MR actuators aiming at determining the representativeness of each model. Bingham, modified Bouc-Wen (BW), and Hysteretic models are compared with experimental results obtained by using the MR actuator RD-8040-1 (LORD Corporation®). These models are revisited in the following sections, prior to presenting the experimental set-up used to characterize the MR actuator. Typical inverse problems are solved to minimize the difference between the studied models with the experimental data. The obtained results demonstrated that the Hysteretic model is better adapted to represent the measured experimental data, presenting lower computational cost and easy implementation.

BINGHAM MODEL

The Bingham model is used to describe the stress-strain behavior of MR fluids (Dyke, 1997; Truong and Ahn, 2012). It is a rather simplified model, depending only on a few parameters. The simplifications imposed by the Bingham model avoids the adequate representation of the hysteresis behavior of MR fluids. The physical model of the MR fluid behavior idealized by Stanway, Sproston, and Stevens (1987), based on the Bingham model, is shown in Fig. 1. The equation that represents the Bingham physical model is given by Eq. (1):

$$F = f_c \text{sign}(\dot{x}) + c_0 \dot{x} + f_0 \qquad (1)$$

where c_0 represents the viscous damping, f_c is the dry friction, f_0 is the force in the accumulator, and F is the force generated by the MR actuator when a displacement x is applied ([·] stands for the time derivative of the variable [ ]).
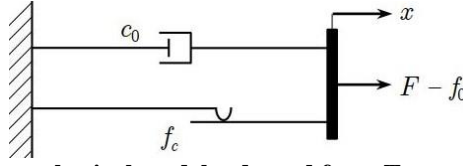
Figure 1: Bingham physical model, adapted from Truong and Ahn (2012).

MODIFIED BOUC-WEN MODEL

The BW model is extensively used for modeling the hysteresis phenomenon associated with non-Newtonian fluids (Wen, 1976). The so-called modified BW model associates a viscous damper c_1 and a linear spring k_1 with the hysteretic phenomenon (Bouc-Wen) to better describe the fast drop in the force when the piston speed of the MR actuator is zero. The modified BW model used in this work follows the formulation given by Dyke (1997). The physical model of the MR fluid behavior based on the modified BW model is shown in Fig. 2.
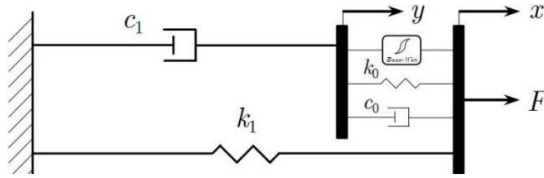
Figure 2: Modified BW model, adapted from Dyke (1997).

Equation (2) describes the physical model shown in Fig. 2:

$$F = c_1\dot{y} + k_1(x - x_0)$$
$$\dot{y} = \frac{1}{c_0 + c_1}\,\alpha z + c_0\dot{x} + k_0(x - y) \tag{2}$$
$$\dot{z} = -\gamma|\dot{x} - \dot{y}|z|z|^{n-1} - \beta(\dot{x} - \dot{y})|z|^n + \delta(\dot{x} - \dot{y})$$

in which c_0 and c_1 represent viscous dampers, k_0 and k_1 are linear springs, x is the displacement of the rod, x_0 is the initial displacement of the rod, y is an intermediary displacement, F is the force generated by the MR actuator, a is a scale factor, and z is the so-called hysteretic variable. The parameters d, g, b, and n should be identified by solving a typical inverse problem combined with experimental results (Dyke, 1997).

HYSTERETIC MODEL

Kwok et al. (2006) proposed a simple parametric model aiming at modeling the hysteretic behavior of MR actuators. The Hysteretic model requires small computational effort as compared to the Bingham and modified BW models. Figure 3 presents the physical system proposed by Kwok et al. (2006), which represents the Hysteretic model.
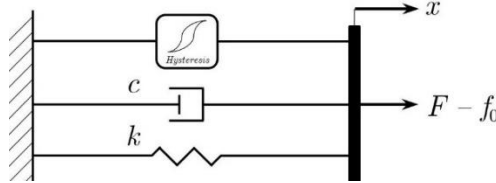
Figure 3: Hysteretic model, adapted from Kwok et al. (2006).

The equations that describe the Hysteretic model are given by Eq. (3).

$$F = c\dot{x} + kx + \alpha z + f_0$$
$$z = \tanh \beta\dot{x} + \delta\mathrm{sign}(x)$$

(3)

According to Kwok et al. (2006), the viscous damping c and the force in the accumulator f_0 are able to slope the force versus velocity curve, as shown in Fig. 4 (see the blue line). The stiffness k is responsible for the vertical spacing of the hysteresis curve. High values indicate increased internal curve spacing at both low and high speeds. High values of k indicate the increase on the internal curve spacing (see the red dashed line). The hysteresis behavior of Fig. 4 is determined by the parameter b. A large value of b leads to a greater slope of the force versus velocity curve at low speeds (see the dotted blue line). The parameter d is responsible for the width of the hysteresis curve (see the dotted blue line), and the scale factor a determines the height of this curve (see the green dotted-dashed line).
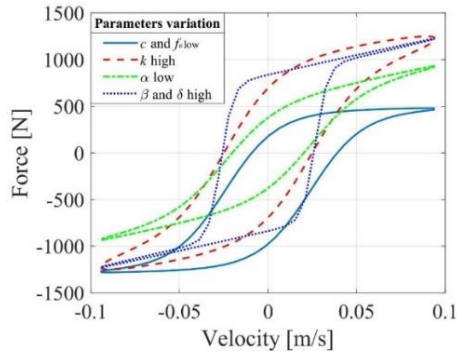
Figure 4: Hysteretic model

EXPERIMENTAL TESTS

In the present work, the MR actuator model RD-8040-1 manufactured by LORD Corporation® was used. The test to determine the dynamic behavior of the MR actuator was performed in the hydraulic servo test machine MTS Landmark® model 37010. Figure 5a shows the MR actuator positioned in the machine where the tests were performed.

The reaction forces generated by the MR actuator were measured by considering different electric currents that were applied in its coils (0 to 1.0 A in increments of 0.2 A). In this sense, a sinusoidal displacement with 3 mm amplitude (peak to peak) and 10 Hz frequency was applied in the system rod. It is worth mentioning that the actuator rod was initially displaced by 30 mm from its distended length, resulting a 31.3 N pre-load. Thus, this value was subtracted from the force vectors measured during the tests. The choice for the current level, frequency, and amplitude was made by considering the operating limits of the MR actuator used.

Figure 5b depicts the curves of time versus force measured by considering the MR actuator without any current applied in its coils and the constant current levels of 0.2 A, 0.4 A, 0.6 A, 0.8 A, and 1.0 A. Notice that the force generated by the actuator increases with the applied electric current. In addition, it is possible to note that there is a saturation region for a current value close to 1.0 A. This is evidenced by the difference between the observed maximum forces for two subsequent electric current values. The difference between the force amplitudes decreases as the electric current increases. It can be observed that the

smallest difference is given between the forces obtained for the electric currents of $0.8\ A$ and $1.0\ A$.

a)   b)
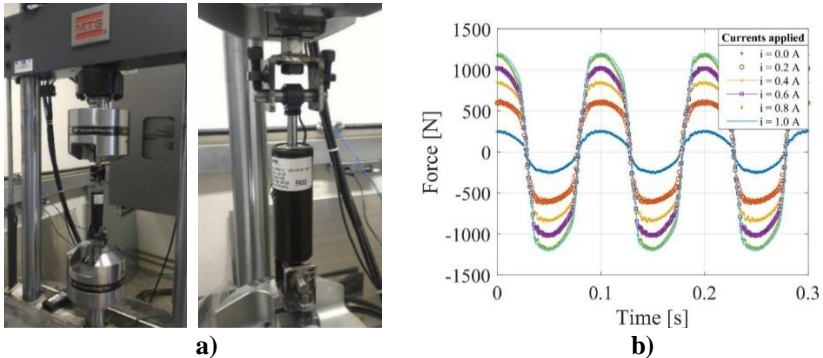
Figure 5: (a) MR actuator positioned in the MTS machine used to perform the experimental tests and (b) force vs time curves by considering different electric currents applied to the MR actuator.

Figure 6a presents the curves of the displacement versus force as measured by considering the MR actuator without any current applied in its coils, and constant current levels of $0.2\ A$, $0.4\ A$, $0.6\ A$, $0.8\ A$, and $1.0\ A$ (same conditions used to obtain Fig. 5b). As expected, the force amplitude increases according to the electric current applied in the actuator coils. Additionally, it can be observed that the difference between the forces exerted by the actuator decreases as the current levels are increased. Figure 6b presents the velocity versus force curves measured by considering different current amplitudes applied in the actuator coils. Notice the appearance of hysteresis cycles, a characteristic behavior of MR actuators.

a)   b)
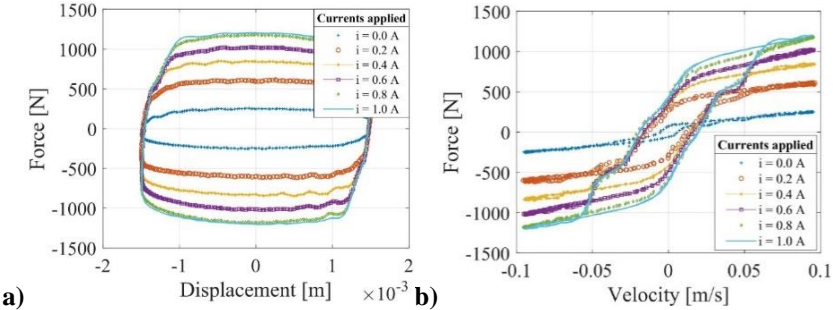
Figure 6: (a) Force versus displacement and (b) force versus velocity curves obtained experimentally.

It is important to note that each experimental test (associated with the applied electrical currents) was performed during 30 *s*. However, the curves presented in Figs. 5a, 5b and 6 were obtained by taking the final 0.3 *s* of the experiments. Additionally, the model updating procedure, presented next, was based on these reduced force vectors.

The experimental tests were not conducted in a controlled temperature environment. MR fluids undergo changes in their rheological properties when subjected to temperature variation. The present contribution did not evaluate this influence.

MODEL UPDATING

In the present work, the optimization algorithm known as Differential Evolution (Storn and Price, 1995) was used to determine the parameters of the evaluated MR models in relation to the results obtained in the experimental tests. Equation 4 shows the objective function used in the minimization algorithm, which is based on the relative error between the numerical and experimental forces:

$$E = \frac{\|F_n - F_e\|}{\|F_e\|} \tag{4}$$

where E is the objective function (error function), F_n is the numerical force vector obtained by using the MR models presented earlier (see F in Eqs. (1), (2), and (3)), and F_e is the experimental force vector.

Table 1 presents the results determined by using the above-mentioned optimizer in the updating of the Bingham model, as well as the considered design space. In this case, an electric current of 1.0 *A* was applied to the actuator coils. Additionally, a sinusoidal displacement with 3 *mm* amplitude (peak to peak) and 10 *Hz* frequency was applied to the actuator rod. The parameters chosen for the optimizer were the following: 100 individuals for the initial population, maximum number of iterations of 200, disturbance rate of 0.5, and crossing probability of 80%. Note that the viscous damper and the dry friction were considered as unknown parameters (c_0 and f_c, respectively; see Eq. (1)). The force

30

in the accumulator f_0 is associated with the pre-load applied in the MR actuator and is equal to -31.2 N. Figure 7a illustrates the convergence of the objective function according to the optimizer iterations (residual error of 25.39 %).

Table 1: Results determined in the updating of the Bingham model.

Parameter	Lower limit	Optimum value	Upper limit
c_0 Ns / m	7000	11100	15000
f_c N	100	250	1000

In this case, f_c is directly related to the yield stress of the MR fluid. Thus, it is understood that the MR actuator remains at rest until a force higher than fc appears. After being subjected to an effort greater than this value, the actuator rod starts to move. Note that f_c is related to the value of electric current applied. Figure 6 shows that the force amplitude increases according to the electric current applied in the actuator coils. Differently, c_0 is related to the plastic viscosity of the fluid and depends on the MR fluid properties.

Figure 7b presents the curves of time versus force related to the experimental measurements and the updated Bingham model. Note that there is a difference with respect to the experimental results, especially where an inversion of the movement direction occurs (in regions where the amplitude of the force is maximum and minimum).

Figure 7c shows the curves of displacement versus force related to the experimental measurements and the updated Bingham model. The associated velocity versus force curves are shown in Fig. 7d. Note that the simplicity of the Bingham model implies a behavior that does not correspond satisfactorily to the actual behavior of the MR actuator, in which the hysteresis is not well represented. However, the behavior of both experimental and numerical curves diverges in many points, evidencing that the model is not representative.
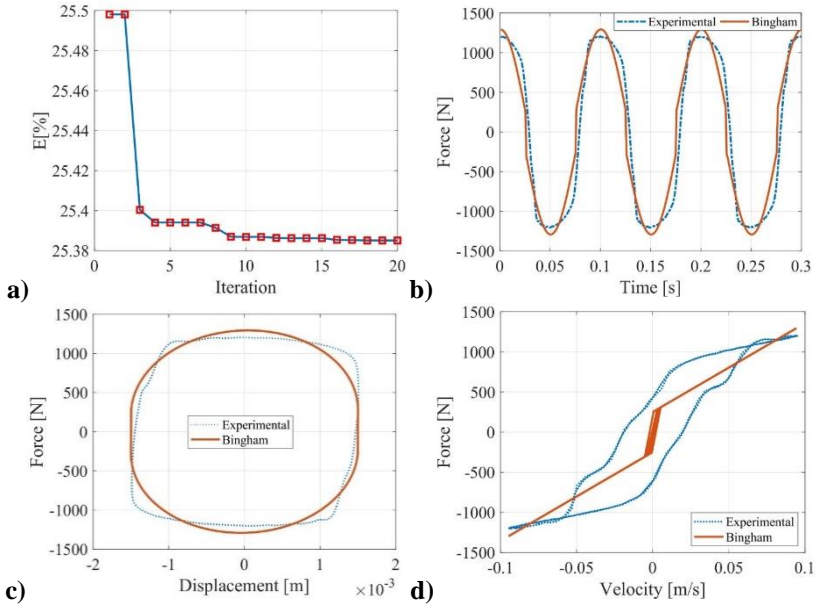
Figure 7: Experimental and numerical responses obtained by using the updated Bingham model.

Table 2: Results determined in the updating of the modified BW model.

Parameter		Lower limit	Optimum value	Upper limit
c_0	Ns/m	$3500\,i + 2000$	$5230\,i + 2863$	$7000\,i + 4500$
c_1	Ns/m	450000	782296	800000
k_0	N/m	$4000\,i + 9000$	$7000\,i + 39789$	$7000\,i + 40000$
k_1	N/m	8000	39101	40000
f_0	N	$500\,i + 100$	$2500\,i + 100$	$2500\,i + 500$
α	N/m	$500\,i + 5$	$549\,i + 7.8$	$2000\,i + 300$
δ	$\left[1/m^2\right]$	$0\,i + 30000$	$0\,i + 30000$	$30000\,i + 70000$
γ	$\left[1/m^2\right]$	$200000\,i + 300000$	$203670\,i + 300122$	$400000\,i + 1500000$
β		$-900000\,i + 500000$	$-899247\,i + 500000$	$-550000\,i + 3000000$
n		$1\,i + 1$	$4\,i + 5$	$4\,i + 5$

Table 2 presents the results determined by using the optimizer for the updating of the modified BW model, as well as the considered design space. Similarly, an electric current of $1.0\,A$ was applied to the actuator coils. Additionally, a sinusoidal displacement with 3 mm amplitude (peak to peak) and 10 Hz frequency was applied to the actuator rod. The

parameters chosen for the optimizer were the following: 200 individuals for the initial population, maximum number of iterations of 250, disturbance rate of 0.5, and crossing probability of 80%.

In this case, 10 parameters were considered as unknown design variables (c_0, c_1, k_0, k_1, f_0, a, d, g, b, and n; see Eq. (2)). A first-degree function of the electric current i was adopted for some of the 10 unknown parameters (Truong and Ahn, 2012; Liem, Truong, and Ahn, 2015). Figure 8a illustrates the convergence of the objective function according to the optimizer iterations.
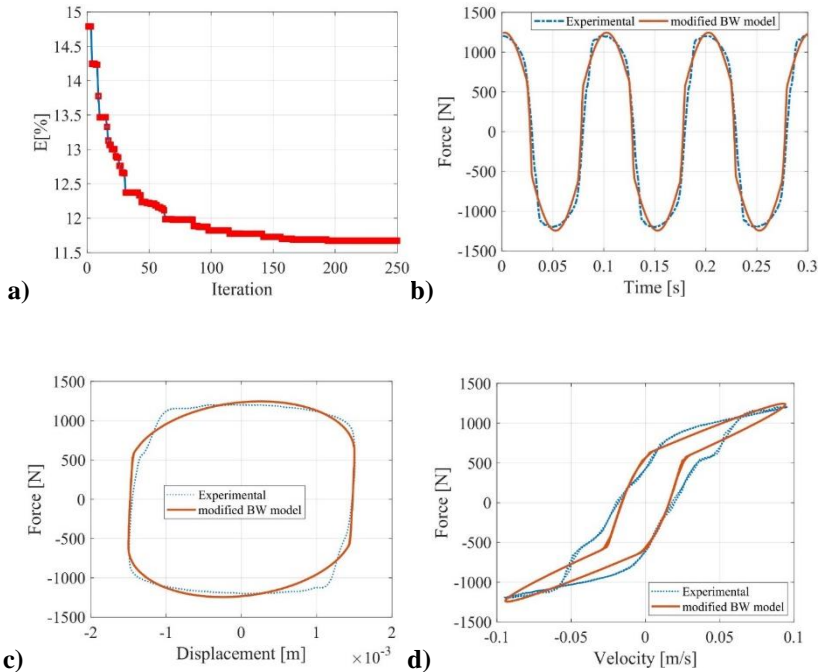
Figure 8: Experimental and numerical responses obtained by using the updated modified BW model.

Figure 8b presents curves of time versus force related to the experimental measurements and the updated modified BW model. Figure 8c shows the curves of displacement versus force related to the experimental measurements and the updated modified BW model. The associated curves of velocity versus force are presented in Fig. 8d. The obtained results show that the modified BW model is more adapted to

represent the MR actuator than the Bingham model. In this case, a residual error of 11.67 % was obtained (25.39 % considering the Bingham model).

Table 3 shows the results determined by using the optimizer for the updating of the Hysteretic model, as well as the considered design space. Similarly, an electric current of 1.0 A was applied to the actuator coils. Additionally, a sinusoidal displacement with 3 *mm* amplitude (peak to peak) and 10 *Hz* frequency was applied to the actuator rod. The parameters chosen for the optimizer were the following: 240 individuals for the initial population, maximum number of iterations of 40, disturbance rate of 0.5, and crossing probability of 80%. In this case, 5 parameters were considered as being unknown (c, k, a, b, and d; see Eq. (3)). Both a first and second-degree functions of the electric current i were adopted for some of the 5 unknown parameters (Kwok et al., 2006). The force in the accumulator f_0 is associated with the pre-load applied in the MR actuator and is equal to -31.2 *N*. Figure 9a illustrates the convergence of the objective function according to the optimizer iterations.

Table 3: Results determined in the updating of the Hysteretic model.

Parameter	Lower limit	Optimum value	Upper limit
c Ns/m	$200\ i + 1690$	$2580\ i + 1690$	$6000\ i + 1690$
k N/m	894	894	894
α N	$50\ i^2 + 500\ i + 90.8$	$181\ i^2 + 550\ i + 90.8$	$500\ i^2 + 1200\ i + 90.8$
β s/m	10	34.7	50
δ	$-2\ i + 0.564$	$0.272\ i + 0.564$	$2\ i + 0.564$

Figure 9b presents the curves of time versus force related to the experimental measurements and the updated Hysteretic model. Figure 9c shows the curves of displacement versus force related to the experimental measurements and the updated Hysteretic model. The associated curves of velocity versus force are presented in Fig. 9d. Note that the curves obtained by using the updated Hysteretic model demonstrated to be close to the experimental ones, leading to an error of 4.59 % (25.39 % considering the Bingham model and 11.67 % considering the modified BW model). However, there are some regions where numerical and experimental curves differ (see Figs. 9c and 9d).
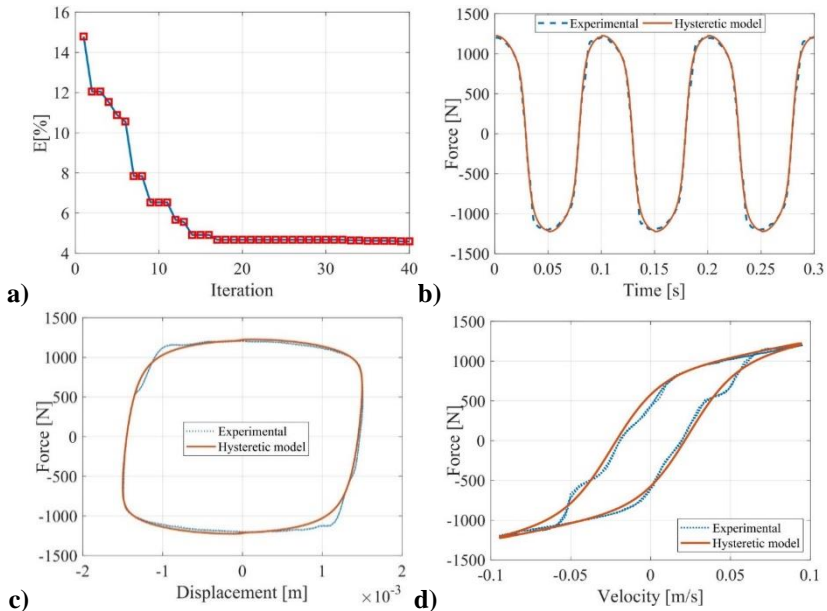
Figure 9: Experimental and numerical responses obtained by using the updated Hysteretic model.

CONCLUSIONS

This work showed the model updating of three parametric mathematical models of MR actuators, namely Bingham, modified BW, and Hysteretic models. Regarding the experimental conditions adopted in the present work, the Bingham model was not able to represent satisfactorily the nonlinear behavior of the MR actuator, presenting a residual error of 25.39 %. A better response was obtained by using the modified BW model, for which an error of 11.67 % was obtained. However, a need for finding better responses was observed, especially by analyzing the model results at low speeds. The Hysteretic model reveled the best results, presenting a residual error of 4.59 %. This model presented lower computational cost and easy implementation, as compared with the Bingham and modified BW models. Thus, it is concluded that the most representative parametric model for the MR actuator is the hysteretic model. Further work will be dedicated to evaluating the Hysteretic model by considering different amplitudes and frequencies applied to the actuator rod. An experimental application of

MR actuators for the vibration control of rotating machines is also scheduled.

REFERENCES

Bai, X., Wereley, N., Choi, Y., (2016). Magnetorheological energy absorber with dual concentric annular valves. Journal of Intelligent Material Systems and Structures, 27: 944-958.

Barber, D., (2013). MR fluids at the extremes: High-energy and low-temperature performance of LORD® MR fluids and devices 4: 74-95.

Cavalini jr, A., Koroishi, E., Borges, A., Pereira, L., Steffen jr, V., (2015). Semi-active vibration control of a rotating shaft by using a magneto rheological damper. In: 23 ABCM International Congress of Mechanical Engineering.

Crosby, M., Karnopp, D., (1973). The active damper: A new concept for shock and vibration control. Shock Vibration Bulletin: 119–133.

Dyke, S., (1997). Acceleration feedback control strategies for active and semi-active control systems: Modeling, algorithm development, and experimental verification. Ph.D. Thesis. Department of Civil Engineering and Geological Sciences. University of Notre Dame.

Klinger, D., Cooperrider, N., Hedrick, J., White, R., Cilzado, A., Sayers, M., Wormley, D., (1976). Guideway vehicle cost reduction. In: National technical information service reports DT-TST, Alexandria Edition (Alexandria): 75-95.

Kwok, N., Ha, Q., Nguyen, T., Li, J., Samali, B., (2006). A novel hysteretic model for magnetorheological fluid dampers and parameter identification using particle swarm optimization. Sensors and Actuators A: Physical, 132: 441-451.

Liem, D., Truong, D., Ahn, K., (2015). Hysteresis modeling of magneto-rheological damper using self-tuning Lyapunov based fuzzy approach. International Journal of Precision Engineering and Manufacturing, 16: 31-41.

Lord Corporation, (2009). LORD Technical Data: RD-8040-1 and RD-8041-1 Dampers. Cary, USA. 2p.

site: http://www.lordfulfillment.com/upload/DS7016.pdf.

Margolis, D., Hrovat, D., (1976). Semi-active heave and pitch control of a high speed tracked air cushion vehicle. In: Intersociety Transportation Conference, 1: 41–49.

Miller, L., Nobles, C., (1988). The design and development of a semi-active suspension for a military tank. SAE Technical Paper 881133.

Stanway, R., Sproston, J., Stevens, N., (1987). Non-linear modelling of an electrorheological vibration damper. Journal of Electrostatics, 20: 167-184.

Storn, R., Price, K., (1995). Differential evolution: a simple and efficient adaptive scheme for global optimization over continuous spaces, Berkeley. CA: International Computer Science Institute.

Truong, D., Ahn, K., (2012). MR fluid damper and its application to force sensorless damping control system. INTECH Open Access Publisher.

Zeinali, M., Mazlan, S., Choi, S., Imaduddin, F., Hamdan, L. (2016). Influence of piston and magnetic coils on the field-dependent damping performance of a mixed-mode magnetorheological damper. Smart Materials and Structures, 25: 1-9.

Zhang, Q., Liu, X., Ren, Y., Wang, L., Hu, Y., (2016). Effect of particle size on the wear property of magnetorheological fluid. Advances in Materials Science and Engineering, 2016: 1-7.

Wen, Y., (1976). Method for random vibration of hysteretic systems. Journal of the engineering mechanics division, 102: 249-263.

Analysis of the Dynamic Behavior of an Onboard Rotor*

Marcelo Samora Sousa Jr
marcelosamora@ufu.br

Advisors: Valder Steffen Jr and Aldemir Ap Cavalini Jr

Abstract: In the present work, the dynamic behavior of a rotating machine subjected to base excitations has been investigated experimentally. Aircraft, nautical, or automotive engines are typical onboard rotors since the base excitations change their dynamic behavior. The mathematical model of the rotor was formulated based on the finite element method. The strain and kinetic energies of the shaft and the kinetic energy of the discs and mass unbalance were considered. A rigid base was used to support the rotating machine. The simulated vibration responses were determined by solving a set of differential equations associated with the rotor model. In this sense, a trapezoidal rule integration scheme coupled with the Newton-Raphson iterative method was used. Analyses in the time and frequency domains for different base excitations were performed to evaluate the dynamic behavior of the rotor system. Thus, numerical and experimental results were compared. The obtained numerical results demonstrate the representativeness of the conveyed onboard rotor model.

Keywords: rotordynamics, onboard rotors, finite element method, experimental investigation.

INTRODUCTION

Fixed-base rotors are commonly studied in rotordynamics. However, many rotating machines are subjected to based excitations, such as helicopter, ship, and quadcopter engines. The dynamic behavior of these systems is changed by the applied based. Kim; Yang; Lin (1986) were one of the first authors to study the dynamic behavior of a rotor under base excitations. The authors analyzed the vibration response of a

---

rotating machine with a flexible shaft subjected to seismic accelerations applied in its base.

The dynamic responses of the helicopter rotor during a maneuvering flight were studied by Zhao (2005). In this case, a mathematical model was proposed taking into account the base excitations. The author compared the numeric results obtained from the proposed model with experimental data measured in a *Sikorsky UH-60 Black Hawk* helicopter. Das; Dutt; Ray (2010) used a magnetic actuator to control the lateral vibrations of an onboard rotor system.

In this context, the present work is devoted to the experimental evaluation of an onboard rotor subjected to different base excitations. The considered rotor test rig is composed by a flexible shaft, one rigid disc, and two self-alignment ball bearings. A rigid base was used to support the rotating machine. The rotating machine was modeled according to the finite element (FE) method. The strain and kinetic energies of the shaft and the kinetic energy of the discs (rigid) and mass unbalance were considered. The simulated vibration responses were determined by solving a set of differential equations associated with the rotor model. A trapezoidal rule integration scheme coupled with the Newton-Raphson iterative method was used. Numerical and experimental results were compared, revealing the representativeness of the conveyed onboard rotor model.

It is worth mentioning that there is a small number of contributions related to the analysis of rotors subjected to base excitations in the literature (Dakel; Baguet; Dufour, 2014).

ROTOR MODELING

The mathematical model of onboard rotors is obtained by using three reference frames, namely the inertial frame $R_0(x_0, y_0, z_0)$, the frame fixed to the rotor base $R_s(x_s, y_s, z_s)$, and the frame fixed to the disc $R(x, y, z)$, as given by Fig. 1.
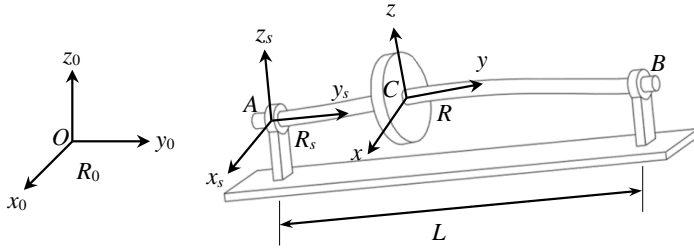
Figure 1: Schematic representation of an onboard rotor (Duchemin, 2003).

The angles ψ, θ, and φ are used to define the movement of the frame R with respect to R_s (see Fig. 2). The orientation of the frame R is described by:

- A rotation ψ around z_s resulting in an intermediate frame R_1 (x_1, y_1, z_1);
- A rotation θ around the new axis x_1 resulting in an intermediate frame $R_2 (x_2, y_2, z_2)$;
- A rotation φ around the axis y (parallel to y_2) resulting in the frame $R(x, y, z)$.
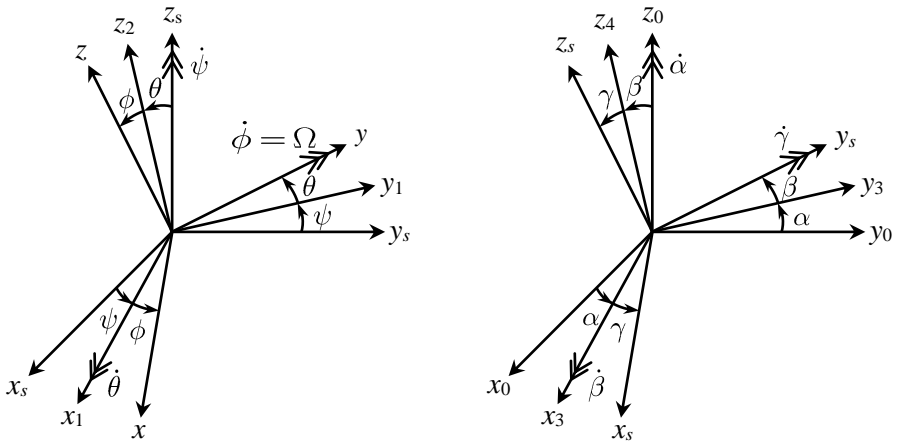
Figure 2: Reference frames for the disc and for the rotor base.

Equation (1) presents the angular velocity of the frame R with respect to R_s.

41

$$\overrightarrow{\Omega_R}^{R_s} = \begin{Bmatrix} 0 \\ 0 \\ \dot\psi \end{Bmatrix}_{R_s} + \begin{Bmatrix} \dot\theta \\ 0 \\ 0 \end{Bmatrix}_{R_2} + \begin{Bmatrix} 0 \\ \dot\phi \\ 0 \end{Bmatrix}_{R} = \begin{Bmatrix} \dot\theta\cos\phi - \dot\psi\cos\theta\sin\phi \\ \dot\phi + \dot\psi\sin\theta \\ \dot\theta\sin\phi + \dot\psi\cos\theta\cos\phi \end{Bmatrix}_{R} \tag{1}$$

The coordinates x_A, y_A, and z_A of the vector $\overrightarrow{OA}$ described in frame R_0 and the angles α, β, and γ define the movement of the base (frame R_s) with respect to R_0. Thus, the orientation of the frame R_s is described by (see Fig. 2):

- A rotation α around z_s resulting in an intermediate frame $R_3(x_3, y_3, z_3)$;
- A rotation β around the new axis x_3 resulting in an intermediate frame $R_4(x_4, y_4, z_4)$;
- A rotation γ around the final axis y (parallel to y_4) resulting in the frame $R_s(x_s, y_s, z_s)$.

Equations (2) and (3) show the vector $\overrightarrow{OA}$, which defines the location of the point A (see Fig. 1), and the angular velocity of the frame R_s with respect to R_0, respectively.

$$\overrightarrow{OA} = \begin{Bmatrix} x_A \\ y_A \\ z_A \end{Bmatrix}_{R_0} = \begin{Bmatrix} x_A\cos\alpha + y_A\sin\alpha\ \cos\gamma - z_A\cos\beta + x_A\sin\alpha - y_A\cos\alpha\ \sin\beta\ \sin\gamma \\ z_A\sin\beta - x_A\sin\alpha - y_A\cos\alpha\ \cos\beta \\ x_A\cos\alpha + y_A\sin\alpha\ \sin\gamma + z_A\cos\beta + x_A\sin\alpha - y_A\cos\alpha\ \sin\beta\ \cos\gamma \end{Bmatrix}_{R_s} = \begin{Bmatrix} X \\ Y \\ Z \end{Bmatrix}_{R_s} \tag{2}$$

$$\overrightarrow{\Omega_{R_s}}^{R_0} = \begin{Bmatrix} 0 \\ 0 \\ \dot\alpha \end{Bmatrix}_{R} + \begin{Bmatrix} \dot\beta \\ 0 \\ 0 \end{Bmatrix}_{R_3} + \begin{Bmatrix} 0 \\ \dot\gamma \\ 0 \end{Bmatrix}_{R_s} = \begin{Bmatrix} \dot\beta\cos\gamma - \dot\alpha\cos\beta\sin\gamma \\ \dot\gamma + \dot\alpha\sin\beta \\ \dot\beta\sin\gamma + \dot\alpha\cos\beta\cos\gamma \end{Bmatrix}_{R_s} = \begin{Bmatrix} \dot\alpha_s \\ \dot\beta_s \\ \dot\gamma_s \end{Bmatrix}_{R_s} \tag{3}$$

The kinetic energy of the disc (see Fig.1) is given by Eq. (4).

$$T_D = \frac{1}{2}M_D\,\overrightarrow{V_C}^{\,2} + \frac{1}{2}\overrightarrow{\Omega_R}^{R_0} I_D \overrightarrow{\Omega_R}^{R_0} \tag{4}$$

where M_D is the mass of the disc, $\overrightarrow{V_C}$ is the translational velocity of the disc with respect to R_0 expressed in R_s, $\overrightarrow{\Omega_R}^{R_0}$ is the angular velocity of the frame R with respect with R_0, and I_D is the tensor of mass inertia moments. Thus,

$$\vec{V}_C = \left(\frac{d\overrightarrow{OC}}{dt}\right)_{R_s} + \overrightarrow{\Omega}_{R_s}^{R_0} \times \overrightarrow{OC} = \begin{Bmatrix} \dot{X} + \dot{u} + \dot{\beta}_s \ Z + w \ - \dot{\gamma}_s \ Y + y \\ \dot{Y} + \dot{\gamma}_s \ X + u \ - \dot{\alpha}_s \ Z + w \\ \dot{Z} + \dot{w} + \dot{\alpha}_s \ Y + y \ - \dot{\beta}_s \ X + u \end{Bmatrix}_{R_s} = \begin{Bmatrix} \dot{u}_C \\ \dot{v}_C \\ \dot{w}_C \end{Bmatrix}_{R_s} \quad (5)$$

$$\overrightarrow{\Omega}_R^{R_0} = \overrightarrow{\Omega}_{R_s}^{R_0} + \overrightarrow{\Omega}_R^{R_s} = \begin{Bmatrix} \dot{\alpha}_s \\ \dot{\beta}_s \\ \dot{\gamma}_s \end{Bmatrix}_{R_s} + \begin{Bmatrix} 0 \\ 0 \\ \dot{\psi} \end{Bmatrix}_{R_s} + \begin{Bmatrix} \dot{\theta} \\ 0 \\ 0 \end{Bmatrix}_{R_2} + \begin{Bmatrix} 0 \\ \dot{\phi} \\ 0 \end{Bmatrix}_R = \begin{Bmatrix} \omega_x \\ \omega_y \\ \omega_z \end{Bmatrix}_R \quad (6)$$

$$I_D = \begin{bmatrix} I_{Dx} & 0 & 0 \\ 0 & I_{Dy} & 0 \\ 0 & 0 & I_{Dz} \end{bmatrix} \quad (7)$$

in which I_{Dx}, I_{Dy}, and I_{Dz} are the mass moments of inertia of the disc, ω_x, ω_y, and ω_z are the angular velocities of the frame R with respect to the frame R_0, u and w are the lateral displacements of the disc along with the directions x_s and z_s, respectively (movement of frame R with respect to R_s), θ and ψ are the angular movements of the disc with respect to the directions x_s and z_s, respectively (Duchemin, 2003; Duchemin *et al.*, 2006).

The kinetic energies of the shaft and mass unbalance (T_S and T_u, respectively) are given by Eq. (8).

$$T_S = \frac{1}{2}\rho S \int_0^L \dot{u}_s^2 + \dot{v}_s^2 + \dot{w}_s^2 \ dy + \frac{1}{2}\rho \int_0^L \left[I_x \omega_x^2 + I_y \omega_y^2 + I_z \omega_z^2 \right] dy$$

$$(8)$$

$$T_u = \frac{1}{2}m_u \ \overrightarrow{V}_D^{\ 2}$$

where u_s, v_s, and w_s are the displacements of the shaft along with the directions x_s, y_s and z_s, respectively, I_x, I_y, and I_z are the area inertia moments of the shaft, ρ is the volumetric density of the shaft, S stands for the cross-section area of the shaft, and m_u is the unbalanced mass. In Eq. (8), the velocity of the point D with respect to R_0 expressed in R_s is:

$$\vec{V}_D = \left(\frac{d\overrightarrow{OD}}{dt}\right)_{R_s} + \vec{\Omega}_{R_s}^{R_0} \times \overrightarrow{OD}\bigg|_{R_s} = \begin{Bmatrix} \dot{X} + \dot{u} + d\Omega\cos\Omega t + \dot{\beta}_s \ Z + w + d\Omega\cos\Omega t \ -\dot{\gamma}_s \ Y + y \\ \dot{Y} + \dot{\gamma}_s \ X + u + d\Omega\sin\Omega t \ -\dot{\alpha}_s \ Z + w + d\Omega\cos\Omega t \\ \dot{Z} + \dot{w} - d\Omega\sin\Omega t + \dot{\alpha}_s \ Y + y \ -\dot{\beta}_s \ X + u - d\Omega\sin\Omega t \end{Bmatrix}_{R_s} \quad (9)$$

where Ω is the rotation speed of the rotor, t is the time vector, and d is the distance between the geometric center of the shaft (point C) to the position of m_u (see Fig. 3).
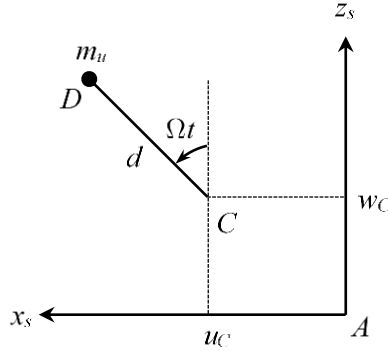
Figure 3: Unbalanced mass.

It is important to point out that the movement of the rotor base (i.e., translations and rotations) does not modify the strain energy U of the shaft since it is independent of the constraints associated with the onboard rotor problem. Thus,

$$U = \frac{1}{2}EI_m\int_0^L \left[\left(\frac{\partial^2 u}{\partial y^2}\right)^2 + \left(\frac{\partial^2 w}{\partial y^2}\right)^2\right]dy + \frac{1}{2}EI_a\int_0^L \left\{\left[\left(\frac{\partial^2 w}{\partial y^2}\right)^2 - \left(\frac{\partial^2 u}{\partial y^2}\right)^2\right]\cos 2\Omega t + 2\frac{\partial^2 u}{\partial y^2}\frac{\partial^2 w}{\partial y^2}\cos 2\Omega t\right\}dy \quad (10)$$

$$I_m = \frac{I_x + I_z}{2} \qquad I_a = \frac{I_x - I_z}{2}$$

where E is Young's Modulus of the shaft.

The FE model of the shaft is derived based on the Euler-Bernoulli beam theory. Two nodes per element and four degrees of freedom per node are used in this case, as presented by Fig. 4 (i.e., displacements u_1, u_2, w_1, and w_2; angular rotations θ_1, θ_2, ψ_1, and ψ_2).
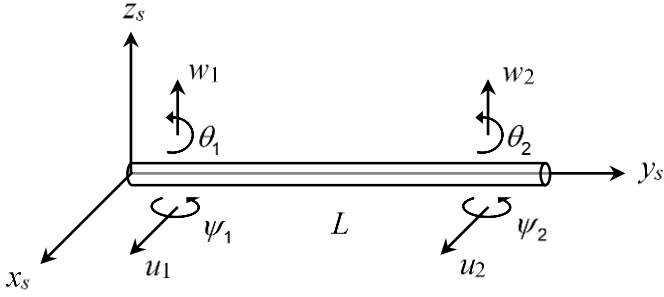
Figure 4: Degrees of freedom associated with the FE of the shaft.

Thus, the vector of nodal degrees of freedom of the shaft is given by:

$$\mathbf{q} = \begin{bmatrix} u_1 & w_1 & \theta_1 & \psi_1 & u_2 & w_2 & \theta_2 & \psi_2 \end{bmatrix}^T \tag{11}$$

The elementary matrices associated with the FE model of the shaft are obtained by introducing the shape functions of Zienkiewicz (1979) into Eq. (8) and Eq. (10). The equations of motion are derived by substituting the obtained equations into the apLagrange's equations. Thus,

$$\mathbf{M\ddot{q}} + \left[\mathbf{D} + \mathbf{D}^*\right]\mathbf{\dot{q}} + \left[\mathbf{K} + \mathbf{K}^*\right]\mathbf{q} = \mathbf{W} + \mathbf{F}(t) + \mathbf{F}^*(t) \tag{12}$$

where **M**, **K**, and **D** are the mass, stiffness, and gyroscopic/damping matrices of the rotor system, respectively. All these matrices are related to the shaft and the discs of the rotor considering the base at rest. **D***, **K***, and **F*** are the matrices associated with the motion of the base. The vector **F** contains the unbalance forces and **W** stands for the weight of the rotating parts.

The Newton-Raphson method in conjunction with the Newmark-type trapezoidal rule integration algorithm is used to obtain the vibration responses of the onboard rotor system (Cavalini Jr *et al.*, 2015).

ROTOR TEST RIG

The rotor test rig used in the present contribution is shown in Fig. 5a. The onboard rotor system is mathematically represented by an FE model with 33 finite elements (Fig. 5b). It is composed of a flexible steel shaft

with 450 mm length and 8 mm of diameter ($E = 205$ GPa, $\rho = 7850$ kg/m^3, $v = 0.29$), one rigid disc D (node #16, 2.523 kg) with 100 mm diameter and 40 mm length ($\rho = 7850$ kg/m^3), two self-alignment ball bearings (B_1 and B_2, located at nodes #5 and #31, respectively), and two displacement sensors are orthogonally mounted on node #16 (S_{16xs} and S_{16zs}) to collect the shaft vibration.
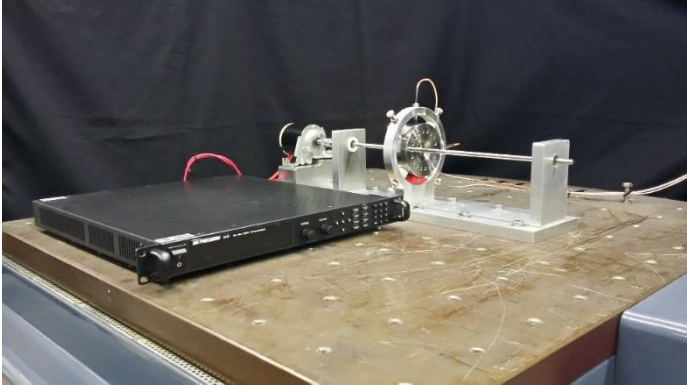
a) Rotor test rig.
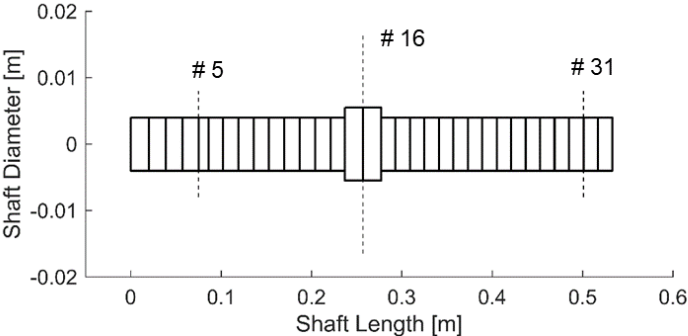
b) Schematic representation.

Figure 5: The rotating machine used in the analysis.

The frequency response functions (FRFs) of the rotating machine at rest were used to update the formulated FE model. Impact forces were applied along the x_s and z_s directions of the disc to measure the experimental FRFs. The displacement sensors were positioned along the same direction of the impact forces (see Fig. 5a) resulting in two FRFs. The analyzer Agilent® (model 35670A) in a range of 0 to 250 Hz and steps of 0.25 Hz was used to perform the measurements.

The Differential Evolution algorithm (Storn and Price, 1995) was used to solve the inverse problem associated with the FE model update,

in which the comparison between the simulated and experimental FRFs was considered as the objective function, as given by Eq. (13).

$$Objective = \sum_{i=1}^{n} \frac{\left\| \mathbf{FRF}_{\text{exp},i} - \mathbf{FRF}_{\text{mod},i} \right\|}{\left\| \mathbf{FRF}_{\text{exp},i} \right\|} \qquad (13)$$

where n is the number of FRFs used in the minimization procedure, $\mathbf{FRF}_{\text{exp}}$ represents the experimental data, $\mathbf{FRF}_{\text{num}}$ is the corresponding numerical results determined by the FE model of the rotor system (see Fig. 5). Only the regions close to the peaks associated with the natural frequencies were taken into account to the objective function.

The initial population of the optimizer was composed of 100 individuals and the inverse problem was solved 10 times. The unknown parameters considered in this problem were: stiffness and damping coefficients of the bearings and the angular stiffness k_{ROT} due to the coupling between the electric motor and the shaft (added around the orthogonal directions x_s and z_s of the node #1; see Fig. 5). The values obtained at the end of the minimization process are presented in Tab. 1. Figure 6 shows the comparison between simulated and experimental FRFs. Note that the numerical and experimental FRFs are close demonstrating the representativeness of the updated FE model.

Table 1: Parameters determined by the model updating procedure.

Parameters	Value	Parameters	Value	Parameters	Value
k_{xx}/B_1	1.365×10^{11}	k_{xx}/B_2	4.113×10^{11}	k_{ROTxs}	203.36
k_{zz}/B_1	1.674×10^{11}	k_{zz}/B_2	2.914×10^{11}	k_{ROTzs}	959.27
ξ_1	0.0527	ξ_2	0.0475		
ξ_3	0.0157	ξ_4	0.0117		

*k: stiffness [N/m]; ξ: damping coefficients.

a) x_s direction.

b) z_s direction.
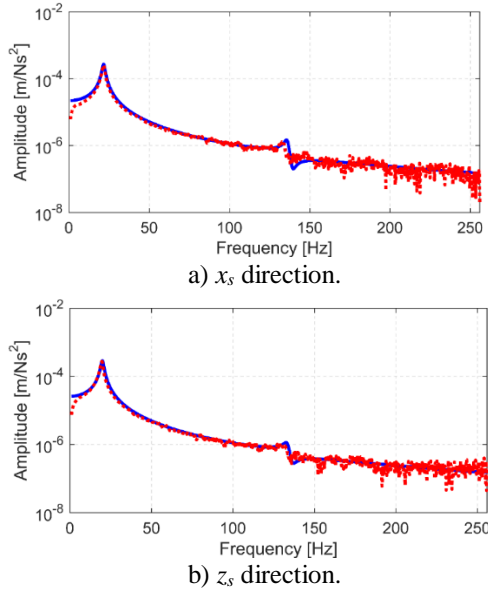
Figure 6: Simulated (---) and experimental (---) FRFs of the rotating machine.

The Campbell diagram determined from the representative FE model of the rotating machine is presented in Fig. 7. The first two critical speeds of the rotor system are, approximately, 1177 rev/min (FW: forward critical speed) and 1375 rev/min (BW: backward critical speed).
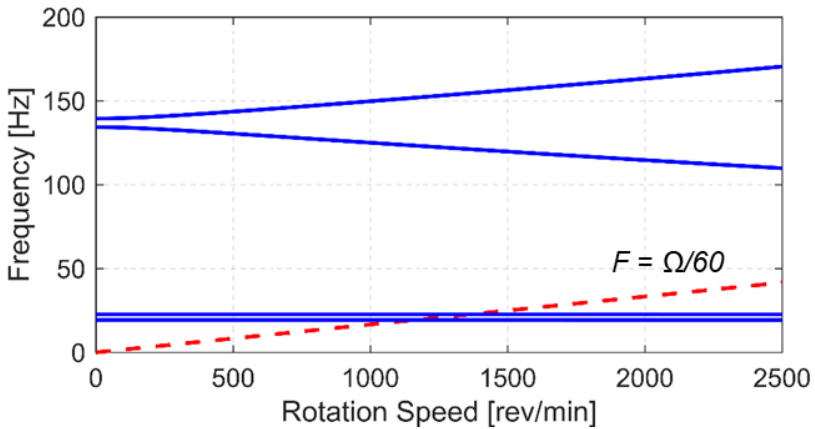
Figure 7: Campbell diagram of the rotating machine.

RESULTS AND DISCUSSION

In this section, impact and sinusoidal excitations are used to evaluate the dynamic behavior of the onboard rotor system presented in this work. Firstly, an impact excitation is considered to study the dynamic behavior of the rotor system. In this case, the rotor was at rest and three different amplitudes were applied along the x_s direction. The vibration responses measured along the same direction of the impact (x_s direction), as well as the base excitations (amplitudes of 3 m/s², 6 m/s², and 9 m/s²), are presented in Fig. 8, Fig. 9, and Fig. 10. Note that the simulated and experimental vibration responses are similar. The excitations.
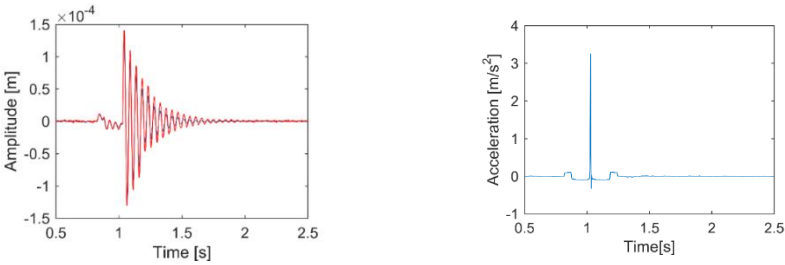
Figure 8: Vibration responses of the rotor along the x_s direction for an impact with 3 m/s² amplitude (---- simulated; ---- experimental).
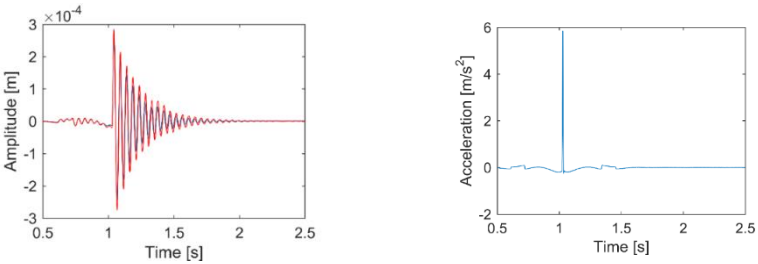
Figure 9: Vibration responses of the rotor along the x_s direction for an impact with 6 m/s² amplitude (---- simulated; ---- experimental).
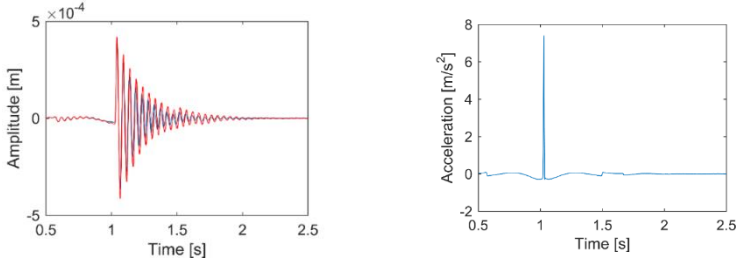
Figure 10: Vibration responses of the rotor along the x_s direction for an impact with 9 m/s² amplitude (---- simulated; ---- experimental).

Figure 11 presents the vibration responses obtained along the x_s direction of the onboard rotor considering a sinusoidal excitation imposed to the base along the same direction, as given by Eq. (14).

$$\ddot{x}_s = \Lambda \sin\left(n \frac{2\pi\, \Omega_{cr}}{60} t \right) \tag{14}$$

where Λ was 2.5 m/s², Ω_{cr} = 1308 rev/min (second BW critical speed of the rotor), and n is a constant used to produce supersynchronous base excitations. In this case, n = 2, 3, 4, and 5 as presented in Fig. 11a, 11b, 11c, and 11d, respectively. The rotation speed of the rotor was 1600 rev/min.

a) $n = 2$.   b) $n = 3$.

c) $n = 4$.   d) $n = 5$.
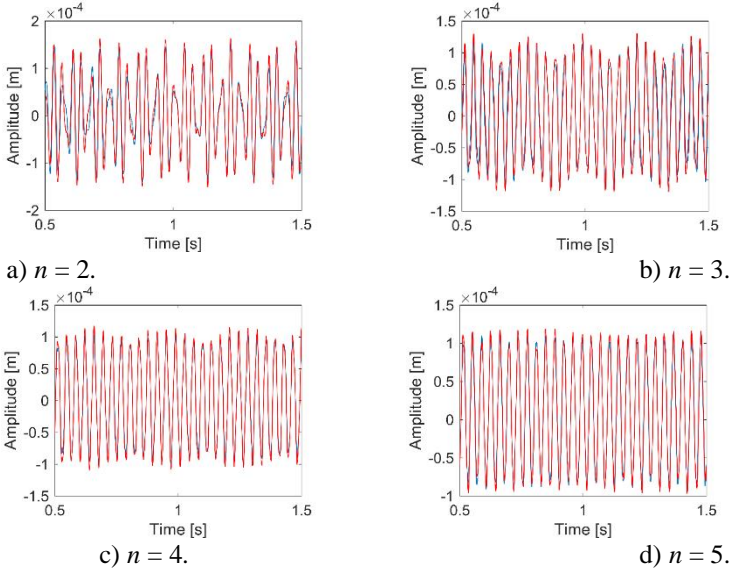
Figure 11: Vibration responses of the rotor at 1600 rev/min considering sinusoidal base excitations along the x_s direction (---- simulated; ---- experimental).

50

CONCLUSIONS

In this work, the dynamic behavior of a rotor system under base excitation was analyzed. An experimental investigation was performed in a rotating machine composed by a horizontal flexible shaft, one rigid disc, and two self-aligning ball bearings. The mathematical model of the rotor was formulated according to the FE method. Analyses in the time and frequency domains for different base excitations were performed to evaluate the dynamic behavior of the rotor system. The considered mathematical model was able to represent the dynamic behavior of the onboard rotor, resulting in small differences between the numerical and experimental vibration responses. Further investigation will be dedicated to the analysis of the onboard rotor in the presence of nonlinear phenomena.

ACKNOWLEDGMENTS

REFERENCES

Cavalini Jr., A.A., Lara-Molina, F.A., Sales. T.P., Koroishi, E.H., Steffen Jr, V., 2015, "Uncertainty analysis of a flexible rotor supported by fluid film bearings". *Latin American Journal of Solids and Structures*, Vol. 12, No. 8, pp. 1487-1504.

Dakel, M., Baguet, S., Dufour, R., 2014, "Steady-state dynamic behavior of an on-board rotor under combined base motions". *Journal of Vibration and Control*, Vol. 20, n. 15, p. 2254-2287.

Das, A.S., Dutt, J.K., Ray, K., 2010, "Active vibration control of unbalanced flexible rotor-shaft systems parametrically excited due to

base motion". *Applied Mathematical Modelling*, Vol. 34, n. 1, p. 2353-2369.

Duchemin, M., 2003, "Contribuition à l'étude du comportement dynamic d'un rotor embarqué". PhD thesis, INSA Lyon, Lyon.

Duchemin, M., Berlioz, A., Ferraris, G., 2006, "Dynamic behavior and stability of a rotor under base excitation". *ASME Journal of Vibration and Acoustics*, Vol. 128, p. 576.

Kim, K. B.; Yang, J. N.; Lin, Y. K. Stochastic response of flexible rotor-bearing system to seismic excitations. Probabilistic Engineering Mechanics. v. 1, n. 3, 1986.

Lalanne, M., Ferraris, G., 1998, "Rotordynamics prediction in engineering". John Wiley & Sons, INC.

Sousa Jr, M. S.. Analysis of the Dynamic Behavior of Onboard Rotor. 2017. 50 f. M.Sc. Dissertation - Universidade Federal de Uberlândia, Uberlândia, MG, Brazil.

Storn, R., Price, K., 1995, "Differential evolution: a simple and efficient adaptive scheme for global optimization over continous spaces". International Computer Science Institute, Vol. 12, No. 1, pp. 1-16.

Zhao, J. Dynamic wake distortion model for helicopter maneuvering flight. 2005. PhD Thesis - School of Aerospace Engineering, Georgia Institute of Technology, Georgia.

Zienkiewicz, O. C. La Méthode des Éléments-Finis. Paris: MacGraw-Hill, 1979. 851p.

Numerical Evaluation of a Composite Hollow Shaft Rotor[*]

Paulo Costa Porto de Figueiredo Barbosa
paulo.barbosa@ufu.br

Advisors: Aldemir Ap. Cavalini Jr. and Valder Steffen Jr.

Abstract: Various applications of composite materials have been prominent in recent years, given their many advantages over the equivalent conventional engineering materials counterparts. Therefore, researchers on the dynamics of the rotating machine are demonstrating interest in replacing metallic by composite shafts, resulting in higher operation speeds, lower overall weight, and optimal structural efficiency. In this sense, some models have been proposed for the computational modeling of rotating machines with composite shafts. A comparison between simplified beam models for composite shafts is presented in this contribution. Additionally, detailed experimental analysis and validation of the implemented models are carried out in terms of the frequency response functions for the free-free condition of the system.

Keywords: Composites shafts, rotor, EMBT, SHBT

INTRODUCTION

The use of composite materials has been growing over the years, mainly in maritime, aeronautical, and automotive industries, due to the range of possibilities in obtaining suitable characteristics for different situations. Rotordynamics is one of the areas with interest in the use of composite shafts since they are a viable solution to overcome the limitations inherent to metal shafts (Silveira, 2001). For systems operating under subcritical conditions (rigid rotors), the goal is to decrease weight and maximize the torque transmission. The low weight of composite shafts allows for the faster run-up and run-down

---

procedures of the machines when compared with the conventional metallic ones (Brush, 1999). However, in supercritical operations (flexible rotors), the vibration responses associated with the shaft bending, dynamic stress, stability, and fatigue should be carefully evaluated (Gupta, 2015).

In composite shafts, it is possible to change the stiffness and damping properties by manipulating some characteristics such as adjusting fiber and matrix composition, fiber orientation, number of layers, stacking sequence, and layer thickness. It allows for the critical velocities to be conveniently changed according to the use of the rotor. Additionally, it is possible to attenuate the vibration amplitudes when the system undergoes critical speeds (Silveira, 2001).

The internal damping can change the dynamic behavior of composite shafts, reducing their vibration amplitudes at critical speeds. However, instability can be achieved under certain conditions (Silveira, 2001). In rotors with metallic shafts, the influence of the internal damping can be omitted in most cases. Nevertheless, in composite shafts, it can be up to twice as large as on the conventional metallic ones (Wettergren and Olsson, 1996). In this context, the characterization of the internal damping is essential to design rotating machines with composite shafts aiming to establish a safe operating condition.

Simplifying hypotheses are commonly used to model composite shafts, allowing for the dynamic behavior of the system to be accurately represented. Various finite element formulations based on the homogeneous beam theory and shell theory have been proposed for the analysis of composite shafts. One of the models evaluated in this study was proposed by Singh and Gupta (1994). The EMBT (Equivalent Modulus Beam Theory) model was developed from the stratification theory and is associated with symmetrical and balanced stacks. The other model used is known as SHBT (Simplified Homogenized Beam Theory), proposed by Sino (2007). This model is based on the direct homogenization of the stiffness and damping of the shaft, being able to be applied to any orientation and stacking sequence, besides taking into consideration the distance of each layer to the neutral axis.

In this context, the present contribution is devoted to the numerical and experimental analyses of the composite hollow shaft of a horizontal rotating machine. The finite element model of the rotor was formulated.

Thus, simulated frequency response functions (FRFs) were determined. The corresponding experimental FRFs were also obtained for comparison purposes.

ROTOR MODEL

Equation (1) presents the differential equation that represents the dynamic behavior of a flexible rotor system operating in a steady state condition (Lalanne and Ferraris, 1998).

$$M\ddot{\delta} + \left[D + \Omega D_g\right]\dot{\delta} + K\delta = W + F_u \tag{1}$$

where M is the mass matrix, D is the damping matrix (e.g., associated with the bearings), D_g represents the gyroscopic effect, and K is the stiffness matrix. The vector δ contains the generalized displacements (i.e., the lateral vibrations of the shaft), Ω is the rotation speed, W stands for the weight of the rotating parts, and F_u represents the unbalanced forces.

Considering the dissipative effects associated with composite materials (Sino, 2007), Eq. (1) is modified as follows:

$$M\ddot{\delta} + \left[D + \Omega D_g + D_i\right]\dot{\delta} + \left[K + \Omega K_i\right]\delta = W + F_u \tag{2}$$

where D_i and K_i are the internal damping and the stiffness matrices, respectively.

The finite element model of the shaft was formulated according to the Timoshenko beam theory with eight four degrees-of-freedom each node, as shown in Fig. 1.
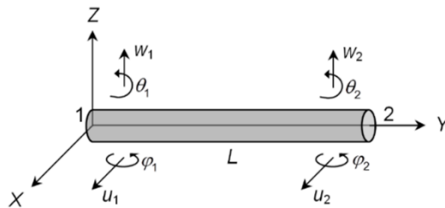
Figure 1: Timoshenko beam element with 4 degrees-of-freedom each node.

Composite hollow shaft

The composite hollow shaft studied in the present work is provided by Rock West Composites®. The shaft is manufactured by using special high-modulus pre-impregnated carbon fiber plies. Figure 2 illustrates the analyzed composite hollow shaft.

Figure 2: Composite hollow shaft used in the present contribution.

The analyzed composite material has twenty layers with the following stacking sequence: [0 0 0 0 90 90 45 -45 0 0 0 45 -45 90 90 0 0 0 0 0/90] (degrees). Table 1 summarizes the physical and geometric properties of the composite hollow shaft.

Table 1: Physical and geometric properties of the composite hollow shaft.

Shaft Properties	Value
Length (m)	0.907
Outer diameter (m)	0.018
Inner diameter (m)	0.0128
Density (kg/m³)	1667

Figure 3 shows a schematic representation regarding the directions of the fibers related to the Cartesian system, which follows the inertial directions defined for the analyzed rotor system (see the inertial directions defined in Fig. 1). In this case, 1, 2, and 3 are orthotropic axes associated with the fiber direction, the transversal direction to the fibers in the ply, and the perpendicular direction to the ply, respectively; φ is the angular direction of the fibers (Sino et al., 2008).
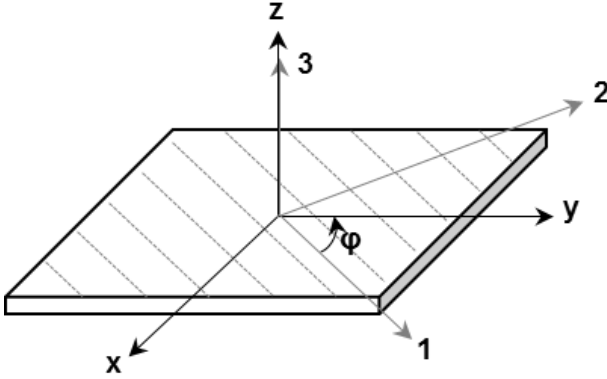
Figure 3: Schematic representation regarding the directions of the fibers with respect to the Cartesian system.

In this work, the composite material is assumed as transversely isotropic and five mechanical constants are required to characterize it. Assuming that each ply is thin enough to be a plate/shell element and a plane stress state, its mechanical properties matrix can be described by Eq. (3):

$$
Q = \begin{bmatrix} \dfrac{E_l}{1-v_{lt}v_{lt}} & \dfrac{E_t v_{lt}}{1-v_{lt}v_{lt}} & 0 \\ \dfrac{E_l v_{tl}}{1-v_{lt}v_{tl}} & \dfrac{E_t}{1-v_{lt}v_{tl}} & 0 \\ 0 & 0 & G_{lt} \end{bmatrix} = \begin{bmatrix} Q_{11} & Q_{12} & 0 \\ Q_{12} & Q_{22} & 0 \\ 0 & 0 & Q_{66} \end{bmatrix} \tag{3}
$$

where E_l and E_t are the longitudinal and transversal Young's modulus associated with each ply p. The shear modulus is given by G_{lt} and v_{lt} is the Poisson's ratio.

The Kelvin-Voigt model (Sino, 2007) was used to determine the damping and stiffness matrices associated with the composite hollow shaft (i.e., D_i^q and K_i^q, respectively; see Eq. (2)), as shows Eq. (4).

$$
\sigma = E\varepsilon + \eta E\dot{\varepsilon} \tag{4}
$$

where σ and ε are the stress and strain fields, respectively, E is Young's modulus, and η is a dimensionless parameter. Note that the Kelvin-Voigt

model comprises two parts, namely the linear stress-strain relationship given by the Hooke's law and the dissipation properties of the composite material.

The associated virtual work δW_s can be written as follows:

$$\delta W_s = \int_0^L \int_S \left(E\varepsilon + \beta E\dot{\varepsilon} \right) \delta\varepsilon \, dS \, dy \tag{5}$$

in which the strain field is given by Eq. (6).

$$\varepsilon = -z \frac{\partial^2 \left(u\cos\Omega t - w\sin\Omega t \right)}{\partial y^2} - x \frac{\partial^2 \left(u\sin\Omega t + w\cos\Omega t \right)}{\partial y^2} \tag{6}$$

Applying Eq. (6) in Eq. (5) and considering $I = \int_s x^2 \, dS = \int_s z^2 \, dS$ and $\int_s xz \, dS = 0$, the virtual work δW_s is obtained, as shows Eq. (7).

$$\delta W_s = \beta EI \int_0^L \left(\frac{\partial^2 \dot{u}}{\partial y^2} \frac{\partial^2 \delta u}{\partial y^2} + \frac{\partial^2 \dot{w}}{\partial y^2} \frac{\partial^2 \delta w}{\partial y^2} - \Omega \frac{\partial^2 w}{\partial y^2} \frac{\partial^2 \delta u}{\partial y^2} + \Omega \frac{\partial^2 u}{\partial y^2} \frac{\partial^2 \delta w}{\partial y^2} \right) dy \tag{7}$$

The generalized forces are obtained applying Eq. (6) into δW = - $F_i^t \delta \mathbf{q}$. The resulting equations are applied on the Lagrange's equations (Lalanne and Ferraris, 1998), leading to the damping and stiffness matrices associated with the composite hollow shaft (finite element matrices C_i and K_i, respectively; see Eq. (2)). The homogenized flexural stiffness EI is also used in Eq. (4) to obtain the strain energy U_s of the shaft and, consequently, the matrix K of Eq. (2). Two homogenization approaches are presented next.

EMBT approach

The homogenized Young's modulus of the composite hollow shaft determined by the EMBT (Equivalent Modulus Beam Theory) approach is given by Eq. (8).

$$E_{eq} = \frac{4(U_1 - U_5)(U_1 - U_3\gamma) - \beta^2 U_2^2}{U_1 - \beta U_2 + \gamma U_3}$$

$$\gamma = \sum_{k=1}^{N} \frac{t_k}{t} \cos 4\theta_k \tag{8}$$

$$\beta = \sum_{k=1}^{N} \frac{t_k}{t} \cos 2\theta_k$$

in which t_p is the thickness of the ply k, t is the thickness of the composite shaft, θ_k is the angular direction of the fibers of the ply k, and N is the number of plies. U_1, U_2, U_3, and U_5 are laminate invariants showed in Daniel and Ishai (1994), as is given by Eq. (9).

$$U_1 = \frac{3}{8}Q_{11} + \frac{3}{8}Q_{22} + \frac{1}{4}Q_{12} + \frac{1}{2}Q_{66}$$

$$U_2 = \frac{4}{8}(Q_{11} - Q_{22})$$

$$U_3 = \frac{1}{8}Q_{11} + \frac{1}{8}Q_{22} - \frac{1}{4}Q_{12} - \frac{1}{2}Q_{66} \tag{9}$$

$$U_4 = \frac{1}{8}Q_{11} + \frac{1}{8}Q_{22} + \frac{3}{4}Q_{12} - \frac{1}{2}Q_{66}$$

$$U_5 = \frac{1}{8}Q_{11} + \frac{1}{8}Q_{22} - \frac{1}{4}Q_{12} - \frac{1}{2}Q_{66}$$

SHBT approach

The homogenized flexural stiffness *EI* of the composite hollow shaft determined by SHBT (Simplified Homogenized Beam Theory) approach is given by Eq. (10).

$$EI = \sum_{p=1}^{N} E_y^p I^p$$

$$I^p = \frac{\pi}{4}(R_p^4 - R_{p-1}^4) \tag{10}$$

where I^p represents the inertia moment of area, R_{p-1} is the inner radius, and R_p is the outer radius; all of then associated with the ply p. The Young's modulus E_y^P of each ply is obtained by using Eq. (11).

$$E_y^p(\varphi) = \cfrac{1}{\cfrac{c^4}{E_l} + \cfrac{s^4}{E_t} + c^2 s^2 \left(\cfrac{1}{G_{lt}} - 2\cfrac{\upsilon_{lt}}{E_t} \right)} \tag{11}$$

where s and c stands for $\sin(\varphi)$ and $\cos(\varphi)$, respectively.

NUMERICAL AND EXPERIMENTAL TESTS

The rotor test rig used in the present work is composed of a horizontal composite hollow shaft, two aluminum discs, and two self-alignment ball bearings. Figure 4 shows the details of the components used in the considered test rig. Table 2 presents the physical and geometric properties of the discs.

a) aluminum discs   b) self-aligning ball bearings
Figure 4: Test rig components.

Table 2: Physical and geometric properties of the discs.

Discs Properties	Value
Thickness (m)	0.016
Outer diameter (m)	0.150
Inner diameter (m)	0.018
Density (kg/m³)	2700
Young's Modulus (Pa)	69×10^9

It is worth mentioning that the considered finite element model of the composite shaft was updated by considering four configurations of the rotor test rig. Figure 5 shows the first configuration, in which the shaft is supported by nylon wires (free-free condition for movement along the X direction). An ET-126 Labworks® electrodynamic shaker was used for excitation purposes, through which a sweep sine excitation signal was applied. The vibration responses of the shaft were measured

using two PCB® model 352C22 accelerometers (see details in Fig. 4). FRFs were obtained using the signal analyzer Agilent® model 35670A (10 Hz to 1 kHz with a resolution of 0.618 Hz).

Figure 5: First configuration of the test rig.

The FRFs were obtained for the free-free condition of the composite hollow shaft by applying excitation signal at L=0.378m along the horizontal direction and the vibration responses were measured by accelerometers installed at L=0.378m and L=0.529m along the same direction of the excitation force. Therefore, both EMBT and SHBT models were updated based on the experimental and numerical FRFs to determine the unknown parameters of the composite hollow shaft. In this case, the Differential Evolution optimization approach was used (Storn and Price, 1995). It is worth mentioning that the shaft model was formulated using 33 finite elements (Lalanne and Ferraris, 1998).

Fig 6 shows the comparison between the experimental and numerical FRFs of the composite hollow shaft as presented in Fig. 5. Note that the EMBT and SHBT models were able to represent the first vibration mode of the composite shaft. It can be observed that the damping was overestimated for the second and third vibration modes.
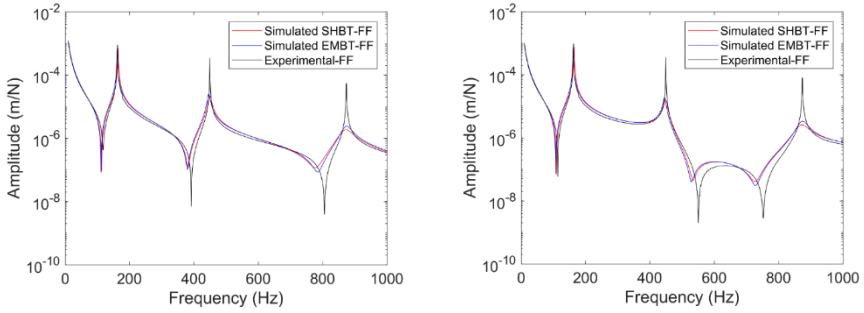
Figure 6: Comparison between the experimental and numerical FRFs obtained considering the first configuration of the test rig.

Figure 7 shows the second configuration adopted for the test rig, in which one disc was connected in the shaft at $L=0.885$m. The corresponding FRFs are presented in Fig. 8. Note that the EMBT and SHBT models were able to represent only the first vibration mode of the composite shaft.

Figure 7: Second configuration of the test rig.
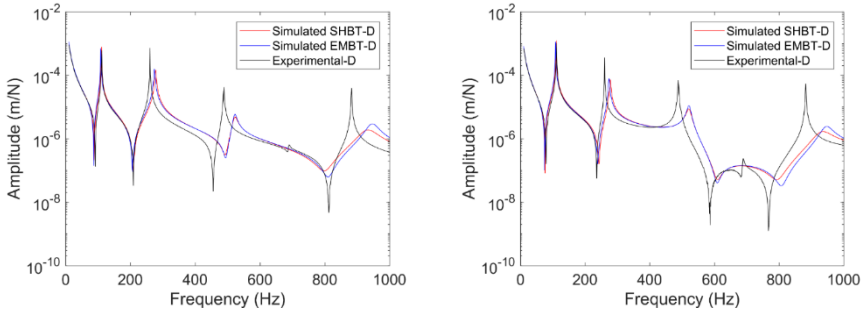
Figure 8: Comparison between the experimental and numerical FRFs obtained considering the second configuration of the test rig.

Figure 9 shows the third configuration adopted for the test rig, in which one disc was connected in the shaft at $L=0.885$m and a ball bearing was included at $L=0.620$m. The corresponding FRFs are presented in Fig. 10. Note that the EMBT and SHBT models were able to represent only the first vibration mode of the composite shaft.
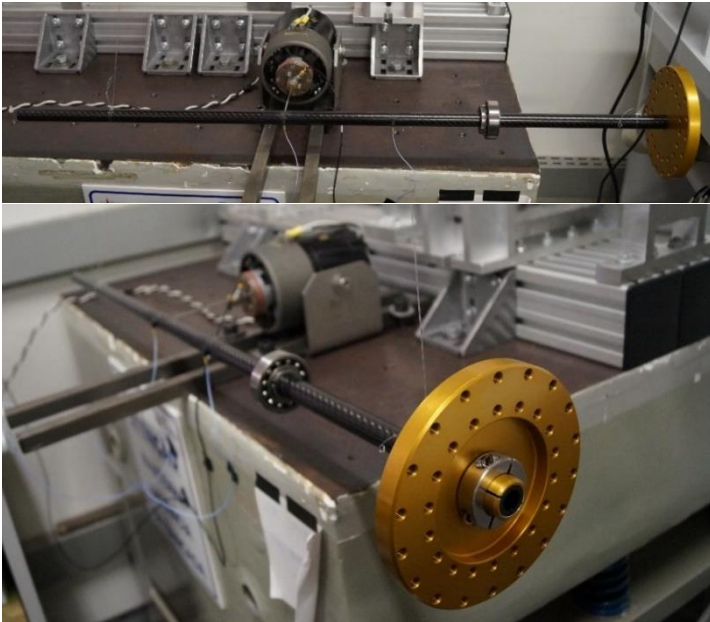
Figure 9: Third configuration of the test rig.
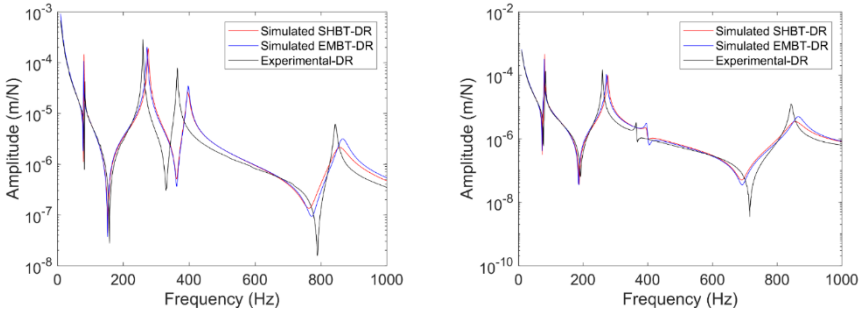
Figure 10: Comparison between the experimental and numerical FRFs obtained considering the third configuration of the test rig.

Figure 11 shows the fourth configuration adopted for the test rig, in which an additional disc was connected in the shaft at L=0.145m and an additional ball bearing was included at L=0.080m. The corresponding FRFs are presented in Fig. 12. Note that the EMBT and SHBT models were able to represent the first and second vibration modes of the composite shaft.

Figure 11: Fourth configuration of the test rig.
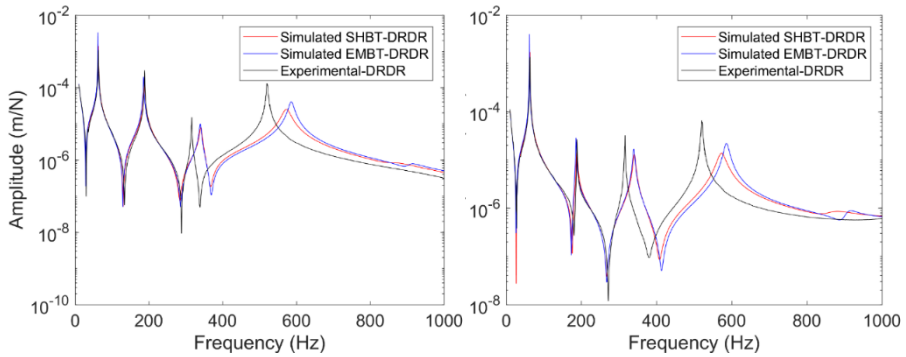
Figure 12: Comparison between the experimental and numerical FRFs obtained considering the fourth configuration of the test rig.

CONCLUSIONS

In this work, the advantages and limitations of composite materials applied in rotating machines were discussed. It was shown the formulation of governing equations modeling the behavior of rotating machines. The modeling of the composite material was formulated adopting the internal damping due to the viscoelastic nature of the polymer matrix. Thus, the rheological behavior of Kelvin-Voigt was assumed in the mathematical formulation of the finite shaft element.

The inclusion of the elastic properties matrix in the formulation of energies and virtual work is not possible since the composite shaft is considered transversely isotropic and has several layers. For this aim, two homogenization models were used (EMBT and SHBT models) through which the equivalent mechanical properties for the shaft are determined.

Numerical and experimental FRFs were obtained considering four different test rigs. In each case, the parameters of the composite shaft were updated by using the so-called Differential Evolution approach. It was demonstrated that only the first vibration mode of the considered test rig configurations could be represented by the corresponding finite element models.

According to Gupta (2015), most studies available in the literature are essentially numerical and there are few experimental results that confirm and validate the effects associated with the use of composite

materials in rotating machines. Thus, as a contribution, this work presented numerical and experimental analyses of the dynamic behavior of a composite shaft and showed the limitations related to the adopted model simplifications. Therefore, it is proposed for future work the implementation of non-linear effects for the characterization of the internal damping. Additionally, more numerical evaluations in comparison with experimental results with the machine under different operating conditions are scheduled.

ACKNOWLEDGMENTS

REFERENCES

BRUSH, M. "Still Spinning After All These Years: A Profile of The Ultracentrifuge". The Scientist, v. 13, p. 16-18, Out. 1999.

GUPTA, K. "Composite Shaft Rotor Dynamics: An Overview". In: Proceedings of VETOMAC, X, 2015, Manchester. Vibration Engineering and Technology of Machinery. p. 79-94.

LALANNE, M.; FERRARIS, G. "Rotordynamics Prediction in Engineering". New York: J. Wiley and Sons, 1998 266p.

SILVEIRA, M. E., "Análise do Comportamento Dinâmico de Rotores em Eixos Bobinados", 2001. 97 p. Masters Thesis, Federal University of Santa Catarina, Florianópolis.

SINGH, S. P.; GUPTA, K. Free Damped Flexural Vibration Analysis of Composite Cylindrical Tubes Using Beam and Shell Theories. Journal of Sound and Vibration. v. 172, p. 171-190, 1994.

SINO, R. "Comportement Dynamique et Stabilite des Rotors: Application aux Rotors Composites", 2007. 157 p. PhD Thesis, INSA - Lyon, Lyon.

SINO, R.; BARANGER, T. N.; CHATELET, E.; JACQUET, G. Dynamic Analysis of a Rotating Composite Shaft. Composites Science and Technology, v. 68, p. 337-345, Fev. 2008.

WETTERGREEN, H.L.; OLSSON, K.O. "Dynamic Instability of a Rotating Asymmetric Shaft with Internal Viscous Damping Supported in Anisotropic Bearings". Journal of Sound and Vibration, v. 195, p. 75-84, Ago. 1996.

Analysis of The Influence of Transversal Cracks on the Static and Dynamic Behaviors of Flexible Shafts[*]

Izabela Batista da Silva
izabela.silva@ufu.br

Advisors: Aldemir Ap. Cavalini Jr. and Valder Steffen Jr.

Abstract: The structural integrity evaluation of rotating machines becomes an important tool for industry, providing safe operating conditions for these types of equipment. A commonly used technique for this purpose is based on the construction of representative mathematical models. This approach has gained prominence due to its ability to avoid possible critical problems in the rotor during its design step, such as the propagation of cracks in stress concentration regions. In this context, this work proposes to evaluate the static and dynamic behavior of a disc-shaft-bearing system in order to verify the influence of an open crack with different severities. Two finite element models were developed in MatLab® (1D) and Ansys® (3D model) environments and the obtained responses were compared with experimental results. A crack was included in the 1D model based on the additional flexibility calculated through the linear fracture mechanics theory. In this context, the concepts of deformation energy release rate, stress intensification factor, and Castigliano's theorem were used. Regarding the 3D model, the crack was simulated by means of a saw cut included in the cross-section of the shaft. The obtained results demonstrate the similarity between the models and the experimental data.

Keywords: Flexible Shafts, Transversal Cracks, Finite Element Models, Static and Dynamic Behaviors

INTRODUCTION

Several advances in research of rotating machines have been observed throughout the last years. According to Ferreira (2010), the major challenge associated with the maintenance of this type of

---

equipment is related to the ability of identifying where and when a fault will occur.

Transversal cracks commonly arise in flexible shafts. These components are subject to the action of cyclic loads that increase the stress concentration in geometric discontinuities (Muszynska, 1994). Numerous techniques for crack detection and identification have gained the attention of researchers due to their industrial application. The economic effect resulting from unplanned stops or damages motivates the research for preventive solutions. In this context, structural health monitoring (SHM) techniques are being proposed in the literature (Farrar and Worden, 2007).

Dimarogonas (1996) employed the relations of the linear fracture mechanics between the strain energy density function and the stress intensification factor, as well as the Castigliano's theorem, to calculate the local flexibility in the shaft due to the crack. Bachschmid, Pennacchi, and Tanzi (2010) pointed out that structural integrity techniques based on vibration signal measurements are widely used for crack identification of rotating shafts because the crack produces a local stiffness reduction and causes changes in the dynamic behavior of the system. The construction of representative mathematical models can be used to evaluate the structural integrity of rotating shafts even in their design step.

In this context, this work aims to evaluate the static and dynamic behavior of a cracked shaft through numerical and experimental investigations. Thus, a disc-shaft-bearing system is used. The numerical analysis was performed by considering two finite element (FE) models, namely a 1D model developed in MatLab® and a 3D model developed in Ansys®. In the 1D model, the crack was added to the shaft by calculating the additional flexibility matrix proposed by Papadopoulos and Dimarogonas (1987). For the 3D model, the crack is simulated as a saw-cut on the cross-section of the shaft.

In the dynamic analysis, numerical and experimental Frequency Response Functions (FRFs) were obtained for the pristine condition of the shaft and considering cracks with 20% and 50% depths. The numerical and experimental shaft deformations were obtained in a region close to the crack by applying static forces.

EXPERIMENTAL PROCEDURE

Figure 1 shows the disc-shaft-bearing system used in this work. The system is assembled like a cantilever beam and is composed of a flexible steel shaft with 1005 mm length and 17 mm diameter ($E = 205$ GPa, $\rho = 7850$ kg/m^3, $v = 0.29$), one rigid disc with 150 mm diameter and 20 mm thickness ($\rho = 7850$ kg/m^3), and two self-alignment ball bearings.
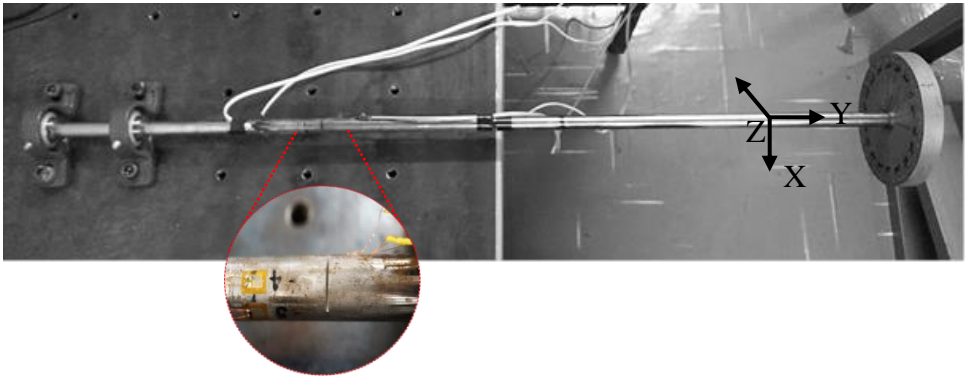
Figure 1: Shaft-bearing-disc test rig used for experimental analysis.

The ADS2000 data acquisition system is used to measure the strain fields in a region close to the crack position (see Fig. 2). Experimental FRFs were measured by applying impact forces along the X and Z directions of the disc (see Fig. 1). The vibration responses were obtained by one accelerometer positioned at the disc along the same direction as the impact forces, resulting in 2 FRFs. The measurements were performed by using the analyzer Agilent (model 35670A) in a range of 0-100 Hz and steps of 0.125 Hz. The bearing stiffness and damping coefficients were determined by solving a typical inverse problem, in which the heuristic optimization technique Differential Evolution (Storn and Price, 1995) was used. The results are shown in Tab. 1.

Table 1: Stiffness and damping coefficients.

Stiffness (N/m)		Damping (Ns/m)		Proportional Damping	
k_{xx} / b_1	$1.30\text{x}10^7$	d_{xx} / b_1	$5.13\text{x}10^2$	γ	1.00
k_{zz} / b_1	$2.50\text{x}10^8$	d_{zz} / b_1	$5.00\text{x}10^4$	β	$1.00\text{x}10^{-5}$
k_{xx} / b_2	$3.35\text{x}10^7$	d_{xx} / b_2	$9.75\text{x}10^2$		
k_{xx} / b_2	$1.00\text{x}10^8$	d_{zz} / b_2	$9.75\text{x}10^3$		

In the experimental procedure, 5 strain gages were used to measure the strain fields close to the crack location at 310 and 340 mm from the shaft bearing (see Fig. 1). The strain-gauge positions are shown in Fig. 2.

| (a) | (b) |
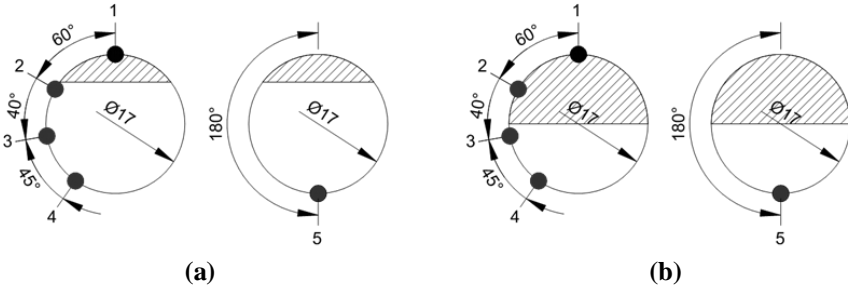
Figure 2: Strain gauges positions for the (a) 20% crack depth and (b) 50% crack depth.

DYNAMIC BEHAVIOR OF ROTATING MACHINES - 1D MODEL

The differential equation that describes the dynamic behavior of flexible rotors is given by Eq. (1) (Lalanne and Ferraris, 1998).

$$\mathbf{M}\ddot{\mathbf{q}}(t)+\left[\mathbf{D}+\Omega\mathbf{D}_g\right]\dot{\mathbf{q}}(t)+\left[\mathbf{K}+\Omega\mathbf{K}_{st}\right]\mathbf{q}(t)=\mathbf{W}+\mathbf{F}_u+\mathbf{F}_m \qquad (1)$$

where $\mathbf{M}$ is the mass matrix, $\mathbf{D}$ is the damping matrix, $\mathbf{D}_g$ is the gyroscopic effect matrix, $\mathbf{K}$ is the stiffness matrix, $\mathbf{K}_{st}$ represents the stiffening for the transient regime, $\mathbf{W}$ stands for the weight of the rotating parts, $\mathbf{F}_u$ is the unbalance forces, $\mathbf{F}_m$ is the vector of forces produced by the bearings to support the shaft, Ω is the rotation speed, and $\mathbf{q}$ is the generalized displacement vector.

The 1D FE model of the system is formulated based on the Timoshenko beam theory, in which the movement of the shaft element is described by using 2 nodes (1 and 2) and 4 degrees of freedom each

node (four lateral displacements - u_1, w_1, u_2, and w_2; four rotations θ_1, φ_1, θ_2, and φ_2). Figure 3 shows the disc-shaft-bearing system, in which the shaft is represented by 38 beam elements. The crack location is assumed to be at element #14 (between nodes #14 and #15). The two self-alignment ball bearings are located at nodes #2 and #6. The disc is located at node #37. The geometric and physical properties are the same as the experimental test rig.
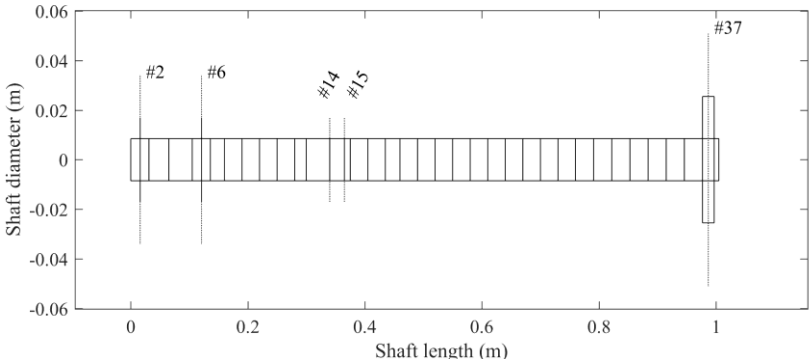
Figure 3: Disc-shaft-bearing FE model.

Crack Modeling

The dynamic model of the shaft FE with a crack is obtained first by using the linear fracture mechanics theory to determine the additional flexibility produced by the crack. This formulation is then explained, assuming a beam element containing a transverse crack with depth α, as shown in Fig. 4. In this case, the cracked FE is subject to the axial forces P_1 and P_7, the shear forces P_2, P_3, P_8, and P_9, the torsional moments P_4 and P_{10}, and the bending moments P_5, P_6, P_{11}, and P_{12}.

(a)   (b)
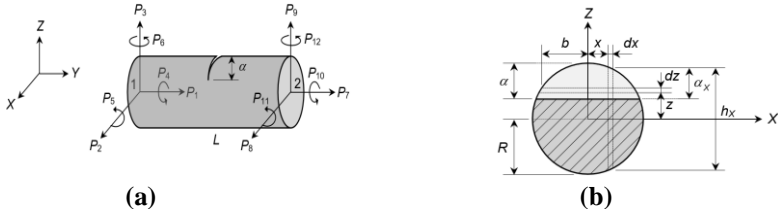
Figure 4: (a) Shaft element with a crack; (b) Details about the cross-section of the crack element. (Cavalini Jr., 2013)

73

According to Darpe, Gupta, and Chawla (2004), it is possible to determine the cracked shaft displacement q_i in the direction of the load P_i by using Castigliano's theorem, as shown in Eq. (2).

$$q_i = \frac{dU}{dP_i} = \frac{\partial U^0}{\partial P_i} + \frac{\partial U^c}{\partial P_i} \tag{2}$$

where U is the total elastic strain energy given by the sum of the elastic strain energy U^0 of the shaft element with crack and the additional strain energy U^c due to the crack presence.

Based on the linear fracture mechanics theory, the additional strain energy U^c is obtained as follows:

$$U^c = \int_A J(A) dA = \int_A \frac{1-\upsilon}{E} \left[\left(\sum_{i=1}^6 K_{Ii} \right)^2 + \left(\sum_{i=1}^6 K_{IIi} \right)^2 + (1+\upsilon) \left(\sum_{i=1}^6 K_{IIIi} \right)^2 \right] \tag{3}$$

where E is the Young's modulus of the shaft, v is the Poisson's ratio, K_{Ii}, K_{IIi}, and K_{IIIi} are the so-called stress intensity factors (SIF). In this case, only the crack load mode K_{Ii} is considered since the principal load is applied normally to the crack plane (Anderson, 2005).

U^c is used to calculate the coefficients of the additional flexibility c_{ij}, as given by Eq. (4).

$$c_{ij} = \frac{\partial^2 U^c}{\partial P_i \partial P_j} \tag{4}$$

The resulting integrals of Eq. (4) are determined using the procedure presented by Papadopoulos (2004). Therefore, the additional flexibility matrix due to the crack is given by Eq. (5).

$$\mathbf{c} = \begin{bmatrix} \bar{c}_{11} & 0 & 0 & 0 & \bar{c}_{15} & \bar{c}_{16} \\ & \bar{c}_{22} & 0 & \bar{c}_{24} & 0 & 0 \\ & & \bar{c}_{33} & \bar{c}_{34} & 0 & 0 \\ & & & \bar{c}_{44} & 0 & 0 \\ & & & & \bar{c}_{55} & \bar{c}_{56} \\ sim. & & & & & \bar{c}_{66} \end{bmatrix} \tag{5}$$

As mentioned, the 1D FE model adopted in this work to represent the shaft has two nodes with four degrees of freedom each node. Therefore, considering only the axial forces P_1 and P_7 and torsional moments P_4 and P_{10} (see Fig. 3), the additional flexibility matrix **c** (Eq. (5)) is represented only by the coefficients c_{55}, c_{56}, and c_{66}. Equation (6) shows that the additional flexibility matrix due to the crack that is included on the flexibility matrix of the healthy shaft ($\mathbf{c}_0$) to obtain the resulting flexibility of the shaft FE with crack.

$$\mathbf{c}_{CE} = \mathbf{c}_0 + \mathbf{c} \tag{6}$$

Equation (7) presents the stiffness coefficients k_ξ and k_η that are obtained from the inverse of $\mathbf{c}_{CE}$ ($k_\xi = \mathbf{c}_{CE}^{-1}(1,1)$, $k_\eta = \mathbf{c}_{CE}^{-1}(2,2)$), which are used to determine the stiffness of the shaft FE with a crack in fixed coordinates $\mathbf{K}_F$. Note that $\mathbf{K}_F$ changes according to the angular position of the shaft.

$$\mathbf{K}_F = \begin{bmatrix} cos(\theta) & -sin(\theta) \\ sin(\theta) & cos(\theta) \end{bmatrix} \begin{bmatrix} k_\xi & 0 \\ 0 & k_\eta \end{bmatrix} \begin{bmatrix} cos(\theta) & sin(\theta) \\ -sin(\theta) & cos(\theta) \end{bmatrix} \tag{7}$$

where θ is the angular position of the shaft ($\theta = \Omega t$; t stands for the time).

The stiffness matrix $\mathbf{K}_{CE}$ of the shaft FE with the transverse crack is obtained by a combination of the matrices derived from the cantilever beam condition, as shown by Eq. (8) and Eq. (9).

$$\mathbf{K}_{XY} = \frac{12EI}{L^3(1+\vartheta_Y)} \begin{bmatrix} -1 & 0 \\ L & -1 \\ 1 & 0 \\ 0 & 1 \end{bmatrix} \begin{bmatrix} K_F(1,1) & \dfrac{L}{2} \\ \dfrac{L}{2} & \dfrac{(4+\vartheta_Y)}{12}L^2 \end{bmatrix} \begin{bmatrix} -1 & L & 1 & 0 \\ 0 & -1 & 0 & 1 \end{bmatrix} \tag{8}$$

$$\mathbf{K}_{YZ} = \frac{12EI}{L^3(1+\vartheta_Y)} \begin{bmatrix} -1 & 0 \\ -L & -1 \\ 1 & 0 \\ 0 & 1 \end{bmatrix} \begin{bmatrix} K_F(2,2) & -\dfrac{L}{2} \\ -\dfrac{L}{2} & \dfrac{(4+\vartheta_Y)}{12}L^2 \end{bmatrix} \begin{bmatrix} -1 & -L & 1 & 0 \\ 0 & -1 & 0 & 1 \end{bmatrix} \tag{9}$$

COMPUTATIONAL PROCEDURE - 3D MODEL

Figure 5 shows the 3D model developed in Ansys®. In this case, the bearings are represented by two connections *Ground to Multiple*. In the shaft, a mesh was created through the sweep method with solid hexahedral and tetrahedral elements. A mesh refinement was used in the crack region considering a 0.001 mm FE size for representativeness purposes. The bearing stiffness and damping coefficients have been adopted as the same used for the 1D model (previously determined by applying a model updating procedure). A saw cut was included transversally on the shaft with two different depths (20% and 50% of the shaft diameter) to represent the crack. The strains were determined by using a static solver with a probe positioned on the shaft according to Fig. 2.
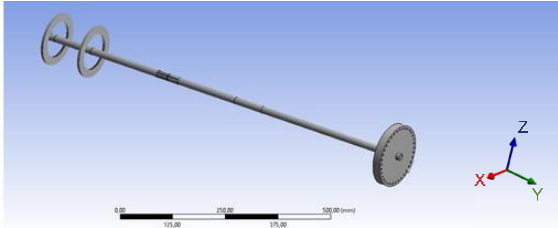
Figure 5: Ansys® 3D model.

RESULTS AND DISCUSSION

Figure 6 presents the numerical (1D and 3D updated models) and experimental FRFs obtained considering the healthy shaft. The FRFs have been obtained from impact forces applied along the *X* and *Z* directions of the disc (Fig. 6a and Fig. 6b, respectively). The corresponding vibration responses were measured along the same direction as the impact forces. The numerical and experimental natural frequencies of the disc-shaft-bearing are shown in Tab. 2. Note that the results obtained by using the 1D model are closer to the experimental data than the ones from the 3D model.
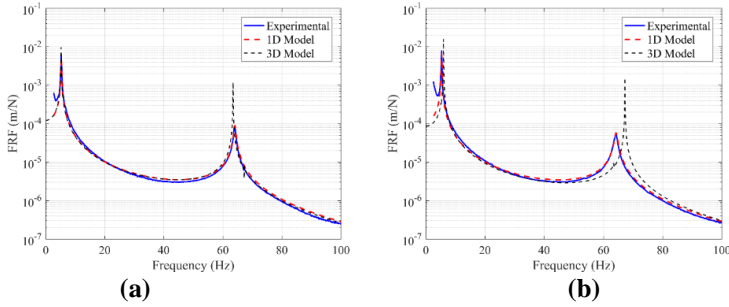
Figure 6: Numerical (updated 1D and 3D models) and experimental FRFs.
(a) Impact forces along the X direction; (b) Impact forces along the Z direction.

Table 2: Numerical and experimental natural frequencies (Hz) of the healthy shaft.

Direction	Experimental	1D model	Error (%)	3D model	Error (%)
1ª (X)	5.25	5.25	0.00	5.25	0.00
2ª (Z)	5.375	5.375	0.00	6.00	11.62
3ª (X)	64.00	64.00	0.00	63.50	0.76
4ª (Z)	64.25	64.25	0.00	67.25	4.46

Table 3 presents the numerical and experimental natural frequencies obtained for the shaft with a 50% crack depth. As expected, the results obtained by using the 1D model are closer to the experimental data than the ones determined by considering the 3D model. It is worth mentioning that the difference between the experimental natural frequencies of the healthy and faulty shaft for a 20% crack depth is smaller than the frequency resolution used to measure the corresponding FRFs, which is 0.125 Hz (Silva, 2018).

Table 3: Numerical and experimental natural frequencies (Hz) of the shaft with a 50% crack depth.

Direction	Experimental	1D model	Error (%)	3D model	Error (%)
1ª (X)	5.125	5.125	0.00	5.125	0.00
2ª (Z)	5.25	5.25	0.00	5.75	9.52
3ª (X)	64.00	64.00	0.00	63.50	0.78
4ª (Z)	64.25	64.25	0.00	67.125	4.47

Figures 7 and 8 show the strain fields determined by using both 1D and 3D models for the healthy and faulty (cracks with 20% and 50% depth) shaft. The experimental strain fields have been measured for comparison purposed. The positions of the strain gauges are presented

in Fig. 2. It is important to highlight that the 1D model assumes linear stress and strain distributions. Figure 7 shows the strain fields measured in the shaft with the 20% crack depth. Note that the numerical and experimental results are similar for different angular positions of the shaft.
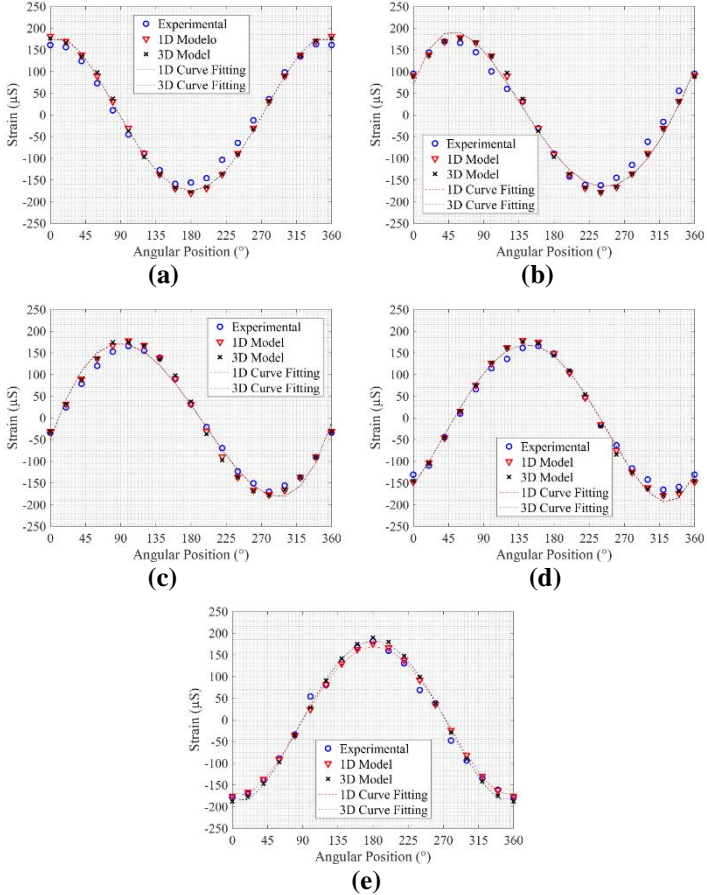
Figure 7: Comparison between the numerical and experimental strains for the shaft with a 20% crack depth. Stain gauges (a) 1, (b) 2, (c) 3, (d) 4, and (e) 5.

Figure 8 compares the results obtained considering the 50% crack depth. Figures 8a, 8b, 8c, and 8d show that the strains obtained by using the 3D model are closer to the experimental data than the ones determined by considering the 1D model, which can be associated with the crack nonlinearity affecting the dynamic behavior of the system. Nonlinear effects are disregarded in the 1D model. The differences

highlighted in Fig. 8d have been also obtained by Bachschmid, Pennacchi, and Tanzi (2010) and are associated with the position of the strain gauge.
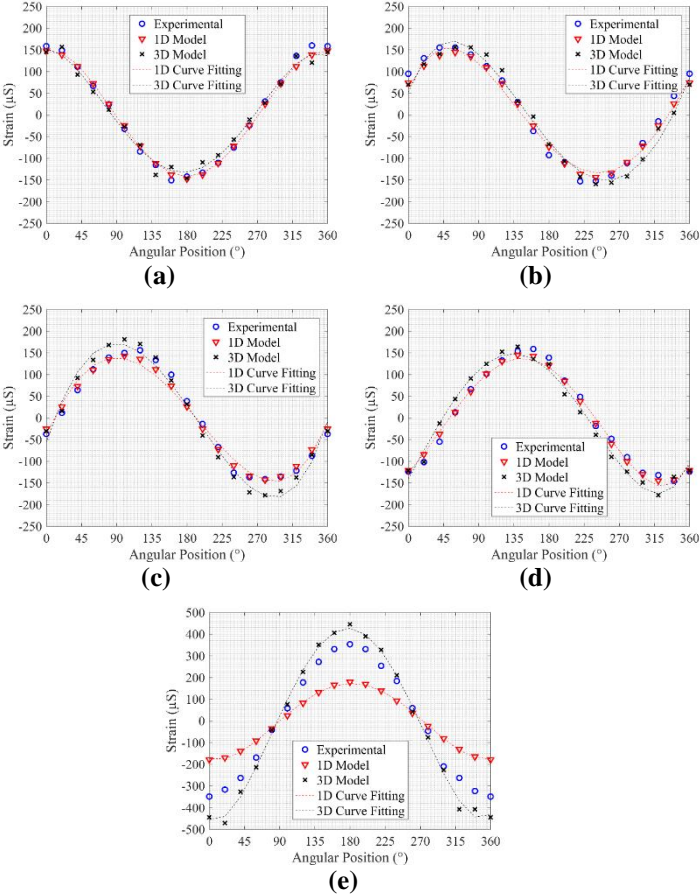
Figure 8: Comparison between the numerical and experimental strains for the shaft with a 50% crack depth. Strain gauges (a) 1, (b) 2, (c) 3, (d) 4, and (e) 5.

FINAL REMARKS

This work was dedicated to the investigation of the static and dynamic behaviors of a cracked shaft through numerical and experimental analyses. Firstly, the FRFs of the system were obtained both for the healthy and faulty (20% and 50% crack depths, for the faulty case) shafts. As expected, few changes were verified on the natural

frequencies with the crack existence. The strain fields of the cracked shaft were measured experimentally in regions close to the crack position. The numerical results obtained by using 1D and 3D FE models were presented for comparison purposes. Different angular positions of the shaft were analyzed. It was possible to observe that the 3D model represents better the shaft only for the 50% crack depth case. Research efforts will be dedicated to include the rotordynamics effects on the considered analyses.

REFERENCES

Anderson, T.L., 2005, "Fracture Mechanics: Fundamentals and Applications", Taylor & Francis, USA, 640 p.

Bachschmid, N., Pennacchi, P. and Tanzi, E., 2010, "Cracked rotors: a survey on static and dynamic behavior including modelling and diagnosis", Springer, 399 p.

Cavalini Jr, A.A., 2013, "Detecção e Identificação de Trincas Transversais Incipientes em Eixos Horizontais Flexíveis de Máquinas Rotativas", 235f. Tese de Doutorado - Universidade Federal de Uberlândia, Uberlândia.

Darpe, A.K., Gupta, K. and Chawla A., 2004, "Coupled bending, longitudinal and torsional vibrations of a cracked rotor", Journal of Sound and Vibration, Vol. 269, No. 1, pp. 33-60.

Dimarogonas, A.D., 1996, "Vibration of cracked structures: a state of the art review", Engineering Fracture Mechanics. Vol. 55, No. 5, pp. 831-857.

Farrar, C.R. and Worden, K., 2007, "An Introduction to Structural Health Monitoring", Philosophical. Transactions of the Royal Society A. Vol.365, pp. 303-315.

Ferreira, B.F., 2010, "Detecção de Trincas em Eixos Rotativos Através de Medição de Vibrações", 101f. Dissertação de Mestrado - Universidade de Brasília, Brasília.

Muszynska, A., 2005. "Rotordynamics", Taylor & Francis Group, 1128 p.

Papadopoulos, C.A. and Dimarogonas, A.D., 1987, "Coupled longitudinal and bending vibrations of a rotating shaft with an open crack", Journal of Sound and Vibration, Vol. 117, pp. 81-93.

Papadopoulos, C.A., 2004, "Some comments on the calculation of the local flexibility of cracked shafts", Journal of Sound and Vibration, Vol. 278, No. 1, pp. 1205–1211.

Silva, I.B., 2018, "Análise da influência de trincas transversais no comportamento estático e dinâmico de eixos flexíveis", 53f. Dissertação de Mestrado - Universidade de Uberlândia, Uberlândia.

Storn, R. and Price, K., 1995. "Differential evolution: a simple and efficient adaptive scheme for global optimization over continuous spaces", International Computer Science Institute, Vol.12, No. 1, pp. 1-16.

Importance of Viscoelastic Dampers and Parametric Uncertainties in Fatigue Analysis[*]

Lauren Karoline de Sousa Gonçalves
laurenkaroline@ufu.br

Advisor: Antônio Marcos Gonçalves de Lima

Abstract: In the design of dynamic structures subjected to multiaxial random load, there are some concerns regarding to fatigue life. A possible solution used to increase fatigue life is the application of a constrained viscoelastic layer in the structure. However, studies with damping layers have been developed considering mean parameters for materials properties and environmental conditions resulting in non-realistic situations that requires the use stochastic finite element models. This work is devoted to compare fatigue failure responses of deterministic and stochastic systems with and without passive constrained damping layer under Gaussian random loadings. Numerical simulations were performed for a three-layer sandwich plate structure applying the Karhunen-Loève expansion. It was evaluated the importance of uncertainties for representation of real structures behavior in a numerical model. The fatigue damage was assessed by using Sines global criterion. The numerical results are presented in terms of envelopes of the frequency responses functions (FRFs), stress responses (PSDs) and fatigue indexes estimated by Sines' criterion.

Keywords: Fatigue analysis, Sines criterion, uncertainties, viscoelastic materials

INTRODUCTION

The development of larger and efficient engineering structures drives the modernization and improvement of industrial processes and products. In this sense, the main concerns during the early design phases or existing systems analysis are the aerodynamic instability, loss of performance of the structure and equipment, as well as vibration-

induced fatigue failures. Accordingly, several studies have considered the viscoelastic materials as suitable for passive control techniques to minimize these effects by their inherent stability and maintenance costs (de LIMA et al., 2014).

In the context of fatigue damage analysis, many authors such as Sines (1959) and Crossland (1956) developed a suitable methodology to estimate high-cycle fatigue life of engineering structures. However, considering that the performance of fatigue damage criteria was questioned since the non-proportionality is not taken into account for ductile materials. Lambert et al. (2010) proposed a probabilistic approach of the Sines' criterion for random stress and load phase shifts. Thus, this methodology is adapted and employed in this work to estimate the Sines' fatigue coefficient expectation of structures incorporating a viscoelastic-damping device and subjected to uncertainties.

However, viscoelastic behavior formulation into the finite element (FE) models is a relevant aspect due to stiffness matrices strongly depend on environmental and operational factors such as temperature and frequency (de LIMA et al., 2014). It is worth noting that these factors are subjected to random effects due to inherent uncertainties of materials properties, environmental conditions and mechanical cyclic loads (NASHIF et al., 1985; ABDESSALEM et al., 2016). Thus, the fatigue analysis of viscoelastic systems subjected to uncertainties was realized using the stochastic finite element methodology (SFEM) in order to observe the response variability of dynamic problems in the frequency domain (GHANEN and SPANOS, 1991).

After a theoretical foundation concerning SFEM and fatigue analysis, a numerical application of a rectangular plate treated by viscoelastic materials subjected to stationary random transverse load is presented. It could be evaluated and quantified the reliability increase of deterministic and stochastic system by incorporation of viscoelastic dampers.

STOCHASTIC FINITE ELEMENT METHOD

This section summarizes the stochastic finite element formulation used to modeling a sandwich plate structure subjected to uncertainties. Sandwich rectangular element considered herein is composed by an

elastic base-plate (1), a viscoelastic core (2) and an elastic constraining layer (3). In the case of SFEM models, uncertainties are introduced in design variables and operating temperature to obtain the exact mass and stiffness matrices of each layers by Karhunen-Loève expansion method (GHANEM and SPANOS, 1991). Karhunen-Loève expansion (KL) approximates a two-dimensional random field $H(x, y, \theta)$ by $\hat{H}(x, y, \theta)$, formed by physical parameters describing the system geometry and random events (GHANEM and SPANOS, 1991). It can be expressed as follows:

$$\hat{H}(x, y, \theta) = \mu + \sum_{r=1}^{\infty} \sqrt{\lambda_r} f_r(x, y) \xi_r(\theta) \tag{1}$$

where μ is the mean value, $\xi_r(\theta)$ represents the Gaussian random variables (zero mean and unit variance) and λ_r and $f_r(x, y)$ are, respectively, eigenvalues and eigenfunctions of the covariance function. Random fields can be estimated solving the follows integral, as proposed by Ghanem and Spanos (1991) methodology and applied by de Lima et al. (2010):

$$H_r(x, y) = \int_{\Omega} C(x, y) f_r(x, y) dx dy \tag{2}$$

where $C(x, y)$ is the covariance function of a random field's bidimensional $H(x, y, \theta)$.

Stochastic elementary matrices of the viscoelastic sandwich plate of each layer are obtained as follows:

$$K_r^{(k)}(\theta) = \overline{K}^{(k)} + \sum_{r=1}^{n} K_r^{(k)} \xi_r(\theta) \tag{3a}$$

$$K_r^{(2)}(\omega, T, \theta) = G(\omega, T) \overline{K}^{(2)} + G(\omega, T, \theta) \sum_{r=1}^{n} K_r^{(2)} \xi_r(\theta) \tag{3b}$$

$$M_r(\theta) = \overline{M} + \sum_{r=1}^{n} M_r \xi_r(\theta) \tag{3c}$$

where $K_r^{(k)}(\theta)$ and $K_r^{(2)}(\omega,T,\theta)$ are elastic $(k=1,3)$ and viscoelastic stochastic stiffness matrices, respectively, and $M_r(\theta)$ is the stochastic mass matrix, which are composed of deterministic $(\overline{K}^{(k)}, \overline{K}^{(2)}, \overline{M})$ and stochastic $(K_r^{(k)}\xi_r(\theta), K_r^{(2)}\xi_r(\theta), M_r\xi_r(\theta))$ parts. $G(\omega,T,\theta)$ is the complex modulus for representation viscoelastic core's frequency-temperature-dependent behavior. The 3M ISD112™ viscoelastic core material is a rubber-like polymer that is provided by the manufacturer in the form of adhesive tapes. Drake and Soovere (1984) suggest analytical expression for complex modulus and shift factor. The follow expression represents their behavior in the intervals $210 \leq T \leq 360K$ and $1.0 \leq \omega \leq 1.0 \times 10^6\,Hz$:

$$G(\omega,T_v) = 430700 + \frac{1200 \times 10^6}{1 + 3.241 \times (i\omega_r/1543000)^{-0.18} + (i\omega_r/1543000)^{-0.6847}} \tag{4a}$$

$$log(\alpha_T) = -3758.4 \times \left(\frac{1}{T} - \frac{1}{290}\right) + 225.06\,log\left(\frac{T}{290}\right) + 0.23273 \times (T - 290) \tag{4b}$$

where T is the temperature in (K), ω_r is the reduced frequency (rad/s), and G is the complex modulus (N/m²).

From elementary mass and stiffness matrices for elastics and viscoelastic layers, as shown in Eqs. (3), global mass and stiffness matrices can be assembled by the system's connectivity, considering the behavior purely elastic and representing the initial strain state. After obtaining these matrices, stochastic system's movement ordinary differential equation is shown on Eq. (5):

$$[Z(\omega,T,\theta)]U(\omega,T,\theta) = F(\omega) \tag{5}$$

where $Z(\omega,T,\theta) = K_e(\theta) + G(\omega,T,\theta)\overline{K}_v(\theta) - \omega^2 M(\theta)$ is the complex frequency response function $U(\omega,T,\theta)$ and $F(\omega)$ are, respectively, displacement and applied loading vectors; $M(\theta), K_e(\theta)$ and $\overline{K}_v(\theta)$ are the global mass and stiffness stochastics matrices. It is important to point-out that in practical applications, the use of condensation methods are required to maximize the computational time gain and reduce the number of degrees of freedom (DOF).

The amplitudes of frequency responses functions (FRFs) to sandwich model with discrete viscoelastic dampers subject to uncertainties can be expressed as follows:

$$\hat{H}(\omega,T,\theta)=\left[K_e(\theta)+G(\omega,T,\theta)\overline{K}_v(\theta)-\omega^2 M(\theta)\right]^{-1} \qquad (6)$$

Power Spectral Density (PSD) is a statistical property normally employed for characterization of the stationary random process in the frequency domain. Stress responses can be expressed via PSD considering a white Gaussian noise random load $\Phi_f(\omega)$ applied, as follows equation:

$$\hat{\Phi}_s(\omega,T,\theta)=CB\hat{H}(\omega,T,\theta)\Phi_f(\omega)\hat{H}(\omega,T,\theta)^H B^T C^T \qquad (7)$$

where $\hat{\Phi}_s(\omega,T,\theta)=\begin{bmatrix}\hat{\Phi}_{xx,xx}(\omega,T,\theta) & \hat{\Phi}_{xx,yy}(\omega,T,\theta) & \hat{\Phi}_{xx,xy}(\omega,T,\theta)\\ \hat{\Phi}_{yy,xx}(\omega,T,\theta) & \hat{\Phi}_{yy,yy}(\omega,T,\theta) & \hat{\Phi}_{yy,xy}(\omega,T,\theta)\\ \hat{\Phi}_{xy,xx}(\omega,T,\theta) & \hat{\Phi}_{xy,yy}(\omega,T,\theta) & \hat{\Phi}_{xy,xy}(\omega,T,\theta)\end{bmatrix}$

for a random stress vector of the form $s(t,T,\theta)=\begin{bmatrix}s_{xx}(t,T,\theta) & s_{yy}(t,T,\theta) & s_{xy}(t,T,\theta)\end{bmatrix}^T$.

SINES' FATIGUE CRITERION

Generation and propagation of cracks lead to fatigue failure that it is a phenomenon characterized as very dangerous, sudden and catastrophic without previous notice (Dowling, 2007). Fatigue cracks usually appear on critical points where the stress levels are higher. This failure type has been studied by some works (Weber, 1999; Taier, Araújo and Godefroid, 2002) and several uniaxial and multiaxial criteria have been developed for performing fatigue damage analysis, as Wohler diagram (Budynas and Nisbett, 2011), Sines' criterion (Sines, 1959) and Crossland's criterion (Crossland, 1956).

Weber (1999) studied several fatigue criteria and concluded that Sines' criterion has better accuracy with a simple formulation, requiring

only two fatigue-related properties. Sines (1959) proposed a stress criterion for multiaxial fatigue which depends on square root of the stress deviatoric tensor second invariant $\left(\sqrt{J_{2a}}\right)$. Thus, Lambert et al. (2010) proposed a probabilistic approach for fatigue damage analysis from Sines' global criterion considering the random nature of the stress state and load phase shifts. Rosa and de Lima (2016) applied this probabilistic approach proposed by Lambert et al. (2010) to describe fatigue in thin plates considering uncertainties concerned to the structure itself.

Thus, to estimate the fatigue index $\left(D_{Sines}\right)$ of viscoelastic systems subjected to parametric uncertainties and multiaxial loadings, Sines' fatigue criterion is formulated as follows:

$$E\left[D_{Sines}\right] \approx \frac{E\left[\sqrt{J_{2a}(\theta)}\right]}{t_{-1}} \leq 1 \tag{8}$$

where t_{-1} is the alternate torsional fatigue resistance. It is important to point out that D_{Sines} with values greater than one indicate fatigue failure.

Li and de Freitas (2002) proposed a procedure for fast evaluation of high-cycle fatigue under multiaxial random loading. The square root of the second invariant of stress deviator was estimated from minimum circumscribed ellipse approach in order to take into account the nonproportional loading effect. Lambert et al. (2010) expanded the ellipse method for a five-dimension prismatic hull circumscribing the loading path of the second invariant as follows:

$$E\left[\sqrt{J_{2a}(\theta)}\right] = \sqrt{E[R_1(\theta)]^2 + E[R_2(\theta)]^2 + E[R_3(\theta)]^2 + E[R_4(\theta)]^2 + E[R_5(\theta)]^2} \tag{9}$$

Each semi-axe $E[R_i(\theta)]$ of prismatic hull is calculated by:

$$E[R_i(\theta)] \approx \lambda_{0,i}\left(\sqrt{2\,ln(k_u N_p)} + \gamma\Big/\sqrt{2\,ln(k_a N_p)}\right) \tag{10}$$

where $\lambda_{n,1}$ is the nth-order spectral moment, $\gamma = 0.5772$ is the Euler-Mascheroni constant and $N_p = (T/2\pi)\sqrt{\lambda_{1,i}^2/\lambda_{2,i}^2}$ is the number of maxima on the gaussian process for $i = (1,...,5)$. Bandwidth parameters, k_u and k_a are defined as follows:

$$k_u = \begin{cases} 1.5\left(1 - e^{(-1.8\delta)}\right) & for\ \delta < 0.5 \\ 0.94 & for\ \delta \geq 0.5 \end{cases}, \quad k_a = \begin{cases} 7\delta & for\ \delta < 0.5 \\ 4.05 & for\ \delta \geq 0.5 \end{cases} \tag{11}$$

where $\delta = \sqrt{1 - \lambda_1^2/(\lambda_0\lambda_2)}$ is the irregularity fator dependente on the spectral moments.

RESULTS AND DISCUSSION

This section outlines the numerical applications and summarizes the responses obtained in terms of FRFs envelopes, PSDs envelopes and Sines' fatigue coefficient. These responses allowed evaluating the importance of considering viscoelastic damping and uncertain variables for fatigue damage analysis of structures in the frequency domain.

Numerical implementation was based on the development made by Khatua and Cheung (1973) and Lima et al. (2010). The structure is a clamped-clamped-free-free rectangular plate made of aluminum, fully treated with a layer of 3M ISD112^{TM} between base-plate and constrained-layer. Sandwich plate dimension is 0.654m×0.527m and it was discretized in 10x10 finite elements mesh with four nodes and seven degrees of freedom per node, which are five in-plane displacement in direction x,y,z (denoted by u_1, v_1, u_3, v_3, w) and two cross-section rotations (denoted by θ_x, θ_y). The thicknesses of the base-plate, the constraining layer, and viscoelastic core are, respectively, 1.0mm, 0.25mm and 0.12mm. The loading is applied on the central node, and data acquired under a frequency band of [0-100 Hz].

In the present study, Kirchhoff's plate theory (Zienkiewicz and Taylor, 2005) is used for elastic base-plate and constraining layer and Mindlin's theory is assumed for viscoelastic core in order to account for transverse shear deformation. All materials are treated as homogeneous, isotropic and with linear mechanical behavior. The plate's mechanical properties are given on Tab.1 for each layer.

Table 1 – Mechanical properties of the sandwich plate

Layer	Young's Module (N/m²)	Poisson ratio	Mass density (kg/m³)
Base plate	70×10^9	0.29	2700
Viscoelastic core	-	0.49	950
Constraining layer	70×10^9	0.29	2700

The first test is intended to evaluate the deterministic distributions of the Sines' fatigue damage criterion for each FE for the structure without and with surface viscoelastic treatment, shown in Fig.1.

(a)   (b)
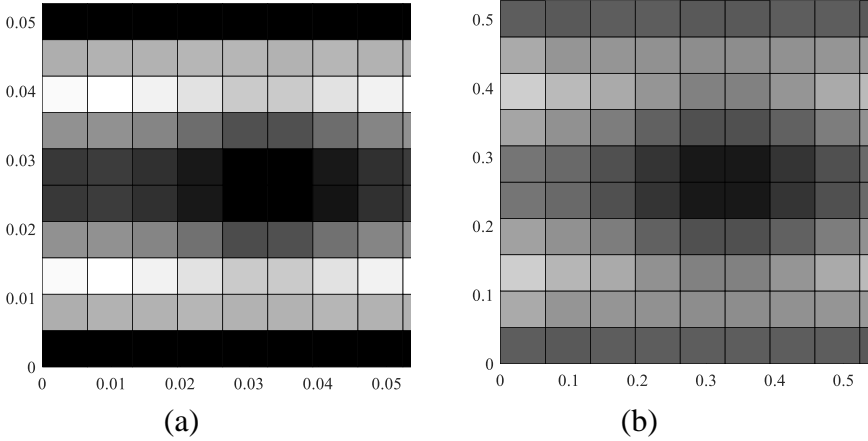
Figure 1: Distribution of $\left\lfloor E\sqrt{J_{2a}} \right\rfloor$ for the base-plate: (a) without treatment: (max.: 1.10 in center and 1.16 in border); (b) with viscoelastic treatment: (max.: 0.90 in center and 0.65 in border).

Analyzing the distribution of $\left\lfloor E\sqrt{J_{2a}} \right\rfloor$, it can be clearly observed the critical elements are located in the central and border parts of the plate, which is expected due to plate symmetry, boundary conditions and nature of the applied external force. Furthermore, Sines' coefficient expectation decreases until 43.96% with viscoelastic treatment in the critical areas. Therefore, viscoelastic material application resulted in substantial reduction of the Sines' coefficient expectation and consequently increase the fatigue life of the base structure.

Fig. 2 shows a comparison between the amplitudes of the FRFs (receptances) of the plate with and without viscoelastic treatment to provide a sense of the efficiency of viscoelastic treatment. From this

result, it is possible to note that the discrete dampers could minimize the first mode's FRF amplitudes around 20%. Thus, it can be clearly perceived the effectiveness of the viscoelastic dampers.
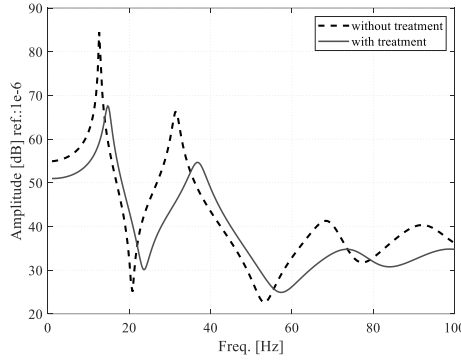
Figure 2: FRF amplitudes of the plate without and with viscoelastic treatment

Another aspect considered as being of great importance is the influence of parameters uncertainties affecting the system behavior. Thus, it is convenient to take into account the random samples using Monte Carlo Simulation (MCS) (Rubinstein, 1981) and Latin Hypercube Sampling (LHS) (Florian, 1992), considering 10% variation of constraining and viscoelastic layers thicknesses and nominal temperature. A convergence analysis via root-mean-square deviation (RMSD) is required in order to estimate the optimal number of samples n_s using Eq. (12). Thus, it is possible to obtain RMSD normalized by its mean, as shown in Fig. 3, concluding that at about 300 samples have a satisfactory convergence for this method.

$$RMSD = \sqrt{\frac{1}{n_s}\sum_{i=1}^{n_s}\left|\mathbf{H}(\omega,T,\theta)-\mathbf{H}(\omega,T)\right|^2} \qquad (12)$$

In the sequence, Eq. (6) and Eq. (7) are used to obtain FRFs envelopes of the displacement by a unitary impulse loading applied and PSDs envelopes of the stress responses in the most critical element. These envelopes are composed by its maximum, mean and minimum values for each frequency ranges, as shown in Fig. 4. It is possible to observe

that the variations in the damping layers thickness and temperature result in fluctuating responses.
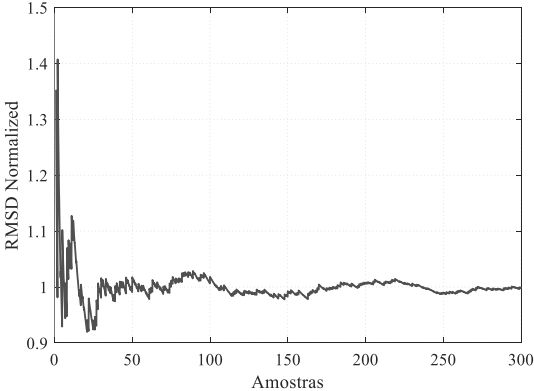
Figure 3: Convergence analysis via RMSD (10% uncertainty levels)

(a)   (b)

(c)   (d)
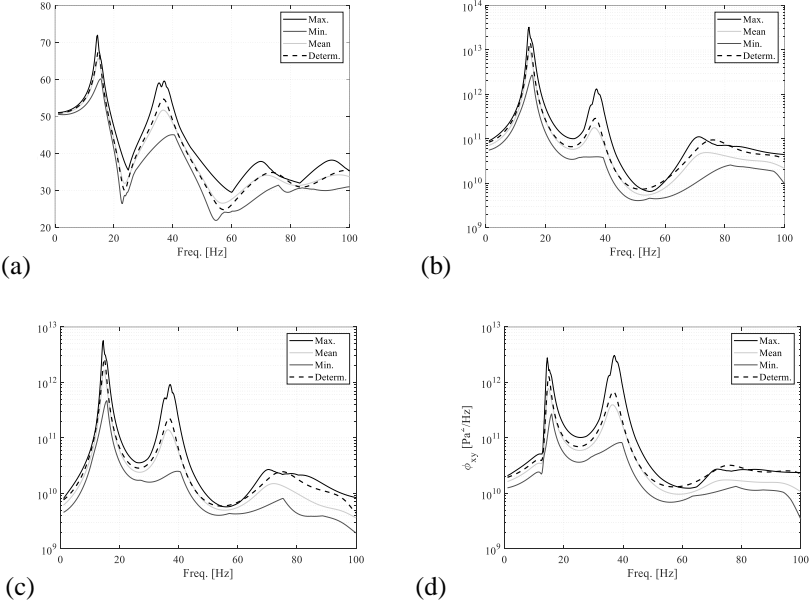
**Figure 4: (a) Displacement FRF envelopes for 10% uncertainty level; (b)–(d)
PSDs of the stress responses in the most critical elements.**

Finally, Sines' fatigue coefficient expectation for each element of the sandwich plate was estimated considering $t_{-1} = 92MPa$ for two million cycles. Table 2 summarizes the maximum values encountered and the

Fig. 5 shows plate plots for maximum, mean and minimum expected values of the coefficient.
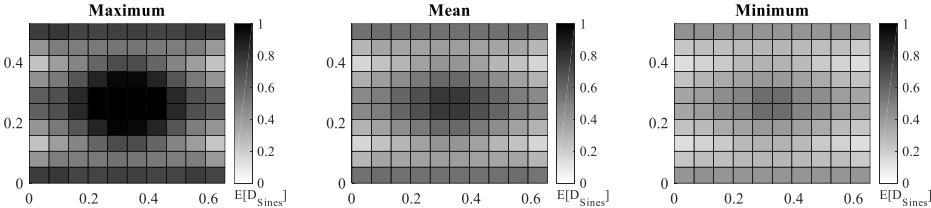
Figure 5: Sines coefficient distribution for 10% level

From Fig. 5 and Tab. 2, it can be observed that the most critical fatigue indexes are in the center plate with coefficient upper than one. Thus, it becomes more obvious the importance of considering uncertainties especially when the system is subjected to random effects. Furthermore, the contour plots of statistical expectation for Sines' coefficient showed that it is possible to notice which elements are more susceptible to failure.

Table 2: Sines' coefficient expectation for center and border of critical elements

	Center	Border
Maximum	1.1803	0.8057
Mean	0.7745	0.5724
Minimum	0.5588	0.4214

CONCLUDING REMARKS

This work analyzed the behavior of viscoelastically-damped structures subjected to uncertainties and showed the importance of parametric uncertainties for fatigue life. The results obtained through the numerical simulations confirmed that the viscoelastic dampers enable to decrease the amplitude of frequency responses functions and increase the fatigue life. The fatigue coefficient distribution enable to identify exactly the critical elements and evidence the random effects in the estimated system life.

Finally, it showed that the deterministic models cannot have reasonable accuracy when the structure are subjected to dynamic loads

or small changes on their design variables. This reinforces the importance of uncertainty analysis during design of the dynamical systems, especially to approach real-world complex behavior and to guarantee comfort, durability, safety and reliability in the presence of mechanical vibrations.

ACKNOWLEDGMENTS

REFERENCES

Abdessalem, A.B., Azaïs, R., Touzet-Cortina, M., Gégout-Petit, A., Puiggali, M., 2016, "Stochastic modelling and prediction of fatigue crack propagation using piecewise-deterministic Markov processes", Proceedings of the Institution of Mechanical Engineers, Part O: Journal of Risk and Reliability, 2016.

Budynas, R.G., Nisbett,J.K., 2011, "Shigley's Mechanical Engineering Design", McGraw-Hill, New York.

Crossland, B., 1956, "Effects of large hydrostatic pressures on the torsional fatigue strength of n
an alloy steel", International Conference on Fatigue of Metals, London.

De Lima, A.M.G., Lambert, S., Rade, D.A., Pagnacco, E., Khalij, L., 2014, "Fatigue reliability analysis of viscoelastic structures subjected to random loads", Mechanical Systems and Signal Processing, Vol.43, p.305-318.

De Lima, A. M. G., Rade, D. A., Bouhaddi, N., 2010, "Stochastic modeling of surface viscoelastic treatments combined with model condensation procedures" Shock and Vibration, Vol.17, n.4-5, p.429-444.

Dowling, N.E., 2007, "Mechanical behaviour of materials: Engineering Methods for Deformation, Fracture and Fatigue", Pearson Prentice Hall, 3rd edition.

DRAKE, M.L., SOOVERE, J.A., 1984, "A design guide for damping of aerospace structures", Vibration Damping Workshop, Long Beach, California.

Florian, A.W., 1992, "An efficient sampling scheme: updates Latin Hypercube sampling", Probabilistic Engineering Mechanics, Vol.7, n.2, p.123-130.

Ghanem, R.G., Spanos, P.D., 1991, "Stochastic finite elements: a spectral approach", Courier Corporation, Mineola, New York, 129 p.

Khatua, T.P., Cheung, Y. K., 1973, "Bending and vibration of multilayer sandwich beams and plates", International Journal for Numerical Methods in Engineering, Vol.6, n.1, p.11-24.

Lambert, S., Pagnacco, E., Khalij, L., 2010, "A probabilistic model for the fatigue reliability of structures under random loadings with phase shift effects", International Journal of Fatigue, Vol.32, p.463-474.

Li, B.; Freitas, M. J. A., 2002, "Procedure for Fast Evaluation of High-Cycle Fatigue Under Multiaxial Random Loading", Journal of Mechanical Design, Vol.124, p.558-563.

Nashif, A.D., Jones, D.I.G., Henderson, J.P., 1985, "Vibration Damping", John Wiley & Sons, New York.

Rosa, U.L., de Lima, A.M.G., 2016, "Fatigue analysis of stochastic systems subjected to cyclic loading in the frequency domain", Proceeding of the 3rd International Symposium on Uncertainties Quantification and Stochastic Modeling, Maresias, Brazil, pp. 1-10.

Rubinstein, R.Y., 1981, "Simulation and the Monte Carlo Method", John Wiley & Sons, New Jersey.

Sines, G., 1959, "Behavior of metals under complex static and alternating stress, in: G. Sines, J.L. Waisman (Eds.), Metal Fatigue" McGraw-Hill, New York, USA.

Taier, R., Araújo, E.C., Godefroid, L.B., 2002, "Fadiga em plataformas offshore fixas com modelos em elementos finitos", REM: Revista Escola de Minas, Vol.55, n.3, p.173-178.

Zienkiewicz, O.C. and Taylor, R.L., 2005, "The finite element method for solid and structural mechanics", Elsevier, 6th edition.

Weber, B., 1999, "Fatigue multiaxiale des structures industrielles sous chargement quelconque", Tese de doutorado - INSA de Lion, Lion, 243 f.

Closed-Loop Poles and Zeros Analysis of a Multi-Copter System Endowed With Tilting Mechanisms[*]

Felipe Machini M. Marques[*]
machini@ufu.br

Abstract: In general, standard multi-copters are classified as an underactuated system since their number of control inputs are insufficient to allow the control of position and orientation independently. In this context, this paper deals with the dynamical modeling of a tilted rotor multi-copter aerial vehicle and the project of a trajectory tracking controller using modern control techniques. The dynamic model is developed using Newton Euler Laws and it is assumed that each rotor is capable of two different movements (tilt laterally and longitudinally) introducing more control inputs to the system. Then, the equations of motion are linearized around the trimmed operating conditions (based on mission applications). For path following applications, linear modern MIMO (Multi-Input Multi-Output) control techniques are applied in order to allow the aircraft to follow a pre-defined trajectory. Finally, the system closed loop behavior, containing either lateral or longitudinal tilting mechanism or without it and also varying its number of rotors, is evaluated mapping its pole and zero position on the real-imaginary axes. Results have shown that the system with lateral tilt mechanism and more number brings the poles further from the imaginary axis and that the presented formulation have limitations due to nonmimimum-phase zeros.

INTRODUCTION

Multi-rotors are included in the category of vertical take-off and landing (VTOL) vehicles having more than two propellers. The number of propellers or rotors defines the resulting thrust force and, consequently, the payload capacity of the aircraft. Over the past decades,

the control capacity of these unmanned aerial vehicles (UAVs) has attracted the attention of researchers. This fact is due to their mechanical simplicity, simple dynamics and simple/low-cost maintenance; thus, they are considered as being ideal robotics platform for the development and testing control strategies (Suiçmez, 2014).

However, standard multi-rotors UAVs possess a limited mobility due to their inherent underact actuation - (Ryll et al, 2012). A quadrotor, for instance, has 4 independent control inputs (the 4 propellers spinning velocities) and, on the other hand, 6 degrees of freedom (DOFs) which represents the system position/orientation in space. Thus, for quasi-hover conditions, a horizontal translation necessarily implies a change in the attitude, and the quadrotor can hover in place only when being in horizontal position with respect to the inertial coordinate frame.

Many authors have investigated different solutions for the underact actuation - problem (Ryll et al, 2012; Badr et al, 2016; Oosedo et al, 2016). Each work proposes new - modification on the aircraft that increases the system's number of DOFs and control inputs. Badr et al (2016) propose an actuation concept for a quadrotor UAV in which the propellers are allowed to tilt about the axes perpendicular to the arms. Ryll et al (2012) and Hintz et al (2014) developed a quadrotor UAV with eight control inputs that allow its independent position and attitude control by tilting the propellers around the axes connecting them to the main body frame.

Further, regarding the potential applications of multi-copters on civilian and/or military missions, evaluating the impact of the tilt mechanism addition on the dynamical behavior of the UAV system have a major influence on its design and operation. Hence, the main contribution of this work is to evaluate the influence of the longitudinal and lateral tilt mechanism addition on the system dynamics by mapping the poles and zeros positions.

The focus of this paper is therefore: develop a generic dynamic model for a tilt rotor multi-rotor considering the aircraft with n rotors and two possible tilt directions, project a MIMO controller for trajectory tracking using modern control theories, map the pole and zero positions for different conditions varying the tilt mechanism and number of rotors.

DYNAMICAL MODELING

The concept of this section is to derive the dynamical model of a generic multi-copter with n rotors such that each rotor is capable of tilting in two different directions (laterally and longitudinally with respect to the rotor's arm) introducing more control inputs to the system. Some considerations must be taken before the model development such as: the aircraft structure and propellers are supposed to be rigid, all the rotors and propeller blades are the same.

KINEMATIC RELATIONS

Three different reference frames will be used in order to model the aircraft dynamics coupled with the rotor tilting as illustrated on Figure 1. The first, an Earth fixed reference frame Inertial Coordinate System denoted by $ICS : \{O_E; x_E, y_E, z_E\}$ used to represent the absolute position of the aircraft. Secondly, a body fixed coordinate frame represented by $BCS : \{O_B; x_B, y_B, z_b\}$ attached to the aircraft. The origin of the body fixed reference frame coincides with the aircraft center of gravity (CG), and its translational velocity and angular velocity vectors are denoted by $\vec{v} = \begin{bmatrix} u & v & w \end{bmatrix}^T$ and $\vec{\omega} = \begin{bmatrix} P & Q & R \end{bmatrix}^T$, respectively, such that P, Q and R are the angular velocities around the x_B, y_B and z_B axis.
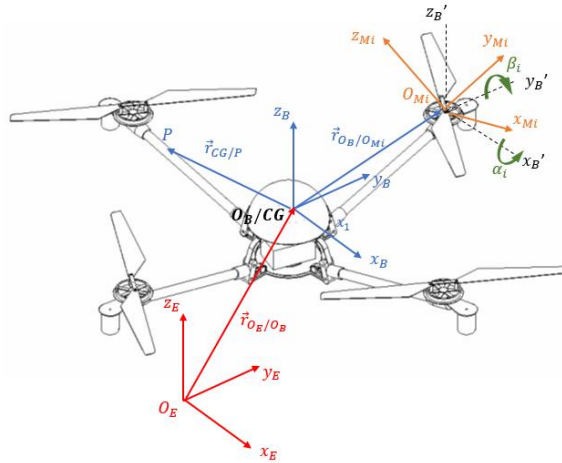
Figure 1: Multi-copter *ICS, BCS* and *MCS* axes configuration.

99

The aircraft altitude can be defined with respect to the *BCS* using the Euler angles, which are represented by $\Theta = [\phi\ \theta\ \psi]^T$ corresponding to the roll, pitch and yaw angles, respectively. The Euler angles angular velocities are expressed as the time rate change of the Euler angles $\dot\Theta = [\dot\phi\ \dot\theta\ \dot\psi]^T$. It must be remarked that $\omega \neq \dot\Theta$ since the ω vector points in the rotation axis, while $\dot\Theta$ only represents the time derivative of the attitude angles. However, these two vectors are correlated by a kinematic relation:

$$\vec\omega = \begin{bmatrix} 1 & 0 & -\sin\theta \\ 0 & \cos\phi & \cos\phi\cos\theta \\ 0 & -\sin\phi & \cos\theta\cos\phi \end{bmatrix} \dot\Theta \tag{1}$$

Any vector, defined at the body-fixed frame (BCS), can be expressed at the *ICS* by using the following rotation matrix R_B^I (Valavanis, 2007),

$$\vec r^{ICS} = R_B^I \cdot \vec r^{BCS} \tag{2}$$

with, $R_B^I = R_z(\psi)R_y(\theta)R_x(\phi)$ and $R_z(\psi)$, $R_y(\theta)$ and $R_x(\phi)$ are rotations around z_E, y_E and x_E axis, respectively.

The motor reference axis $MCS : \{O_{Mi}; x_{m_i}, y_{m_i}, z_{m_i}\}$, $i = 1...n$ is the frame associated to each of the ith propulsive group, with x_{m_i} representing the laterally tilting actuation axis, y_{m_i} the longitudinally tilting actuation axis and z_{m_i} the propeller actuated spinning axis that is coincident with the thrust force direction (Ryll et al, 2012). The lateral and longitudinal tilt angles are denoted by α_i and β_i, respectively. Further, the ith propulsion system position w.r.t the *BCS* is denoted by $\vec r_{CG/P} = [l\cos\gamma_i\ \ l\sin\gamma_i\ \ z_{CG}]^T$, where l represents the multi-rotor arm length, γ_i the angle between the rotor's arm and the x_B direction and z_{CG} the distance of the rotor center of gravity to the x_B / y_B plane. Also, any vector in the *MCS* reference frame can be written on the *BCS* by a rotational matrix, following the rotation sequence around z_M, y_M and x_M, which can be represented by:

$$R_M^B(\gamma_i) = \begin{bmatrix} \cos\gamma_i & -\sin\gamma_i & 0 \\ \sin\gamma_i & \cos\gamma_i & 0 \\ 0 & 0 & 1 \end{bmatrix} \begin{bmatrix} \cos\alpha_i & 0 & \sin\alpha_i \\ 0 & 1 & 0 \\ -\sin\alpha_i & 0 & \cos\alpha_i \end{bmatrix} \begin{bmatrix} 1 & 0 & 0 \\ 0 & \cos\beta_i & -\sin\beta_i \\ 0 & \sin\beta_i & \cos\beta_i \end{bmatrix} \tag{3}$$

Consequently, a vector on the *MCS* can be written on the *BCS* using the rotational matrix R_M^B.

EQUATIONS OF MOTION

The multi-rotor equations of motion are derived using the Newton-Euler formulation for a generic six degrees of freedom rigid body system. Thus, the equations for linear and angular body motion, written on the BCS, are:

$$
\begin{bmatrix} \sum F_x \\ \sum F_y \\ \sum F_z \end{bmatrix} = m \begin{bmatrix} \dot{u} - Rv + Qw \\ \dot{v} - Pw + Ru \\ \dot{w} - Qu + Pv \end{bmatrix} \tag{4}
$$

$$
\begin{bmatrix} \sum M_x \\ \sum M_y \\ \sum M_z \end{bmatrix} = \begin{bmatrix} I_{xx}\dot{P} + QR(I_{zz} - I_{yy}) - I_{yz}(\dot{R} + PQ) \\ I_{yy}\dot{Q} + PR(I_{xx} - I_{zz}) + I_{xz}(P^2 + Q^2) \\ I_{zz}\dot{R} + PQ(I_{yy} - I_{xx}) + I_{xy}(QR + \dot{P}) \end{bmatrix} \tag{5}
$$

where $F = \begin{bmatrix} F_x & F_y & F_z \end{bmatrix}$ and $M = \begin{bmatrix} M_x & M_y & M_z \end{bmatrix}$ are the external force and moment applied at the center of mass of the vehicle. $I_{xx}, I_{yy}, I_{zz}, I_{xy}, I_{yz}$ and I_{xz} are the components of the rotational inertia matrix of the vehicle with respect to the body coordinate frame.

Concerning the external forces, it is mainly composed of thrust, drag and gravitational components. Assuming the most commonly type of propulsion system used for UAVs (DC motors), the thrust force generated by the propeller can be considered as proportional to the propeller angular speed (Huang et al, 2009):

$$
T = \left(\frac{K_\tau K_v \sqrt{2\rho\pi r_{prop}^2}}{K_t} \Omega \right)^2 = k\Omega^2 \tag{6}
$$

with K_t a proportional constant relating the torque produced by the electric motor and its electrical current, K_v relates the motor voltage and

its angular velocity, K_τ is relative to the motor torque and thrust, r_{prop} is the blade disc radius, ρ the density of the surrounding air and Ω the rotational velocity of the motor shaft.

Once the thrust T acts in the z direction of the MCS, the force generated by each rotor can be written on the BCS using the matrix transformation presented in Eq. (3).

As presented in Marques (2016), a drag force due to the viscosity of the vehicle surrounding air is considered in the model which can be simplified by expressing this force as proportional to the linear velocity of the aircraft and always acting in the opposite direction of the body movement. Hence, the drag force on the BCS is written as:

$$\vec{F}_D^{BCS} = -k_d \vec{v}_B = \begin{bmatrix} -k_{dx}u \\ -k_{dy}v \\ -k_{dz}w \end{bmatrix} \tag{7}$$

where k_d is a friction constant which can be split in three directions of the BCS (x_B, y_B and z_B).

Also, a constant gravitational force pointing always to the z-direction of the *ICS* acts on the aircraft center of gravity. The components of this force at the *BCS* are obtained from the rotation matrix (Eq. (2)), as follows:

$$\vec{F}_{grav}^{BCS} = \left(R_B^I \right)^T . F_{grav}^{ICS} = \begin{bmatrix} mg \sin\theta \\ -mg \sin\phi \cos\theta \\ -mg \cos\phi \cos\theta \end{bmatrix} \tag{8}$$

The moments acting in the *BCS* are mainly generated by propeller system actuation and how they are distributed on the UAV center of mass. Hence, the torque produced by the spinning propeller is obtained by the following relation:

$$\vec{\tau}_T = \vec{r}_{CG/P} \times F_T^{BCS} \tag{9}$$

being $\vec{F}_T^{BCS}$ the thrust force vector written on the *BCS* and

$\vec{r}_{CG/P} = \begin{bmatrix} l\cos\gamma_i & l\sin\gamma_i & z_{CG_i} \end{bmatrix}^T$ the motor position vector with respect to the multi-rotor center of gravity.

Afterward, since the mass of the aircraft is generally small, the gyroscopic effect of the blades must be accounted in the dynamic model. This torque is an outcome of the propellers angular momentum direction change along the flight (Roskam, 2001), and is calculated with respect to the multi-rotor center of gravity considering the two tilting directions (α_i and β_i). First, the motor angular velocity with respect to the aircraft *CG* is written as:

$$\vec{\omega}_{prop} = \begin{bmatrix} \cos(\alpha_i)\dot{\beta_i}+P & \dot{\alpha_i}+Q & -\sin(\alpha_i)\dot{\beta}+R \end{bmatrix}^T \qquad (10)$$

where $\dot{\alpha}_i$ and $\dot{\beta}_i$ are each rotor angular velocity rate of change.

Assuming that the propeller blades have the same moment of inertia (I_M) and are spinning around the z_M direction of the *MCS*, the gyroscopic effect is obtained by the cross product between the motor angular velocity (Eq. (10)) and the angular momentum generated by the n propellers ($\vec{H} = \begin{bmatrix} 0 & 0 & \sum\limits_{i=1}^{n} J_{Mi}\vec{\Omega}_i \end{bmatrix}$):

$$\vec{\tau}_G = \left(\dot{\vec{H}}\right)_{ICS} = \left(\frac{d\vec{H}}{dt}\right)_{BCS} + \omega_B \times \vec{H} \qquad (11)$$

Considering that the propeller angular speed variation is negligible and the propeller moment of inertia is constant, then $\left(d\vec{H}/dt\right)_{BCS} = 0$. Further, the fan torque is also an external torque component due to the air aerodynamic drag on the propeller blades cross section that acts on the rotor spinning axis (z_M) and can be modeled as (Asselin, 1965):

$$\vec{\tau}_{F_{MCS}} = \begin{bmatrix} 0 & 0 & \sum\limits_{i=1}^{n} -b\Omega_i^2 \end{bmatrix}^T \qquad (12)$$

where b is a proportional constant relating the resulting drag torque with the propeller angular speed. Equation (12) can be written on the *BCS* using the relation on Eq. (3).

The mathematical model of a generic tilt multi-rotor with n rotors is obtained substituting the calculated forces and moments in Eqs. (4) and

(5) also considering the kinematic relations presented on Eq. (1) forming a nine degree of freedom dynamical system. The number of inputs depends on the number of motors and tilting actuators.

In order to apply modern control techniques, such as the Linear Quadratic Regulator (LQR), the derived equations of motion must be linearized in order to form a LTI (Linear Time Invariant) system (Marques, 2016). Once the equations were linearized, the first order differential equations can be written in the state space format:

$$\dot{\vec{x}} = A\vec{x} + B\vec{u}$$
$$\vec{y} = C\vec{x} + D\vec{u}$$

(13)

with $\vec{x} = \{u \quad v \quad w \quad P \quad Q \quad R \quad \varphi \quad \theta \quad \psi\}$ being the state vector, $\vec{y}$ the output measured signals, A the dynamic matrix and B the input matrix. Since the measured signals are considered to be exactly the state vector, then C is an identity matrix and D is a zero matrix.

In most applications concerning trajectory tracking problems, the position of the aircraft with respect to the ICS is the desired control variable (Valavanis, 2007). In order to include the vehicle position, the state vector is expanded and three new kinematic relations are added to the problem. They concern the linear velocities ($\vec{V}_x, \vec{V}_y$ and $\vec{V}_z$) written as a function of the temporal derivatives of (x_E, y_E and z_E) (Etkin, 1985).

MODERN CONTROL

In terms of autonomous systems development, modern control theory has revealed to be a valuable control technique for multi-copter autonomous flight applications as presented in (Suiçmez, 2014). Moreover, for multi-variable or problems, these techniques can be more efficient since the control loop gains are calculated simultaneously while the stability condition are guaranteed.

Therefore, on this work, the Linear Quadratic Regulator (LQR) with state feedback is applied to guarantee stability and good signal tracking capability. The LQR strategy control consists in making zero order closed loop system that forces all the states to the equilibrium position. Mainly concerned with trajectory tracking characteristics, the tracking error ($\vec{e}(t)$) is defined as:

$$\vec{e}(t) = \vec{r}(t) - \vec{x}(t) \tag{14}$$

with $\vec{r}(t)$ the tracking command vector containing the reference values for the states desired to be tracked which can be represented as a p order differential equation:

$$\overset{(p)}{r} = \sum_{i=1}^{p} a_i \overset{p-i}{r} \tag{15}$$

Furthermore, the LQR problem can be extended to the LQT (*Linear Quadratic Tracking*) problem increasing the system order following the internal model principle, where the error (Eq.(14)) is driven to zero. The problem can be treated as a servomechanism design which contains the reference model (Eq.(15)) written in the state space form as (Lawretsky and Wise, 2013):

$$\dot{\vec{z}} = \tilde{A}\vec{z} + \tilde{B}\vec{\mu} \tag{16}$$

where the vector μ represents the plant input vector and z is the expanded state vector containing the plant and p error derivatives ($\dot{z} = \begin{bmatrix} e & \dot{e} & \cdots & \overset{(p-1)}{e} & x \end{bmatrix}^T$). Further, assuming that the control law is represented by:

$$u(t) = -K_c z \tag{17}$$

The feedback gain matrix $K_c = \begin{bmatrix} K_p & K_{p-1} & \cdots & K_1 & K_x \end{bmatrix}$ is obtained solving a cost-function minimization problem in a manner that the closed loop matrix system ($\tilde{A} - \tilde{B}K_c$) is stable (Burns, 2001):

$$J = \int_0^\infty \left((z)^T Q_k(z) + \mu^T R_k \mu \right) dt \tag{18}$$

where $Q_k = Q_k^T \geq 0$, $R_k = R_k^T \geq 0$ and $\left(\tilde{A}, Q_k^{1/2} \right)$ are detectable.

Therefore, for a given state space LTI system, there is a gain matrix K_c which can minimize the cost function and bring all states (including the error) to zero simultaneously. The cost function minimization problem (Eq. (18)) can be solved using the Riccati equations (Burns, 2001).

SIMULATIONS AND RESULTS

The derived dynamical model and control theory application will be evaluated concerning the stability properties for different input signals. Thus, the state-space linear model uses the physical properties obtained experimentally as presented on Table 1 from Marques (2018). Later, the model is used to calculate the gain matrices ($K_c = \begin{bmatrix} K_p & K_{p-1} & \cdots & K_1 & K_x \end{bmatrix}$) for each tilt mechanism (lateral, longitudinal and none) solving Eq. (18). Finally, it must be regarded that the weighting matrices Q_k and R_k are maintained the same, and the reference signal is set as a step input ($\dot{r} = 0$, $p = 1$, $a_1 = 0$ in Eq. (15)) in all position directions (x_E, y_E and z_E).

POLE AND ZEROS LOCATION ANALYSIS

One method to evaluate the stability of MIMO system is to examine the poles and zeros of the closed-loop transfer function. The closed-loop system ($A_{cl} = \tilde{A} - \tilde{B}K_c$) can be determined obtaining the eigenvalues (λ) of the closed loop matrix (A_{cl}) through the following eigenvalue problem:

$$A_{cl}v = \lambda v \qquad (19)$$

Table 1: Quadcopter properties.

Property	Description	Value
m	Mass	2.326 kg
L	Hexarotor arm length	0.32 m
k_d	Drag Coefficient	$4.8 \ 10^{-2}$ Ns/m
I_{xx}	Moment of inertia with respect to x axis	0.168 kgm^2
I_{yy}	Moment of inertia with respect to y axis	0.168 kgm^2
I_{zz}	Moment of inertia with respect to z axis	0.309 kgm^2
K_v	Electric motor voltage coefficient	$4.19 \ 10^{-3}$ Vs/rad
K_t	Torque/current electric motor coefficient	$4.19 \ 10^{-3}$ Nm/A
C_Q	Thrust electric motor coefficient	$1.037 \ 10^{-3}$
C_T	Torque electric motor coefficient	0.01458
G	Gravity	9.81 m/s^2
ρ	Air density	1.225 kg/m^3
r_{propc}	Propeller radius	0.14 m
C_D	Propeller rotational drag coefficient	$6.4 \ 10^{-4}$ Ns/m

First, checking the open-loop poles of the linearized system, i.e. the eigenvalues of A matrix, it has 3 poles at $\lambda = -0.006$ while the other are at $\lambda = 0$ even if the yaw dynamics are included. Hence, the system has a decaying oscillatory response for some modes ($\lambda = -0.006$), which may be related to the linear velocity due to drag effect, and a steady response for others ($\lambda = 0$).

Moreover, Fig. 2 show the pole mapping for the closed loop system considering 5 different actuation mechanisms: no tilt mechanism, 2 and 4 longitudinal tilting mechanisms (α) and 2 and 4 lateral tilting mechanisms (β). It is important to note that the tilt mechanism is added to the system and works together with the spinning rotors. The poles closer to the origin are presented on Fig. 2.

It can be concluded, from Fig, 2 that all the closed-loop poles (eigenvalues) are on the left half plane of the Real/Imaginary axis assuming real negative values. Thus, the solution is a decaying exponential (oscillatory or not) so the system converges to a finite value, i.e. the system is considered as asymptotically stable.

Now, analyzing the poles positions it can be noted that some of them have shifted their position considering different actuation configurations, which is represented by the arrows on the figures. Adding the tilting mechanism to the system brought the poles visible on Fig. 2 (left) further from the imaginary axis compared to the open-loop poles, meaning that the pole natural frequency and/or the damping ratio has increased. Thus, the system is able to respond faster and/or more smoothly.

Further, regarding Fig. 2 (right), the poles tends to shift radially, meaning that the damping ratio is maintained while the natural frequency is increased, on this case the system will respond faster. This phenomenon is more effective when the lateral tilting mechanism is added the system and also when the number of tilting mechanisms is increased.

The zeros, or the numerator's roots of each transfer function of the closed-loop system, can also play a major role on it's response. According to Hoagg and Bernstein (2007), having an open-right-plane zero, an input signal can be unbounded, a phenomenon known as non-minimum-phase zero, directly affecting the steady state system's response.

The zero mapping is presented on Fig. 3 for all system transfer functions five different scenarios as stated previously. One observes from the figures that the zero distribution does not follow a specific pattern. However, on Fig. 3 (right), it can be seen that there are some zeros on the right half plane of the Real/Imaginary plane. This represent a non-minimum-phase zero, but their influence over the system shall be small since they are close to the Imaginary axis. This effect must be checked carefully via time response analysis.

Figure 2: Closed-loop poles for a first order integrator controller (step input signal) for five actuator configurations: no tilt, 4 lateral tilt, 2 lateral tilt, 4 longitudinal tilt and 2 longitudinal tilt.
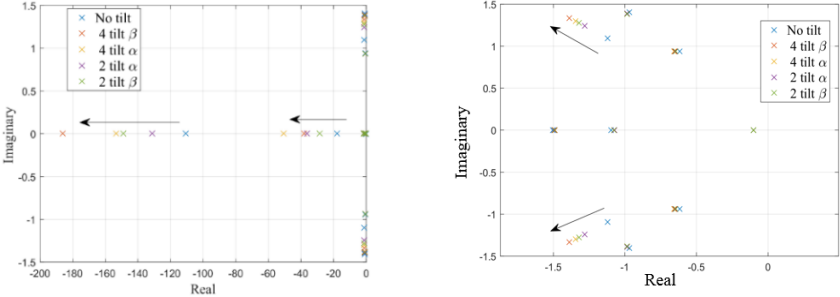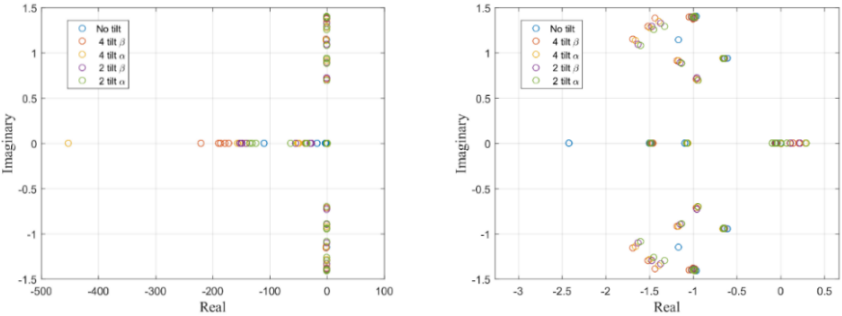

Figure 3: Closed-loop zeros for a first order integrator controller (step input signal) for five actuator configurations: no tilt, 4 lateral tilt, 2 lateral tilt, 4 longitudinal tilt and 2 longitudinal tilt.

CONCLUSIONS

In summary, the objective of this present work was to derive the dynamical model of a generic multi-rotor UAV equipped with a tilting rotor mechanism either on the longitudinal or lateral directions and analyze the dynamical impact of the mechanism addition using pole zero mapping. The addition of the tilting mechanism to the system increases the number of signal inputs, hence the under actuation problem can be solved, however, as observed on Figs. 2 and 3 has shifted the poles and zero positions.

From the pole zero analysis, the tilting mechanism addition affected the poles and zero positions of the closed-loop system considering the same weighting matrices. In general, when equipped with the tilt mechanism, the poles shift to a further position from the origin on the Real/Imaginary axis as shown on Fig 2. Thus, it is expected from the system to respond faster. Moreover, similarly to the type of tilting mechanism, the number of tilting mechanism on the multi-copter has also affected the poles position, mainly because the non-linear effects contribution can't be counter-balanced by the actuators.

Furthermore, it was also detected that the closed-loop system has zeros on the right half of the Real/Imaginary plane known as *non-minimum phase zeros*. These zeros can have a major influence on the steady state response since that, even the system reaching the dynamical equilibrium (zero forces and moments) the plant input signal tends to amplify as one of the states grow. This phenomenon should be clearly observed when analyzing the time response for a ramp input signal.

REFERENCES

Asselin, M. An Introduction to Aircraft Performance. Reston, Virginia: AIAA, 1965

Badr, S., Mehrez, O. and Kabeel, A. E., "A Novel Modification for a Quadrotor Design", International Conference on Unmanned Aircraft Systems (ICUAS), IEEE, 2016.

Blaauw, D., Flight Control System for a Variable *Stability Blended-wing-body Unmanned Aerial Vehicle*, Master Thesis, 187 pp, University of Stellenbosch, Matieland, South Africa, 2009.

Burns, R. S. *Advanced Control Engineering*. Oxford: Plant a Tree, 2001.

Etkin, B., *Dynamics of Flight. Stability and Control,* 3rd edition. Wiley, New York, 1985.

Hintz, C., Torno, C. and Carrillo, L. R. G, "Design and Dynamic Modeling of a Rotary Wing Aircraft with Morphing Capabilities", International Conference on Unmanned Aircraft Systems (ICUAS), IEEE, Orlando, Florida, USA, 2014.

Hoagg, J. B. and Beernstein, D. S. "Nonminimum-phase zeros – much to do about nothing – Revisited: Part II", IEEE Control System Magazine, vol 27, pp 47-57, 2007.

Huang, H., Hoffmann, G.M. and Waslander, S. L., Tomlin, C. J. "Aerodynamics and Control of Autonomous Quadrotor Helicopters in Aggressive Maneuvering", International Conference on Robotics and Automation, IEEE, 2009.

Lavretsky, E. e Wise, K. A. *Robust and Adaptive Control*, London: Springer, 2013

Marques F. M. M., *Modeling, Simulation and Control of a Generic Tilting Rotor Multi-Copter*, MsC Thesis, Federal University of Uberlândia, Uberlândia – MG, Brazil, 2018.

Marques F. M. M., *Modeling, Simulation and Control of a Multi-rotor Aircraft*, Monography, Federal University of Uberlândia, Uberlândia – MG, Brazil, 2016.

Marques, F. M. M., *Modeling, Simulation and Control of a Generic Tilrotor Multi-copter*. Master Thesis, 99 pp, Federal University of Uberlândia, Uberlândia – MG, Brazil, 2018.

Oosedo, A., Abiko, S., Narasaki, S., Kuno, A., Konno, A. and Uchiyama, M., "Large attitude change flight of a quad tilt rotor unmanned aerial vehicle", Advanced Robotics, 30:5, 325-337, 2016.

Roskam, J. *Airplane Flight Dynamics and Automatic Flight Controls*. Lawrence, KS: DAR Corporation, 2001.

Ryll, M., Bulthoff, H. H. and Giordanno, P. R., "Modeling and control of a quadrotor UAV with Tilting Propellers", International Conference on Robotics and Automation (IEEE), Saint Paul, Minesota, USA, 2012.

Suiçmez E. C., *Trajectory Tracking of a Quadrotor Unmanned Aerial Vehicle (UAV) Via Attitude and Position Control*. Tubitak: Middle East Technical University, 2014.

Valavanis, K. P. *Advances in Unmanned Aerial Vehicles*. Dordrecht, Netherlands: Springer, 2007.

Using an operating condition compensation approach for EMI-based damage detection in a rotating machin*

Karina Mayumi Tsuruta
karinamt@ufu.br

Advisor: Valder Steffen Jr. and Aldemir Ap. Cavalini Jr.

Abstract: The electromechanical impedance is a condition-based maintenance (CBM) methodology that uses sensors network to evaluate health condition of mechanical systems. Piezoelectric transducers are used as sensors and actuators to damage detection. Such approach monitors changes in the electric impedance of piezoelectric transducers that are bonded to the host structure. Normally the evaluation of the impedance responses is performed by using damage metrics, which permit to quantify the influence of damage. This is possible because the electrical impedance of the sensor is directly related to the mechanical impedance of the structure. However, the frequency response functions (FRFs) resulting from this method are susceptible to environmental and operational conditions that must be accounted for in order to avoid false diagnostics. Thus, the aim of this paper relies on the correct detection of incipient damages in rotating shafts under operating condition by using a real-time Impedance-based Structural Health Monitoring (ISHM) method. For this purpose, a data normalization procedure for compensation of changes in environmental and operating conditions is used to minimize changes in impedance signatures resulting from these external influences. Changes on dynamic load result from altering the rotation speed while temperature changes stem from daily room temperature variations. The compensation technique is based on a hybrid optimization method associated with a given damage metrics. Additionally, a statistical model is used for threshold determination based on the Statistical Process Control (SPC) method. Experimental results show that an incipient damage associated with temperature and dynamic loads effects could be successfully detected with a probability of detection above 95 % confidence for most of the sensors used

---

INTRODUCTION

The ability to detect fatigue cracks in an early stage can be very helpful since this is an important issue in terms of structural health monitoring (SHM) methods. The importance attributed to this problem is addressed to the serious consequences when cracks are not early identified in rotating systems. Among the SHM (Structural Health Monitoring) techniques devoted to crack detection in rotor dynamics, the ones based on vibration measurements are recognized as useful tools since they lead to satisfactory results even when the damage location is not accessible. However, although widely used in the industry, when applied to non-ideal conditions, such techniques can detect cracks that eventually have already spread significantly along the cross section of the shaft, usually above 40% of its diameter (Bently and Hatch, 2002).

Therefore, currently, the attention of the researchers is turning to more sophisticated methods that can identify incipient cracks (cracks that spread up to 25% of shaft diameter), which represent a type of damage that are hardly observable in ordinary vibration analysis (Cavalini et al., 2014).

One of the SHM techniques that has been used to detect damage in rotating machines under operating conditions is the method based on the electromechanical impedance (Cavalini et al., 2014), which has been successfully applied before in aeronautical (Park et al., 2003; Raju, 1997; Sohn *et al*., 2003) and civil structures (Park *et al.,* 2000; Hu *et al.,* 2014; Silva *et al*., 2016). This technique measures the electrical impedance of a piezoelectric material (PZT patch) bonded on the surface of the host structure (or embedded into it). The electrical impedance of the PZT patch is directly related to the mechanical impedance of the structure. Thus, any change in the mechanical properties of the host structure (e.g. due to a growing crack) will be reflected in the measured electrical impedance signature. A damage metric is normally used to quantify the severity of the failure by means of statistical equations that represent the changes between a baseline (pristine) condition and another test measurement (Park et al., 2005)

The impedance based SHM (ISHM) technique has advantages over other SHM techniques (Lim et al., 2011). The mathematical model of the structure is not required, which allows the application of the proposed technique in complex systems. Additionally, the results generated by the technique are easy to interpret and they are prone to be adapted to continuous monitoring. In order to ensure high sensitivity to incipient damage, the electrical impedance is measured at high frequencies (typically higher than 30 kHz). The PZT patches have a wide linearity range, being lightweight and durable.

In this context, the objective of this work is to develop a damage detection approach for the shafts of rotating machines under operating condition by using the ISHM method. A compensation technique is applied to minimize the external influences due to variations in the room temperature, rotation speed, and unbalance condition. Although the ISHM can provide high sensitivity to incipient damage, the measured impedance signals can drift significantly due to effects of temperature change and dynamic loads (Rabelo et al., 2016; Park et al., 1999; Grisso and Inman, 2009). These influences, if not compensated for, will affect the final damage indices, providing a false indication of the structure's current condition.

For these experiments, three rotation speeds were considered (600 RPM, 900 RPM, and 1200 RPM). The room temperature ranged from 17 °C to 26 °C. Temperature was measured through a thermocouple (AD590 – Analog Devices). The compensation technique is based on a hybrid optimization method associated with a given damage metric. Additionally, a statistical model proposed by Rabelo et al. (2016) was used for threshold determination based on the Statistical Process Control (SPC) method. Experimental results show that an incipient damage could be successfully detected even for the cases in which temperature and dynamic loads effects are considered. A probability of detection above 95 % confidence was reached for most of the sensors used.

IMPEDANCE ELECTROMECHANICAL METHOD

The SHM method based on electromechanical impedance was first proposed in Liang et al. (1994). The method uses piezoelectric transducers coupled to the structure to monitor changes in the stiffness,

damping, and mass properties. Due to the difficulty of obtaining the mechanical impedance of the structure, electrical impedances are measured by using piezoelectric transducers coupled to the system. Assuming that the PZT (Lead Zirconate Titanate) properties do not vary over time, changes in the electrical impedance will be directly related to changes in mechanical impedance, which is affected by the presence of damage (Soh et al., 2003; Park et al.,2000; Liang et al., 1994). The electromechanical model that describes and quantifies the measurement process is showed in Fig. 1.
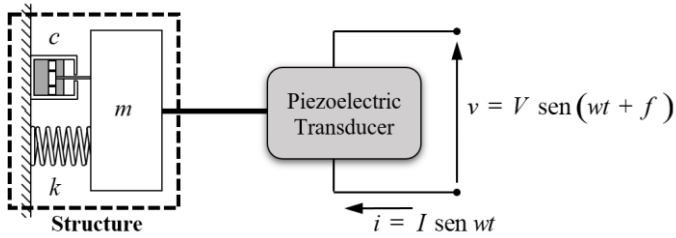
Figure 1:- Electromechanical Model of the impedance-based structural health monitoring method (Liang et al., 1994).

Based on the system showed in the Fig. 1, the admittance $Y_a(\omega)$ of the piezoelectric transducer is a combined function involving the mechanical impedance of the PZT actuator $Z_{ma}(\omega)$ and the structure $Z_{me}(\omega)$, according to Eq. (1). As showed in Eq. (1), the impedance function is a frequency complex function that presents real and imaginary parts.

$$Y_a(\omega) = I(\omega)\,\omega a \left\{ \varepsilon_{33}^T \left[1 - I(\omega)\delta\right] - \frac{Z_{ma}(\omega)}{Z_{ma}(\omega) - Z_{me}(\omega)} d_{3x}^2 \hat{Y}_{xx}^E \right\} \quad (1)$$

where $\hat{Y}^E_{xx}$ is the complex Young's modulus of the PZT patch with zero electric field, d_{3x} is the piezoelectric coupling constant in the arbitrary x direction at zero electric field, ε^T_{33} is the dielectric constant at zero stress, δ is the dielectric loss tangent to the PZT patch, a is a geometric constant of the PZT patch, and is ω the frequency.

The electrical impedance is obtained from both the direct and inverse effects of the piezoelectric transduces. The direct effect (or sensor

effect) is characterized by producing a voltage as the piezoelectric transducer is mechanically deformed in the elastic phase, and the inverse effect (or actuator effect) is verified as the PZT patch is subjected to a voltage and deforms mechanically (Liang et al., 1994; Grisso et al., 2009)

Damage Metric

The evaluation of the structure integrity is performed based on the comparison between impedance functions measured before and after damage happens. The visual comparison is not sufficient to draw a decision. Consequently, it is necessary the use of quantitative criteria; thus, scalar parameters able to numerically represent the difference between the two measures are employed, the so-called damage metrics (Naidu *et al.,* 2004).

There are many damage metrics used to evaluate the integrity of mechanical structures (Boehme et al., 2010). In this context, one of the most used statistical models found in the literature is the RMSD (Root Mean Square damage) and its definition is given by Eq. (2) (Grisso, 2004; Peairs, 2006).

$$RMSD = \left\{ \sum_{i=1}^{n} \frac{\left[\mathrm{Re}\left(Z_{1i} \right) - \mathrm{Re}\left(Z_{2i} \right) \right]^2}{\mathrm{Re}\left(Z_{1i} \right)^2} \right\}^{1/2} \tag{2}$$

Where $R_e(Z_{1i})$ is the real part of the impedance signature without damage (baseline) at frequency i, $R_e(Z_{2i})$ is the real part of the impedance signature associated with the structure for an unknown condition, and n is the total number of the points used in the measurements.

Temperature Compensation with optimization procedure

Temperature variation effects are known to cause horizontal (frequency) and vertical (amplitude) shifts in the impedance signatures. A review of temperature variation effects and temperature methods can be found in Rabelo et al., (2015) and Baptista et al. (2013).

Figure 3 shows a flowchart to illustrate the proposed temperature compensation methodology. The method starts by obtaining the impedance signatures of the healthy system ($Imp_{baseline}$; temperature $T_{baseline}$). The impedance signatures of the system for an unknown condition ($Imp_{unknown}$; temperature $T_{unknown} \neq T_{baseline}$) are also required, so that the optimizer is responsible for shifting their effective frequency and amplitude. The $Imp_{unknown}$ signatures are compared with the $Imp_{baseline}$ ones by means of a given objective function, i.e., a damage metric, as presented by Eq. (2) and Eq. (3) ($Imp_{baseline} = Z_1$ and $Imp_{unknown} = Z_2$).
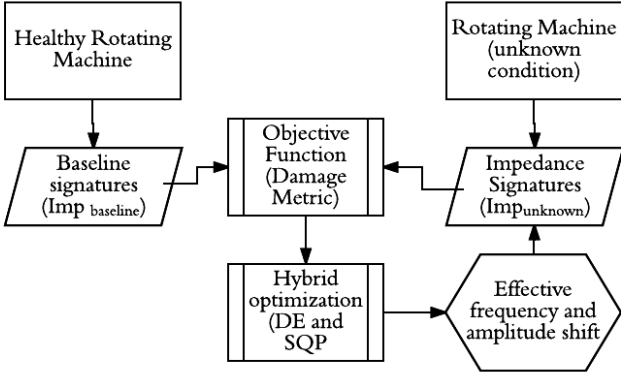
Figure 2: Proposed temperature compensation flowchart.

If the procedure converges to a minimum value of the objective function, the effects of temperature variation are compensated through the frequency shift and vertical shift design variables. If this is not the case, the optimization procedure continues the search with new frequency and amplitude shifts. The optimization process continues iteratively until convergence is assured, which corresponds to temperature compensation (if the objective function is close to zero) or a damage indication associated with temperature compensation.

In the present contribution, the proposed hybrid optimization technique is primarily devoted to minimizing the influence of temperature variation during the impedance measurement process. The hybrid optimization technique theory is well explained in Rabelo et al. (2017).

STATISTICAL THRESHOLD DETERMINATION

A reliable SHM system should be able to provide diagnosis with a pre-configured level of confidence based on the pristine conditions of the host structure. In many experimental tests, it is recommended that the measured data is cleansed to eliminate spurious or degraded signals that might have resulted from acquisitions and processes associated with excessive noise, signal dropouts, or even an external cause such as power failure (Park and Inman, 2011). In this contribution, the measured impedance signatures were cleansed by using the Chauvenet's Criterion (which is used only once). This allows performing outlier detection. As recommended in the literature (Park and Inman, 2011), subsequent applications of the mentioned criterion could implicate in loosing important data from the experimental tests.

Statistical Threshold Determination

The concepts behind Statistical Process Control allow to establish limits in a control chart so that a threshold can be established using the upper control limit. These limits can be defined so that 95.45 % or 99.73 % of data from a normally distributed population remains, if these control limits are established as expressed in Eq. (3).

$$\begin{array}{l} \bar{x} \pm 2s \ \ for \ \ 95.45\% \ \ confidence \\ \bar{x} \pm 3s \ \ for \ \ 99.73\% \ \ confidence \end{array} \tag{3}$$

where $\bar{x}$ is the sample mean and s is the sample standard deviation.

In SHM, the upper control limit is of interest for the threshold determination. Although the expressions in Eq. (3) can provide the threshold calculation, it should be noted that the sample mean and sample standard deviation are inferences from the population parameters (i.e., unknown values). Therefore, a more robust methodology is proposed by using the upper limits of the confidence intervals for the population mean and standard deviation according to Eq. (4) and Eq. (5), respectively.

$$\left[\bar{x} - \frac{st_{v;\alpha/2}}{\sqrt{N}} \leq \mu_x \leq \bar{x} + \frac{st_{v;\alpha/2}}{\sqrt{N}} \right] \qquad v = N - 1 \tag{4}$$

$$\left[\frac{vs^2}{\chi^2_{v;\alpha/2}} \leq \sigma^2_x < \frac{vs^2}{\chi^2_{v;1-\alpha/2}} \right] \qquad v = N - 1 \tag{5}$$

where μ_x and σ^2_x are the population mean and variance, respectively, $\bar{x}$ and s^2 are the sample mean and variance, respectively, $t_{v;\alpha/2}$ has a Student t distribution with v degrees of freedom, α is the significance level and $\chi^2_{v;\alpha/2}$ has a Chi-Square distribution.

Hence, the upper limit of the confidence intervals was used and the threshold for each PZT transducer was determined according to Eq. (6).

$$PZT_{threshold} = \mu_{x\max} + 3\sigma_{x\max} \tag{6}$$

where μ_{xmax} is the upper limit for the population mean and σ_{xmax} is the upper limit for the population standard deviation, both obtained by choosing 5 % of significance level α.

METHODOLOGY

Figure 3 shows the test rig used to evaluate the ISHM method to detect damage in rotor shaft in different operational conditions. This rotor is composed of a flexible steel shaft with 800 mm length and 17 mm diameter, two rigid discs, both with 150 mm diameter and 20 mm thickness (approximately 2.6 kg), and an aluminum rotor pulley with 140 mm diameter and 20 mm thickness (approximately 0.48 kg). The shaft is supported by two roller bearings. The system is driven by a direct current (DC) electric motor of 0.5 HP (Varimot® model BN90M). The interaction between the electric motor and the shaft is minimized by means of a special coupling named Lami-Torq (Acoplast® model GTG 402 100). A schematic drawing of the rotor is shown in Fig. 4.
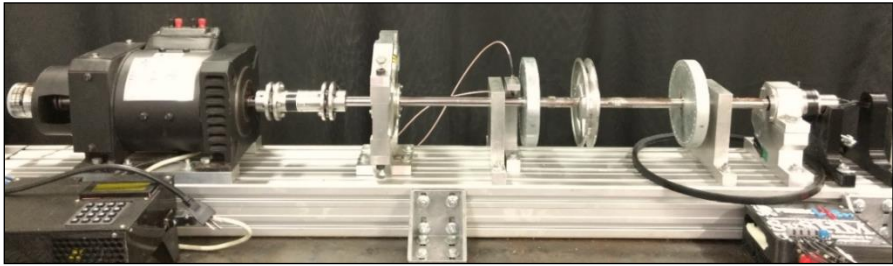
Figure 3: Test rig used in the ISHM tests with the objective of detecting damage during rotor operation.

In Fig. 4, the main dimensions between the transducers and the sensors over the rotor shaft can be seen. The PZT patches are named as PZT#1, PZT#2, and PZT#3. Note that three piezoelectric transducers were distributed along the shaft oriented at 90 ° from each other. Each transducer is composed by three PZT patches electrically connected in parallel, except for the PZT2 which has four PZT patches. The PZT patches have 10 mm length, 3 mm width, and 1 mm thickness. The location of the transducers was decided based on previous results from modal analysis. An epoxy adhesive was used to bond the PZT patches to the shaft.

A slip ring with ten circuit connections (Michigan Scientific's S-Series Slip Ring - C556019) was used to measure the impedance signal of the PZT patches for the test rig under operation condition (see Fig. 5 (a). Figure 5 (b) shows the setup used to connect the slip ring to the shaft. The slip ring can transfer electrical signals from fixed to rotating parts (and vice versa) with low noise interference, even for the rotor operating at high speeds. According to the manufacturers, the device can transfer electrical signals from accelerometers with the rotor operating in a range of 0 -12,000 RPM. Figure 7 (c) shows the impedance measurement system. This device is connected to a computer to obtain the impedance signatures (Finzi et al., 2011). The frequency range was determined experimentally based on the density of peaks: 230 - 270 kHz for all the PZT patches. It is worth mentioning that the high frequency range, as previously mentioned, enables the ISHM method to detect incipient damage in a localized region (Park et al., 1999).
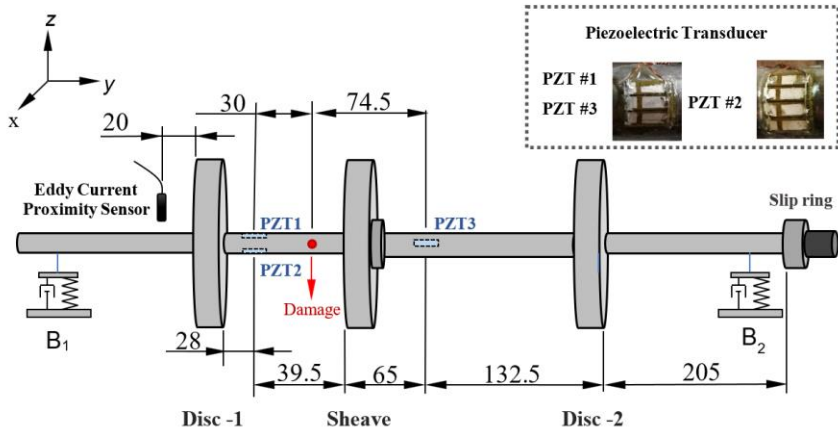
Figure 4: Rotor main dimensions: transducers and sensors position on the rotor.
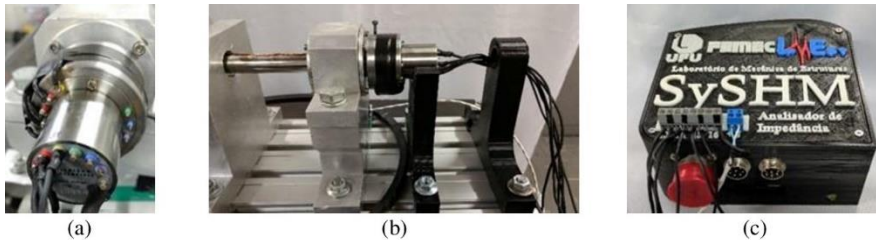
Figure 5: (a) Slip ring; (b) Set-up of the slip ring connection to the shaft; (c) Impedance measurement system.

The tests with the proposed methodology included the analysis of an incipient damage with the rotor under operating condition. For the first test, a steel nut was bonded on the shaft surface (mass of 4.89 g) close to the rotor pulley (30 mm from the PZT1 and PZT2). This structural condition is called w/ Nut along the present work. Figure 8a shows the position of the damage. Next, the rotor was evaluated under different operating conditions. Three rotation speeds were considered (600 RPM, 900 RPM, and 1,200 RPM) for three unbalance levels (unbalance masses added to the Disc-1). It is worth mentioning that UB1 was determined from the residual rotor unbalance distribution. Figure 8 (b) shows the eddy current proximity sensors used to measure the lateral shaft displacement. Figures 4 and 6 (c) shows the position of the sensors.
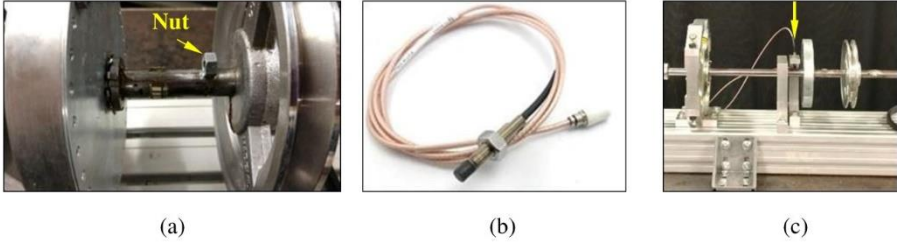
Figure 6: (a) Steel nut; (b) Eddy current proximity sensor; (c) Sensor location in the rotor test rig.

EXPERIMENTAL RESULTS

Table 1 shows the experimental configurations adopted to obtain the rotor impedance signatures. For each 18 runs, 30 impedance measurements were performed by using 1024 averages per frequency point. In this case, the structure conditions are associated with the damage and unbalance level. Note that the unbalance level UB_1 and no damage presence is considered as the rotor pristine condition. It should be mentioned that the impedance baseline used as reference in the hybrid compensation algorithm (Z_1 in Eq. (2)) was the pristine condition acquired with the rotor operating at 600 RPM.

Table 1: Experimental configurations adopted to obtain the rotor impedance signatures.

Run	Structure condition	Damage (steel nut)	Unbalance level	Rotation speed [RPM]	Denomination
1	Pristine (baseline)	-	UB_1	600	P600
2	Pristine	-	UB_1	900	P900
3	Pristine	-	UB_1	1200	P1200
4	Str Cnd. 1	w/ Nut	UB_1	600	D600
5	Str Cnd. 1	w/ Nut	UB_1	900	D900
6	Str Cnd. 1	w/ Nut	UB_1	1200	D1200

Figure 7 shows the shaft lateral displacements measured along the x and z directions considering the different rotor operating conditions (unbalance level and rotating speed). These vibration responses were acquired by using the eddy current proximity sensors presented in Fig. 6 (b). The results indicate that the vibration responses increase according to the rotation speed and unbalance level. The impedance signatures can

be directly influenced by these effects, requiring special data normalization in order to ensure reliable damage identification.

Regarding the hybrid minimization algorithm used to compensate for the environmental and rotor-operating conditions (unbalance level and rotating speed), the evolutionary optimizer DE was performed 5 times considering 10 individuals in the initial population (this is one of the advantages of DE). The RMSD damage metric was used as objective function. The impedance signatures were digitally filtered with a 3rd order Savitsky-Golay Finite Impulse Response (FIR) smoothing filter with a frame size of 31.
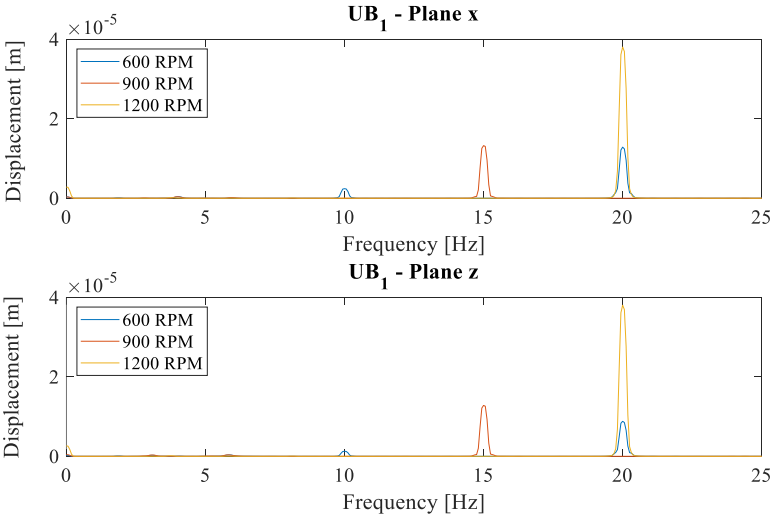
Figure 7: Displacement (Eddy current proximity sensor): (a) direction *x*; (b) direction *z*.

Figure 8(a) shows the impedance signatures measured considering the runs #1 to #3 without compensation. Figure 8 (b) presents the same measurements after compensation. These results provide a qualitative assessment of the ISHM regarding the effect of rotating speed. Note that shifts in both horizontal and vertical directions are present in Fig. 8 (a). However, after the compensation procedure it can be seen that the resonance peaks are closer to the baseline signature (at 600 RPM).
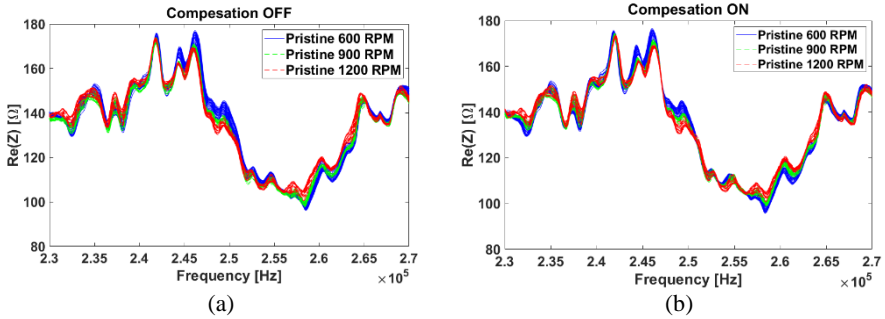
Figure 8: Impedance signatures for different rotation speeds. (a) without compensation; (b) with compensation.

Analysis #1: Added mass (4 g nut).

Figure 9 (a) shows the impedance signatures acquired by using PZT#1 (see Fig. 4). The curves represent the mean of all measurements performed at each run showing the effect of the added mass (w/ Nut). The Pristine condition corresponds to the mean of all measurements performed at runs #1 to #3 (see Tab. 1). The following three conditions are related to the mean signatures acquired in runs #4, #5, and #6 (D600, D900, and D1200, respectively). Significant changes can be observed in the impedance signals when compared to the measure performed from the pristine condition. Figure 9(b) presents the RMSD values obtained before and after applying the compensation procedure. The compensated damage indexes associated with the pristine conditions were used to establish the statistical threshold for damage identification.

In Fig. 9 (b), it can be observed that in only 10 % of the 30 measures obtained at run #4 (D600; see Tab. 1) were able to detect the damage presence. Thus, a significant portion of false negatives (90 %) was present in this case. However, for the majority of the cases in runs #5 and #6 (D900 and D1200, respectively), the added mass could be detected. Additionally, this result presents a False Positive Rate of 0 % with a hit rate of 64.44 %. In this context, a false positive is a case when damage index surpasses the threshold but the structure is at a pristine condition. The hit rate corresponds to the amount of cases when the damage indices have surpassed the threshold considering all test measures.
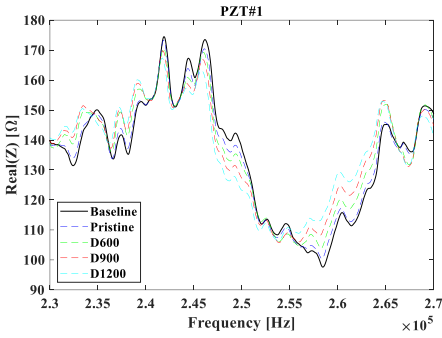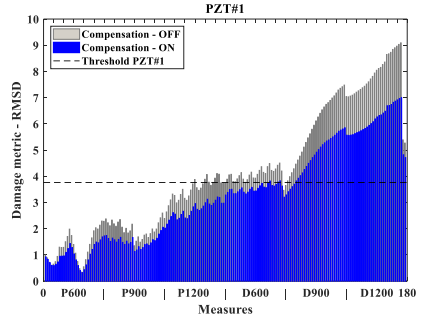
Figure 9: Impedance signatures from PZT#1 considering the effect of added mass. (a) Compensated impedance signatures; (b) RMSD damage indices and statistical threshold.

Similarly, Fig. 10 (a) and 13 (b) show the global results with RMSD damage metric by using the sensors PZT#2 and PZT#3, respectively, considering the effect of the added mass. It can be observed that the damage indices were minimized as a result of the application of the compensation technique. However, only the sensor PZT#2 was able to detect at all times the presence of the added mass.
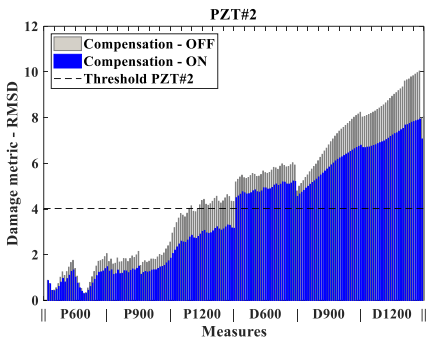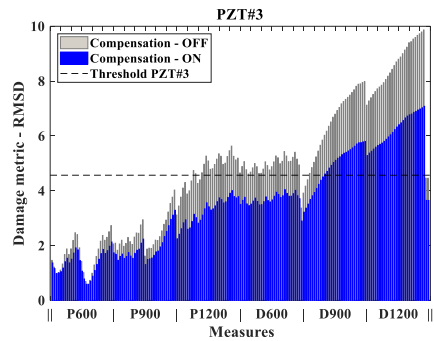
Figure 10: *RMSD* damage indices and statistical threshold. (a) PZT#2; (b) PZT#3.

CONCLUSION

The results shown in the present contribution demonstrate the efficiency of the impedance-based SHM method combined with a data normalization technique for detecting damages in rotating shafts. Data normalization was used for the compensation of environmental and

operational conditions. The test was performed on a rotor shaft that was subjected to room temperature variations throughout the days as the experiments were performed, as well as changes in the rotational speed in the range of 600 RPM to 1200 RPM. An added mass (a 4 g nut) was tested in order to introduce damage in the monitored structure. High frequency ranges provided good localization sensitivity for the damage scenarios investigated in this work.

By analyzing the overall performance of the sensors, it was observed that PZT2 provided better detectability since this sensor was made with four PZT patches connected in parallel as opposed to sensors PZT1 and PZT3 which had only three PZT patches connected in parallel. It should be noted that a substantial amount of averages (1,000) associated with the knowledge regarding the dynamic behavior of the signals stemming from the monitored structure, with the addition of a digital filter were required to obtain a reliable diagnosis.

In this contribution, the changes on the operational condition (rotational speed) and room temperature were minimized by using a hybrid optimization method. A damage metric was used as objective function for the associated minimization problem, namely the RMSD. This data normalization technique enabled to establish a statistical threshold based on SPC theory, which was used to estimate the overall performance of each sensor regarding the probability of false positive and its hit rate (or probability of detection - POD).

Finally, the authors see this contribution as a necessary step for the development of a robust impedance-based structural health monitoring system, which will provide an automated and real-time assessment of the structure's ability to serve its intended purpose.

ACKNOWLEDGMENTS

REFERENCES

Baptista, F., G., Budoya, D., E., Almeida, V., A., D, Ulson, J., A., C., 2013, "An experimental study on the effect of temperature on

piezoelectric sensors for impedance-based structural health monitoring" Sensors, v. 14(1), p. 1208-1227

Bently D. E. and Hatch C. T., 2002, "Fundamentals of rotating machinery diagnostics", Ed. Minden: Bently Pressurized Bearing Company,725p.

Boehme, B. Roellig, M., Wolter, K.-J., 2010, "Measurements of Viscoelastic Material Properties of Adhesives for SHM Sensors under Harsh Environmental Conditions". In: 11th. Int. Conf. on Thermal, Mechanical and Multiphysics Simulation and Experiments in Micro-Electronics and Micro-Systems. EuroSimE.

Cavalini Jr., A. A., Finzi Neto, R. M., Steffen Jr., V., 2014, "Impedance-based fault detection methodology for rotating machines", Structural Health Monitoring, Vol.14(3), pp. 228-240.

Farrar, C. R. and Worden, K., 2013, "Structural Health Monitoring: a machine learning perspective", Ed. John Wiley & Sons Ltd, Chichester, England, 631p.

Finzi Neto, R. M., Steffen Jr., V., Rade, D. A., Gallo, C. A, Palomino, L. V., 2011, "A low-cost electromechanical impedance-based SHM architecture for multiplexed piezoceramic actuators". Structural Health Monitoring, Vol.,10(4), p. 393-401.

Grisso, B. L. 2004, "Considerations of the impedance method, wave propagatiom. Amd wireless systems for structural health monitoring", 108f. Dissertation, Virginia Polytechnic Institute and State University, Virginia.

Grisso, B. L., Inman, D. J., 2009, "Temperature corrected sensor diagnostics for impedance-based SHM". Journal of Sound and Vibration, v. 329, p. 2323-2336.

HU, X., ZHU, H., WANG, D., , 2014, "A study of concrete slab damage detection based on the electromechanical impedance method", Sensors, v. 14, n. 10, p. 19897-19909.

Liang C., Sun F., P., Rogers, C. A., 1994, "Coupled electromechanical analysis of adaptive material systems: determination of the actuator power consumption and system energy transfer". Journal of Intelligent Material System and Structure, V. 5, p. 12–20.

Lim, H. J., Kim, M. K., Sohn, H. Park, C. Y., 2011, "Impedance based damage detection under varying temperature and loading conditions". NDT&E International, v. 44, Issue 8,p. 740–750.

Naidu, A. S. K., Soh, C. K., 2004, "Damage severity and propagation characterization with admittance signatures of piezo transducers". Journal Smart Material and Structures, v.13,p. 393-403.

Park G, Kabeya K, Cudney H., H., Inman, D. J., 1999, "Impedance-based structural health monitoring for temperature varying applications", JSME International Journal, V. 42, p. 249–258.

Park, G., Cudney, H., Inman, D. J., 2000, "Impedance-based health monitoring of civil structural components." Journal of Infrastructure System, V. 6, pp.153-160.

Park, G., Inman, D.J., 2005, "Impedance-based structural health monitoring." In: Inman DJ, Farrar CR, Lopes V Jr, et al. [Damage prognosis for aerospace, civil and mechanical system]. 1st ed. John Wiley & Sons, Chichester, p.1-12.

Park, G., Sohn, H., Farrar, C.R., Inman, D. J., 2003, "Overview of piezoelectric impedance-based health monitoring and path forward", Shock and Vibration, Vol.35, 451–463.

Peairs, D. M., 2006, High Frequency Modeling and Experimental Analysis for Implementation of Impedance-based Structural Health Monitoring. 150 f. Thesis – Virginia Polytechnic Institute and State University, Virginia.

Rabelo, D. S. ; Tsuruta, K. M. ; De Oliveira, D. D. ; Cavalini, A. A. ; Neto, R. M. Finzi ; Steffen Jr., V., 2017, "Fault Detection of a Rotating Shaft by Using the Electromechanical Impedance Method and a Temperature Compensation Approach", Journal of Nondestructive Evaluation, V. 36, p. 1-13, 2017.

Rabelo, D. S., Finzi Neto, R., M., Steffen Jr. V., 2015, "Impedance-based structural health monitoring incorporating compensation of temperature variation effects". In: Proceedings of the 23rd ABCM International Congress of Mechanical Engineering, 6-11 December 2015, Rio de Janeiro, RJ, Brazil.

Rabelo, D. S., Steffen Jr., V., Finzi Neto, R. M., Lacerda, H. B., 2016, "Impedance-based structural health monitoring and statistical method for threshold-level determination applied to 2024-T3 aluminum panels under varying temperature", Structural Health Monitoring,Vol. 1 (1), 1-17.

Raju, V., 1997, "Implementing impedance-based health monitoring", PhD Thesis, Virginia Polytechnic Institute and State University, Blacksburg.

Silva, R. N. F., Tsuruta, K. M., Finzi Neto, R. M., Steffen Jr., V., 2016, "The use of electromechanical impedance based structural health monitoring technique in concrete structures", Journal of Nondestructive Test, p.1-13.

Sohn, H., Farrar, C. R. , Hemez, F. M., Shunk, D. D., Stinemates, D. W., Nadler, B. R. A., 2003, "Review of Structural Health Monitoring Literature: 1996–2001", Los Alamos National Laboratory, USA.

Fuzzy Logic as a Tool for Uncertainty, Robustness and Reliability Analyses of Mechanical Systems[*]

Arinan De Piemonte Dourado
arinandourado@ufu.br

Advisor: Valder Steffen Jr.

Abstract: The main goal of this work is to evaluate fuzzy logic as a tool for uncertainty, robustness and reliability analyses of mechanical systems. Firstly, the so-called α-level optimization technique is evaluated in the context of uncertainty analysis of rotating systems. The proposed approach is used to predict the extreme responses of a flexible rotor supported by hydrodynamic bearings with uncertainties affecting geometry and oil properties. Afterwards, fuzzy logic is evaluated as a tool for robust optimization by means of a novel fuzzy logic balancing approach formulated to enhance the so-called IC method balancing robustness. Fuzzy logic tools, particularly fuzzy logic transformation and defuzzification procedures, are used to define a preprocessing stage in which system vibration responses sets are evaluated in order to obtain a more representative unbalance condition. Finally, a novel fuzzy logic reliability-based design methodology is proposed, revising the traditional fuzzy logic reliability index. The resulting reliability design methodology consists of a nested algorithm in which an inner optimization loop is used to obtain the uncertain variables limits and an outer optimization loop evaluates a predefined fuzzy reliability index within the previously obtained bounds. Obtained results confirm fuzzy logic as a prominent tool for uncertainty, robustness and reliability analyses.

Keywords: Fuzzy Logic, Uncertainty Analysis, Robustness and Reliability

INTRODUCTION

Mechanical systems in general are subjected to the effects of inherent uncertainties that arise mainly due to operational fluctuations, manufacturing errors, damage, wear or merely due to the lack of

---

knowledge regarding the system itself. These effects can be directly related to system performance, durability and reliability and usually are unaccounted for in design stages.

Hence, this chapter is focused on the evaluation of fuzzy logic, a simpler mathematical representation of system uncertainties, for uncertainty, robustness and reliability analyses. Uncertainty analysis can be viewed as a mathematical process that aims to obtain system extreme responses when exposed to the effect of uncertainties. Robustness can be interpreted as the system sensitivity with respect to the influence of uncertainties; consequently, robust system responses are as less sensitive as possible to system fluctuations. Reliability emphasizes on the achievement of predefined constraints related to design stability and/or safety performance.

The fuzzy logic approach is an intuitive technique based on fuzzy sets (Zadeh, 1965) and on the possibility theory (Zadeh, 1968). In the fuzzy set theory, the inherent uncertainties are described as incomplete and/or inaccurate information, represented by means of weighted intervals. Despite being relatively recent, fuzzy set theory is gaining more attention and successful applications have been reported in the literature (Möller, Graf and Beer, 2000; Möller and Beer, 2004; Ozben, Huseyinoglu and Arslan, 2014; De Abreu *et al.*, 2015).

In the present contribution, a fuzzy uncertainty analysis methodology is evaluated for extreme response prediction of a flexible rotor supported by hydrodynamic. In the sequence, a robust balancing approach based on fuzzy set theory is evaluated for rotating machines. Finally, a fuzzy reliability-based design methodology is evaluated for the reliability-based design of mechanical systems.

FUZZY UNCERTAINTY ANALYSIS

In a fuzzy logic formulation, uncertainties are represented as fuzzy sets in which an element can belong, not belong, or partially belong to the set. This formulation yields in a notion of a graded membership, as represented by the so-called membership function. As presented by Dubois and Prade (1997) there are different interpretations for a fuzzy set membership function. In the so-called degree of uncertainty interpretation, the membership function is viewed as the degree of

possibility that a determined parameter u has the value of a specific element x of the fuzzy set.

Based on the degree of uncertainty concept and through the fuzzy set theory, systems uncertainties can be modeled as fuzzy variables. The uncertain parameters are modeled as fuzzy numbers, where the actual value of the parameter is unknown, but limited to an interval weighted by a membership function. Let X be a universal classical set of objects whose generic elements are denoted by x. The subset A $(A \in X)$ is defined by the classical membership function $\mu_A: X \rightarrow \{0,1\}$, shown in Fig. 1, in which $\tilde{A}$ represents the fuzzy set and x_l and x_r are the lower and upper bounds of the fuzzy set support, respectively. Furthermore, a fuzzy set $\tilde{A}$ is defined by means of the membership function $\mu_A: X \rightarrow [0,1]$, being $[0,1]$ a continuous interval. The closer the value of $\mu_A(x)$ is to 1, more x belongs to $\tilde{A}$.

A fuzzy set is completely defined by (where $0 \leq \mu_A \leq 1$):

$$\tilde{A} = \left\{ \left(x, \mu_A(x) \right) \middle| x \in X \right\} \tag{1}$$

a) Fuzzy set.   b) The α-levels.
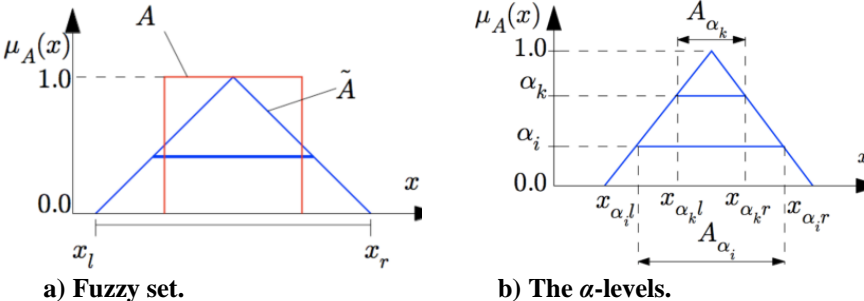
Figure 1:- Fuzzy set and α-level representation

The fuzzy set $\tilde{A}$ can be represented by means of subsets that are denominated α-levels (see Fig. 1), which correspond to real and continuous intervals. In order to perform an uncertainty analysis this α-levels vectors must be mapped onto the mechanical system model. In this contribution we considered a two stage procedure known as α-level optimization (Möller, Graf and Beer, 2000) illustrated by Fig. 2. In the first stage, the input vector that corresponds to the fuzzy parameter is discretized by means of the α-level representation (see Fig. 2). Thus, each element of the fuzzy parameter vector is considered as an interval.

The second stage is related to solving an optimization problem. This optimization problem consists in finding the maximum or minimum value of the output at each α-level.
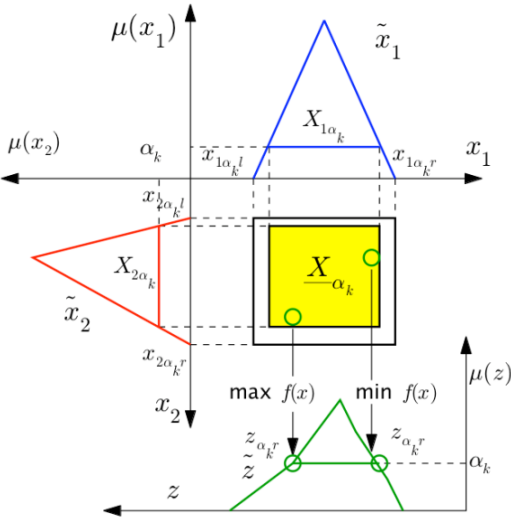
Figure 2: The α-Level optimization

Fuzzy uncertainty analysis application

In this analysis, the Finite Element (FE) model of a rotor test rig composed by a flexible steel shaft, three rigid discs, and two hydrodynamic bearings was derived following the model proposed by Lalanne and Ferraris (1998).

In the FE model both fluid film bearings are modeled as cylindrical bearings with constant radial clearance as proposed by Capone (1986). However, experimental diameter measures reveal a quasi-conic shape (non-constant radial clearance) for both bearings. Consequently, the radial clearance is an uncertain parameter, and uncertainty analysis is necessary to accurately predict the dynamic behavior of the rotating machine.

Hence, an uncertainty analysis of the described rotating machine was performed considering three uncertainty scenarios, namely the introduction of uncertainties in the radial clearance of both bearings (scenario 01), the influence of uncertainties in the oil viscosity (scenario

02), and the influence of both uncertain parameters on the dynamic behavior of the rotating machine (scenario 03). The analysis were performed considering the rotor operating at 1200 *rpm*. The uncertain parameters were modeled by using fuzzy triangular numbers as illustrated in Table 1.

Table 1: Uncertainty scenarios and its respect fuzzy variables.

Scenarios	Deterministic parameters	Uncertainty intervals
Scenario 01	$C = 76.2\ \mu m$	$51.82\ \mu m \leq C \leq 100.58\ \mu m$
Scenario 02	$T_{oil} = 22.5^o C$	$15.3^o C \leq T_{oil} \leq 29.7^o C$
Scenario 03	$C = 76.2\ \mu m$	$51.82\ \mu m \leq C \leq 100.58\ \mu m$
	$T_{oil} = 22.5^o C$	$15.3^o C \leq T_{oil} \leq 29.7^o C$

Figure 3 shows the orbits determined in the measuring planes S_1 (near the first bearing) and S_2 (near the second bearing – furthest from the motor coupling) by the proposed fuzzy uncertainty analysis, highlighting the obtained lower and upper limits (when $\alpha = 0$), and the associated experimental orbit. Note that the displacements determined by applying the uncertainty scenarios in the FE model can predict satisfactorily the dynamic behavior of the rotor, whereas in scenarios 01 and 03 the obtained uncertainty envelopes completely encompass the experimental orbit.

Despite the predicted uncertainty envelope underestimation of the experimental orbit in scenario 02, it is important to remember that the intervals associated with the oil film temperature were defined by following the same variation as adopted for the radial clearance (i.e., ± 32.0%). Different uncertainty intervals could increase the prediction accuracy for scenario 02. Finally, obtained results suggest that a combination of both considered uncertain parameters (i.e., the radial clearance and the oil film temperature) are affecting the dynamic behavior of the rotating machine, which is expected in industrial rotating machines supported by journal bearings. Therefore, the combination of both uncertain parameters leads to an addition effect on the vibration response of the rotor system.
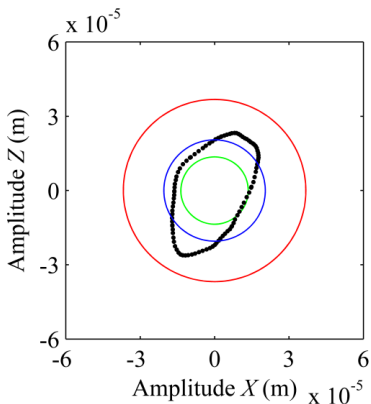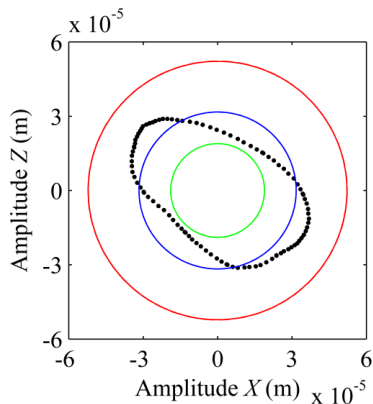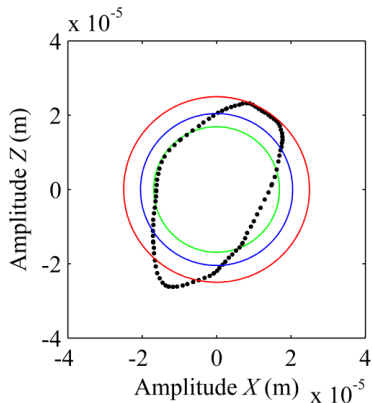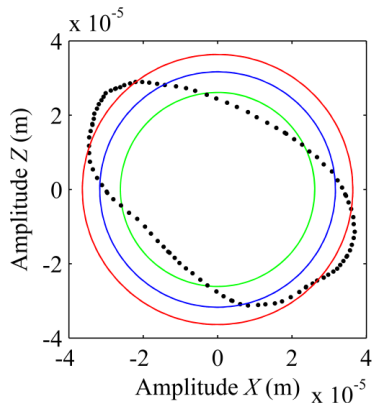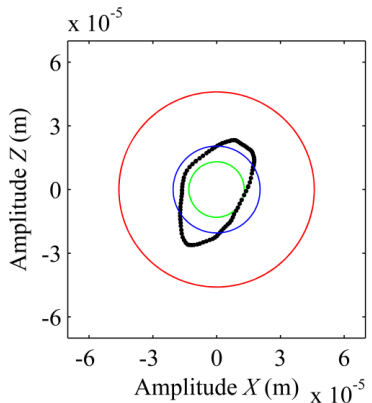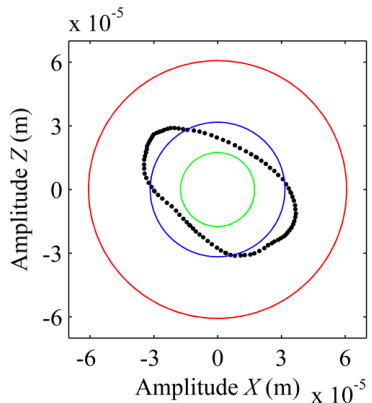
Figure 3: Envelope of the orbits for the considered uncertainty scenarios
(---- lower limit / α = 0; ---- upper limit / α = 0; ---- nominal; •••• experimental)

In this section the fuzzy logic approach was used to evaluate the dynamic responses of a flexible rotor supported by oil film bearings. Three uncertainty cases were analyzed and obtained results illustrates the ability of the proposed fuzzy methodology to predict the real upper and lower limits of the uncertainty envelope. Further information regarding the results presented in this section can be found in Dourado, Cavalini Jr., and Steffen Jr. (2017).

NON-PARAMETRIC ROBUST BALANCING APPROACH

In this section, a fuzzy robust optimization approach is evaluated in terms of rotor balancing applications. The proposed non-parametric approach is aims to enhance an existing balancing technique robustness. The proposed methodology is based on the concepts of fuzzy sets and defuzzification. Further information on the presented procedure can be found in Carvalho *et al.*, 2018.

Fuzzy robust balancing

Balancing is a systematic procedure for adjusting the radial mass distribution of a rotor to approximate its barycenter to the geometric centerline, thus reducing the vibration amplitude and lateral forces applied to the bearings and surrounding structures due to unbalancing (Eisenmann and Eisenmann JR, 1998). The so-called influence coefficients method (IC method) is one of the most used balancing procedure in industrial applications. In the IC method, trial weights are positioned at specific locations along the rotor to determine the vibration responses sensitivity to unbalance variations. Then, correction weights and their corresponding angular positions are determined so that the vibration amplitudes of the rotor system are minimized.

In this section, a revised IC balancing methodology based on fuzzy logic approach is evaluated in terms of overall balancing robustness. In the proposed methodology, fuzzy sets are used to model the rotor unbalance condition. Treating the unbalance condition as a fuzzy set, i.e., $unb = \{(u, \mu_{unb}(u^*)) | u^* \in U\}$, where u is a measured data and μ is the membership function of the unbalance fuzzy set, the resulting fuzzy numbers are weighted intervals that indicate the condition of the rotor. In this way, $\mu_{unb} = 0$ indicates a balanced condition, $\mu_{unb} = 1$ indicates an

unbalanced condition, and $0 < \mu_{unb} < 1$ indicates a condition that could either be balanced or unbalanced.

The knowledge contained in the rotor vibration responses measured over a long period is incorporated into an unbalance fuzzy set, by adapting the method proposed by Pota, Esposito and De Pietro (2013) to extract fuzzy interpretation of a data set. The transformation scheme is based on the application of the statistical hypothesis tests (i.e., Fisherian test). Then, from the derived rotor unbalance fuzzy sets, an unbalance condition (i.e., vibration amplitudes and associated angular positions) is obtained through a defuzzification process, i.e. a process to aggregate the information contained in a fuzzy set into a single value. The resulting unbalance condition is introduced in the IC method algorithm for balancing purposes. Thus, the conventional IC algorithm is extended by means of a preprocessing stage based on fuzzy logic analysis. In this preprocessing procedure, system uncertainties manifested in the measurement data set are assessed and considered in resulting unbalance condition.

Hence, the proposed balancing methodology can be summarized as follows: *i*) the fuzzy transformation is used to determine fuzzy sets associated with the measured vibration amplitudes and corresponding phase angles; *ii*) a defuzzification technique is applied in each fuzzy set resulting in equivalent vibration amplitudes and phase angles; *iii*) these values are introduced in the IC method to determine correction weights and corresponding angular positions.

Fuzzy balancing evaluation

In order to evaluate the effectiveness of the proposed methodology, experimental analysis was performed considering a test rig composed by a horizontal flexible shaft, two rigid discs, and supported by rolling and oil film bearings. The goal in applying the proposed balancing approach is to obtain vibration amplitudes that are less sensitive to operational fluctuations of the rotating machine.

The set of vibration responses was generated by considering the oil film temperature (T_{oil}) and rotation speed (Ω) as uncertain variables. During 24 hours of experimental tests, T_{oil} was allowed to vary from 22 °C to 29 °C and Ω was limited in the interval 500 rev/min to 700

rev/min (changes in steps of 50 rev/min). Table 2 presents the fuzzy unbalance condition, the obtained correction weights, and the corresponding angular positions. The results obtained by the deterministic IC method are presented for comparison purposes.

Table 2: Experimental application of the robust and deterministic balancing approaches.

	Unbalance [μm / degrees]	Correction weight [g]	Angular position [degrees]
Fuzzy	26.16/-83.2	21.78	-140.0
Deterministic	27.61/-79.9	29.07	-160.0

Table 3 presents the minimum and maximum experimental vibration amplitudes obtained for the balanced rotating machine. In this case, the robust and deterministic IC methods are compared . Note that the conventional IC method presented variations of 2.9 μm and 3.2 μm (with respect to the horizontal and vertical directions, respectively), while the robust approach results in a variation of 2.2 μm in both directions. However, higher maximum vibration amplitudes were obtained by the proposed approach (see Table 3). Nonetheless, the goal of the proposed approach is not to reduce the maximum overall vibration amplitude of the rotating system but rather to reduce the system sensitivity to the uncertain scenarios.

Aiming at further assessing the proposed methodology performance, another experimental test was performed, in which the rotor system was driven out of its operational speed range boundary. In this particular test, constant oil temperature (23 ± 0.5 °C) was considered for simplicity, while Ω was allowed to reach 1000 rev/min (i.e., 300 rev/min higher than the uncertainty interval upper bound). Figure 4 presents both the robust and deterministic balancing results obtained in this extrapolation test

Table 3: Vibration amplitudes of the balanced rotor obtained during the experimental tests.

	Horizontal direction		Vertical direction	
	Robust	*Deterministic*	*Robust*	*Deterministic*
Maximum[μm]	14.2	12.5	12	8.5
Minimum[μm]	12	9.6	9.8	5.3
Variation [μm]	2.2	2.9	2.2	3.2

In the extrapolation analysis presented in Figure 5, the proposed approach also leads to smaller variation of the vibration amplitude. The vibration amplitude along the horizontal direction changed from, approximately, 14 μm to 40 μm. In the vertical direction, the vibration amplitude changes from 10 μm to 32 μm. Regarding the deterministic balancing, the vibration amplitudes changed from, approximately, 8 μm to 42 μm and 6 μm to 35 μm along the horizontal and vertical directions, respectively. These results suggest that the revised IC method is able to provide smaller vibration amplitudes even in scenarios where the rotor system is exposed to operating conditions outside the considered uncertainty intervals.

As previously mentioned, the goal of the proposed methodology is to reduce the sensitivity of the system to operational fluctuations, rather than reducing the maximum observed vibration amplitude. The presented results indicate that the proposed robust IC method leads to less sensitive balancing responses as compared to the standard IC method. This robustness increment was achieved through the simple addition of a preprocessing stage in which fuzzy logic tools are used to define a more representative rotor unbalance condition. Also, it is worth mentioning that the robust IC method resulted in a correction weight 25% lighter than the value obtained by the deterministic approach.
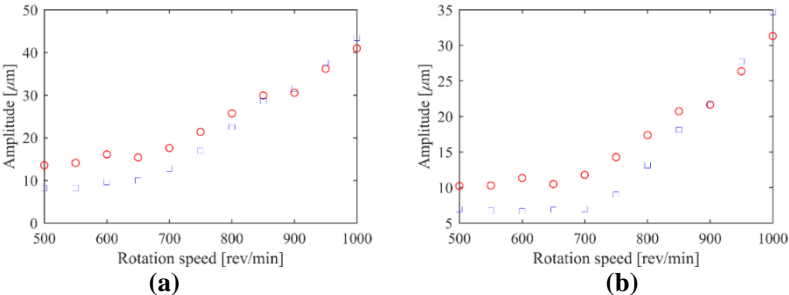

Figure 4: Extrapolation of the rotation speeds considering the robust and deterministic IC method (□ deterministic; ○ robust): a) horizontal direction; b) vertical direction.

FUZZY RELIABILITY-BASED DESIGN

In this section a novel fuzzy reliability-based design methodology is discussed. This methodology is based on the possibility concept and

fuzzy states assumptions. Thus, the associated reliability-based optimization (RBO) problems are solved through a nested algorithm. An inner optimization loop is used to obtain the uncertain variables limits and an outer optimization loop evaluates a predefined fuzzy reliability index within the previously obtained bounds. The performance of the proposed approach is evaluated through a benchmark function. A deep dive on this formulation can be found in Dourado *et al.* (2019).

Fuzzy reliability analysis

In deterministic design problems, the solution is obtained on a given constraint boundary or at the intersection of constraints boundaries. However, if any perturbation arises in the vector of design variables, the violation of some operational/design constraints could emerge resulting in an infeasible condition. Thus, a reliability measure must be assessed to find reliable and feasible solutions considering the effects of uncertainties.

In traditional fuzzy reliability analysis (Wang *et al.*, 2017), the uncertain information is represented as a set of fuzzy parameters. Fuzzy limit state functions (*FLSF*) are defined with respect to the vector of fuzzy parameters, as given by Eq. (2).

$$FLSF_j = S_j - R_j = g_j(\mathbf{x}) \tag{2}$$

in which R_j and S_j are the so-called structural strengths and stresses, respectively, $g_j(\mathbf{x})$ is defined from the inequality constraints of the problem, and $j = 1, \ldots, N$ (N is the number of constraints).

A critical surface (hypersurface $g_j(\mathbf{x})=0$) is defined, separating the variable space into two parts, namely failure domain ($\{\mathbf{x}/\ g_j(\mathbf{x})>0,\ x_i \in R^n\}$) and safety domain ($\{\mathbf{x}/\ g_j(\mathbf{x})\leq0,\ x_i \in R^n\}$). Therefore, reliability is defined as the difference between structural stress and strength. The limit state functions $FLSF_j$, the structural strengths R_j, and structural stresses S_j are treated as fuzzy variables.

Following the α-level representation, $FLSF_j$ can be rewritten as an interval with respect to the α-level α_k ($FLSF_{j\alpha k} = g_j(\mathbf{x}_{\alpha k})$). Thus, a reliability index $\eta_{j\alpha k}$ is obtained as presented by Eq. (3) (index similar to the probabilistic reliability coefficient β).

$$\eta_j' = \frac{FLSF_{jL}'}{FLSF_{jR}' - FLSF_{jL}'} \quad (3)$$

where η_j' is obtained considering only the support of the fuzzy limit state function $FLSF_j'$. $FLSF_{jR}'$ and $FLSF_{jL}'$ correspond to the upper and lower bounds of fuzzy variable $FLSF_j'$ support, respectively (limits of the interval $FLSF_{j'\alpha0} = [FLSF_{j'\alpha0l}, FLSF_{j'\alpha0r}]$).

In the proposed methodology, the possibility distribution of a fuzzy set is evaluated only by the fuzzy set support. Thus, the formulated fuzzy reliability metric value will be equal even if different shapes of membership functions are considered, eliminating fuzzy metric dependence of the membership function. Regarding Eq. (3), the proposed formulation leads to positive values of η_j' when a failure state is achieved ($g_j(\mathbf{x})>0$). Otherwise, negative values of η_j' could represent either safety or transient states. If $\eta' \leq -1$, the system is definitely in a safety state since is $g_j(\mathbf{x}) < 0$. Thus, in order to ensure safety, the proposed metric must necessarily be lower or equal to -1. The final possible configuration is when η_j' would belong to the interval (-1,0] and $g_j(\mathbf{x})$ could either be positive or negative defining then a transient state.

Note that the proposed approach results in a nested optimization procedure. An inner optimization loop is carried out to determine $FLSF_R'$ and $FLSF_L'$, which corresponds to the maximum and minimum values of $FLSF'$, respectively. Then, an outer optimization loop is performed to minimize η_j' with respect to predefined uncertain limits (within $[FLSF_L', FLSF_R']$).

Numerical Evaluation

Aiming in evaluate the proposed reliability design optimization methodology, a benchmark RBO problem, namely nonlinear limit state problem (Qu and Haftka, 2004), is considered. The results obtained by using the probabilistic analysis IRA-DE (Lobato *et al.*, 2017) is also presented for comparison purposes.

The fuzzy reliability problem is mathematically represented as shows Eq. (4). This problem was originally formulated as containing two design variables (x_{d1} and x_{d2}) and two random variables (x_{r1} and x_{r2}). Following a 5σ model (i.e. $x_r = \mu \pm 5\sigma$) the design test case random

variables were converted into fuzzy variables, defined by the support intervals [3.5, 6.5] and [1.5, 4.5] for the variables x_{f1} and x_{f2}, respectively.

$$FLSF = x_{f_1} - 0.2 x_{d_1} x_{d_2} x_{f_2}^2$$
$$\begin{cases} \min x_{d_1}^2 + x_{d_2}^2 \\ \min \eta'(FLSF) \end{cases} \tag{4}$$

Figure 5 presents the Pareto's curve and variation of the $FLSF'$ support obtained by using the proposed reliability approach, in which the safety, transient, and failure domains are indicated. As expected, the value of the cost function increases as the reliability index η' decreases. Alos, $FLSF'$ support increases as $\eta' \to -\infty$ ($FLSF_R'$ and $FLSF_L'$ tend to negative values) indicating an incremental increase on the design safety.

The presented results illustrates the efficiency and flexibility of the proposed fuzzy methodology, as represented by its capability of obtaining safety, transient, or failure system design configurations. The example discussed show that the proposed approach can effectively assess reliability in design problems with uncertain quantities without the necessity of defining either a probability density function or a possibility distribution.
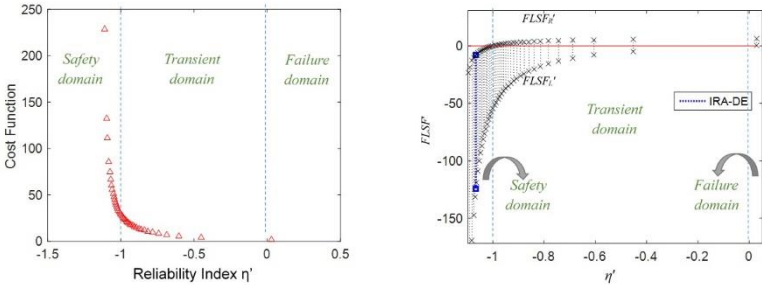
a) **Pareto's curve**   b) **FLSF′ behavior**

Figure 5: Pareto's curve and FLSF′ behavior corresponding to the optimal design solutions of the nonlinear limit state problem.

REFERENCES

Capone, G., 1986, "Orbital Motions of rigid symmetric rotor supported on journal bearings", La Meccanica Italiana, Vol. 199, pp. 37-46.

Carvalho, V. N., Rende, B. F. R., Silva, A. D. G., Cavalini Jr, A. A., Steffen Jr, V., 2018, "Robust Balancing Approach for Rotating Machines Based on Fuzzy Logic", Journal of Vibration and Acoustics, Vol. 140(5).

De Abreu, G. L. C. M., Maesta, M.F., Lopes, V. Jr, De Marqui, C. Jr; Faria, C.T., Inman, D.J., 2015, "Active angular control of a sectioned airfoil using shape memory alloys and fuzzy controller", Journal of the Brazilian Society of Mechanical Sciences and Engineering, Vol. 37, pp. 1555-1567.

Dourado, A. D. G., Cavalini Jr, A. A., and Steffen Jr., V., 2017, "Uncertainty quantification techniques applied to rotating systems: A comparative study", Journal of Vibration and Control, Vol. 24(14).

Dourado, A. D., Lobato, F. S., Cavalini Jr., A. A., and Steffen Jr., V., 2019, "Fuzzy Reliability-Based Optimization for Engineering System Design", International Journal of Fuzzy Systems.

Dubois, D., Prade, H., 1997, "The three semantics of fuzzy sets", Fuzzy Sets and Systems, Vol. 90, pp. 141-150.

Eisenmann, R. C., Eisenmann, R. C. Jr, 1998, "Machinery malfunction, diagnosis and correction" New Jersey: Prentice Hall, Inc.

Lalanne, M., and Ferraris, G., 1998, "Rotordynamics prediction in engineering". John Wiley & Sons, INC.

Lobato, F. S., Gonçalves, M. S., Jahn, B., Cavalini Jr., A. A., Steffen Jr., V., 2017, "Reliability-Based Optimization Using Differential Evolution and Inverse Reliability Analysis for Engineering System Design", Journal of Optimization Theory and Applications.

Möller, B., Beer, M., 2004, "Fuzzy Randomness, Uncertainty in Civil Engineering and Computational Mechanics", Springer-Verlag.

Möller, B., Graf, W., Beer, M., 2000, "Fuzzy structural analysis using α-level optimization. Computational Mechanics", Vol. 26, pp. 547-565.

Ozben, T., Huseyinoglu, M., Arslan, N., 2014, "Fuzzy logic model for the prediction failure analysis of composite plates under various cure

temperatures", Journal of the Brazilian Society of Mechanical Sciences and Engineering, Vol. 36, pp. 443-448.

Pota, M., Esposito, M., De Pietro, G., 2013, "Transforming Probability Distributions into Membership Functions of Fuzzy Classes: A Hypothesis Test Approach", Fuzzy sets and Systems, Vol. 233, p. 52-73.

Qu, X.; Haftka, R. T., 2004, "Reliability-Based Design Optimization Using Probabilistic Sufficiency Factor", Structural and Multidisciplinary Optimization, Vol. 27(5), pp. 314-325.

Wang, C., Qiu, Z., Xu, M., Qiu, H., 2017, "Novel Fuzzy Reliability Analysis for Heat Transfer System Based on Interval Ranking Method", International Journal of Thermal Sciences, Vol. 116, pp. 234-241.

Zadeh, L., 1965, "Fuzzy sets", Information and Control, Vol. 8, pp. 338-353.

Zadeh, L., 1968, "Fuzzy sets as basis for a theory of possibility", Fuzzy Sets and Systems, Vol. 1, p. 3-28.

Analysis of Thermohydrodynamic Models Dedicated to the Bearings of a Francis Hydropower Unit*

Jefferson Silva Barbosa
jsbarbosa@ufu.br

Advisors: Aldemir Ap Cavalini Jr and Valder Steffen Jr

Abstract: This work is dedicated to the computational modeling of the hydrodynamic bearings used in a Francis hydropower unit. To represent the dynamic behavior of the bearings, a thermohydrodynamic approach is performed, in which the thermal effects due to the viscous friction of the oil film are computed through the simultaneous solution of the Reynolds and energy equations. Three hydrodynamic bearings of the hydropower unit are analyzed using simplifying hypotheses, namely, a tilting-pad thrust bearing, a tilting-pad radial bearing, and a cylindrical journal bearing. The numerical results obtained in the present work demonstrated to be similar to the corresponding data provided by the manufacturer. It is worth mentioning that the present work was developed under the context of the R&D project Robust Modeling for the Diagnosis of Defects in Generating Units (02476-3108/2016) conducted by ANEEL (Brazilian Electric Energy Agency). This project is carried out at the Federal University of Uberlândia, Brazil, with the financial support of the companies CERAN, BAESA, ENERCAN, Foz do Chapecó, and CPFL Energia.

Keywords: hydrodynamic bearings, thermohydrodynamic models, Francis hydropower unit.

INTRODUCTION

Bearings are mechanical elements responsible for supporting rotating shafts, which can be axial or radial (thrust or journal bearings, respectively), depending on the direction of the applied load (Dourado et al., 2019). Bearings can be further classified as roller (or ball),

hydrodynamic, and magnetic bearings. Hydrodynamic bearings can present fixed or variable geometries, such as the tilting-pad bearings. These bearings are widely applied in the industry and show greater stability, allowing them to operate in higher rotating speeds (Barbosa, 2018). Hydrodynamic bearings are widely used in hydropower units due to their load capabilities (Vance, Zeidan, and Murphy, 2010).

The mathematical simulation of hydropower units is an indispensable resource for engineers, allowing a comprehensive understanding of the dynamic behavior of the system and the prediction of undesired operating conditions (Dourado et al., 2019). In this context, the development of models for representing hydrodynamic bearings becomes mandatory.

The theoretical studies of Osborn Reynolds (Reynolds, 1886) resulted in a differential partial equation obtained from simplifications applied to the Navier-Stokes equation. The pressure field in the oil film can be determined by solving the Reynolds equation. In the approach proposed by Reynolds (1886), the oil film temperature is considered constant. However, due to the motion between the bearing parts, part of the kinetic energy is converted into thermal energy. The oil temperature increases and, consequently, the oil viscosity decreases. Aiming to obtain accurate hydrodynamic bearing models, Dowson (1962) solved the Reynolds equation considering changes in the oil film temperature. In this thermohydrodynamic model (THD), the thermal effects are considered by associating the energy equation with the modified Reynolds equation.

The Francis hydropower unit considered in the present work is composed by a vertical shaft, a generator unit, a Francis turbine, and three bearings, namely a combined tilting-pad thrust/journal bearing located at the top of the generator, a tilting-pad journal bearing located at the bottom of the generator, and a cylindrical journal bearing located close to the Francis turbine. Is this work, THD models are applied for determining the pressure and temperature fields in the three hydrodynamic bearings of the considered hydropower unit. The maximum pressure, maximum temperature, and minimum oil film thickness are also determined.

THD BEARING MODEL

In this section, the THD models used to represent the tilting-pad thrust bearing (TPTB), the tilting-pad radial bearing (TPJB), and the cylindrical journal bearing (CJB) of the Francis hydropower unit are presented. The equilibrium condition for the considered models was obtained by equating the external load applied to the bearings with the hydrodynamic forces, which were determined by integrating the pressure distribution over the projected area of the bearings. The equilibrium of momentum was also achieved for the TPTB and TPJB. The pressure and the temperature fields generated in the oil film were obtained. Details on the THD models for the considered hydrodynamic bearings can be found in Barbosa (2018).

Tilting pad thrust bearing

Figure 1 illustrates the physical model of the TPTB, in which the pad inner and outer radii are given by r_1 and r_2, respectively, θ_{pivot} and r_{pivot} are the angular and radial positions of the pivot, respectively, θ_0 stands for the pad angular length, α_p and α_r are the pad rotational angles at the pivot along the r and s directions, respectively, and h_h is the oil film thickness.
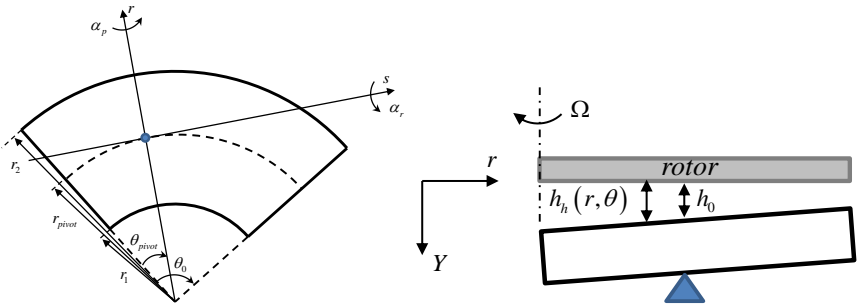
Figure 1: Physical model of the TPTB.

The hydrodynamic forces are determined by calculating the equilibrium position of the bearing. For this aim, the angles α_p and α_r and the oil film thickness at the pivot h_0 should be determined, as shown in Eq. (1) and Eq. (2).

$$\mathbf{X} = \begin{bmatrix} h_0 & \alpha_r & \alpha_p \end{bmatrix} \tag{1}$$

$$f_1 = \mathbf{F}_Y + \mathbf{F}_w \to 0$$

$$f_2 = M_r = \int_{r_1}^{r_2} \int_{\theta_1}^{\theta_2} p_h \cdot r^2 \cdot \sin\left(\theta - \theta_{pivot}\right) \cdot d\theta \cdot dr \to 0$$

$$f_3 = M_s = \int_{r_1}^{r_2} \int_{\theta_1}^{\theta_2} p_h \cdot r \left(r \cdot \cos\left(\theta - \theta_{pivot}\right) - r_{pivot} \right) \cdot d\theta \cdot dr \to 0 \tag{2}$$

Equation (1) represents the vector of design variables that are to be determined. $\mathbf{F}_Y$ and $\mathbf{F}_w$ are the hydrodynamic force and external loading, respectively, f_1 stands for the equilibrium of forces, f_2 and f_3 refer to the equilibrium of momentum along the directions r and s, respectively. Figure 2 shows the flowchart regarding the iterative process associated with the THD-TPTB model.

Figure 2: Procedure for determining the hydrodynamic forces in TPTB (Barbosa, 2018, adapted).

Tilting pad journal bearing

Figure 3 presents the schematic representation of a TPJB, in which Ω is the rotation speed of the shaft, R is the shaft radius, R_S is pad radius, O_P, O_E, and O_S are the pivot center of rotation, shaft center, and pad center, respectively, h_0 is the bearing radial clearance, and α is the pad angle relative to the pivot.
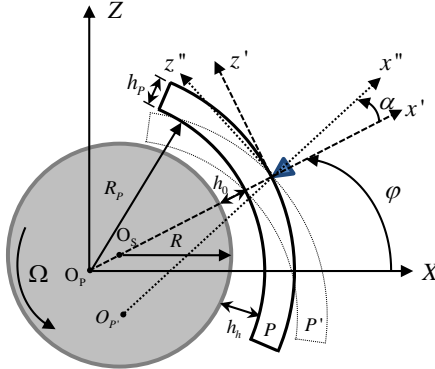
Figure 3: Physical model of the TPJB.

The THD-TPJB model is formulated based on four reference frames, as given by Fig. 4. The first one is placed at the center of the bearing: inertial frame I (X, Y, Z). The second frame indicates the position of the j-th pad in the bearing: auxiliary system B (x, y, z). Each pad has its own auxiliary frame, i.e., the mobile system B' (x', y', z'). The last system follows the inner surface of the pad, i.e., the curvilinear mobile system B'' (x'', y'', z'').

The hydrodynamic supporting forces in TPJB are determined at the equilibrium positions of the shaft and the pads (equilibrium of momentum). In this case, the position of the shaft center O_E (X_r, Z_r) and the angle α of each pad can be determined, as given by Eq. (3) and Eq.(4).

$$\mathbf{X} = \begin{bmatrix} X_r & Z_r & \alpha_1 & \alpha_2 & \dots & \alpha_N \end{bmatrix} \tag{3}$$

$$f_1 = \mathbf{F}_R + \mathbf{F}_w \to 0$$
$$f_2 = M_{R_1} = F_{xm_1} \cdot (R_S + h_S) \to 0$$
$$f_3 = M_{R_2} = F_{xm_2} \cdot (R_S + h_S) \to 0 \tag{4}$$
$$\vdots$$
$$f_{N+1} = M_{R_N} = F_{xm_N} \cdot (R_S + h_S) \to 0$$
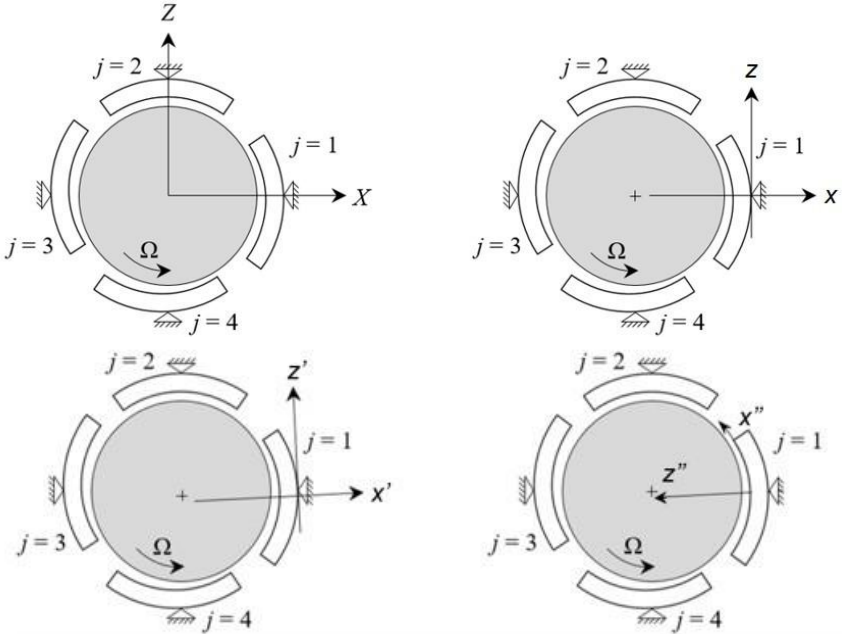
Figure 4: Reference frames: a) Inertial system; b) auxiliary system; c) mobile system; d) curvilinear mobile system (Russo, 1999, adapted).

Equation (3) represents the vector of design variables that should be obtained. In Eq.(4), $\mathbf{F}_R$ and $\mathbf{F}_w$ are the hydrodynamic force and external load, respectively, f_1 stands for the equilibrium of forces, and f_2, f_3, … f_{N+1} represents the equilibrium of momentum. Figure 5 shows the flowchart concerning the procedure for determining the hydrodynamic forces according to the THD-TPJB model.
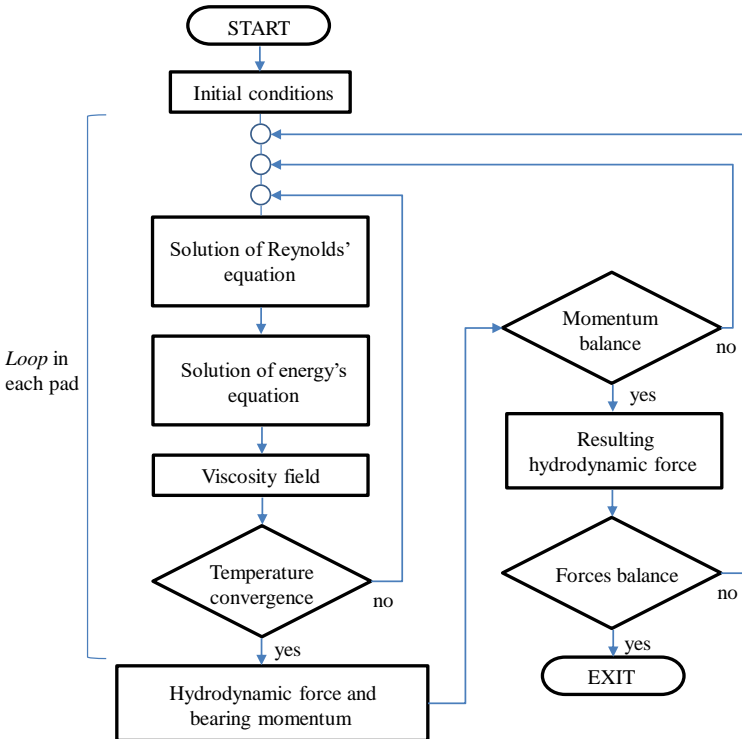
Figure 5: Procedure for determining the hydrodynamic forces in TPJB (Barbosa, 2018, adapted).

Cylindrical guide bearing

Figure 6 presents the main geometric parameters of the CJB. In this case, R is the shaft radius, L_h is the bearing length, C is the radial clearance, e is the eccentricity (radial displacement from the center of the shaft O_E to the center of the bearing), α_h is the angle that defines the angular position of the shaft center, and Ω is the rotation speed of the shaft.

The hydrodynamic supporting forces in CJB are determined at the equilibrium position of the shaft. In this case, the position of the shaft center $O_E(X_r, Z_r)$ should be determined, as shown in Eq. (5) and Eq.(6).

$$\mathbf{X} = \begin{bmatrix} E & \alpha_h \end{bmatrix} \tag{5}$$

$$f_1 = \mathbf{F}_w + \mathbf{F}_h \to 0 \tag{6}$$
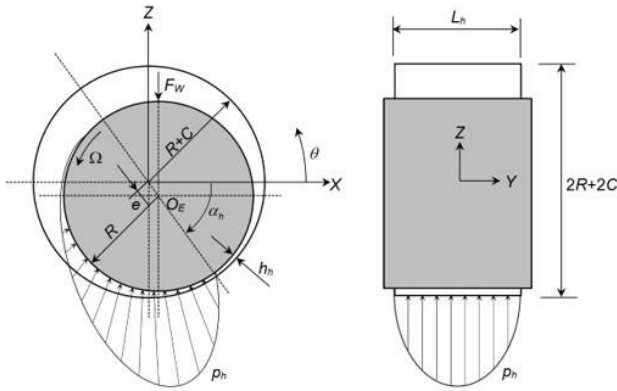
Figure 6: Physical model of the CJB (Cavalini Jr et al., 2017, adapted).

Equation (5) represents the vector of design variables that are to be determined. In Eq.(6), $\mathbf{F}_h$ and $\mathbf{F}_w$ are the hydrodynamic force and external load, respectively, and f_1 refers to the equilibrium of forces. Figure 7 shows the flowchart concerning the procedure for determining the hydrodynamic forces according to the THD-CBJ model.
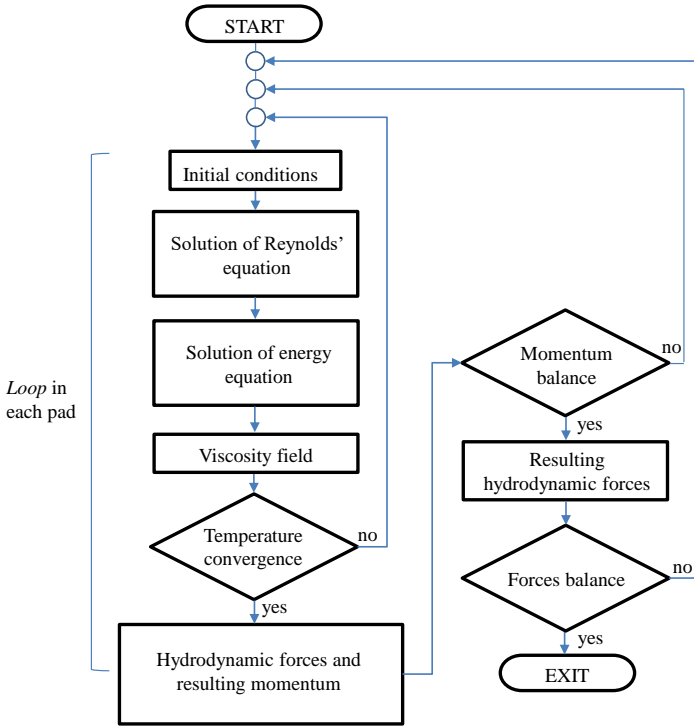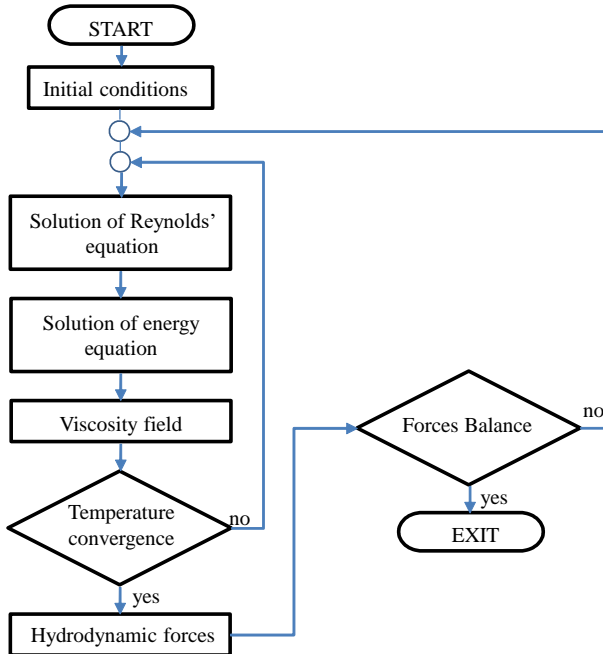

Figure 7: Procedure for determining the hydrodynamic forces in CJB (Barbosa, 2018, adapted).

NUMERICAL RESULTS

This section is dedicated to the numerical results obtained by using the THD models of the hydrodynamic bearings of the Francis hydropower unit. There are particularities regarding the geometry and lubrication form of each bearing, which are detailed next. It is important to note that the operating conditions in which the bearings are analyzed were provided by the manufacturer of the hydropower unit.

Figure 8 shows the location of the bearings in the considered hydropower unit. This machine presents a Francis turbine with 44.58 MW nominal power, operates at 300 rpm, 24 poles generator, 60 Hz frequency, 13,800 V voltage, and 2,027.5 A current.
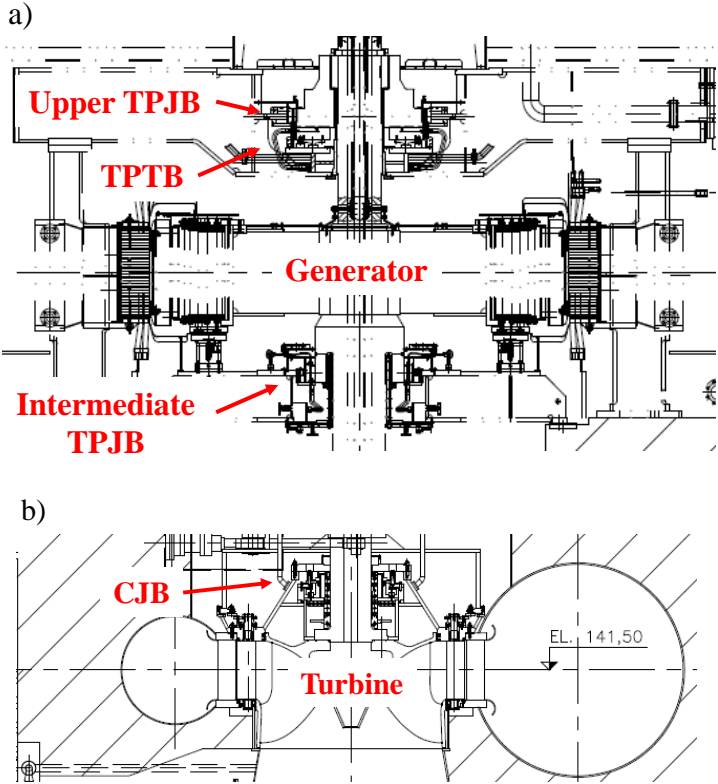
Figure 8: Assembly of the bearings, turbine and generator in the GU: a) Upper part of GU; b) Bottom part of GU. (Barbosa, 2018, adapted).

Tilting-pad thrust bearing

Table 1 presents the geometric properties and operating parameters of the TPTB. Table 2 shows the results obtained by using the implemented THD-TPTB model. The data provided by the manufacturer are also presented for comparison purposes. Note that similar results were obtained, which demonstrates the representativeness of the implemented THD-TPTB model. Figure 9 shows the associated pressure and temperature fields.

Table 1: Geometric properties and operating parameters of the TPTB.

Parameters	Values
Inner radius	310 mm
Outer radius	660 mm
Pivot radius	485 mm
Pad angle	45°
Number of pads	6
Arc pivot/arc pad	0.6
Rotation speed	300 rpm
Oil type	ISO VG 68
Load bearing	2300 kN

Table 2: Results obtained with the THD-TPTB model and provided by the manufacturer.

Properties	Manufacturer	Present work	Difference (%)
P_{max} (MPa)	6.90	6.93	0.43
T_{max} (GPa)	69.25	64.51	6.84
h_{min} (μm)	58.79	50.65	13.85

It is important to note in Fig. 9a, Fig. 9b, and Fig. 9c that the region of the pad in which the hydrodynamic pressure has a maximum magnitude is located on the right side of the pad. This effect is due to the direction of rotation of the shaft. Thus, the region with maximum pressure depends on the direction of the rotation. Additionally, the region of maximum temperature (see Fig. 9d and Fig. 9e) is observed in the upper right part of the pad due to the advection heat transfer mechanism (velocity components along with the directions θ and r).
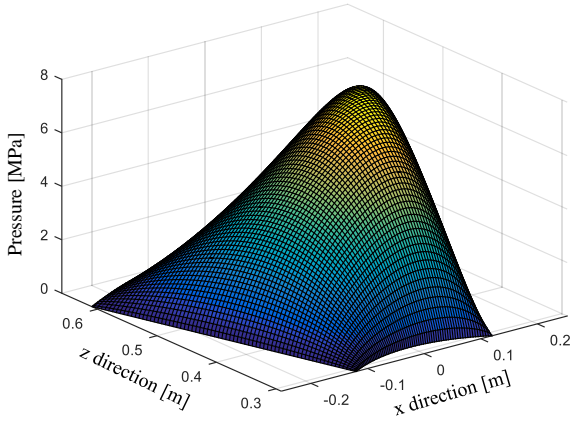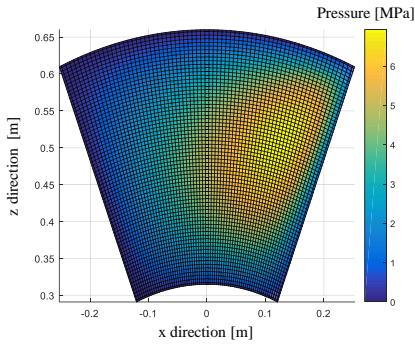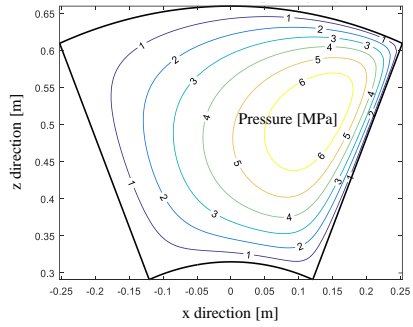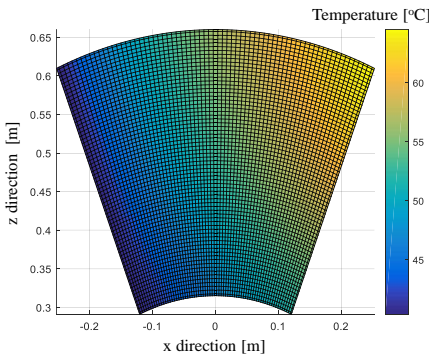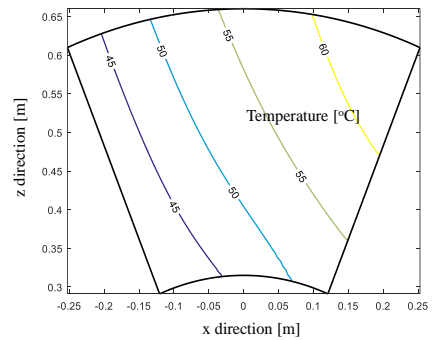
Figure 9: Pressure and temperature fields of the TPTB. a) 3D Pressure field; b) Upper view of pressure field; c) Lines of constant pressure; 2D Temperature field; e) Lines of constant temperature (Barbosa, 2018).

Tilting-pad journal bearing

Figure 10 presents one of the pads of the considered TPJB. Zone 1 corresponds to the oil recess, whereby part of the lubricant flows to the oil reservoir. In this region, it is assumed that the manometric pressure is null. Zone 3 refers to the active region of the bearing, in which the pressure field is formed. Zone 4 also corresponds to the oil outlet. The pivot point of the pad is represented by the 2. The parameters related to the TPJB are shown in Tab. 3.
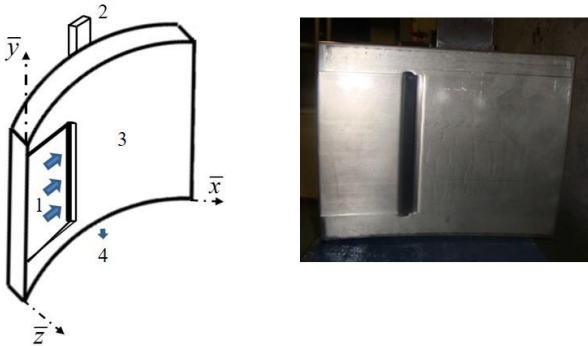
Figure 10: Representation of the TPJB. a) Important regions; b) Inner surface of the TPJB. (Barbosa, 2018).

Table 3: Geometric properties and operating parameters of the TPJB.

Parameters	Values
Inner diameter	934 mm
Shaft diameter	930 mm
Radial clearance	250 µm
Length of bearing	197 mm
Pad thickness	67 mm
Pad angle	60°
Number of pads	6
Arc pivot/arc pad	0.6
Angular position of the pivots in the bearing	0°/60°/120°/180°/240°/300°
Rotation speed	300 rpm
Oil type	ISO VG 68
Loading bearing	90.6 kN

Table 4 shows the results obtained by using the implemented THD-TPJB model. The data provided by the manufacturer are also presented for comparison purposes. Note that similar results were obtained, which demonstrates the representativeness of the implemented THD-TPJB

model. Figure 11 presents the associated pressure and temperature fields.

Table 4: Results obtained with the THD-TPJB model and provided by the manufacturer.

Properties	Manufacturer	Present work	Difference (%)
P_{max} (MPa)	4.761	4.767	0.13
T_{max} (GPa)	52.84	56.40	6.74
h_{min} (µm)	72.70	75.67	4.09

a)

b)
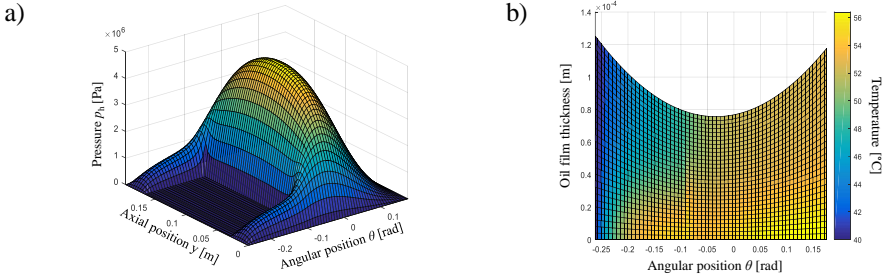
Figure 11: Pressure and temperature fields for the TPJB. a) Pressure field; b) Temperature field. (Barbosa,2018).

Cylindrical journal bearing

Figure 12 shows one part of the considered CJB (two-part bearing). Zone 1 corresponds to the mixing region between the heated oil and the cold oil, which is injected into the bearing by means of the hole outlined in 3. Zone 2 corresponds to a recess, where the oil coming from the mixing region flows to the active zone of the bearing (zone 4).

a)   b)
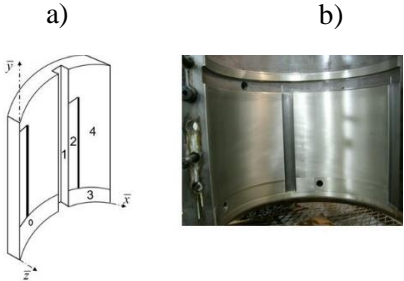
Figure 12: Representation of CJB. a) Important regions; b) Internal surface of CJB. (Barbosa, 2018).

Note that there are four cold oil injection holes, four mixing regions, and four recesses. The pressure on zones 1, 2, and 3 are considered null because the thickness of the oil film is much larger in these regions than in the active ones. Therefore, the pressure field in these regions is significantly lower compared to the actives zones of the bearing. The parameters of the CJB are shown in Tab. 5.

Table 5: Geometric properties and operating parameters of the CJB.

Parameters	Values
Inner diameter	550.4 mm
Shaft diameter	550 mm
Radial clearance	200 µm
Length of the bearing (active zone)	330 mm
Rotation speed	300 rpm
Oil type	ISO VG 68
Operating condition #1	81.5 kN at 300 rpm
Operating condition #2	188 kN at 583 rpm
Operating condition #3	219 kN at 300 rpm

The maximum pressure, maximum temperature, and minimum oil film thickness for the three different operating conditions (see Tab. 5) are shown in Tab. 6. Figure 13 presents the associated pressure and temperature fields obtained for condition #1. In this case, the manufacturer omitted the corresponding data.

Table 6: Results obtained with the THD-CJB model.

Operating condition	α_h [°]	E	P_{max} [MPa]	T_{max} [°C]	h_{min} [µm]
81.5 kN at 300 rpm	34.48	0.392	1.425	68.80	121.56
188 kN at 583 rpm	36.97	0.437	3.425	108.85	112.61
219 kN at 300 rpm	40.81	0.513	4.314	105.03	97.47

Figure 12a shows the regions where the pressure is null due to the recesses present in regions 1, 2, and 3 of the CJB (see Fig. 11a). In Fig. 12b, it is possible to observe low oil temperature regions. These regions correspond to the regions where the mixture between the heated oil and the cold oil occurs.

Table 6 demonstrates that the maximum pressure increases according to the external load, as well as the shaft eccentricity E and the angular position α_h of the shaft center. As expected, the oil film thickness

decreases according to the external load. However, the maximum temperature was achieved for operating condition #2. This result is associated with the considered shaft rotation speed.

a)

b)
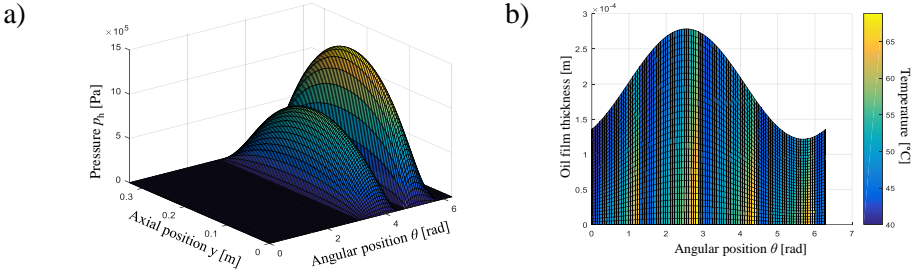
Figure 13: Pressure and temperature field for CJB. a) Pressure field; b) Temperature field. (Barbosa, 2018).

FINAL REMARKS

In this work, the hydrodynamic bearings of a Francis hydropower unit were analyzed according to dedicated THD models. In this approach, the pressure and temperature fields, as well as the maximum pressure, maximum temperature, and minimum oil film thickness were determined. The results obtained for the tilting-pad thrust bearing (TPTB) and tilting-pad journal bearing (TPJB) were similar to the data provided by the manufacturer. The results associated with the cylindrical journal bearing (CJB) demonstrated to be physically consistent. Further research work will be dedicated to include these models in the finite element model of the rotating machine. The development of surrogate models for these bearings based on the THD approach is also scheduled.

ACKNOWLEDGMENTS

the R&D project Robust Modeling for the Diagnosis of Defects in Generating Units (02476-3108/2016).

REFERENCES

Barbosa, J.S., 2018, "Análise de Modelos Termohidrodinâmicos para Mancais de Unidades Geradoras Francis", Universidade Federal de Uberlândia, Uberlândia, Brasil, 92 p.

Cavalini Jr., A.A., Silva, A.D.G., Lara-Molina, F.A., Steffen Jr., 2017, "Dynamic Analysis of a Flexible Rotor Supported by Hydrodynamic Bearings with Uncertain Parameters" Meccanica, Vol. 52, pp. 2931-2943.

Dowson, D., 1962, "A Generalized Reynolds Equation for Fluid Film Lubrication" International Journal of Mechanical Sciences, Vol. 4, pp. 159-170.

Dourado, A.P., Barbosa, J.S., Sicchieri, L., Cavalini Jr., A.A., Steffen Jr., V, 2019, "Kriging Surrogate Model Dedicated to a Tilting-Pad Journal Bearing" Proceedings of the 10th International Conference on Rotor Dynamics - IFToMM, Vol.1, Rio de Janeiro, Brazil, pp. 347-358.

Reynolds, O., 1886, "On the Theory of Lubrication and its Application to Mr. Beauchamp Tower's Experiments, Including an Experimental Determination of the Viscosity of Olive Oil" Philosophical Transactions of Royal Society of London, Vol. 177, pp. 157-234.

Russo., F.H., 1999, "Identificação das Propriedades Dinâmicas de Mancais Segmentados Híbridos – Teoria e Experimento", Universidade Estadual de Campinas, Campinas, Brasil, 183 p.

Vance, J., Zeidan, F., Murphy, B., 2010, "Machinery Vibration and Rotordynamics," Wiley, New Jersey.

Force Identification in Hydropower Turbine Considering rubbing contact[*]

Tobias Souza Morais[*]
tobias@ufu.br

Raul Carreira Rufato[**]
raulc.rufato@hotmail.com

Abstract: A force identification process applied to a hydropower generating unit with localized rubbing contact is presented in this work. A model-based methodology for force identification of mechanical systems is presented, aiming at both detecting and monitoring the appearance and development of abnormal forces. The identification methodology based on orthogonal functions was developed considering that the modal base of the healthy rotating system is known, which permits to perform the modal force identification by using a reduced number of measures. The methodology conveyed is based on the integration property of orthogonal functions, which transforms the matrix differential equation that governs the dynamic behavior of the system into an algebraic equation. Herein, the methodology is applied to a Francis hydropower unit, intending to demonstrate its applicability for industrial and complex systems. The vertical machine is supported by three radial bearings and a thrust bearing. A rub contact is considered as fault and its forces were identified. The obtained results demonstrated that the proposed modal force identification methodology can be potentially used to evaluate the forces actuating on the hydraulic turbine.

Keywords: hydropower unit, rubbing, orthogonal functions, modal force identification.

INTRODUCTION

The force identification can be used to establish a procedure to evaluate the operating condition of the machine. Linear and non-linear forces are commonly found in these rotor systems. The identification of the forces, coupled with the model, allows to determine the level of stresses, what gives a way to determine the expected remaining life of the component. The method used to identify the forces must be reliable and its limitations should be well known in order to exclude false positive diagnostic and increase the confidence on the identification process.

Hereafter, an industrial application of the procedure established in Morais et al. (2017) is numerically presented considering a rubbing contact on the rotating system. The forces acting on a Francis hydropower unit are those generated by the unbalance of the rotating system, the weight of the machine, the hydraulic force acting at the Francis turbine, and the magnetic pull force due to the generator. This type of machine is commonly supported by hydrodynamic bearings, which present stiffness dependency of the shaft displacement inside the bearing. In this way, linear and non-linear forces are also included in the simulations. The forces are identified first by considering the system without the contact and considering the rubbing contact at the generator of the hydropower unit.

DYNAMICAL MODEL DESCRIPTION

The hydropower unit in this study is able to generate 44.58 MW. It is composed of a vertical rotating shaft supported by hydrodynamic bearings with a Francis turbine driving the rotating system. The first bearing is a radial tilting pad bearing. It is combined with a thrust tilting pad bearing located above the generator, which supports vertically the shaft. There are two other radial bearings, being one tilting pad bearing right below the generator and, the other one, a cylindrical bearing mounted above the Francis turbine.

The forces acting in normal conditions over the rotating shaft are the unbalance, its weight, the electromagnetic forces at the generator, the hydraulic forces at the turbine, as well as the linear and non-linear

bearing forces due to the differences between the actual bearing stiffness parameter and the bearing parameter used on the system modeling.

The mathematical model of the rotating shaft was developed by using a current finite element (FE) approach. A Timoshenko's beam element with six degrees of freedom per node and two nodes by element were considered. The shaft model has 26 nodes. Figure 2 shows a schematic representation of the finite element model (FEM). The material used for the shaft is the stainless steel with elasticity modulus E=205 GPa; density, ρ=7,870 kg/m³; and Poisson's ratio v=0.29. The total shaft length is 9.088 m. Six points are considered as concentrated masses, thus representing the discs of the exciter, the thrust block mass, the generator mass, two other masses to assemble the bearings, and the Francis turbine mass. The total rotating mass of the finite element is 134,521 kg. Its difference from the actual nominal condition is 0.02%. The bearing parameters used in the shaft FEM model are considered as being constant at the rotational speed of the machine and were calculated from the fabricant's manual of the bearings. An unknown linear and a cubic stiffness with constant coefficient will be considered to introduce unknown forces in the system. These forces will disturb the system including uncertainties on the bearing parameters. They will be identified, thus generating confidence on the proposed bearing parameter forces identification process.
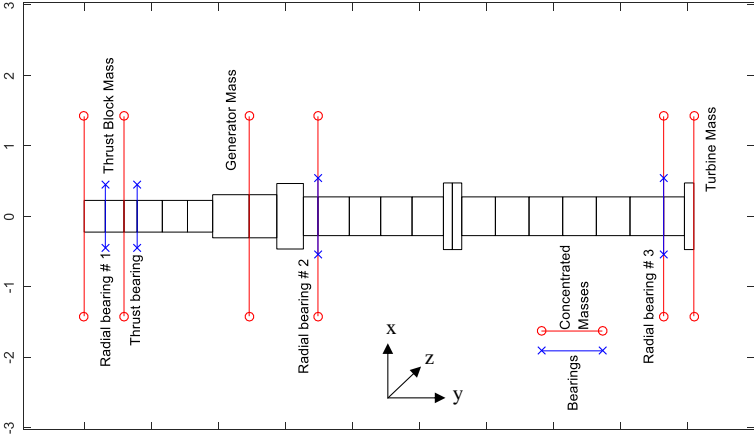
Figure 1: Finite element model of the rotating shaft.

Equation (1) represents the dynamic behavior of the flexible rotating system supported by the bearings and excited by external forces.

$$M\ddot{x}(t) + [C + \Omega C_g]\dot{x}(t) + [K + K_T + K_{bc} + K_{bv}]\,x(t) = W + F_u + F_{EM} + F_H + F_{rub} \ (1)$$

Where M is the FE mass matrix of the rotating shaft, C is the sum of the structural damping matrix and the bearing damping, and C_g is the gyroscopic matrix. K is the stiffness matrix of the shaft, K_T is the stiffening effect due to the torque, K_{bc} is a constant stiffness of the bearing that can be determined using a simplified approach just to give an idea of its magnitude and, K_{bv} is the variable stiffness of the bearing that is used to adjust the constant stiffness used to the bearing. The constant stiffness must be used to generate the modal base of the system, and the force generated by the variable stiffness is given by $F_B = -K_{bv}x(t)$. This force is identified as presented on the following section. The displacement vector is represented by x(t) and the rotational speed is given by Ω. W gives the weight; F_u represents the unbalance forces. The above mathematical model was adapted from Lalanne and Ferraris (1997), where six degrees of freedom per node are taken into account. F_{EM} is the electromagnetic pull force introduced at the generator (see the corresponding expression in Paraskevopoulos, Sparis and Mouroutsos (1984)). F_H stands for the hydraulic forces acting at the turbine as presented by Dörfler, Sick and Coutu (2013). It is worth mentioning that F_{EM} and F_H are function of the shaft eccentricity related to the shaft lateral displacements.

Finally, F_{rub} is the force generated due to the contact between the rotor and the stationary part. Figure 2 shows the rubbing model proposed by Toshio and Ishida (2001), with the coordinates system used. Considering k_e as the stiffness of the stationary part, the radial force generated by this stiffness at the time of contact is given by Eq. (2). In which r is the radial displacement vector and δ is the gap between the shaft and the stator at the time of contact.

$$F_K = \begin{cases} -k_e(r - \delta)\frac{r}{|r|} & (para\ r \geq \delta) \\ 0 & (para\ r \geq \delta) \end{cases} \tag{2}$$

For the force generated by damping, c_e is considered the damping coefficient of the stator and the radial force generated is given by Eq. (3).

$$F_C = \begin{cases} -c_e \dot{r} \dfrac{r}{|r|} & (para\ r \geq \delta) \\ 0 & (para\ r \geq \delta) \end{cases} \tag{3}$$

The equivalent damping coefficient c_e can be determined by the restitution coefficient by measuring the energy before and after contact through experiments with the same materials used on the machine.

It can be observed, at the time of contact, the occurrence of a friction force in a tangential direction, given by Eq. (4). In which μ is the friction coefficient.

$$F_f = |F_f| = \mu(|F_k + F_C|) \tag{4}$$

Assuming V_t as the tangential velocity at the center of the rotor. The friction force acts on the opposite direction of V_t when ($V_t+\omega r >0$ and on the same direction when ($V_t+\omega r$)<0.

Thus, considering the forces generated at the time of contact in the equation of the system movement, it is possible to determine the machine's response at the time of contact.
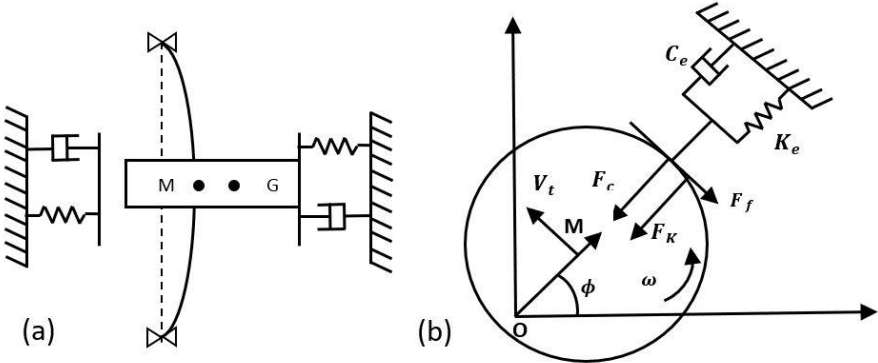
Figure 2: Rubbing model applied to rotary systems.

167

FORCE IDENTIFICATION PROCEDURE

The proposed modal force identification is based on orthogonal functions. A set of real functions $\phi_k(t)$, k=1,2,3 … to be orthogonal in the interval $[a, b] \subset \mathbb{R}$, if Eq. (5) is satisfied, Spiegel (1976).

$$\int_a^b \phi_m(t)\phi_n(t)dt = K \text{ , where } \begin{cases} K = 0 \Rightarrow m \neq n \\ K \neq 0 \Rightarrow m = n \end{cases} \tag{5}$$

The set of functions is said orthonormal if Eq. (6) holds:

$$\int_a^b \phi_m(t)\phi_n(t)dt = \delta_{mn} \tag{6}$$

where δ_{mn} is the Kronecker delta, i.e., δ_{mn}=0 if $m \neq n$ or δ_{mn}=1 if $m=n$, and $\sigma_k(t)$ is the set of orthonormal functions. The following property, related to the successive integration of the orthogonal base, holds for a set of r orthonormal functions in the interval $[0,t]$ (Paraskevopoulos, Sparis and Mouroutsos (1984)):

$$\int_0^t \underset{n \ times}{\cdots} \int_0^t \sigma(\tau)d\tau^n \cong [P]^n \sigma(\tau) \tag{7}$$

where $[P] \subset \mathbb{R}^{r,r}$ is a square matrix with constant elements, called operational matrix of integration and $\sigma_m(t)=\{ \sigma_0(t) \ \sigma_1(t) \ \dots \ \sigma_r(t)\}^{tr}$ is the base of the orthonormal series, and the superscript tr is the transpose of the matrix. In fact, if the orthogonal base used is complete, i.e., the series are not truncated, Eq. (6) is an equality. However, in practice truncated bases are used in such a way that the order of matrix $[P]$ can be handled mathematically. The orthogonal base and the operational matrix related to various types of orthogonal functions are found in Steffen and Rade (1991). In the present case, the Fourier orthogonal base was used. Fourier orthogonal series and its operational matrix of integration for a period in the interval given by $[0,T]$ can be found in Spiegel (1976).

The differential equation of dynamic systems can be split into two main parts aiming to identify the forces acting on the system (either linear or non-linear). On the left-hand side, the inertia, dissipative and

linear elastic forces are considered; on the right-hand side, the unknown forces acting on the system are shown. The differential equation that represents the dynamic behavior of the system is given by Eq. (1).

Based on the main mode shapes of the linear system considering the matrices **M, K,** and $\mathbf{K}_{bc}$ it is possible to transform the differential equation into another equation written using modal coordinates, i.e., the modal base is given by the v first mode shapes. Consequently, the modal transformation applied to x(t) is written as
:

$$x(t) = \phi q(t) \tag{8}$$

Where ϕ is the mode shape matrix considering v lower modes, and $q(t)$ is the modal response. The Eq. (9) is obtained applying the modal transformation (Eq. (8)) and pre-multiplying both sides of the resulting equation by the transpose of the matrix ϕ.

$$m\ddot{q}(t) + c\dot{q}(t) + kq(t) = \phi^{tr}[W + F_u + F_{EM} + F_H + F_B + F_{rub} - \Omega C_g \dot{x}(t) - K_T x(t)] \tag{9}$$

The modal matrices m, c, and k are the modal mass, modal damping, and modal stiffness matrices, respectively, naming the modal force $\phi^{tr}[W+F_u+F_{EM}+F_H+F_B+F_{rub}-\Omega C_g\dot{x}(t)-K_Tx(t)]$ as $f(t)$, to reduce the system equation length. In the sequence of the development it is possible to expand the modal responses $q(t)$ and $f(t)$ in series of orthogonal functions, as presented by Eq. (9), moreover, using the integration property of orthogonal functions, and the properties given by the Eq. (11). In the present contribution, the Fourier orthogonal function was chosen considering the harmonic characteristics of the vibration responses of rotating systems. Consequently, e^{tr} is given by Eq. (12).

$$q(t) = Q\sigma(t) \; and \; f(t) = F\sigma(t) \tag{10}$$

$$1 = e^{tr}\sigma(t) \; and \; t = e^{tr}[P]\sigma(t) \tag{11}$$

$$e^{tr} = [1 \; 0 \; \cdots \; 0]_{1xr} \tag{12}$$

After some manipulations the Eq. (13) can be determined. All parameters of the right side of Eq. (13) are known. so the left side hand of this equation is easily identified. Finally using Eq. (10), the modal forces in time domain are obtained.

$$F[P]^2 = [m \; \vdots \; -mq(0) \; \vdots \; -m\dot{q}(0) - cq(0) \; \vdots \; c \; \vdots \; k] \begin{pmatrix} Q \\ e^{tr} \\ e^{tr}[P] \\ Q[P] \\ Q[P]^2 \end{pmatrix} \quad (13)$$

NUMERICAL RESULTS

In order to simulate the response of the system, the Newmark time integration method was associated with the Newton-Raphson iteration procedure to integrate the matrix equation of motion presented by Eq. (1). The time step used to solve the ordinary differential equation is $1\,ms$. The system of equations was reduced by considering six mode shapes. The first mode shape of the system was disregarded and the next six lower mode shapes were included in the dynamics of the system. The first mode shape represents the rigid body motion around the shaft axis. Considering non-symmetric bearings, the natural frequencies of the system are the following: 15.34 Hz, 15.41 Hz, 16.50 Hz, 18.95 Hz, 19.31 Hz, 23.24 Hz and, 23.68 Hz. Figure 3 presents the Campbell Diagram for the symmetric bearing system.

Nine displacement responses determined at the three radial bearings were considered as known and available for the force identification procedure (two radial displacements and one axial displacement for each radial bearing). The rotational speed of the machine is constant and equals to 300 rpm. An unbalance of 50.00 kgm / 0^0 is added at the generator position. The contact force was considered to be occurring at the generator. The parameters considered on the model are the contact stiffness k=1e10 N/m and the damping C=10 Ns/m. The friction coefficient was considered mi=0.1 and the clearance between the shaft and the stator was considered to be 1e-6 m.

Figure 3 presents the electromagnetic pull force along the x and z directions and the hydraulic forces along the x and y directions when the contact was occurring. Those forces presented are used as input of the system and are identified by the proposed method.
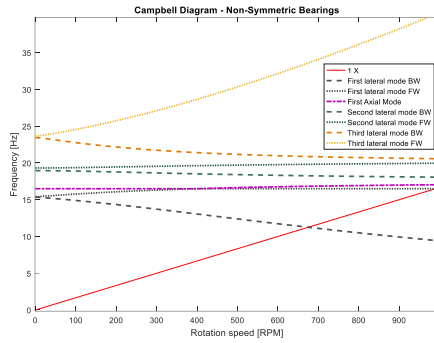
Figure 3: Campbell Diagram of the rotating system supported by non-symmetrical bearings.

Two case studies were analyzed and the modal forces were identified. In the first case, it was considered just the nominal condition of the system with no contact between the rotor and the stator. In the second case, a contact was introduced in the model at the generator position.
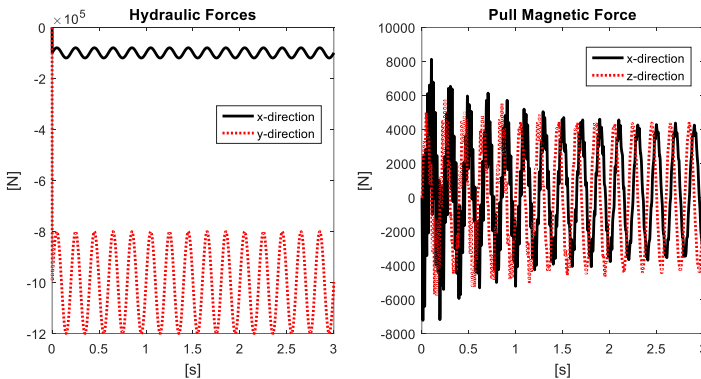
Figure 4: Hydraulic forces (left) and electromagnetic pull (right) acting at the turbine rotor.

First Case Study: Asymmetric bearings

A slight non-symmetric bearing configuration was considered. Thus, the system studied presents different natural frequencies and mode shapes along x and z directions. The bearings stiffness coefficients are given in the Tab. 1. The coupled coefficient is disregarded. The forces considered acting on the system are those related to the nominal operating condition. The system time responses are presented in Fig. 5, where the system simulated response with the identified modal forces

are also presented. The same displacement response is depicted in Fig. 6 in the frequency domain. It can be observed that only the harmonic related to rotational speed has significant amplitude on the signal. To perform force identification, 2,401 terms were used to expand the orthogonal Fourier basis. The identified modal forces are presented in Fig. 7. A good agreement between the identified modal force and the one used to simulate the system is observed.

Table 1: Asymmetric bearing stiffness coefficients

	Stiffness x-direction, [N/m]	Stiffness y-direction, [N/m]	Stiffness z-direction, [N/m]
Radial bearing # 1	9.646e8	-	9.746e8
Radial bearing # 2	1.390e9	-	1.490e9
Radial bearing # 3	6.194e7	-	6.294e7
Thrust Bearing	-	1.515e9	-

Figure 5: Comparison of the system response considering the identified modal forces with the real modal forces introduced in the simulated model (time domain).
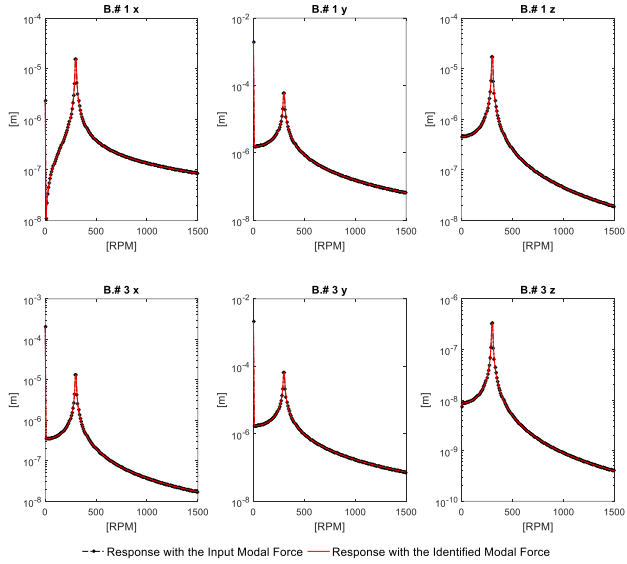
Figure 6: Comparison of the system response considering the identified modal forces with the real modal forces introduced in the simulated model (frequency domain).
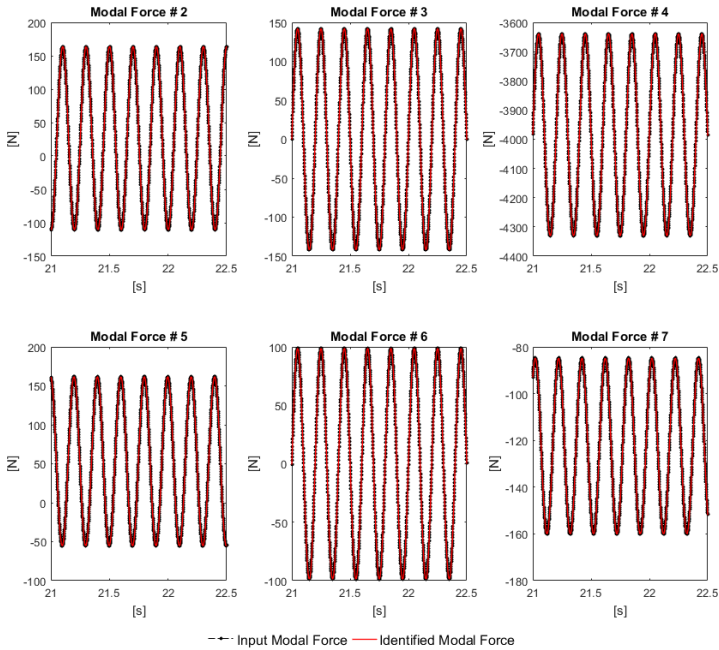
Figure 7: Identified modal forces with the real modal forces introduced in the simulated model (time domain).

173

Here, it was considered a non-linear force acting at the generator due to the contact between the rotor and the stator. The force parameters used were presented above. The overall nominal system parameters are the same as presented in the first case studied. The system responses and the system responses simulated with the identified modal forces are depicted in Fig. 8 (time domain) and in Fig. 9 (frequency domain). The same number of terms were considered in the expansion, as presented in the first case study. Figure 10 presents the identified modal forces. As it can be observed, the modal forces are satisfactorily identified. As higher harmonics were introduced in the system, the modal base used to simulate this case study is not enough, since higher mode shapes have to be included so that the dynamic behavior of the rotating system is well represented.
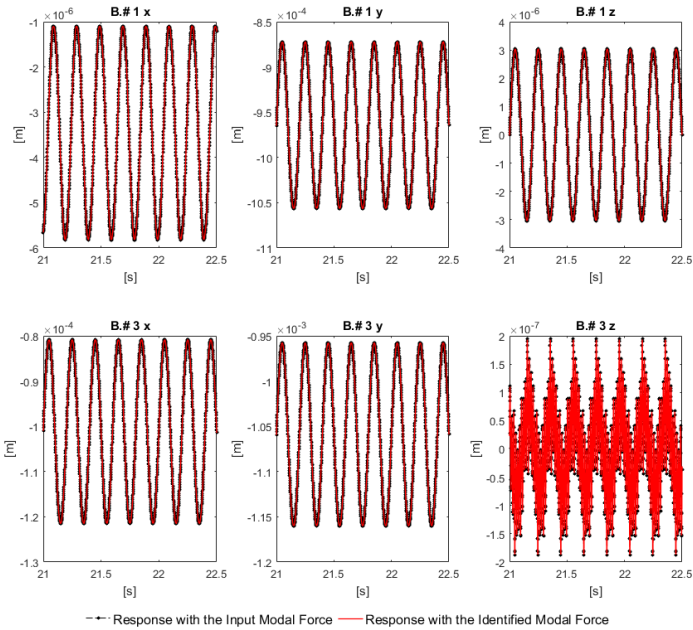
Figure 8: Comparison of the system response considering the identified modal forces with the real modal forces introduced in the simulated model (time domain).

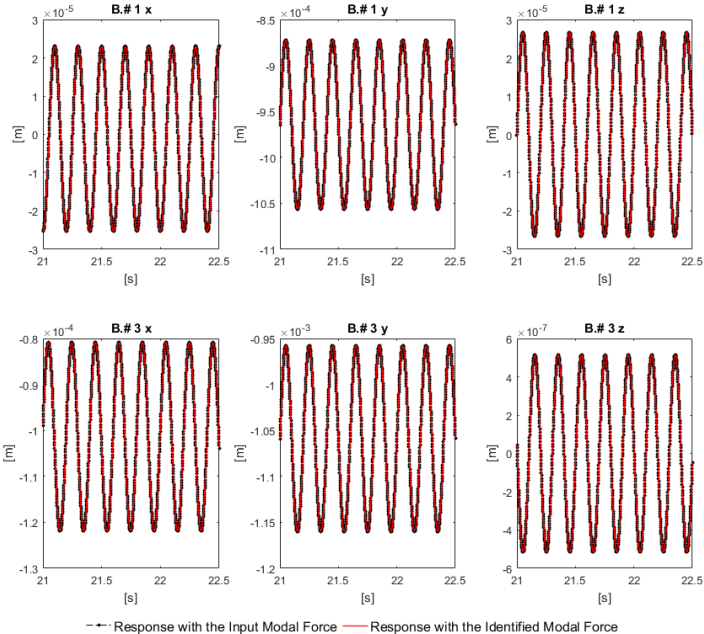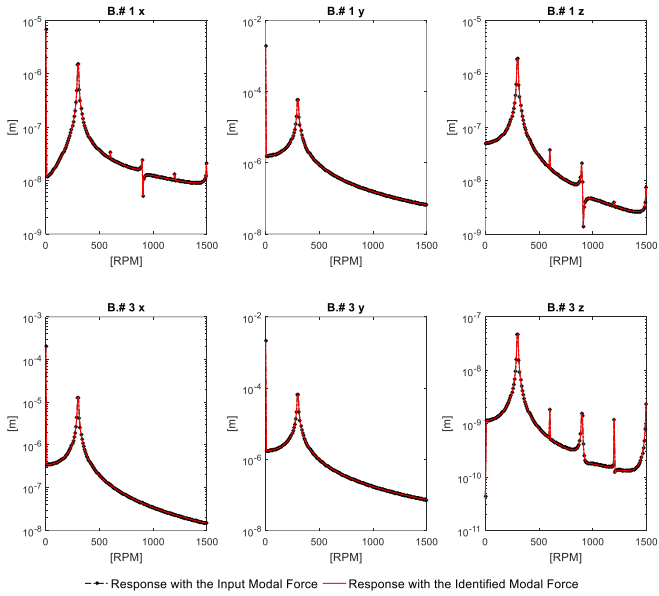**Figure 9: Comparison of the system response considering the identified modal forces with the real modal forces introduced in the simulated model (frequency domain).**
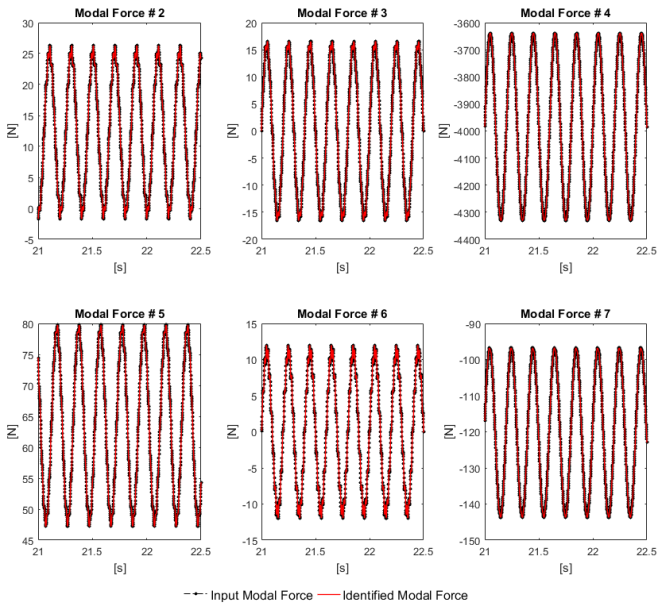
Figure 10: Identified modal forces with the real modal forces introduced in the simulated model (time domain).

175

CONCLUSION

A simulated industrial application of a force identification procedure based on orthogonal functions was presented in this chapter. Here, a modal base decomposition of measured responses of the rotating system is executed aiming to reduce the number of sensors used on the identification procedure. A rubbing contact force acting at the generator was introduced to evaluate the fault identification. The results showed a good agreement between the identified modal forces and the ones used on the simulations. The identified modal forces can be introduced at the finite element model in order to evaluate the stresses the system is subjected to under operational condition. Therefore, the remaining expected life in service, considering a fatigue analysis can be performed. Further work will be dedicated to the experimental validation of the conveyed methodology.

ACKNOWLEDGMENTS

REFERENCES

Dörfler, P.; Sick, M.; Coutu, A.. Flow-Induced Pulsation and Vibration in Hydroelectric Machinery: Engineer's Guidebook for Planning, Designand Troubleshooting, Springer-Verlag, London, 2013.

Lalanne, M., Ferraris, G., "Rotordynamics Prediction in Engineering", 1997, John Wiley & Sons, 2nd edition.

Melo, G.P., Steffen Jr., V., "Mechanical Systems Identification Through Fourier Series Time-Domain Technique", Journal of The Brazilian Society of Mechanical Sciences, 1993, vol. 15, n°. 2, pp. 124-135.

Morais, T.S.; Leao, L. S. ; Cavalini Jr., A. A. ; Steffen Jr, V. . Rotating Machinery Health Evaluation by Modal Force Identification. In: Icedyn - International Conference on Structural Engineering Dynamics, 2017, Ericeira. International Conference on Structural Engineering Dynamics, 2017.

Morais, T.S., Steffen Jr, V., Bachschmid, N. "Time-Varying Parameter Identification Using Orthogonal Functions". Journal of Physics: Conference Series, 2008, 135(1):12072.

Pacheco, R.P., Steffen Jr., V., "On the Identification of Non-Linear Mechanical Systems Using Orthogonal Functions", International Journal of Non-Linear Mechanics", 2004, n°. 39, pp. 1147-1159.

Pacheco, R.P., Steffen Jr., V., "Using Orthogonal Functions for Identification and Sensitivity Analysis of Mechanical Systems". Journal of Vibration and Control, 2002, 8, 993-1021.

Pacheco, R.P., Steffen Jr., V., "Using Orthogonal Functions for Identification and Sensitivity Analysis of Mechanical Systems". Journal of Vibration and Control, 2002, 8, 993-1021.

Paraskevopoulos, P.N., Sparis, P.D.; Mouroutsos, S.G. "The Fourier Series Operational Matrix of Integration". International Journal of Systems Science, Hants, 1984, v. 16, n. 2, p. 171-176.

Steffen, Jr, V., Rade, D.A., "An Identification Method of Multi-Degree-Of-Freedom System Based on Fourier Series". The International Journal of Analytical and Experimental Modal Analysis, 1991, p.271-278.

Spiegel, M.R., "Análise de Fourier, Mcgraw-Hill", 1976, São Paulo

Toshio, Y., Ishida, T.. Linear and Nonlinear Rotordynamics: A Modern Treatment with Applications. New York: Wiley, 2001.

Wan, S.; He, Y.. Investigation on Stator and Rotor Vibration Characteristics of Turbo-Generator under Air Gap Eccentricity Fault, Transactions of the Canadian Society for Mechanical Engineering, 2011.

Evaluation to the Structural Health Monitoring, based on Electromechanical Impedance Signals, applied in Concrete Structures*

Raquel Naiara Fernandes Silva
raquelfernandes@ufu.br

Abstract: The malfunction of a structure can lead to considerable economic loss as well as a great inconvenience in the lives of the population that uses it. In this sense, studies and experiments should be conducted in order to provide resources for reliable evaluation regarding their status, thus establishing criteria to ensure their use within safety standards. In recent years, researchers have focused on the economic aspects and structural safety. In this sense, Structural Health Monitoring techniques (SHM - Structural Health Monitoring) have been widely studied to increase safety and reduce maintenance costs. Therefore, we studied the SHM technique based on impedance E/M applied in concrete structures, from bonded and embedded sensors in them.

Keywords: Smart structures, Structural Health Monitoring, Concrete structure.

INTRODUCTION

In civil engineering, concrete structures are susceptible to several types of damage that may appear since the manufacturing process phase. In the early stage, for example, during concrete cure, cracks could be initiated due to high mechanical stresses induced by the hydration process (Naaman and Reinhardt, 1995). It is worth mentioning that the durability of this type of structures are related to mechanical, physical, and chemical deterioration, namely: corrosion of reinforcing fibers, concrete carbonation, and large temperature differences (Gilber and Ranzi, 2011).

Thus, researchers have developed structural health monitoring techniques to detect damages in early stages. There are many publications about SHM techniques for concrete structures based on

---

vibration (Dilena *et al.*, 2011), optic fiber (Villalba and Casas, 2013), and electromechanical impedance (Park *et al.*, 2006; Chalioris *et al.*, 2016). The method based on vibration uses low excitation frequencies (global techniques) and, consequently, it is not possible to detect damages in early stages (Banks *et al.*, 1996). The second technique applied presents some disadvantages, as the concrete is brittle and heterogeneous (several sizes of aggregates). At low level of load the structures cracks, which can result in a break and debonding of the optical fiber (Villalba *et al.*, 2013). The ISHM evaluated in this work shows promise results (Park *et al.*, 2006), since it is simple and easy to implement. However, this methodology has some disadvantages, such as influence of the temperature (Banks *et al.*, 1996).

The electromechanical impedance method for structural health monitoring (ISHM) purposes is basic on the verification of changes in the mechanical impedance of the monitored structure, comparing the scenarios with and without damage. The measurement of the mechanical impedance is performed indirectly, through the electrical impedance by using piezoelectric transducers coupled to the host structure or incorporated into it. The measurements are performed for the pristine condition of the structure (baseline) and during its useful lifetime. Considering that the coupling properties between the PZT patch and the structure are kept constant, the presence of damage can be verified by observing changes on the electrical impedance signatures. This change can be quantified by the so-called damage metrics (Liang *et al.*, 1994).

One of the first published reports on this subject for civil structures showed that the electromechanical impedance method was successful applied for crack detection in the context of loading and unloading of a prototype formed by a part of a bridge. This structure was made with reinforced concrete (Soh *et al.*, 2000). Other studies have also obtained promising results, for example, in detecting damage in concrete plates where the damage was produced from a cutting blade (Na and Lee, 2012). In another study, the influence of the concrete cure on the impedance signals was considered (Quin *et al.*, 2011). For this aim, a piezoelectric transducer was introduced in a concrete plate during its manufacturing. It was found that the impedance signals change as the samples were subjected to compression. However, the authors did not conduct more detailed studies in the presence of incipient damages

during the tests. A study about the influence on the impedance signals of the detachment of the piezoelectric transducers was performed by Tawie and Lee (2010). In this case, the sensors were bonded to the steel fibers used to reinforce concrete structures. In another study, the technique was used to detect carbonation in this type of structures (Talakokulaa *et. al,* 2016). The influence of temperature and loading on the impedance signals measured by a piezoelectric sensor coated with a protection capsule of cement and epoxy was also investigated (Dongyu *et al.*, 2015). In recent years, the SHM are being used to detect incipient damages with the objective of promoting timely maintenance and extending the operational life of the structures (Silva, 2017).

Therefore, this research has as main objective to study the structural integrity monitoring, based on the electromechanical impedance technique, with a view to its application in concrete structures, considering some parameters that may influence the diagnosis of the damage, such as temperature and type of electromechanical coupling. In addition, it is also proposed to know and compensate for these parameters through the mathematical treatment of impedance signatures. For this, the electromechanical impedance technique was applied to concrete test bodies in order to properly understand the monitoring process, in addition to refining the methodology.

ELETROMECHANICAL IMPEDANCE METHOD – A REVIEW

The ISHM method was first presented in 1994 (Liang *et al.*, 1994). The method uses piezoelectric transducers coupled to the structure to monitor changes in its stiffness, damping, and mass. Due to the difficulty of obtaining the mechanical impedance of the structure, the electrical impedance measurements are obtained by using piezoelectric transducers coupled on or into the host structure. If the properties of the PZT patch (Lead Zirconate Titanate) do not vary over time, changes in the electrical impedance will be directly related to changes in the mechanical impedance, which is affected by the presence of damage (Park *et al.*, 2005). A well-known single-degree-of-freedom (DOF) electromechanical model that describes the measurement process is showed in Fig. 1.
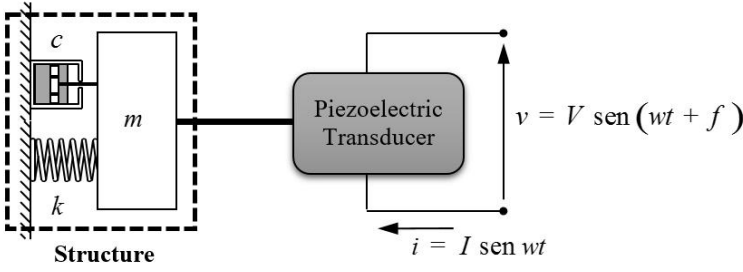
Figure 1: DOF Electromechanical Model of the ISHM method (Liang *et al.*, 1994).

Based on the system showed in Fig. 1, the admittance Y_a (ω) of the piezoelectric transducer is the combined function between the mechanical impedance of the PZT actuator Z_{ma} (ω) and the structure Z_{me} (ω), according to Eq. (1). The impedance is a frequency dependent complex function.

$$Y_a(\omega) = I(\omega)\omega a \left\{ \varepsilon_{33}^T [1 - I(\omega)\delta] - \frac{Z_{ma}(\omega)}{Z_{ma}(\omega) - Z_{me}(\omega)} d_{3x}^2 \hat{Y}_{xx}^E \right\} \qquad (1)$$

where $\hat{Y}^E_{xx}$ is the complex Young's modulus of the PZT patch with zero electric field, d_{3x} is the piezoelectric coupling constant in the arbitrary x direction at zero electric field, ε^T_{33} is the dielectric constant at zero stress, δ is the dielectric loss tangent to the piezoelectric transducer, a is a geometric constant of the PZT patch, and is ω the frequency. To obtain the electrical impedance, both the direct and inverse effects of the piezoelectric transducer are used. The direct effect (or sensor effect) is characterized by producing a voltage when the piezoelectric transducer is mechanically deformed in the elastic phase, and the inverse effect (or actuator effect) appears when a piezoelectric ceramic patch is subjected to a voltage, resulting a mechanical deformation (Farrar *et al.*, 2005).

The detection and evaluation of the structure integrity is based on the comparison between the impedance signatures acquired in the healthy and damaged (or unknown condition) structure. A visual examination is not enough, since it gives only a qualitative comparison. Consequently, it is necessary the use of a quantitative criterion. Thus, damage metrics are employed, i.e., scalar parameters are properly defined so that they

can numerically represent the difference between the two signals (without and with damage) (Naidu and Soh, 2004).

For the ISHM approach, various damage metrics can be used to evaluate the integrity of the structure (Palomino *et al.*, 2011). As an example, one of the most commonly used metrics is the RMSD (Root Mean Square Deviation) whose definition is given by Eq. (2).

$$RMSD = \left\{ \sum_{i=1}^{n} \frac{[Re(Z_{1i}) - Re(Z_{2i})]^2}{Re(Z_{1i})^2} \right\}^{1/2} \tag{2}$$

where $Re(Z_{1i})$ is the real part of the impedance measure without damage (baseline) at the frequency i. $Re(Z_{2i})$ is the real part of the impedance measurement at the frequency i for a new structural configuration and n is the total number of points used in the measurements.

STATISTICAL THRESHOLD DETERMINATION

The concepts behind Statistical Process Control allow to establish limits in a control chart so that a threshold can be established using the upper control limit. These limits can be defined so that either 95.45 % or 99.73 % of data from a normally distributed population remains, if these control limits are defined as expressed in Eq. (3).

$$\bar{x} \pm 2s \; for \; 95.45\% \; confidence$$

$$\bar{x} \pm 3s \; for \; 99.73\% \; confidence \tag{3}$$

where $\bar{x}$ is the sample mean and s is the sample standard deviation (Park *et al.*, 2000).

In SHM, the upper control limit is interest for the threshold determination. Although the expressions given by Eq. (8) can provide the threshold calculation, it should be noted that the sample mean and sample standard deviation are inferences from the population parameters (i.e., unknown values). Therefore, a more robust methodology is proposed by using the upper limits of the confidence intervals for the population mean and standard deviation according to Eq. (4) and Eq. (5), respectively (Finzi Neto *et al.*, 2011).

$$\left[\bar{x} - \frac{st_{v;\alpha/2}}{\sqrt{N}} \leq \mu_x \leq \bar{x} + \frac{st_{v;\alpha/2}}{\sqrt{N}}\right] v$$
$$= N - 1 \tag{4}$$

$$\left[\frac{vs^2}{\chi^2_{v;\alpha/2}} \leq \sigma_x^2 < \frac{vs^2}{\chi^2_{v;1-\alpha/2}}\right] v = N - 1 \tag{5}$$

where μ_x and σ^2_x are the population mean and variance, respectively, $\bar{x}$ and s^2 are the sample mean and variance, respectively, $t_{v;\alpha/2}$ has a Student t distribution with v DOF, α is the significance level and $x^2_{v;\alpha/2}$ follows a Chi-Square distribution.

Hence, the upper limit of the confidence intervals was used and the threshold for each PZT transducer was determined through Eq. (6).

$$PZT_{threshold} = \mu x_{max} \tag{6}$$

where μx_{max} is the upper limit for the population mean and σx_{max} is the upper limit for the population standard deviation, both obtained by choosing 5 % for the significance level α.

EXPERIMENTAL APPLICATIONS

In this work, the tested concrete specimens were made of fiber reinforced concrete, which is widely used in civil engineering constructions. This composite material is made with Portland cement concrete (cement paste, aggregates and water) and steel fibers. Due to the proportions of each material used and additives, the properties of this composite exhibit a great variation. The steel fibers were distributed throughout the volume of the material, thus generating more rigid and resistant composite.

Two concrete samples were used in the tests (prismatic forms). In the first case, two piezoelectric sensors were bonded to the studied structure surface and in the second case, two smart capsules were embedded to the concrete, giving rise to said intelligent structures.

In both cases, a prismatic concrete specimen with steel reinforcement fibers was prepared, with the dimensions 150 x 150 mm^2 in the transversal section and length of 500 mm, a compressive strength of 40 MPa (f_{ck}) was obtained after 28 days of the sample hydration process. After molding, densification and finishing, the prismatic bodies were placed into a humid chamber for 48 hours. The entire molding and curing procedure adopted is standardized by ABNT NBR 5738: 2015.

Concrete Structures Monitoring with Sensors bonded to the surface

For this procedure, two sensors named PZT1 and PZT2, were bonded to the surface of the specimen (Fig. 2).
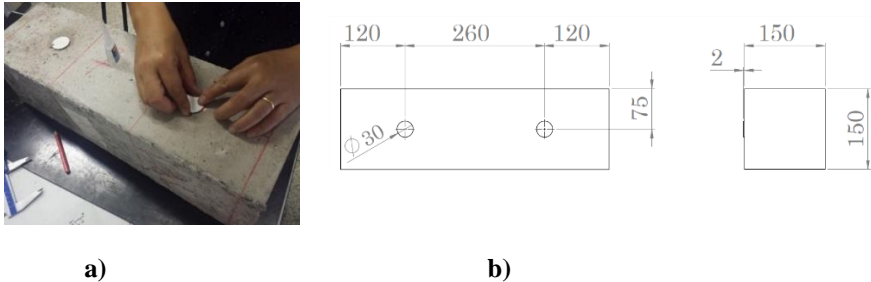
a)   b)
Figure 2: Prismatic specimen: (a) Concrete specimen with PZT1 and PZT2 bonded; (b) Schematic showing the positions of the sensors.

To produce the damage in the structure, a flexural toughness test was performed after 47 days of curing for the sample. This test was based in the method C1609 (2012). The electromechanical servo hydraulic MTS machine with 100 kN capacity to compression was used. The specimen was properly labeled in order to facilitate the alignment and positioning in the testing machine. It also facilitates the installation of the yoke device (Fig. 3(a)). Figure 3(b) shows the load application on the flexural toughness test.
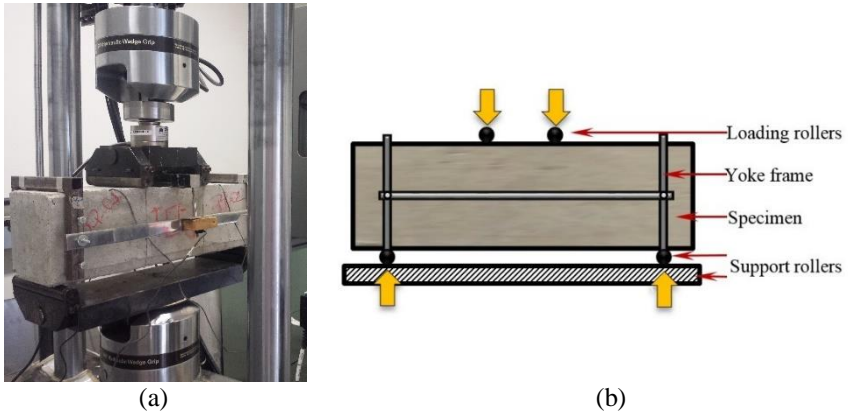
Figure 3: (a) Specimen on the testing machine; (b) Schematic representation of the test as based on the ASTM method C1609 (2012).

The measurements of the electrical impedance were made before and after the damage generation. The equipment used is the impedance analyzer Agilent 4294A (Fig. 4 (a)). Two frequency bands were used: 10kHz to 30kHz and 80kHz to 120kHz, with 401 points. These frequency ranges have been selected from the method of trial and error. Using the methodology above, cracks have been created in the center of the specimen as showed in the Fig. 4 (b).
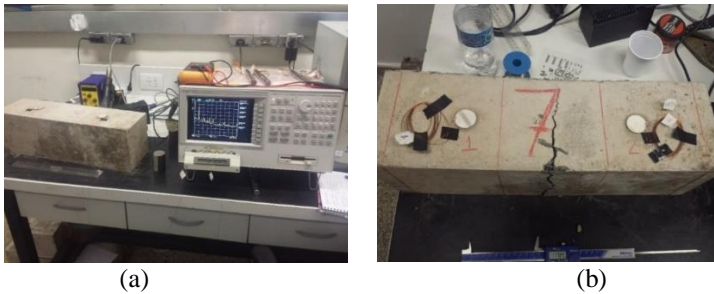
Figure 4: (a) Test instrumentation; (b) Specimen damaged.

Analyzing the results obtained from the PZT #1 for the first frequency band (10-30) kHz, it was observed that the real part of the impedance signal measured after the damage changed significantly as compared with the baseline (Fig. 5(a)). In order to quantify these changes, the impedance signals were numerically treated by using Eq. 2. Various damage metrics were used to perform a quantitative analysis; however, in the present work we present only one of them, since the results from the other damage metrics lead to similar results. Figure 5(b)

shows the RMSD damage metric obtained. The six first states refer to the baseline signal versus baseline comparison and the other seven states refer to the baseline versus the damaged signal (cracked specimen).

(a)   (b)
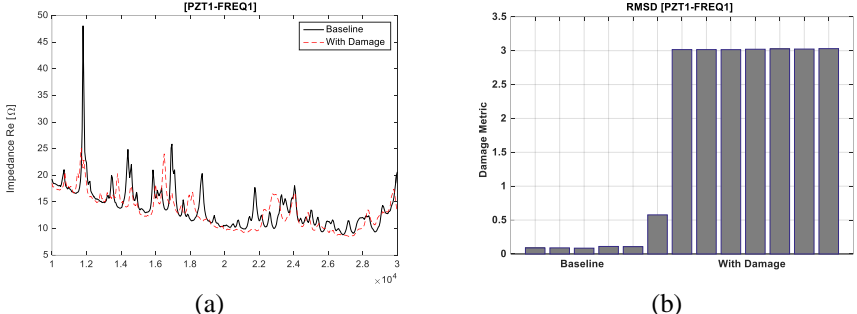
Figure 5: PZT #1 ([10-30] kHz): (a) Impedance Re signal; (b) Damage Metric -RMSD.

The baseline versus baseline responses have small influence on the damage metric values since external noise and temperature effect are negligible. As can be seen on the results from the PZT #1, the frequency bands present the same behavior. Therefore, it can be concluded that the impedance method is capable of detecting damage in the structure. A similar behavior is found for the PZT #2 signal for the same frequency range (Fig. 6 (a) and Fig. 6 (b)).

(a)   (b)
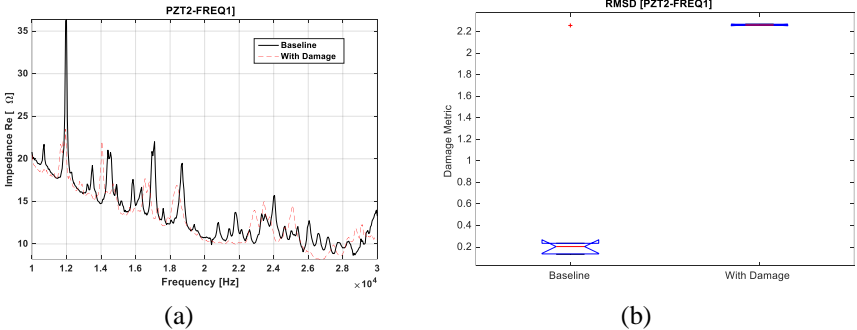
Figure 6: PZT #2 ([10-30] kHz): (a) Impedance Re signal; (b) Boxplot – RMSD.

For the two piezoelectric transducers, the second band frequency, [80-120] kHz, the signals are capable of detecting the cracks; however, the results show that this frequency band is less sensitive to detect

damage (Fig. 7). It is important to notice that higher frequencies are less sensitive to external noise.

(a)   (b)
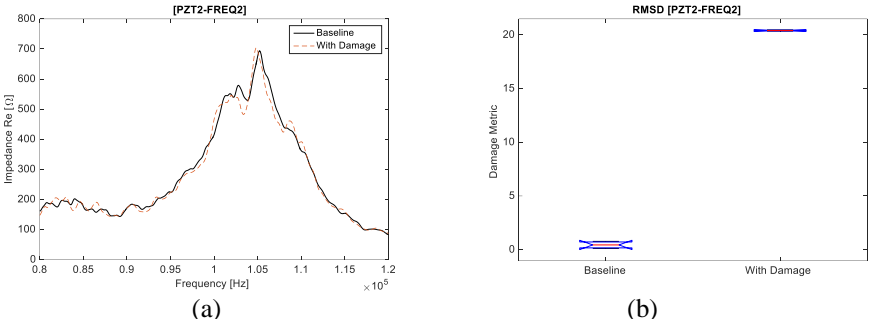
Figure 7: PZT #2 ([80-120] kHz): (a) Impedance Re signal; (b) Boxplot – RMSD.

The results presented allowed us to conclude that the electromechanical impedance method is a real alternative to detect damages in concrete structures with sensors bonded to the surface.

Monitoring of Smart Concrete Structures

Next, the smart capsule was tested for ISHM purposes using a concrete specimen (500 x 150 x 150 mm), as shown in Fig. 8 (a). Two smart capsules were embedded in the concrete specimen. The approximate positions of the capsules are depicted in Fig. 8 (b).

(a)   (b)
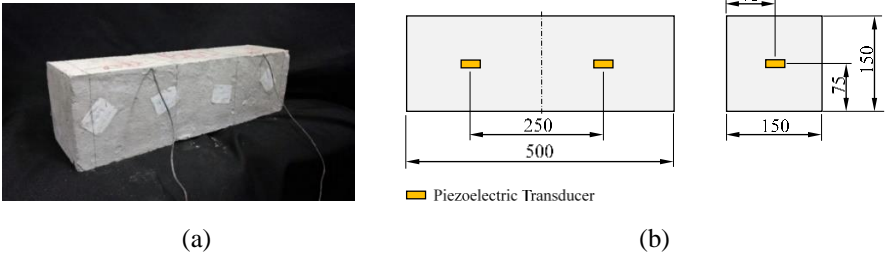
Figure 8: Prismatic specimen: (a) Concrete specimen with smart capsule embedded; (b) Schematic showing the positions of the smart capsules (mm).

The monitoring of structural integrity was performed by applying the ISHM technique before and after the generation of damage in the prismatic specimen. The influence of temperature was included at this

stage applied the optimization technique, which can be consulted in Silva (2017).

For the evaluation of the temperature effect, the specimen was properly positioned inside the thermal chamber, as previously described. In this case, 2,000 frequency points resolution were acquired using the SySHM impedance meter in the frequency band of 30 kHz to 80 kHz. For each condition, the impedance signatures were acquired 30 times. The tests were performed for the environmental temperature at 25°C. The damage was introduced in the prismatic concrete specimen through a flexural toughness test as based on the ASTM method C1609. An MTS Hydraulic Servo Bending Machine was used to apply the required effort, for which the yoke device was used (Fig. 9).

(a)   (b)

Figure 9: (a) Prismatic specimen inside the climatic chamber and damage; (b) Crack charactering the damage.

The impedance signatures obtained from PZT#1 (see Figs. 10(a) and 10 (b) for both the healthy and damaged prismatic specimen are presented in these figures, for which the responses measured at 25°C is show. Note that the real part of the impedance signal measured for the damaged condition changed significantly as compared with the baselines (pristine conditions for the temperature considered). To quantify these changes in the impedance signatures, a damage metric RMSD was used.
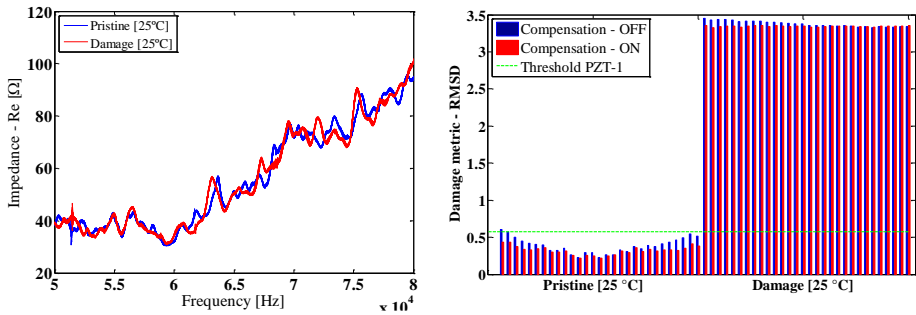
Figure 10: Prismatic Specimen with smart capsule (PZT#1/25°C): (a) Impedance signal; (b) Compensated damage metric RMSD and threshold value.

The first thirty measures refer to the baseline and the other thirty are associated with the damaged condition. Note that the damage was successfully identified. The threshold value was calculated, thus guaranteeing 99% confidence for the probability of detecting damage. A similar behavior was found by using the PZT#2. Once again, the temperature compensation was efficient, thus avoiding neither false positives nor false negatives during the monitoring diagnosis.

CONCLUSIONS

In the present contribution, two experimental procedures to evaluate the impedance based SHM technique and detect damage in concrete structure was performed. For this purpose, two prismatic samples of concrete reinforced with steel fibers were tested.

Initially a monitoring was carried out from piezoelectric sensors bonded to the studied surface. The measurements of the real part of the electromechanical impedance of the sample were collected before and after the damage was performed using an impedance analyzer. The results showed that the electromechanical impedance method is an interesting alternative to detect damages in concrete structures. The second application proposes a SHM technique dedicated to concrete structures using smart capsules embedded in the specimens to detect damages. The main advantage of this approach is related to the possibility of obtaining a clear indication of the presence of incipient damage in concrete structures through the smart capsule impedance responses. In this context, it was observed that the impedance signatures obtained from the smart capsules are sensitive to damage and

temperature variation. In addition, the temperature compensation method based on optimization was successful in compensating the influence of temperature on the signals, thus avoiding false diagnostics in the monitoring process.

The presented results permitted to conclude electromechanical impedance method is an interesting alternative for detecting damage in concrete structures, with sensor bonded or embedded in the structure studied. Temperature compensation is required to avoid false positives in the analyses. Further studies will be focused on real-world concrete structures.

AKNOWLEDMENTS

REFERENCES

American Concrete Institute. ASTM C1609. Standard Test Method for Flexural Performance of Fiber- Reinforce Concrete (Using Beam with Third-Point Loading). Pennsylvania, 9 p. 2012

Brazilian Association of Technical Standards. NBR 5738. Concrete: procedure of molding and curing of specimens. Rio de Janeiro, 2015. 6 p.

Banks, H.T., Inman, D.J., Leo, D.J. and Wang, Y. An experimentally validated damage detection theory in smart structures, Journal of Sound and Vibration, 191, 859–880, 1996.

Chalioris, C. E., Karayannis, C. G., Angeli, G. M., Papadopoulos, N. A., Favvata, M. J., Providakis, C. P. Applications of smart piezoelectric materials in a wireless admittance monitoring system (WiAMS) to structures -Tests in RC elements. Case Studies in Construction Materials, v. 5, p. 1-18, 2016.

Dilena, M., Morassi, A., Perin, M., Dynamic identification of a reinforced concrete damaged bridge, Mechanical Systems and Signal Processing, 25, 2990–3009, 2011.

Dongyu X., Sourav B., Yanbing W., Shifeng H., Xin C., Temperature and loading effects of embedded smart piezoelectric sensor for health monitoring of concrete structures, Construction and Building Materials, 76, 187-193,2015.

Farrar, C. R., Lieven, N. A. J., Bemend, M. T., An introduction to damage prognosis. In: AUTOR. Damage Prognosis for aerospace, civil and mechanical systems. Bristol: John Wiley & Sons, pp. 1-12. 2005.

Finzi Neto, R. M.; Steffen Jr.V.; Rade, D. A.; Gallo, C. A.; Palomino, L. V., A low-cost electromechanical impedance-based SHM architecture for multiplexed piezoceramic actuators. Journal of Structural Health Monitoring. v. 10, n. 4, p. 391-402, 2011.

Gilbert, R. I.; Ranzi, G., 2011, Time Dependent Behavior of Concrete Structures, 1ed. USA e Canada, Spon Press, 2011.

Liang, C., Sun, F. P., Rogers. C. A., coupled electro-mechanical analysis of adaptive material systems-determination of the actuator power consumption and system energy transfer. Journal Intelligent Material Systems and Structures (1994) 12-20.

Na S., Lee H. K. A technique for improving the damage detection ability of the electro-mechanical impedance method on concrete structures. Smart Materials and Structures, 21, n. 8, p. 085024, 2012.

Naidu, A. S. K, Soh C. K., Damage severity and propagation characterization with admittance signatures of piezo transducers. Journal Smart Materials and Structures, 13, 393-403, 2004.

Palomino, L. V., Moura Jr., J. R.V., Tsuruta, K. M., Rade, D. A., Seffen Jr., V., Impedance-based health monitoring and mechanical testing of structures. Smart Structures and Systems, V. 7, No.1, pp. 15-25, 2011.

Peairs D. M., High Frequency Modeling and Experimental Analysis for Implementation of Impedance-based Structural Health Monitoring. 2006. 150 f. Thesis – Virginia Polytechnic Institute and State University, Virginia.

Quinn, W.; Kelly, G.; Barrett, J. Development of an embedded wireless sensing system for the monitoring of concrete. Journal Structural Health Monitoring, p. 381-392, 2011.

Park, S., Ahmad, S., Yun, C. B., Roh, Y. Multiple crack detection of concrete structures using impedance-based structural health

monitoring techniques. Experimental Mechanics, v. 46, n. 5, p. 609-618, 2006.

Soh C. K., Tseng K. k-H., Bhalla S., Gupta A., Performance of smart piezoceramic patches in heath monitoring of a RC bridge. Smart Material Structures, 9, 533-542, 2000.

Park, G., Cudney, H., Inman, D. J, Impedance-based health monitoring of civil structural components. ASCE Journal of Infrastructure Systems, 6, 153-160. 2000.

Park, G., Inman, D. J., Damage, D. J., Prognosis for Aerospace, Civil and Mechanical System. Chapter 13 "Impedance-Based Structural Health Monitoring". Inman, C. R. Farrar, V. Lopes Jr, V. Steffen Jr (Eds). John Wiley & Sons, ISBN: 978-0-470-86907-9. 2005.

Silva, R. N. F. Electromechanical Impedance Based Structural Health Monitoring Technique Applied on Concrete Structures. 146 f. 2017. PhD Thesis, Federal University of Uberlândia, Uberlândia.

Talakokulaa V., Bhallab S., Ballc R. J., Bowend C.R, Pescec G.L., Kurchaniae R., Bhattacharjeeb B., Guptab A., Paine K., Diagnosis of carbonation induced corrosion initiation and progressionin reinforced concrete structures using piezo-impedance transducers. Sensors and Actuators A; 242, 79-91,2016.

Tawie R., Lee H. K., Piezoelectric-based non-destructive monitoring of hydration of reinforced concrete as an indicator of bond development at the steel–concrete interface. Cement and Concrete Research, 40, 1697-1703, 2010.

Villalba, S., Casas, J. R., Application of optical fiber distributed sensing to health monitoring of concrete structures, Mechanical Systems and Signal Processing, 39, 441–451, 2013.

Introduction to synthetic inductors circuits and its application in multimodal vibration attenuators[*]

Bruno Gabriel Gustavo Leonardo Zambolini Vicente
brunozv@ufu.br

Abstract: The synthetic inductors are the basis electronics to composing circuits for electromechanically energy extraction when using piezoelectric patches. In this chapter, basics formulations deductions are exposed and an experimental evaluation of a multimodal vibration attenuator indicates some relevant issues.

Keywords: synthetic inductors circuits, multimodal vibration attenuator, piezoelectric materials.

INTRODUCTION

The use of the electromechanical coupling in the technique of vibration attenuation consists essentially in the extraction of the reactive energy of capacitive nature of piezoelectric transducers. From the point of view of electric circuits, the elementary pathway consists of coupling inductors to the terminals of the piezoelectric, providing absorption of the capacitive reactive by the inductor (Belincourt, 1981). However, as shown in Zambolini-Vicente (2014), at low frequencies, the values of inductances that must be coupled to the piezoelectric elements reach values above the milli-Henrys (mH), making it impossible to use discrete inductors, which are built through coils, in which the total number of turns is directly proportional to the value in *henries* of the desired inductive parameter, directly impacting the mass and volume of the component (Sedra and Smith, 2009). The solution, in this case, is the use of synthetic inductors, which are electronics that can emulate large inductance values (Horowitz and Hill, 2017). In this way, we present in this chapter the complete theoretical deduction of three types of circuits for synthetic inductors and, in sequence, the application of these circuits

---

[*] doi - 10.29388/978-85-53111-97-8-0-f.195-208

in devices of multimodal attenuation based on current flowing technique of Behrens (2003).

LARGE INDUCTOR CIRCUITS: SYNTHETIC INDUCTORS PRINCIPLES

The piezoelectric material presents behavior that identifies it as a capacitive material (Holterman & Graen, 2013), generating capacitive reactive, given by $X_C = 1/sC$, where C is the capacitive parameter of the piezo, which must be balanced by an inductive reactive $X_L = sL$, imposing on the value of the inductive parameter, L, quadratic dependence inversely proportional to the complex frequency, s, according to the following equation:

$$X_L = X_C \rightarrow sL = \frac{1}{sC} \quad \rightarrow L = \frac{1}{s^2 C} \tag{1}$$

In order to establish a reference on the attenuation capacity of passive shunts using synthetic inductors, a comparison was made based on the experimental tests of the circuit-based inductors gyrators of Tellegen (TELLEGEN, 1948), Riordan circuit (1967) and the circuit of Antoniou (1969). These circuits were chosen because they demand a smaller number of electronic components, together with the fact that they are some of the configurations of greater prominence in the related literature.

Synthetic inductor *gyrator* of Tellegen

Since the advent and advances of transistor technology and the popularization of operational amplifier circuits (or op-amp), the Berndt & Dutta-Roy circuit (1969) presented in Fig. 1 makes use of only one op-amp and consists of a rather simplified option for the use in electronic circuits of a gyrator for the simulation of an inductor.
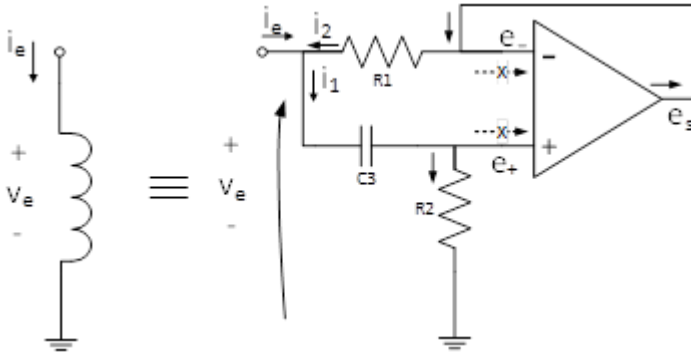
Figure 1: Berndt & Dutta-Roy (1969) implementation of gyrator for the synthetic inductor.

In order to elucidate the mapping of the circuit of Fig.1 in a synthetic inductor gyrator, the operational amplifier is considered as an ideal, that is, the currents entering the device via + and - terminals are considered null as well as the ratio of amplifier, $e_s = A(e_+ - e_-)$, has the gain parameter A with infinite value, i.e. the amplifier will maximize the value of the voltage difference of the inputs up to the limit of the circuit supply (Horowitz & Hill., 2017). It is important to highlight that the circuit has the objective of producing, between its terminals, voltage/current behavior (v_e e i_e) identical to that of an inductor, that is, a circuit with inductive reactance of $X_L = sL$, so that it is possible to tune it so as to eliminate the capacitive reactance of the piezoelectric material. Observing the circuit of Fig. 1 and remembering the concept of voltage resistive divider, we have for e_+:

$$e_+ = \left(\frac{R_2}{R_2 + X_{C_3}}\right) v_e \qquad (2)$$

$$e_- = e_s \rightarrow e_s = A(e_+ - e_s) \qquad (3)$$

Isolating e_s from Eq. (3) imposing the relation of e_+, it results the following expression:

$$e_s = \left(\frac{A}{1+A}\right)\left(\frac{R_2}{R_2 + X_{C_3}}\right) v_e \qquad (4)$$

197

Through the reorganization of A and imposing the condition of ideality of *amp-op* ($A \to \infty$), this leads to the following relationship:

$$e_s = \left(\frac{1}{1/A+1}\right)\left(\frac{R_2}{R_2+X_{c_3}}\right)v_e \xrightarrow{A \to \infty} e_s = \left(\frac{R_2}{R_2+X_{c_3}}\right)v_e \tag{5}$$

By analyzing the currents at the input node,

$$i_e = i_1 - i_2 \quad ou \quad i_e = \frac{v_e}{R_2+X_{c_3}} - \frac{e_s-v_e}{R_1} \tag{6}$$

and applying Eq. (5) to eliminate e_s and highlighting v_e,

$$i_e = v_e\left[\frac{1}{R_2+X_{c_3}} - \left(\frac{R_2}{R_2+X_{c_3}}\right)\frac{1}{R_1} + \frac{1}{R_1}\right] \tag{7}$$

one can isolate the ratio i_e/v_e as follows:

$$\frac{i_e}{v_e} = \frac{R_1+X_c}{(R_2+X_{c_3})R_1} = \frac{1}{R_2+X_{c_3}} + \frac{X_{c_3}}{(R_2+X_{c_3})R_1} \tag{8}$$

According to Berndt & Dutta-Roy (1969), the first term of the direct member of Eq. (8) tends to be much smaller than the second, since it has the capacitive reactance X_c in the numerator. By adopting this simplification, obtaining the impedance $Z_e = v_e/i_e$ and factoring the denominator and numerator by X_c, one obtains:

$$Z_e = \frac{v_e}{i_e} = \left(\frac{R_2}{X_{c_3}} + 1\right)R_1 = R_1 + \frac{R_1 R_2}{X_{c_3}} \tag{9}$$

knowing that $X_{c_3} = 1/sC_3$ and apllying Eq. (9),

$$Z_e = R_1 + sR_1R_2C_3 \tag{10}$$

Evaluating Eq. (10), it is clear that the circuit generates impedance with real part (the resistance R_1) and imaginary part with reactance of inductive nature, since it meets the profile $X_L=sL$, being, in this case, the parameter inductive bond given by $L=R_1R_2C_3$. Berndt & Dutta-Roy (1969) points out in his work the need to maintain the resistor R_2 at a fixed value, chosen in such a way to stabilize the voltage in the op-amp,

leaving the resistance R_1 to be used as a variable parameter for tuning. Although this does not directly affect the real part of the generated impedance, it does not influence the quality factor Q of the circuit, the relation between the real and the imaginary part, given by $Q=X/R$, which represents the energy in fact to the resistive part (Horowitz & Hill, 2017).

Riordan synthetic inductor

In the line of research of the gyrators for the synthetic inductive circuits, Riordan's work (1967) presents an alternative to the article by Sheahan & Orchad (1966) that makes use of op-amps, as shown in Fig. 2, providing less need of compensation or branch balancing in relation to the gyrator configurations that employ current dependent sources. In this case, at least for low frequencies, the achievable quality factor Q is limited mainly to losses in the capacitor used in the circuit. However, the main aspect of the circuit in question is its ability to provide, in theory, purely reactive impedance, without the resistive term, i.e. $Z_e=sL$ which means great advantage in terms of the Q factor.
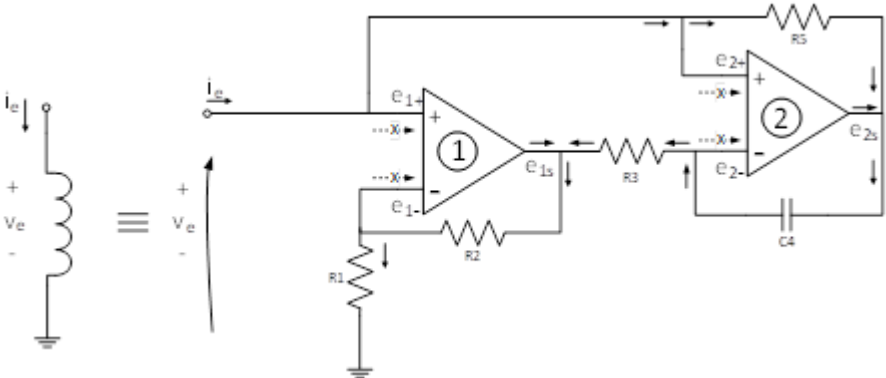
Figure 2: Riordan (1967) synthetic inductor circuit.

As is the case for the gyrator circuit, the inductance provided by the Riordan (1967) arrangement (Fig. 2) is deduced from its voltage/current ratio (impedance $Z_e=v_e/i_e$). Thus, it is most determined v_e e i_e, starting with the *op-amp1*, which leads to e_{1+} e e_{1-}:

$$e_{1+} = v_e \quad \text{and} \quad e_{1-} = \left(\frac{R_1}{R_1+R_2}\right)e_{1s} \tag{11}$$

Being $e_{1s}=A_1(e_{1+} - e_{1-})$, where A_1 is the *op-amp1* gain, applying Eq. (11) it achieves the Eq. (12):

$$e_{1s} = A_1\left(v_e - \left(\frac{R_1}{R_1+R_2}\right)e_{1s}\right) \tag{12}$$

Isolating e_{1s} da Eq. (12), factoring by A_1 and imposing $A_1 \to \infty$:

$$e_{1s}\left(1/A_1 + \left(\frac{R_1}{R_1+R_2}\right)\right) = v_e \xrightarrow{A \to \infty} e_{1s} = \left(\frac{R_1+R_2}{R_1}\right)v_e \tag{13}$$

In the negative input node of op-amp2, with the electric tension e_{2-}, the current through the capacitor C_4 will be the same as that R_3, since, assuming the ideal op-amp 2, there will be no current at its input terminals. Equationing the currents in this node, we have the following expression:

$$\frac{e_{2s}-e_{2-}}{X_{C_4}} = \frac{e_{2-}-e_{1s}}{R_3} \tag{14}$$

$$e_{2-} = \frac{X_{C_4}e_{1s}+R_3 e_{2s}}{R_3+X_{C_4}} = \left(\frac{X_{C_4}}{R_3+X_{C_4}}\right)e_{1s} + \left(\frac{R_3}{R_3+X_{C_4}}\right)e_{2s} \tag{15}$$

With A_2 as the op-amp2 gain, when applying its amplification equation, $e_{2s}=A_2(e_{2+} - e_{2-})$ in Eq. (3.15), such that $e_{2+}=v_e$, results:

$$e_{2s} = A_2\left(v_e - \left(\frac{X_{C_4}}{R_3+X_{C_4}}\right)e_{1s} + \left(\frac{R_3}{R_3+X_{C_4}}\right)e_{2s}\right) \tag{16}$$

Applying Eq. (3.13) in e_{1s}, isolating e_{2s} in the previous equation and imposing the condition that $A_2 \to \infty$ reaches,

$$e_{2s}\left(\frac{1}{A_2} - \left(\frac{R_3}{R_3+X_{C_4}}\right)\right) = \left(v_e - \left(\frac{X_{C_4}}{R_3+X_{C_4}}\right)\left(\frac{R_1+R_2}{R_1}\right)v_e\right) \tag{17a}$$

$$\rightarrow e_{2s}\left(\frac{R_3}{R_3+X_{C_4}}\right) = v_e\left(1 - \left(\frac{X_{C_4}}{R_3+X_{C_4}}\right)\left(\frac{R_1+R_2}{R_1}\right)\right) \qquad (17b)$$

resulting,

$$e_{2s} = v_e\left(\frac{R_1R_3-X_{C_4}R_2}{R_1R_3}\right) \qquad (18)$$

As in the negative input node of the op-amp 2, also at the positive input, with voltage e_{2+}, there will be no electric current. Equationing the currents in this node, we can establish the following direct relation between i_e e v_e, through the application of Eq. (18):

$$i_e = \frac{v_e - e_{2s}}{R_5} \rightarrow i_e = \frac{v_e}{R_5}\left(1 - \frac{R_1R_3 - X_{C_4}R_2}{R_1R_3}\right) \qquad (19)$$

From previous equation, isolating the relation $Z_e = v_e/i_e$,

$$Z_e = \frac{v_e}{i_e} = \frac{R_1R_3R_5}{R_2X_{C_4}} \qquad (20)$$

and, with $X_{c4}=1/sC_4$, applying in Eq. (20):

$$Z_e = s\frac{R_1R_3C_4R_5}{R_2} \qquad (21)$$

From Eq. (21), it is noted that the final impedance is purely reactive and the inductive parameter obtained is given by $L=R_1R_3C_4R_5/R_2$. In its original work, Riordan (1967) discusses limitations in the quality factor Q regarding the interchangeability of capacitor C_4, as well as in the worsening of the quality factor Q that happens when coupling resistive or capacitive elements to the final synthetic inductor. In fact, in view of the capacitive nature of the piezoelectric, the next topic approaches the configuration of Antoniou (1969), which minimizes this effect.

Antoniou synthetic inductor

Antoniou (1969) presents a new approach to the development of gyrators circuits, including in their analysis stability conditions of the frequency response, which lead to a more robust and stable

configuration for low frequencies, especially below 1kHz, range of interest in systems mechanics. In Fig.3 the circuit with op-amps developed by Antoniou (1969) is shown.

According to Sedra & Smith, (2009) ideal operational amplifiers in the negative feedback loop will, after the permanent regime of the circuit, cancel the difference between the voltages at their input terminals e$_+$ and e$_-$, becoming virtual short circuits (Boylestad, 2012; Horowitz and Hill, 2017). By observing the circuit of Fig. 3, the input voltage will propagate at the indicated points, causing the current flow as indicated.
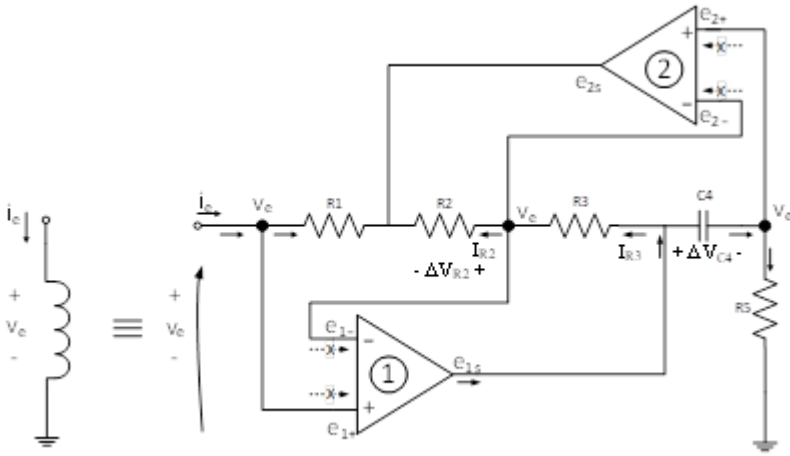
Figure 3: Antoniou (1969) synthetic inductor.

Since there is no electric current in input terminal e_{2+}, the voltage drop in C_4 will be:

$$\Delta V_{C4} = X_{C4}I_{C4} = X_{C4}\frac{v_e}{R_5} \tag{22}$$

The circulating current in R_3 resistor is obtained by:

$$(\Delta V_{C4} + v_e) - v_e = R_3 I_{R_3} \tag{23}$$

Substituting the Eq. (22) in (23), follows:

$$X_{C4}\frac{v_e}{R_5} = R_3 I_{R_3} \quad \rightarrow \quad I_{R_3} = \frac{X_{C4}}{R_3 R_5}v_e \tag{24}$$

In the other side, $I_{R2}=I_{R3}$, since there is no current inflow at the ideal op-amps inputs. In this way, the e_{2S} is given through:

$$e_{2S} = v_e - \Delta V_{R2} = v_e - I_{R_2}R_2 \rightarrow \quad e_{2S} = v_e - \frac{R_2 X_{C4}}{R_3 R_5} v_e \quad (25)$$

From the entry point of view, the voltage in R_1 will be the voltage drop caused directly by the input current i_e, since there is also no current in e_{1+} input:

$$i_e = \frac{(v_e - e_{2S})}{R_1} \quad (26)$$

Applying Eq. (25) in (26), achieves the following expression for i_e:

$$i_e = \frac{\left(v_e - \left(v_e - \frac{R_2 X_{C4}}{R_3 R_5} v_e\right)\right)}{R_1} \rightarrow i_e = \frac{R_2 X_{C4}}{R_1 R_3 R_5} v_e \quad (27)$$

From Eq. (27), $z_e = v_e/i_e$, and substituting $X_{C4} = 1/sC_4$, there is obtained:

$$z_e = \frac{sR_1 R_3 C_4 R_5}{R_2} \quad (28)$$

Equation (28) is the synthetic impedance obtained by the arrangement, which is purely reactive, in which the inductance parameter is identical to that of Riordan, $L=R_1 R_3 C_4 R_5/R_2$. Despite the same value obtained, Antoniou (1969) shows that the provision of the feedbacks of the scheme minimizes the worsening of the quality factor, but despite the improvement of the stability level, the apparatus presents more oscillations in its transient, especially in higher rates of arise voltage.

SYNTHETIC INDUCTORS APPLIED IN MULTIMODAL VIBRATION ATTENUATOR

For the experimental evaluation of each of the synthetic inductors studied, and based on the current flowing technique Behrens et al. (2003), which consist of circuits that allow current path only at the

frequencies of interest (Fig. 5a), were constructed prototypes of multimodal attenuators to be coupled to the piezoelectric installed in the structure, according to the example of Fig. 5b.
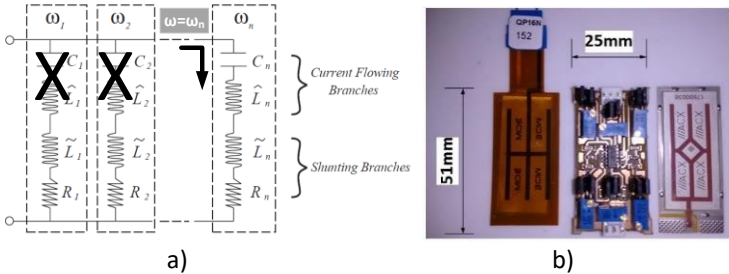
Figure 4: Multimodal current flowing circuit (a); prototype based on gyrators (b).

The test apparatus used to evaluate the performance of the multimodal prototypes, seen in detail in Fig. 5a, consists of a clamped-free aluminum beam with a coupled ACX® QP15N piezo, capacitance C_{PZT}=75.3 nF, attached to an inertial table, according to Fig. 5b. Using an Agilent® 35670A analyzer for signal collection, impact tests were performed with an Endveco® 2302 hammer, capturing acceleration through a Piezotronics® 352C22 accelerometer, then obtaining FRFs from the structure.
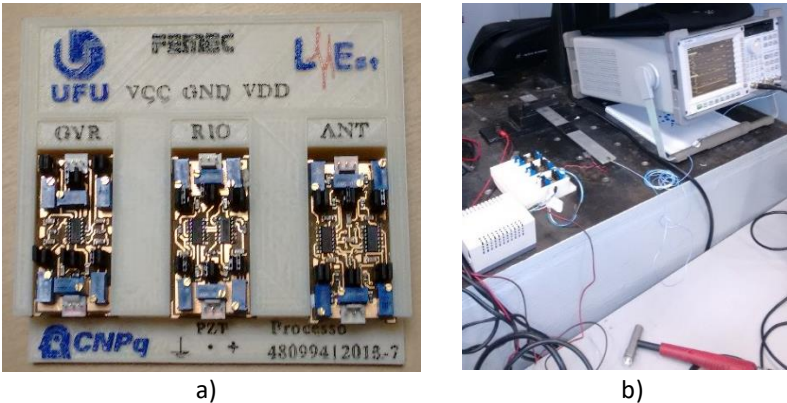
Figure 5: Multimodal attenuator prototypes gyrator, Riordan and Antoniou (a); experimental set-up test.

For the adjustment of the circuit parameters, the formulation proposed by Behrens et al (2003) was used, describing the structure for

simulation through the adaptation of Zambolini-Vicente's work (Zambolini-Vicente, (2014)). The values determined by these procedures are listed in Tabs. 1 to 3.

Table 1: Multimodal current flowing prototype gyrator parameters adjustments.

	Natural Freq.	Current flowing Capacit.	Set-up circuit parameters $(R \rightarrow R_i)$ $(L_i \rightarrow R_3)$		L_i adjust		
					Constant		Adjustable
	f_n	C_i	R_i	$L_i = \hat{L}_i + \tilde{L}_i$	R_2	C_3	R_1
	[Hz]	[μF]	[kΩ]	[H]	[Ω]	[μF]	[kΩ]
#1 mode	29,000	10,00	2,92	403,0	2200	10,00	18,3
#2 mode	183,50	1,000	1,84	10,74	1500	1,000	7,16
#3 mode	512,50	1,000	1,32	1,377	820,0	1,000	1,68

Table 2: Multimodal current flowing prototype Riordan parameters adjustments.

	Natural Freq.	Current flowing Capacit.	Set-up circuit parameters $(R \rightarrow R_i)$ $(L_i \rightarrow R_3)$		L_i adjust				
					Constant				Adjustable
	f_n	C_i	R_i	$L_i = \hat{L}_i + \tilde{L}_i$	R_1	R_2	C_4	R_5	R_3
	[Hz]	[μF]	[kΩ]	[H]	[kΩ]	[kΩ]	[μF]	[kΩ]	[Ω]
#1 mode	29,000	10,00	2,92	403,0	120,0	1,25	10,00	1,25	336,0
#2 mode	183,50	1,000	1,84	10,74	150,0	4,73	1,000	4,73	71,60
#3 mode	512,50	0,100	1,32	2,245	330,0	12,7	0,100	12,7	68,00

Table 3: Multimodal current flowing prototype Antoniou parameters adjustments.

	Natural Freq.	Current flowing Capacit.	Set-up circuit parameters $(R \rightarrow R_i)$ $(L_i \rightarrow R_3)$		L_i adjust				
					Constant				Adjustable
	f_n	C_i	R_i	$L_i = \hat{L}_i + \tilde{L}_i$	R_1	R_2	C_4	R_5	R_3
	[Hz]	[μF]	[kΩ]	[H]	[kΩ]	[Ω]	[μF]	[Ω]	[Ω]
#1 mode	29,000	1,000	2,92	430,1	10,00	820,0	1,000	10,00	3530
#2 mode	183,50	1,000	1,84	10,74	22,00	1500	10,00	22,00	33,30
#3 mode	512,50	0,100	1,32	2,245	27,00	2200	10,00	27,00	67,80

After adjusting the parameter values, the FRFs were obtained for the cases in which the piezoelectric is open circuit, short-circuited and connected to the developed circuits. Fig. 6 shows the curves obtained.
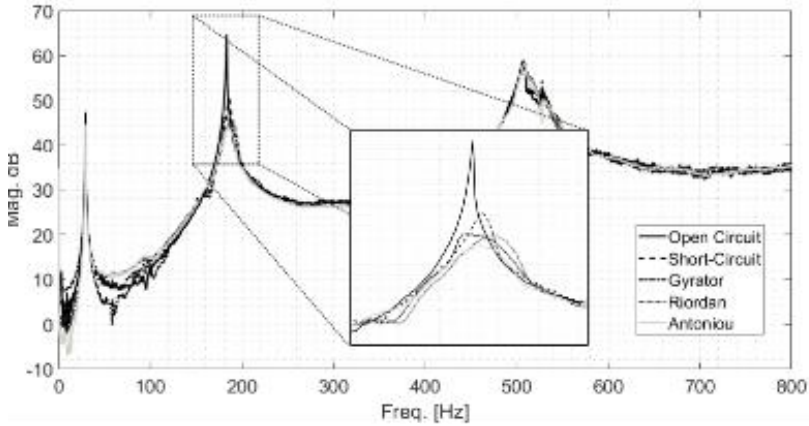
Figure 6: FRFs of tested attenuators. 2nd mode in detail.

From the experimental data, Tab. 4 was constructed by computing the frequency deviations Δf and mode-to-mode attenuations percentual variation of the loss factor, taking the open circuit condition as reference, given by $\Delta\eta_\% = (\eta_{Prot} - \eta_{OC})/\eta_{OC}$, with η_{Prot} and η_{OC} the loss factor of prototype and open circuit set-up, as follows:

Table 4: Attenuators performance: Δf and mode-to-mode inserted attenuation.

	1st mode (29,0Hz)			2nd mode (183,5Hz)			3rd mode (507,0Hz)		
	Δf(Hz)	η	$\Delta\eta_\%$(%)	Δf(Hz)	η	$\Delta\eta_\%$(%)	Δf(Hz)	η	$\Delta\eta_\%$(%)
Open Circuit	-	0,00967		-	0,00304		-	0,01218	
Short Circuit	0,0	0,01370	↑41,66	-2,5	0,02589	↑752,6	-1,0	0,01366	↑12,15
Gyrator	0,0	0,03039	↑214,2	2,5	0,06594	↑2072	-1,0	0,01364	↑12,00
Riordan	0,0	0,00893	↓7,700	-5,0	0,06495	↑2039	-1,0	0,01775	↑45,80
Antoniou	0,0	0,00897	↓7,200	-1,5	0,07646	↑2419	-1,0	0,01561	↑28,20

Regarding the frequency deviations, it is noted that the circuits did not impose, in a generalized way, a consistent structural modification, being a possible explanation for the fact that there is no significant increase of mass in the structure. Talking about the attenuations obtained, it can be seen that the circuits performed well in all modes, especially the Antoniou synthetic inductor circuit, which attenuated more than Riordan in all three modes.

CONCLUSIONS

For the current flowing multimodal vibration attenuators circuits presented in this work, it can be observed that the scheme with inductors gyrators presented superior performance to the Riordan and Antoniou for the 1st mode and compatible to the Riordan in the 2nd mode, which comes as a surprise when taking as reference the study for the monomodal schemes related in Zambolini-Vicente et al (2016). An explanation for such phenomenon may be the fact that in the gyrator PCB less material was eliminated in the plate milling process, since its electronics demand fewer components, thus giving rise to a capacitive effect that helps to remove charge from the piezoelectric. This hypothesis gains support when it is noticed that in the 3rd mode, of higher frequency, the gyrator circuit loses capacity of absorption of reactive of piezoelectric, since that depends, for capacitors, of the inverse of the frequency. Analyzing by frequency bands, near the 1st mode one must use gyrator topology, with performance well above the Riordan and Antoniou configurations; for the 2nd mode, it is important to highlight the exceptional performance of the three multimodal circuits, which can be inferred that any of them can be used in this frequency environment, with the highest performances recorded; for the 3rd mode, the Riordan and Antoniou circuits are equivalent, with advantage to the first. With the range from 29Hz to 183.5Hz in mind, the gyrator circuit is more advantageous; already for the range of 183.5Hz to 507Hz, Antoniou's synthetic inductor configuration gives indications of being the most appropriate. In addition, it is noted that for the two modes of higher frequency multimodal electronic circuits achieve performance of at least 40% above.

ACKNOWLEDGMENTS

REFERENCES

Antoniou, A., "Realization of gyrators using operational amplifiers and their use in RC-active network synthesis". Proc. Inst. Elec. Eng., 116: 838-1850, 1969.

Behrens, S. Moheimani, S. O. R., Fleming, A. J., "Multiple mode current flowing passive piezoelectric shunt controller", Journal of Sound and Vibr. 266 (2003) 929–942.

Berlincourt, D. "Piezoelectric ceramics: Characteristics and applications". J Acoust Soc Am. 70:1586–1595. (1981).

Berndt, D. F.; Dutta-Roy, S. C., "Inductor simulation with a single unity gain amplifier", IEEE Journal of Solid State Circuits, SC-4: 161-162, 1969.

Holterman, J., Groen, P. An Introduction to Piezoelectric Materials and Applications. Ed Stichting Applied Piezo, 2013, 307pg.

Horowitz, P., Hill, W., "A Arte da Eletrônica: Circuitos Eletrônicos e Microeletrônica". Ed. Bookman, 2017. ISBN-13: 978-8582604342.

Riordan, R. H. S. "Simulated inductors using differential amplifiers". Electron. Lett., vol. 3, no. 2, pp. 50–51, 1967.

Sheahan, D. F., Orchad, H. J., "High-quality transistorised gyrator", Electronics Letters. Year: 1966, Volume: 2 , Issue: 7. Pages: 274 – 275.

Sedra, A. S.; Smith, K. C. Microeletrônica. 6ª Edição / Editora: Oxford. ISBN13: 9780195323030, ISBN10: 0195323033, 2009.

Tellegen, B. D. H., "The gyrator, a new electric network element". Philips Research Reports, 3, 81-101, April, 1948.

Zambolini-Vicente, B. G. G. L., 2014, "Projeto robusto de Circuitos Shunt para o controle passivo de vibrações de estruturas compostas", 97fl: il. Dissertação (mestrado) – Universidade Federal de Uberlândia, Programa de Pós-Graduação em Engenharia Mecânica.

Zambolini-Vicente, B. G. G. L.; Silva, L. A., Lima, A. M. G. "Experimental Evaluation Of Synthetic Inductors Applied In Passive Shunt Circuits To Vibration Mitigation". Revista Interdisciplinar de Pesquisa em Engenharia. v.2, p.131 - 141, 2016.

Robust Model-Based Balancing Approach[*]

Vinícius Nunes Carvalho
viniciusnunes@ufu.br

Advisors: Aldemir Ap Cavalini Jr and Valder Steffen Jr

Abstract: Rotating machines are affected by many different problems from which unbalance is the most common one. Thus, this work is devoted to the development of an alternative balance approach, in which the representative model of the rotating machine is identified and then the unbalance forces are determined by solving a typical inverse problem. In this case, the inherent uncertainties that affect balancing performance are taken into account. This approach aims to overcome the limitations faced by the most frequently used methods, such as the influence coefficient method. The robust balancing methodology is based on a mono-objective optimization procedure where the uncertainties treated as random variables. An additional unbalance distribution along the rotor was considered as the uncertain parameter, which was modeled as a Gaussian field and represented by Monte Carlo simulations (MC simulations). Numerical and experimental investigations have been performed on a rotor system composed of a horizontal flexible shaft, three rigid discs, and two ball bearings. The results indicate the effectiveness of the proposed technique.

Keywords: rotating machine, balance technical, robustness, Monte Carlo simulations.

INTRODUCTION

According to Eisenmann and Eisenmann (1998), balancing is a systematic procedure used to approximates the barycenter of a given rotor system to its geometric centerline. Consequently, the forces and resulting vibration amplitudes applied to the bearings are attenuated. Different balancing techniques were proposed over the years, such as the so-called signal based methods, i.e., modal balancing, four-run

---

without phase, and influence coefficients method (Steffen Jr and Lacerda, 1996; Wowk, 1998; Bently and Hatch, 2002).

Although widely used in the industry, signal based techniques present some adverse aspects. As an example, many of these balancing techniques consider a linear relationship between unbalance excitation and the resulting vibration. However, if the structure presents nonlinear dynamic behavior, the obtained results, regarding the correction weights and corresponding angular positions, are not satisfactory. Additionally, these methods require trial weights (known masses positioned at specific locations of the rotor) to determine the unbalance response sensitivity for constant rotation speed. Therefore, the signal based balancing techniques are considered time-consuming and dependent on the measuring and balancing plane locations (Kang et al., 2008).

Aiming at overcoming the limitations faced by the signal based techniques, an alternative methodology was presented by Saldarriaga et al. (2010). The proposed model based technique does not require a linear relationship between unbalance and vibration responses, i.e., the technique performs well even for the nonlinear cases. Besides, trial weights are not necessary. However, a reliable model of the rotating machine is mandatory. The unbalance is identified by solving a typical inverse problem through evolutionary techniques such as Genetic Algorithm, Simulated Annealing, Particle Swarm Optimization, Ant Colony, and Differential Evolution. This class of algorithms mimic specific natural phenomena and is attracting the attention of an increasing number of authors due to their capability of working successfully in complex optimization problems.

In this context, the present work presents the numerical and experimental results obtained in the balancing of a horizontal rotating machine taking into account the inherent uncertainties that may affect the balancing performance. Thus, a model-uncertainty-based balancing technique is proposed. Besides, it is expected that the robust balancing keeps the vibration amplitudes under acceptable values (defined by proper balancing standards) for longer operation periods. The proposed methodology is based on a robust optimization approach, in which the additional unbalance distribution (i.e., uncertain parameter) is treated as a random variable. The uncertainty is modeled as a Gaussian field and represented by Monte Carlo simulations. The effectiveness of the

proposed methodology was evaluated through numerical and experimental tests performed on a rotor system composed of a horizontal flexible shaft, three rigid discs, and two ball bearings. In this case, the additional unbalance distribution can be understood as being the unbalance force generated, for example, by the accumulation of solid waste in industrial exhaust fans that increases over time.

ROTOR MODEL

The finite element model (FE model) of rotating machines encompasses different sub-systems, such as the shaft, discs, couplings, and bearings. The differential equation that describes the dynamic behavior of flexible rotors supported by ball bearings is presented by Eq. (1) (Lalanne and Ferraris, 1998).

$$\mathbf{M}\ddot{\mathbf{q}} + \left[\mathbf{D} + \Omega\mathbf{D}_g\right]\dot{\mathbf{q}} + \mathbf{K}\mathbf{q} = \mathbf{W} + \mathbf{F}_u + \mathbf{F}_s \tag{1}$$

where $\mathbf{M}$ is the mass matrix, $\mathbf{D}$ is the damping matrix, $\mathbf{D_g}$ is the gyroscopic matrix, $\mathbf{K}$ is the stiffness matrix, and $\mathbf{\Omega}$ is the shaft rotation speed. $\mathbf{W}$ stands for the weight of the rotating parts, $\mathbf{F_u}$ represents the rotating unbalance forces, and $\mathbf{F_s}$ represents the supporting forces applied to the rotor by the bearings, and $\mathbf{q}$ is the generalized displacement vector.

The shaft FE model is formulated from the Timoshenko beam theory with two nodes and four degrees of freedom per node (i.e., two displacements and two rotations). Due to the size of the matrices involved in the equation of motion, the pseudo-modal method (Lalanne and Ferraris, 1998) is used to reduce the dimension of the FE model. Through this procedure a reduced equation of motion is obtained as illustrated by Eq. (2).

$$\mathbf{M}_m\ddot{\mathbf{\eta}} + \left[\mathbf{D}_m + \Omega\mathbf{D}_{gm}\right]\dot{\mathbf{\eta}} + \mathbf{K}_m\mathbf{\eta} = \mathbf{W}_m + \mathbf{F}_{um} + \mathbf{F}_{sm} \tag{2}$$

in which $\mathbf{\eta}$ is the generalized displacement vector in modal coordinates ($\mathbf{q} = \mathbf{\Phi\eta}$) and $\mathbf{\Phi}$ is the modal matrix containing the n first vibration modes of the non-gyroscopic and non-damped system. Additionally,

$$\mathbf{M}_m = \mathbf{\Phi}^T \mathbf{M} \mathbf{\Phi} \qquad \mathbf{D}_m = \mathbf{\Phi}^T \mathbf{D} \mathbf{\Phi} \qquad \mathbf{D}_{gm} = \mathbf{\Phi}^T \mathbf{D}_g \mathbf{\Phi}$$

$$\mathbf{K}_m = \mathbf{\Phi}^T \mathbf{K} \mathbf{\Phi} \qquad \mathbf{W}_m = \mathbf{\Phi}^T \mathbf{W} \qquad \mathbf{F}_{um} = \mathbf{\Phi}^T \mathbf{F}_u \qquad \mathbf{F}_{sm} = \mathbf{\Phi}^T \mathbf{F}_s$$

(3)

where $\mathbf{M}_m$ is the modal mass matrix, $\mathbf{D}_m$ is the modal damping matrix, $\mathbf{D}_{gm}$ is the modal gyroscopic matrix, $\mathbf{K}_m$ is the modal stiffness matrix, $\mathbf{W}_m$ is the modal weight vector, $\mathbf{F}_u$ is the modal unbalance forces, and $\mathbf{F}_s$ is the modal supporting forces.

MODEL-BASED BALANCING TECHNIQUE

The model-based balancing method begins by inserting a set of randomly generated masses and their corresponding angular positions to each balancing plane of the representative FE model. Simulated time-domain responses are obtained for each generated unbalance force. The vibration responses are determined at the same positions along the shaft for which the responses were acquired from the rotor for an unknown unbalance condition (the original configuration of the rotor). Figure 1 shows a flowchart to illustrate the robust balancing methodology, as proposed by Carvalho et al. (2017).
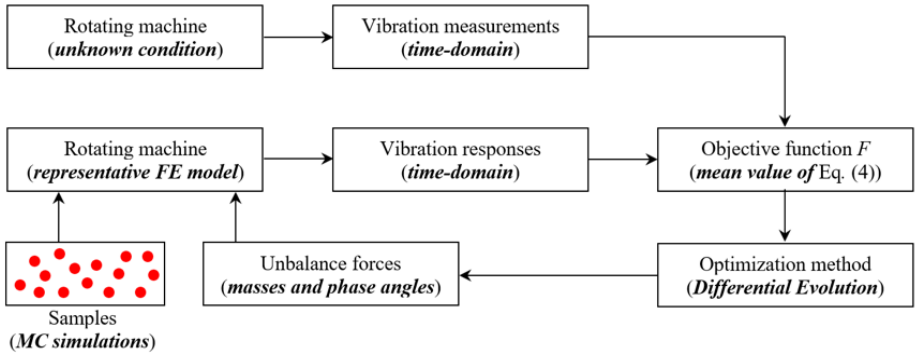

Figure 1: Robust balancing methodology flowchart.

The goal of the proposed methodology is to increase the robustness of the model based balancing technique. In this sense, MC simulations are performed simultaneously with the optimization procedure to identify the system unbalance condition. MC simulations generate different uncertain scenarios during the solution of the associated

212

inverse problem. The optimization algorithm known as Differential Evolution (Storn and Price, 1995) proposes correction masses together with their corresponding angular positions that optimally represent the vibration measurements of the rotating machine, which are computed by using the FE model. The scenarios generated by MC are considered by calculating the arithmetic mean of the obtained FE model vibration responses (i.e., arithmetic mean of the values determined the objective function F presented in Eq. (4)).

$$F = \sum_{i=1}^{n} \frac{\left\| q_i^{FE\,model}(x) - q_i^{original} \right\|}{\left\| q_i^{original} \right\|} \tag{4}$$

where n is the number of sensors used in the procedure, $q_i^{FE\,model}(x)$ is the i-th vibration response obtained by using the FE model, x is the vector containing the proposed correction masses and their corresponding angular positions, and $q_i^{original}$ is the i-th vibration response measured on the rotor for its the original configuration.

If the best result of Eq. (4) corresponds to a minimum, the unbalance affecting the rotor is identified. This means that the identified correction masses and their corresponding angular positions are capable of reproducing the unbalance responses of the rotor associated with its original configuration. If F does not find a value close to zero, the optimization method will propose new unbalance configurations and the process will continue iteratively until convergence. In order to balance the rotor, it is necessary to add 180^0 to the previously found angular positions (correction masses).

The proposed robust balancing methodology can consider uncertainties affecting, for instance, the unbalance distribution along the shaft, the stiffness and damping parameters of the bearings (i.e., due to fixation problems and wear), and the dimensions of the discs and shaft (i.e., due to the fabrication process). Therefore, the balancing performs better as robust correction masses and associated angular positions are determined. Variations on the rotor geometrical and physical properties (or even the unbalance distribution) are considered during the balancing process, which explains the good performance of the proposed approach.

NUMERICAL APPLICATION

The rotor test rig that is taken as reference for this numerical analysis is presented in Fig. 2a. The flexible shaft of the test rig was mathematically represented by using 33 finite elements (see Fig. 2b; steel shaft with 800 mm length and 17 mm of diameter; $E = 205$ GPa, $\rho = 7850$ kg/m³, $\upsilon = 0.29$). Three rigid discs are coupled to the shaft, namely the D_1 (node #14; 2.637 kg; according to the FE model), D_2 (node #26; 2.649 kg; both of steel and with 150 mm diameter and 20 mm thickness; $\rho = 7850$ kg/m³), and D_3 (node #19; 0.478 kg; aluminum disc; $\rho = 2700$ kg/m³). The system is supported by two self-alignment ball bearings B_1 and B_2 located at nodes #4 and #32, respectively. Displacement sensors are orthogonally mounted on the node #8 (S_{8X} and S_{8Z}) and node #12 (S_{12X} and S_{12Z}) to collect the shaft vibration. An electric DC motor drives the system.
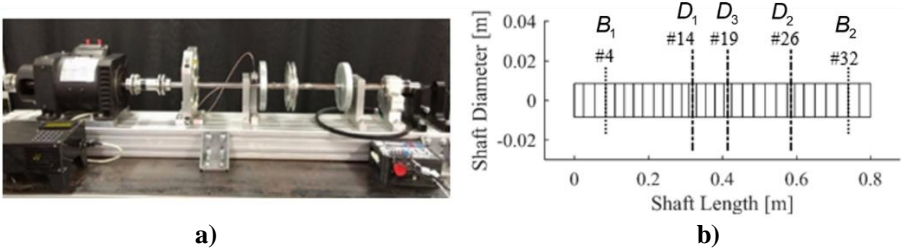
Figure 2: Rotating machine used in the numerical simulations of this work: a) Test rig; b) FE model.

The parameters of the representative FE model were obtained by means of a model updating procedure, whereas a heuristic optimization technique Differential Evolution (Storn and Price, 1995) was used to determine the unknown parameters of the model, namely the stiffness and damping coefficients of the bearings, the proportional damping added to $\mathbf{D}$ (coefficients γ and β; $\mathbf{D}_p = \gamma\mathbf{M} + \beta\mathbf{K}$), and the angular stiffness k_{ROT} due to the coupling between the electric motor and the shaft (added around the orthogonal directions X and Z of the node #1).

The proposed identification process (i.e., the comparison between simulated and experimental frequency response functions, FRFs) was performed 10 times, considering 100 individuals in the initial population

of the optimizer. The objective function adopted by the optimization process takes into account only the regions close to the FRFs peaks associated with the four first rotor natural frequencies. The experimental FRFs were measured on the test rig for the rotor at rest by applying impact forces along the X and Z directions of both discs, separately. The response signals were obtained by the two proximity probes positioned along with the same directions of the impact forces, resulting in 8 FRFs (range of 0 to 200 Hz and steps of 0.25 Hz). Table 1 summarizes the parameter values determined at the end of the minimization process.

Table 1: Parameters determined by the model updating procedure.

Parameters	Values	Parameters	Values	Parameters	Values
$^*k_X / B_1$	9.982×10^5	$^*k_X / B_2$	2.431×10^6	γ	2.598
$^*k_Z / B_1$	2.004×10^6	$^*k_Z / B_2$	9.997×10^7	β	2.12×10^{-10}
$^{**}d_X / B_1$	81.196	$^{**}d_X / B_2$	164.941	$^{***}k_{ROT}$	986.778
$^{**}d_Z / B_1$	199.042	$^{**}d_Z / B_2$	105.531		

$^*k$: stiffness [N/m]; $^{**}d$: damping [Ns/m]; $^{***}k_{ROT}$: stiffness [N/rad].

Figure 3 compares a simulated and an experimental FRF (with the impact along the X direction of D_1 and sensor S_{12X}) considering the parameters shown in Tab. 1, thus validating the updating procedure performed.
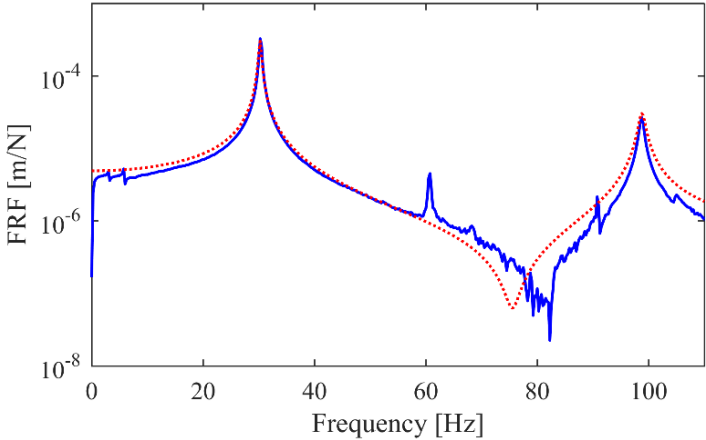

Figure 3: Updated model (......) and experimental (——) rotor FRFs.

The proposed robust balancing methodology was evaluated considering a residual unbalance condition in the rotor FE model to generate the vibration measures used as a reference. Therefore, an unbalance of 637.5 g.mm/-90° was applied to the disc D_1 of the rotor FE

model. The system rotation speed was kept constant at 1200 rev/min. The proposed balancing procedure was applied considering discs D_1 and D_2 as the balancing planes (2 balancing and 2 measuring planes).

Figure 4 shows the vibration responses of the unbalanced rotor system measured by using the sensors S_{12X} and S_{12Z}. Similar results were found by using the sensors S_{8X} and S_{8Z}.
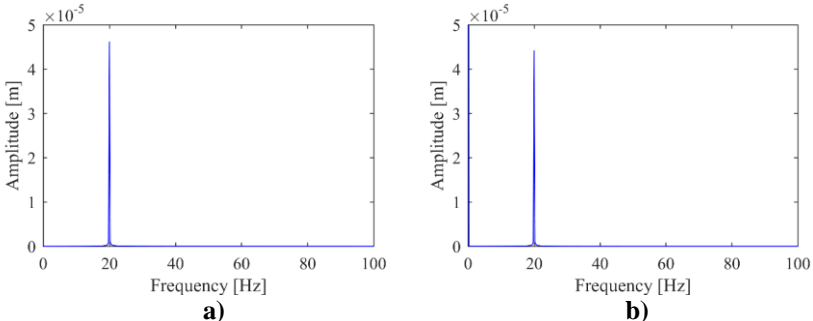
Figure 4: Vibration responses of the unbalanced rotor system: a) sensor S_{12X}; b) sensor S_{12Z}.

In the present work, the additional unbalance distribution (i.e., uncertain parameter) was applied to the disc D_1. It is worth mentioning that the random variables were modeled as Gaussian random fields, in which the convergence of the MC simulations was achieved considering 400 samples. Table 2 shows the intervals associated with the considered uncertainty scenario.

Table 2: Uncertainty scenario applied in disc D_1.

Unbalance condition	Uncertainty limits
Unbalance [g.mm]	$6.375 \leq F_u \leq 637.45$
Angular position [degrees]	$-180 \leq \theta \leq 180$

Table 3 presents the correction masses (unbalance level) and corresponding angular positions obtained by the proposed robust balancing approach. The results obtained by the determinist model based balancing technique (disregarding additional unbalance distribution) is also presented for comparison purposes. As expected, it can be verified that the deterministic approach reaches the same unbalance condition imposed to the rotating machine (i.e., 637.5 g.mm/-

90° applied to the disc D_1; angular position $+180^o$ to balancing purposes).

Table 3: Correction masses and angular positions determined by the proposed methodology.

Parameters	Robust	Deterministic
Unbalance / D_1 [g.mm]	985.2	637.5
Angular position / D_1 [degrees]	145.5	90
Unbalance / D_2 [g.mm]	1201.2	0
Angular position / D_2 [degrees]	5.6	0

In order to evaluate the robustness of the results presented in Tab. 3, different additional unbalance distributions were applied to disc D_1. Table 4 summarizes the considered unbalance scenarios (unbalances and their corresponding angular positions within the defined limits; see Tab. 2).

Table 4: Additional unbalance distributions were applied in disc D_1.

Scenarios	Unbalance [g.mm]	Angular position [degrees]
1	6.375	45
2	637.45	45
3	6.375	135
4	637.45	135
5	6.375	-135
6	637.45	-135
7	6.375	-45
8	637.45	-45

Table 5 presents the maximum vibration amplitudes determined at the positions of both measuring planes considering the balanced rotor system. Note that only the scenarios 6 and 8 lead to vibration amplitudes when the deterministic approach was applied, demonstrating the effectiveness of the proposed robust methodology.

Scenarios	Deterministic [μm]		Robust [μm]	
	S_8	S_{12}	S_8	S_{12}
1	8.8	17.2	2.7	2.1
2	55.5	98.4	54	81
3	8.8	16.6	3.4	1.1
4	55.2	86.1	51	81.1
5	8.1	15.6	3.5	9.2
6	**43.3**	**66**	**51.5**	**81.1**
7	8.1	16.3	2.8	2
8	**43.7**	**81.4**	**47.2**	**83**

EXPERIMENTAL APPLICATION

Figure 5 shows the vibration responses of the unbalanced rotor system measured by all the sensors considered. The rotation speed was 1200 rev/min.
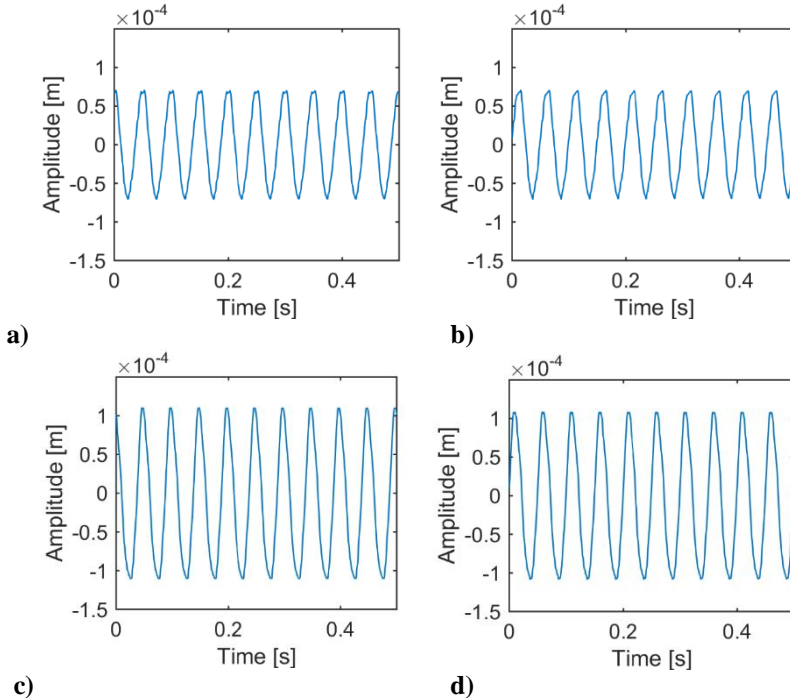

a)

b)

c)

d)

Figure 5: Vibration responses of the unbalance rotor system: a) sensor S_{8X}; b) sensor S_{8Z}; c) sensor S_{12X}; d) sensor S_{12Z}.

The additional unbalance distribution (uncertain information) was applied to the disc D_1. The random variables were modeled as Gaussian random fields, so that the convergence of the MC simulations was achieved by considering 400 samples. Table 6 shows the intervals associated with the uncertainty scenario defined. These values were chosen from a previous analysis presented in Carvalho et al. (2017).

Table 6: Uncertainty scenario applied in the disc D_1.

Unbalance condition	Uncertainty limits
Unbalance [g.mm]	$6.375 \leq F_u \leq 637.45$
Phase angle [degrees]	$-180 \leq \theta \leq 180$

Table 7 presents the correction masses and corresponding angular positions obtained by using the proposed robust balancing approach. The results obtained by applying the determinist model-based balancing technique is also presented for comparison purposes. As expected, the results obtained through the robust and deterministic approaches are different. It is worth mentioning that the deterministic model based balancing technique was proposed by Saldarriaga et al. (2010).

Table 7: Design space and the results obtained by using the robust and deterministic balancing approaches.

Parameters	Design space	Robust	Deterministic
Unbalance / D_1 [g.mm]	0 to 10000	1407	1009
Angular position / D_1 [degrees]	-180 to 180	94.39	157.36
Unbalance / D_2 [g.mm]	0 to 10000	2620	821
Angular position / D_2 [degrees]	-180 to 180	-116.74	-89.34

Figure 6 presents the vibration responses of the unbalanced rotor system and the corresponding signals determined at the end of the optimization process associated with the robust balancing. Note that the proposed methodology was able to reproduce the vibration responses of the rotating machine. Similar results were obtained for the sensors S_{12X} and S_{12X}.
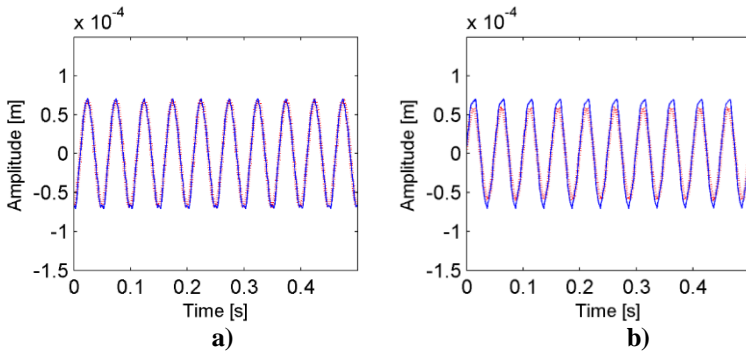
Figure 6: Vibration responses of the unbalance rotor system (——) and the corresponding simulated data (......): a) sensor S_{8X}; b) sensor S_{8Z}.

The correction masses determined by using the robust and deterministic balancing approaches were applied separately on the balancing planes of the rotating machine. As mentioned, 180^0 was added to the obtained angular positions for balancing purposes.

Table 8 shows the vibration amplitudes of both the unbalanced and balanced rotating machine by using robust and deterministic balancing approaches. Note that robust balancing resulted in vibration amplitudes that are lower than those obtained by using the deterministic method, thus demonstrating to be better adapted to identify the unbalance condition of the rotor.

In order to evaluate the robustness of the results presented in Tab. 8, different additional unbalance distributions were applied to disc D_1. Table 9 summarizes the considered unbalance scenarios (unbalance and corresponding angular positions within and overcoming the defined limits).

Table 8: Vibration amplitudes of the balanced and unbalanced rotating machine.

		Sensors			
		S_{8X}	S_{8Z}	S_{12X}	S_{12Z}
Deterministic approach	*Unbalanced* [μm]	69.23	68.26	109.5	108.4
	Balanced [μm]	29.87	27.36	60.75	58.60
	Reduction [%]	56.85	59.92	44.52	45.94
Robust approach	*Unbalanced* [μm]	69.23	68.26	109.5	108.4
	Balanced [μm]	14.11	12.21	29.30	28.94
	Reduction [%]	79.62	82.11	73.24	73.30

Table 9: Additional unbalance scenarios applied in disc D_1.

Scenarios	Unbalance [g.mm]	Angular position [degrees]
1		0
2		90
3	338.8	180
4		270
5		0
6		90
7	1054.9	180
8		270
9		0
10		90
11	1759.8	180
12		270

Table 10 presents the variation between the vibration amplitudes of the unbalanced rotor and with the addition of the masses (showed in Tab. 7) to the disc D_1. As expected, note that the robust balancing approach presented a smaller variation on the vibration responses as compared with the deterministic approach.

Table 10: Variation between the vibration amplitudes of the unbalanced rotor and considering the additional unbalance scenarios.

	Sensors			
	S_{8X}	S_{8Z}	S_{12X}	S_{12Z}
Deterministic approach [μm]	155.62	144.03	271.23	260.99
Robust approach [μm]	135.44	126.32	224.39	214.66
Reduction [%]	12.97	12.30	17.27	17.75

FINAL REMARKS

In the present work, a robust model-based balancing technique was proposed. The uncertain information was modeled as a set of random variables, which are introduced in the balancing procedure by means of MC simulations during the solution of the associated inverse problem. Different additional unbalance distributions were considered aiming at simulating the unbalance force generated by the accumulation of solid waste in industrial exhaust fans that increases over time, for example. The numerical and experimental results demonstrated the efficiency of the proposed methodology. Finally, the obtained results show that the proposed robust methodology is able to increase the balancing robustness. Further work encompasses the analysis of different sources of uncertainties. Experimental verification of the proposed technique in a rotating machine installed in an industrial plant is scheduled.

ACKNOWLEDGMENTS

REFERENCES

Bently, D.E. and Hatch, C.T. "Fundamentals of Rotating Machinery Diagnostics". Bently Pressurized Bearing Company, First printing, Minden, NV, USA, 2002.

Carvalho, V. N., Dourado, A. G. S., Rende, B. R. F., Cavalini Jr, A. A. and Steffen Jr, V., Robust Modal Based Balancing Approach for Flexible Rotors", ICEDYN 2017, Ericeira, Portugal.

Eisenmann, R.C. and Eisenmann Jr, R.C. "Machinery Malfunction Diagnosis and Correction". Prentice Hall, Inc., New Jersey, 1998.

Kang, Y., Chang, Y. -P., Tseng, M. -H., Tang, P. -H. and Chang, Y. -F, "A modified approach based on influence coefficient method for balancing crank-shafts", 2000, Journal of Sound and Vibration, 234(2), 277-296.

Lalanne, M. and Ferraris, G., "Rotordynamics prediction in engineering", John Wiley & Sons, INC., 1998.

Saldarriaga, M. V., Steffen Jr, V., Der Hagopian, J. and Mahfoud, J., "On the balancing of flexible rotating machines by using an inverse problem approach", 2010, Jornal of Vibration and Control, 17(7) 1021-1033.

Steffen Jr, V. and Lacerda, H.B. "On the Balancing of Flexible Rotors". The International Journal of Analytical and Experimental Modal Analysis, 11, 1996, pp. 96-105.

Storn, R. and Price, K. Differential evolution: a simple and efficient adaptive scheme for global optimization over continuous spaces. International Computer Science Institute, v. 12, n. 1, p. 1-16, 1995.

Wowk, V. "Machinery Vibration: Balancing". McGraw-Hill Professional, First edition, 1998.

Kriging Surrogate Models Dedicated to the Cylindrical Journal Bearing of a Francis Hydropower Unit*

Leonardo Campanine Sicchieri and Jefferson Silva Barbosa
leo_sicchieri@ufu.br

Advisors: Aldemir Ap Cavalini Jr and Valder Steffen Jr

Abstract: Francis hydropower generating units are rotating machines composed of a vertical shaft commonly supported by four hydrodynamic bearings: one combined tilting-pad bearing (journal and thrust bearings; TPJB and TPTB, respectively), one intermediate TPJB located close to the generator, and one cylindrical journal bearing (CJB) located close to the Francis turbine. Firstly, the thermohydrodynamic (THD) models associated with the bearings of were coupled to the finite element model of a Francis hydropower unit to obtain its vibration responses. However, the numerical solution of the equations of motion demonstrated to be costly computationally. Thus, kriging surrogate models were obtained to represent the bearings. In this paper, details on the surrogate model used to represent the CJB of the rotating machine are presented. The position of the shaft center at the bearing position, inlet oil temperature, and radial clearance were considered as input values for the kriging model. The corresponding outputs were the maximum oil film pressure, maximum oil film temperature, and hydrodynamic supporting forces. The obtained results demonstrated that the kriging surrogate model was able to represent the CJB with a low computational cost as compared to its conventional THD model.

Keywords: Kriging surrogate models, rotordynamics, cylindrical journal bearing, Francis hydropower unit.

INTRODUCTION

Bearings are mechanical elements responsible for supporting rotating shafts, which can be classified as axial or radial (thrust or journal bearings, respectively), depending on the applied load direction

---

(Dourado et al., 2019). Regarding its geometry, they can have fixed or variable geometries (tilting-pad bearings). Tilting-pad bearings have greater stability, allowing to operate in high rotating speeds. Thus, its bearings are widely applied in the industry (Barbosa, 2018). Due to the high load capacity, hydrodynamic bearings are commonly used in large rotating machines, such as in hydropower generating units (Vance and Murphy, 2010).

The mathematical simulation of hydropower units is an indispensable resource for engineers, allowing a comprehensive understanding of the dynamic behavior of the system and prediction of undesired operating conditions. In this context, the development of mathematical models for representing the dynamic behavior of hydrodynamic bearings becomes indispensable.

The theoretical studies of Reynolds (Reynolds, 1886) resulted in a differential partial equation obtained from simplifications on the Navier-Stokes' equation. Solving the Reynolds' equation, the pressure field in the oil film of hydrodynamic bearings can be determined. In this case, the oil film temperature is considered constant. However, due to the motion between the bearing housing and the shaft, part of the resulting kinetic energy is converted into thermal energy. The oil temperature increases and, consequently, the oil viscosity decreases. Aiming to develop more accurate hydrodynamic bearing models, the Reynolds' equation must be solved considering variations on the oil temperature (Dowson, 1962). Thus, THD models should be used, in which thermal effects are considered by associating the Reynolds' and energy equations.

The dynamic behavior of Francis hydropower generating units can be represented by mathematical models composed of shaft, generator, bearings, and turbine. The resulting equation of motion is solved using numerical integration methods. If no linearization is used to represent the bearings (linear stiffness and damping coefficients), this numerical procedure presents high computational cost, in which, approximately, 90% is associated with the solution of the THD models. The shaft model is usually based on the finite element model, the generator and turbine are represented by rigid discs, while THD models are solved using the finite volume method.

Thus, it is interesting to replace the conventional THD models with a faster estimation procedure. In this sense, metamodeling approaches can be used (Kleijnen, 2009; Xiaobo, 2017). There are several metamodeling techniques proposed in the literature, such as responses surfaces, neural networks, inductive learning, and Kriging (Simpson et al., 2001). Kriging is an interpolation method capable of handling deterministic data. This approach demonstrated to be effective for various applications due to the wide range of correlation functions which may be chosen.

In this work, a kriging surrogate model was obtained to represent the CBJ of a Francis hydropower unit. The position of the shaft center at the bearing position, inlet oil temperature, and radial clearance were considered as input values for the kriging model. The corresponding outputs were the maximum oil film pressure, maximum oil film temperature, and hydrodynamic supporting forces. The obtained results demonstrated that the kriging surrogate model was able to represent the CJB with a low computational cost as compared to its conventional THD model.

The main contribution of this work is demonstrating the efficiency of the obtained kriging surrogate model to predict the behavior of a complex bearing used in a large-scale rotating machine. It is worth mentioning that the present work was developed under the R&D project Robust Modeling for the Diagnosis of Defects in Generating Units (02476-3108/2016) conducted by ANEEL (Brazilian Electric Energy Agency) with the financial support of the companies CERAN, BAESA, ENERCAN, and Foz do Chapecó. In this case, a model-based approach was proposed aiming to detect incipient faults in a Francis hydropower unit.

CYLINDRICAL JOURNAL BEARING

In this section, the mathematical formulation of the CBJ model associated with a Francis hydropower unit is presented. In this THD approach, the modified Reynolds' and energy equations are solved simultaneously. The complete description of the THD model for CJB can be found in Barbosa et al., 2017.

Figure 1 represents a CJB and its main geometrical parameters, where R is the shaft radius, L_h is the length of bearing, C is the radial clearance, e is the eccentricity (radial displacement from the shaft center O_E to the bearing center), α_h is the angle that defines the angular position of the shaft center, h_h is the minimum oil film thickness, p_h is the pressure distribution along the oil film, F_w is the external force applied on the shaft, and Ω is the rotation speed of shaft.
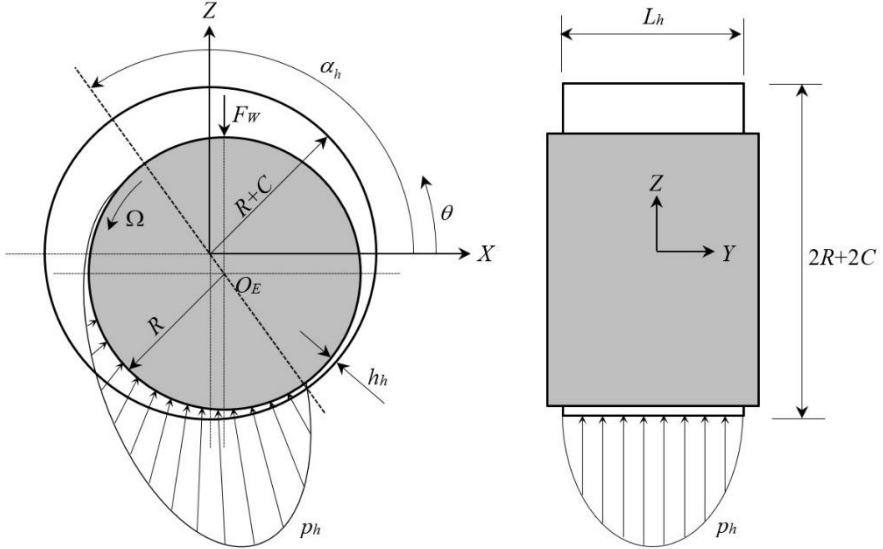

Figure 1: Schematic representation of a CJB (Adapted from Cavalini Jr et al., 2017).

Equation (1) presents the dimensionless Reynolds' equation used to determine the pressure field along the oil film of the CBJ (see Fig. (1)).

$$\left(\frac{1}{2\pi}\right)^2 \frac{\partial}{\partial \bar{x}}\left(\bar{F}_2 \bar{h}_h^3 \frac{\partial \bar{p}_h(\bar{x},\bar{y})}{\partial \bar{x}}\right) + \left(\frac{R}{L_h}\right)^2 \frac{\partial}{\partial \bar{y}}\left(\bar{F}_2 \bar{h}_h^3 \frac{\partial \bar{p}_h(\bar{x},\bar{y})}{\partial \bar{y}}\right) = \left(\frac{1}{2\pi}\right)\frac{\partial}{\partial \bar{x}}\left[\bar{h}_h\left(1 - \frac{\bar{F}_1}{\bar{F}_0}\right)\right] + \frac{\partial \bar{h}_h}{\partial \bar{t}} \quad (1)$$

where,

$$\bar{x} = \frac{x}{2\pi R} \qquad \bar{y} = \frac{y}{L_h} \qquad \bar{z} = \frac{z}{C} \qquad \bar{\mu} = \frac{\mu}{\mu_0}$$

$$\bar{p}_h = \frac{p_h(x,y)C}{\mu_0 \Omega R} \qquad \bar{t} = \Omega t$$

(2)

228

$$\bar{F}_0 = \int_0^1 \frac{1}{\bar{\mu}} d\bar{z} \qquad \bar{F}_1 = \int_0^1 \frac{\bar{y}}{\bar{\mu}} d\bar{z} \qquad \bar{F}_2 = \int_0^1 \frac{\bar{z}}{\bar{\mu}} \left(\bar{z} - \frac{\bar{F}_1}{\bar{F}_0} \right) d\bar{z} \qquad (3)$$

in which μ_0 is the oil viscosity in the reference temperature T_0 and the dimensionless oil film thickness is defined as being:

$$\bar{h}_h = 1 - \bar{x}_R \cos\theta - \bar{z}_R \sin\theta \qquad (4)$$

where,

$$\bar{x}_R = E\cos\alpha_h \qquad \bar{z}_R = E\sin\alpha_h \qquad E = e/C \qquad (5)$$

being E the dimensionless eccentricity of the shaft center as related to the bearing center.

The temperature field of the oil can be determined using the energy equation in the two-dimensional form applied to an incompressible fluid, as given by Eq. (6). In this case, it is assumed that the heat transfer in the bearing occurs predominantly along the radial direction. Consequently, the heat transfer along the axial direction is neglected (Daniel, 2012).

$$\rho c_p \left(u \frac{\partial T(x,z)}{\partial x} + w \frac{\partial T(x,z)}{\partial z} \right) = k_t \left(\frac{\partial^2 T(x,z)}{\partial x^2} + \frac{\partial^2 T(x,z)}{\partial z^2} \right) +$$
$$2\mu \left[\left(\frac{\partial u}{\partial x} \right)^2 + \left(\frac{\partial w}{\partial z} \right)^2 \right] - \frac{2}{3} \left(\frac{\partial u}{\partial x} + \frac{\partial w}{\partial z} \right)^2 + \left(\frac{\partial u}{\partial z} + \frac{\partial w}{\partial x} \right)^2 + \left(\frac{\partial v}{\partial z} \right)^2 + \left(\frac{\partial v}{\partial x} \right)^2 \qquad (6)$$

where c_p and k_t are specific heat capacity and thermal conductivity of the oil, respectively, and u, v, and w are its velocity components along the X, Y, and Z directions, respectively, as shown in Eq. (7), Eq. (8), and Eq. (9).

$$u = \frac{\partial p_h}{\partial x} \int_0^z \frac{z}{\mu} dz + \left(\frac{\Omega R}{F_0} - \frac{F_1}{F_0} \frac{\partial p_h}{\partial x} \right) \int_0^z \frac{dz}{\mu} \tag{7}$$

$$w = \frac{\partial p_h}{\partial y} \int_0^z \frac{z}{\mu} dz + \left(\frac{\partial p_h}{\partial y} \frac{F_1}{F_0} \right) \int_0^z \frac{dz}{\mu} \tag{8}$$

$$v = -\int_0^{h_h} \left(\frac{\partial u}{\partial x} + \frac{\partial y}{\partial y} \right) dz + \frac{\partial h_h}{\partial t} \tag{9}$$

The temperature field is used to determine the oil viscosity, which is used in the modified Reynolds' equation to obtain the associated pressure field. The relationship between temperature and oil viscosity used in the present contribution is given by Eq. (10) (Seeton, 2006).

$$\mu(T) = a \exp\left(\frac{b}{T + 273.15 + c} \right) \tag{10}$$

where T is the oil temperature in Celsius and a, b, and c are the coefficients that should be determined according to the oil properties.

Finally, the hydrodynamic supporting forces are calculated by integrating the pressure field on the bearing area, as shown in Eq. (11). Figure 2 presents the procedure used to determine the hydrodynamic forces of the CBJ based on its THD model.

$$\begin{Bmatrix} F_x \\ F_z \end{Bmatrix} = -\int_{-L_h/2}^{L_h/2} \int_0^{2\pi} p_h \begin{Bmatrix} \cos\theta \\ \sin\theta \end{Bmatrix} R d\theta dy \tag{11}$$
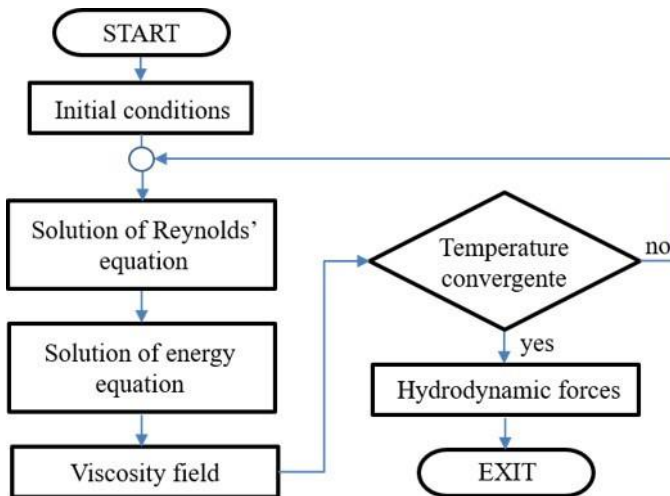
Figure 2: Physical model of the CJB (Adapted from Barbosa et al., 2019).

KRIGING MODELING

Surrogate models are an interesting alternative to replace complex mathematical models of mechanical systems for simple ones, reducing the associated computational costs. In this application, input and output values are correlating using mathematical functions, such that any output values can be determined for any input values within a defined space. According to Simpson et al. (2019), the metamodeling process is composed of three steps:

i. Sampling: definition of the numerical or experimental procedure to determine the samples associated with the input and output values of the real system or its model;

ii. Formulation: definition of the functions used for correlating the considered input and output values;

iii. Adjustment: correlation of the input and output values through the functions defined in the formulation step to determine the surrogate model.

The kriging formalism is used in the present work as the metamodeling technique. The main difference among the kriging formalism and other approaches relies on the exploitation of spatial correlations between the function values to adjust the average behavior of the regression model. Some characteristics of the kriging method are described below, as presented by Xiaobo (2017), Simpson et al. (2019), and Wang et al. (2008).

The general expression for the kriging method is given by Eq. (12).

$$y(\mathbf{x}) = f(\mathbf{x}) + Z(\mathbf{x}) \tag{12}$$

where $y(\mathbf{x})$ is the output values associated with the input vector $\mathbf{x}$, $f(\mathbf{x})$ is a known polynomial function of $\mathbf{x}$, and $Z(\mathbf{x})$ is the realization of a normally distributed Gaussian random process with mean zero and variance σ^2.

The function $f(\mathbf{x})$ is deterministic and equivalent to the global approximation of the design space. $Z(\mathbf{x})$ creates localized deviations so that the kriging model interpolates the sampled data points. The covariance matrix of $Z(\mathbf{x})$ is given by Eq. (13).

$$Cov\left[Z\left(\mathbf{x}^i\right), Z\left(\mathbf{x}^j\right)\right] = \sigma^2 \mathbf{R}\left[R\left(\mathbf{x}^i, \mathbf{x}^j\right)\right] \tag{13}$$

in which $\mathbf{R}$ is the correlation matrix and $R(\mathbf{x}^i, \mathbf{x}^j)$ is the correlation function between any two of the n_s sampled data points $\mathbf{x}^i$ and $\mathbf{x}^j$. $\mathbf{R}$ is a symmetric matrix with ones along its diagonal.

The correlation function $R(\mathbf{x}^i, \mathbf{x}^j)$ is specified by the user. The main correlation functions are shown in Tab. 1, where θ_k are the unknown correlation parameters used to fit the model, and the x^i_k and x^j_k k-th components of the sample points $\mathbf{x}^i$ and $\mathbf{x}^j$, respectively.

Table 1: Correlation models.

Correlation models	$R(\mathbf{x}^i, \mathbf{x}^j)$
Linear	$\max\left\{0, 1 - \theta_k \left\| x_k^i - x_k^j \right\|\right\}$
Gaussian	$\exp\left(-\sum_{k=1}^{n_s} \theta_k \left\| x_k^i - x_k^j \right\|^2 \right)$
Exponential	$\exp\left(-\sum_{k=1}^{n_s} \theta_k \left\| x_k^i - x_k^j \right\| \right)$
Cubic	$1 - 3\xi_k^2 + 2\xi_k^3 \qquad \xi_k = \min\left\{1, \theta_k \left\| x_k^i - x_k^j \right\|\right\}$

Predicted estimates $\hat{y}(\mathbf{x})$ at untried values of $\mathbf{x}$ (new input data points) can be estimated as shown in Eq. (14).

$$\hat{y}(\mathbf{x}) = \hat{\beta} + \mathbf{r}^T(\mathbf{x})\mathbf{R}^{-1}(\mathbf{y} - \mathbf{f}\hat{\beta}) \tag{14}$$

in which $\mathbf{y}$ is a column vector of length n_s containing the output values associated with each sampled data point, $\mathbf{f}$ is a matrix containing the input values associated with each sampled data point, $\mathbf{r}^T(\mathbf{x})$ is the correlation vector of length n_s between an untried value of $\mathbf{x}$ and the sampled data points $\{\mathbf{x}^1, \mathbf{x}^2, ..., \mathbf{x}^{ns}\}$ as given by Eq. (15), and $\hat{\beta}$ is estimated using Eq. (16).

$$\mathbf{r}^T(\mathbf{x}) = \left[R\left(\mathbf{x}, \mathbf{x}^1\right), R\left(\mathbf{x}, \mathbf{x}^2\right), ..., R\left(\mathbf{x}, \mathbf{x}^{ns}\right) \right]^T \tag{15}$$

$$\hat{\beta} = \left(\mathbf{f}^T \mathbf{R}^{-1} \mathbf{f}\right)^{-1} \mathbf{f}^T \mathbf{R}^{-1} \mathbf{y} \tag{16}$$

The variance is estimated as follows:

$$\hat{\sigma}^2 = \frac{(\mathbf{y} - \mathbf{f}\hat{\beta})^T \mathbf{R}^{-1} (\mathbf{y} - \mathbf{f}\hat{\beta})}{n_s} \tag{17}$$

In tab. 1, θ_k is obtained by the maximum likelihood estimate method. The best kriging model is found by solving the k-dimensional

unconstrained nonlinear optimization problem given by maximizing Eq. (18).

$$-\frac{[n_s \ln(\hat{\sigma}^2) + \ln(\mathbf{R})]}{2} \tag{18}$$

It is worth mentioning that depending on the considered correlation function, the resulting kriging metamodel can either provide an exact or inexact interpolation of the adopted data point.

Precision metrics are used to validate the generated kriging metamodel. In this contribution, the R^2 (Determination Coefficient), *RMSE* (Root Mean Square Error), and *RMSE$_{rel}$* (Relative Root Mean Square Error) were considered. The determination coefficient R^2 is effective to test the accuracy of approximated models. Its definition is given by Eq. (19). In this case, R^2 approaches 1 as the kriging model is more accurate.

$$R^2 = 1 - \frac{\sum\limits_{k=1}^{n_s}\left(x_k - \hat{y}_k\right)^2}{\sum\limits_{k=1}^{n_s}\left(x_k - \bar{y}\right)^2} \tag{19}$$

RMSE is a metric of general precision which can be applied to verify the accuracy of approximated models. As the value of *RMSE* approaches to 0, more accurate and representative the metamodel becomes. Equation (20) presents the definition of the *RMSE* metric.

$$RMSE = \sqrt{\frac{\sum\limits_{k=1}^{n_s}\left(x_k - \hat{y}_k\right)^2}{n_s}} \tag{20}$$

RMSE$_{Rel}$ stands for the global relative difference between the approximated model and the original input data points. As the value of *RMSE$_{rel}$* approaches to 0, more accurate and representative the metamodel becomes. Equation (21) presents the definition of the *RMSE$_{rel}$* metric.

$$RMSE_{rel} = \frac{1}{n_s \bar{y}} \sqrt{\sum_{k=1}^{n_s} \left(x_k - \hat{y}_k \right)^2} \qquad (21)$$

NUMERICAL RESULTS

In this section, the numerical results associated with the kriging surrogate model of the CJB used in the considered Francis hydropower unit are shown. The rotating machine considered in this work presents 44.58 MW nominal power, 13,800 V nominal electric voltage, 2,027.5 A nominal current, and operates at 300 RPM. As mentioned, the considered Francis hydropower generating unit is composed of a vertical shaft supported by four hydrodynamic bearings: one combined TPJB-TPTB, one intermediate TPJB located close to the generator, and one CJB located close to the Francis turbine. Figure 3 presents the inner surface of the CJB, in which some regions of oil recirculation (inlet and outlet) can be observed. Its main dimensions and operating parameters are presented in Tab. 2.
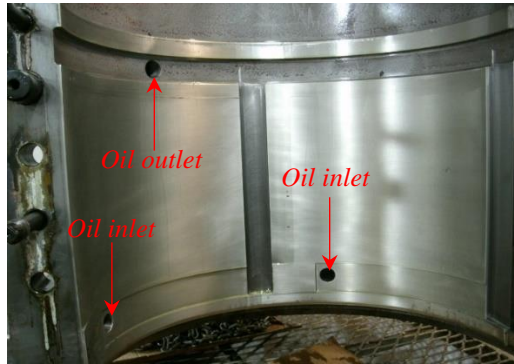

Figure 3: Inner surface of the CJB used in the considered Francis hydropower unit.

Table 2: Geometrical and operating parameters of the CJB.

Parameter	Value
Inner diameter	550.4 mm
Shaft diameter	550 mm
Length of bearing	330 mm
Rotation speed	300 rpm
Oil type	ISO VG 68
Coefficients used in Eq. (10) according to the oil properties	$a = 5.506 \times 10^{-9}$ $b = 5012$ $c = 0.1248$

Computational simulations present, in general, systematic errors instead of random ones. It means that repeated simulations made by virtual machines always considering the same input parameters will result in the same outputs. Therefore, a good sample technique must take into account all sample space. In this context, the sampling technique used in the present work was the rectangular planning to minimize the possibility of biased samples (Sacks et al., 1989; Lophaven et al., 2002).

The rectangular planning is composed by 4000 samples, in which the input parameters are the inlet oil temperature T_i, radial clearance C of the bearing, and the position of the shaft center (E and α_h, as shown in Eq. (5)). The output values are the hydrodynamic supporting forces along the x and z direction, F_X and F_Z, respectively, maximum pressure P_{max}, and maximum temperature T_{max} of the oil film. Table 3 shows the lower and upper limits considered for each input variables.

Table 3: Considered intervals for the input variables.

Parameter	Interval
T_i	[25, 45] °C
C	[150, 250] µm
E	[0.1, 0.45]
α_h	[0, 360] degrees

To develop of kriging predictor, zero-order, first order, and second order regression polynomials can be used, as well as the correlation functions presented in Tab. 1. According to Dourado et al. [1] and Xiaobo [6], second-order polynomials are more appropriated for nonlinear models. Thus, the second order polynomial was adopted. Preliminary results demonstrated that the exponential function presents a better correlation than other functions, and, therefore, it was used in the present work.

The procedure for validation of the kriging methodology consists of comparing the results obtained by using the CBJ-THD model (original model) and the corresponding kriging metamodel. In this case, 256 additional samples (not used to construct the kriging model) were used. Figure 4 shows the original and estimated hydrodynamic supporting forces along the X and Z directions of the CBJ, as well as the results associated with the maximum pressure and maximum oil film

temperature. It can be observed that the formulated kriging model was able to represent the CBJ-THD model.

Table 4 presents the values of R^2, *RMSE*, and *RMSE$_{rel}$* calculated for the additional samples analyzed. Note that the values of R^2 are close to 1, the values of *RMSE$_{rel}$* are less than 1.4%, and the values of *RMSE* are small as compared to the magnitude of the parameters, which demonstrate the representativeness of the formulated kriging model.

Table 4: Precision metrics.

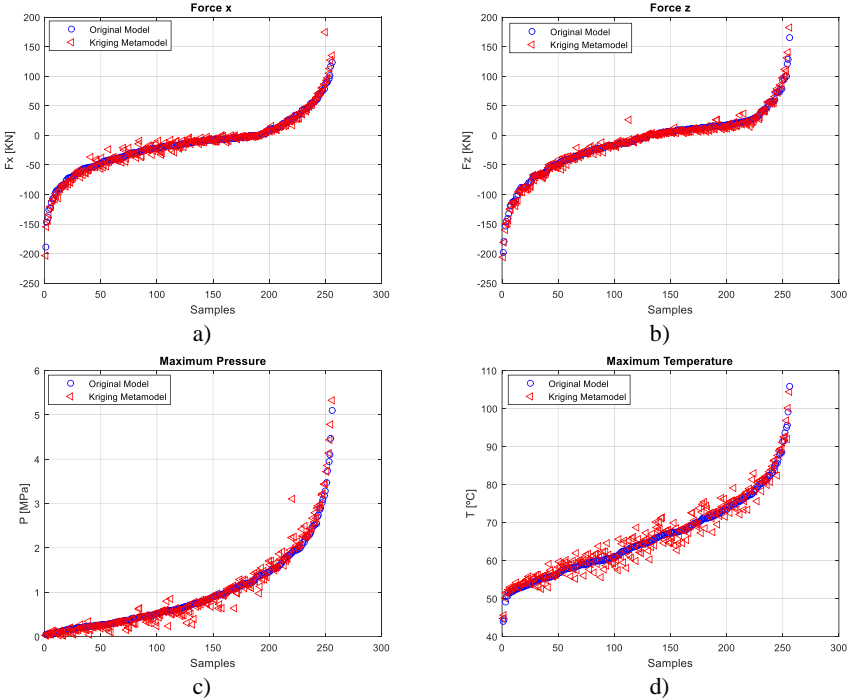| Output	R^2	RMSE	RMSE$_{rel}$
F$_X$	0.9865	7.7507 kN	1.3925 %
F$_Z$	0.9943	5.2171 kN	0.8873 %
P$_{max}$	0.9717	0.1471 MPa	0.9426 %
T$_{max}$	0.9637	1.9893 ℃	0.4127 %

Figure 4: Validation response a) supporting force in the x-direction, b) supporting force in the z-direction, c) maximum pressure and d) maximum temperature.

It is worth to mention that only 2 sec, approximately, are necessary to compute the supporting forces, maximum pressure, and maximum

temperature by using the formulated kriging model. Differently, around 10 min is necessary to compute the same outputs the conventional CBJ-THD model.

FINAL REMARKS

In this contribution, a surrogate model approach was evaluated for reducing computational cost associated with a THD mathematical model of a bearing used in a Francis hydropower unit. The rotor is composed of a vertical rotor and four hydrodynamic bearings. However, only the kriging model of the CBJ is presented.

The effectiveness of the proposed methodology was demonstrated by comparing the results obtained using the original THD bearing model and the formulated kriging model. It could be observed that the kriging model could represent the hydrodynamic supporting forces, maximum pressure, and maximum temperature in the oil film of the CBJ.

In this case, different values for the position of the shaft center, inlet oil temperature, and radial clearance were considered. Moreover, the computational cost associated with the kriging surrogate model is significantly smaller than the THD model. Thus, the kriging methodology is a powerful approach that can be used in rotordynamics analyses.

Further work will be dedicated to applying this methodology in the other bearing of the considered Francis hydropower unit. The coupling between the finite element model of the rotor and the kriging models of the bearings are also scheduled.

ACKNOWLEDGEMENTS

REFERENCES

Barbosa, J.S., "Análise de Modelos Termohidrodinâmicos para Mancais de Unidades Geradoras" Universidade Federal de Uberlândia, 2018.

Barbosa, J.S., Sicchieri, L.C., Silva, A.D.G., Cavalini Jr, A.A., Steffen Jr, V., "Theoretical and Experimental Analysis of Hydrodynamic and Thermohydrodynamic Models of Cylindrical Bearings" In: 24th ABCM International Congress of Mechanical Engineering, 2017, Curitiba, Parana, Brazil.

Cavalini Jr., A.A., Silva, A.D.G., Lara-Molina, F.A., Steffen Jr., 2017, "Dynamic Analisys of a Flexible Rotor Supported by Hydrodynamic Bearings with Uncertain Parameters" Meccanica, Vol. 52, pp. 2931-2943.

Daniel, G.B., "Desenvolvimento de um Modelo Termohidrodinâmico para Análise em Mancais Segmentados", Universidade Estadual de Campinas, 2012.

Dourado, A.P., Barbosa, J.S., Sicchieri, L.C., Cavalini Jr., A.A., Steffen Jr., V., "Kriging Surrogate Model Dedicated to a Tilting-Pad Journal Bearing", Proceedings of the 10th International Conference on Rotordynamics – IFToMM, Vol. 1, Rio de Janeiro, Brazil, 2018, pp. 347-358.

Dowson, D. "A generalized Reynolds Equation for Fluid-film Lubrication." International Journal of Mechanical Sciences 4.2, 1962, pp. 159-170.

Kleijnen, J.P.C., "Kriging Metamodeling in Simulation: A Review" European Journal of Operational Research, 2009, Vol. 192, pp. 707-716.

Lophaven, S. N., Nielsen, H. B., & Søndergaard, J. "DACE: a Matlab kriging toolbox". IMM, Informatics and Mathematical Modelling, The Technical University of Denmark, 2002.

Reynolds, O. "On the Theory of Lubrication and its Application to Mr. Beauchamp Tower's Experiments, Including an Experimental Determination of the Viscosity of Olive Oil", Philosophical Transactions of Royal Society of London, 1886, Vol. 177, pp. 157-234.

Sacks, J., Welch, W. J., Mitchell, T. J., & Wynn, H. P. "Design and analysis of computer experiments." Statistical science, 1989, Vol.4, pp. 409-435.

Seeton, C.J., "Viscosity-temperature Correlation for Liquids", Tribology Letters, 2006, Vol. 22, pp-67-78.

Simpson, T.W., Peplinski, J.D., Koch, P.N., Allen, J.K., "Metamodels for Computer-based Engineering Design: Survey and Recommendations", Engineering with Computers, Journal of Operational Research, 2001, Vol.17, pp. 129-150.

Vance, J., Zeidan, F., Murphy, B., "Machinery Vibration and Rotordynamics", Wiley, New Jersey, 2010.

Xiaobo, Z., "Comparison of Response Surface Method and Kriging Method for Approximation Modeling" In: 2nd International Conference on Power and Renewable Energy (ICPRE), IEEE, 2017, pp. 66-70.

Wang, H., Li, E., Li, G. Y., & Zhong, Z. H. "Development of metamodeling based optimization system for high nonlinear engineering problems." Advances in Engineering Software, 2008, Vol. 39, n. 8, pp. 629-645.

Esperamos que este livro contribua para o debate político e filosófico sobre a educação. Afirmamos que caso seja infringido qualquer direito autoral, imediatamente, retiraremos a obra da internet. Reafirmamos que é vedada a comercialização deste produto.